2021

Compressible Hydrodynamics of Few Body Optical Vortices

Jasmine M. Andersen

Compressible Hydrodynamics of Few Body Optical Vortices

A Dissertation

Presented to

the Faculty of the College of Natural Sciences and Mathematics

University of Denver

In Partial Fulfillment

of the Requirements for the Degree

Doctor of Philosophy

by

Jasmine M. Andersen

November 2021

Advisor: Mark Siemens

Author: Jasmine M. Andersen
Title: Compressible Hydrodynamics of Few Body Optical Vortices
Advisor: Mark Siemens
Degree Date: November 2021

Abstract

The ubiquity of vortices nearly rivals that of the innumerable fluids and spaces in which they live. Not only do they exist in systems such as superfluids, superconductors, optical fields, or cold atomic gases, for example, but they also exist in our atmospheres, oceans, and even in our veins. This makes understanding and accurately predicting the dynamics of vortices in various systems a relevant and meaningful endeavor.

From a typical hydrodynamic perspective, vortices move within a given fluid because of the background fluid density and phase gradients at the vortex location. However, we find that these gradients alone are insufficient for describing vortex motion. Vortex ellipticity plays a crucial role in vortex dynamics in two-dimensional fluids, particularly during nucleation and annihilation events of oppositely charged vortex pairs. This dissertation presents a novel hydrodynamic theory that accounts for vortex ellipticity that applies to both quantum and classical hydrodynamic settings. This is achieved by viewing the two-dimensional vortex as a virtual three-dimensional circular vortex projected into the two-dimensional plane whose orientation (otherwise referred to as vortex tilt) quantifies the degree of ellipticity. The vortex ellipticity is coupled to the density gradient of the fluid, and accurate predictions of vortex motion can be made, even during nucleation and annihilation events.

A linear optical experiment used to test the new hydrodynamic theory is also discussed in detail. The experiment consists of free-space laser propagation and a spatial light modulator that projects computer generated holograms for producing vortex beams. Procedures for generating effective holograms and efficiently measuring vortex beams include a novel colinear phase-shifting digital holography technique using composite holograms that enables both amplitude and phase measurement of optical beams. Modal decompositions of experimentally generated fields show that our methods can yield vortex purities $> 99.9\%$ in the intended mode. Additional experimental details and alignment requirements are also introduced.

This experimental setup is used for two test cases that are compared with the new hydrodynamic theory: (i) a single, tilted vortex in a Gaussian beam and (ii) the annihilation of an oppositely charged vortex pair in a Gaussian beam. In both cases we find agreement between the experimental results and the hydrodynamic theory, confirming not only that the theory accurately predicts vortex motion, but also that optical systems can be described hydrodynamically. Lastly, because of the compressible fluid nature of optical systems, we show that annihilation dynamics can be altered by simply changing the initial core overlap between an oppositely charged vortex pair. Both numerical simulations and experiments confirm that annihilation dynamics are highly impacted by the initial condition, and one can even prevent the annihilation between oppositely charged vortex pairs by simply modifying this initial core overlap.

Acknowledgements

I would like to thank Prof. Mark Siemens for your encouragement and support, especially during difficult times where my personal life demanded so much of me. I am indebted to the grace you extended to me during those times. To Prof. Mark Lusk, thank you for your important contributions to our group, and your continual encouragement of me and my career. I am a better physicist and experimentalist thanks to you both. I would like to thank Prof. Davor Balzar, Prof. Maria Calbi and Prof. Shannon Murphy for serving on my committee and supporting my journey.

I would like to thank Drew Voitiv for your collaboration and relentless willingness to help. This was all possible because of your partnership. To colleagues Geoff Diederich, Dan Hammerland, Angie Davidson, Alisha Humphries, Mike Roos, Noah De Leeuw, Jon Huihui, and Sean Morgan: you all have supported me in many ways, including pushing for equity in the field. I will forever be grateful.

To Mr. Bluhm, thank you for the coolest demos and instilling in me a love of physics. To Dr. Dove, Dr. Davis, Dr. Krantz, Dr. Denn, Dr. Huber, Dr. Kuo, the CO/WY AAPT, and the MSUD SASC crew: thank you for providing the best education and being a community that continued to support me through my PhD.

Last, but certainly not least, thank you to family and friends for believing in me and putting up with my chronic stress and absence during my pursuit of higher education. And to Nate, a million thank yous. You stayed by my side through tears and joy and never once doubted me. I could imagine no better partner than you.

There are countless others. To all of you, thank you. I dedicate this thesis to all of the students, past, present and future, who are or have been told that they don't fit the bill. Keep going. Find support. And, know that you are worthy.

Table of Contents

List of Figures

I

Motivation, Context, and a Novel Hydrodynamic Theory for Noncircular Vortices

Chapter 1

Introduction

1.1 A Brief History of Vortices

In his lifetime (1452-1519), Leonardo da Vinci studied many of life's curiosities. Among them was the phenomenon of vortices in fluid systems, inspired by his observations of the flow of water in seas, rivers, and canals [1], and by his interest in the flow of blood within veins and the heart of the human body [2]. A drawing of his depicting blood traveling through the heart is shown in Figure 1.1. He also devised experiments to study fluid flow in various types of tanks and used seeds of panic grass to observe the motion of vortices in the fluid [1]. In addition to his study of vortex motion within veins and other fluids, da Vinci is considered to have foreshadowed much of today's interest in the phenomenon of turbulence. For the motion of water pouring from a spout into a pool, he described it as "... this movement being sometimes rapid and sometimes slow, and turning sometimes to the right, sometimes to the left, now up, and now down, turning over and turning back upon itself..." [2]. Along with his descriptions, his documents also contain various drawings of vortices, including those of water from a faucet plunging into a body of water shown in Figure 1.1 (b), creating the turbulent motion that he described.

Figure 1.1: Drawings of Leonardo da Vinci's depicting vortices in the flow of blood through an aortic valve (left) and the turbulent structure of water pouring from a spout (right). Credit: Royal Collection Trust/© Her Majesty Queen Elizabeth II 2019, Reprinted from [1].

While incomplete and scattered throughout his work, the general description of vortices and fluid flow provided a vital insight for the field of fluid mechanics.

In 1644, Renee Descartes hypothesized that the motion of the planets around the sun was due to a large vortex centered at the sun [3]. In his theory, the rotational motion of the planets was due to the motion of the larger vortex, dragging them along with its rotation just like the leaves on the surface of a whirlpool would move [3]. But, shortly thereafter in 1687, Newton claimed that vortices on the outer edge of the solar system should move at a faster rate than those close to the center, and this contradicted the ideas behind Descartes' theory [3, 4]. Newton's theory of gravity soon replaced the vortex theory of planetary motion due to its ability to better predict other physical phenomena such as the rising and lowering tides, while Descartes' vortex theory could not [5].

It was not until 1858 that the the first formal mathematical study of vortices was performed by Helmholtz [6]. He was the first to define a vortex line and vortex

filament, and described the motion of a small volume of the fluid [6, 7]; he also accounted for the frictional forces between each of the fluid elements and with boundaries [6, 7]. This foundation for vortices resulted in Lord Kelvin's theory of atoms in 1867 where he aimed to describe atoms and their spectra in terms of vortex filaments [7, 8]. Of course we know that these theories were replaced by the Rutherford model of the atom later in the 1900's [9], which more closely resembles our current understanding of atoms.

Skipping ahead, in 1961 Hurricane Esther was the first hurricane to have its image taken by a satellite [10]. Shortly thereafter in 1964, Feynman wrote his famous set of lectures on physics [11]. In them, he commented on what he considered as the most important unsolved problem of classical physics:

> "There is a physical problem that is common to many fields, that is very old, and that has not been solved. It is not the problem of finding new fundamental particles, but something left over from a long time ago—over a hundred years. Nobody in physics has really been able to analyze it mathematically satisfactorily in spite of its importance to the sister sciences. It is the analysis of circulating or turbulent fluids."
>
> — Richard P. Feynman, The Feynman Lectures on Physics Vol 1

Later in 1979, Saffman wrote that it may be useful to view turbulent fluids as a superposition of interacting vortices, suggesting the need to understand vortex dynamics and interactions in coherent systems [12].

Since then, technological advancements have allowed for the expansion of the study of vortices to a vast collection of systems. The most intuitive places to find vortices are those we encounter most in our every day lives, such as atmospheric or

oceanic systems [13]. In oceanic systems, large vortices are formed across the globe due to the complex ocean current networks which depend on tidal forces, Coriolis forces, winds, temperature gradients, salinity and more [14]. Unfortunately, just like the seeds of panic grass used by da Vinci to locate the vortices, these vortices contain large levels of micro-plastic pollution, with collections of plastic waste that pile up near the centers.

Other places that vortices are found and have been studied include super fluids such as Helium II [15, 16] and cold atomic gases [17], free electron beams [18], and superconductors [19, 20]. Parallels have even recently been made between the phase defects in protein waves of live starfish membranes to point vortices in two-dimensional Bose–Einstein condensates (BECs), showing that the relevance of studying vortex dynamics extends to important biological processes [21]. Vortices can also be found in laser beams [22], and they have become a common topic of study for the field of optics [23]. While there is extensive interest in each of the mentioned areas, the experimental work of this dissertation is focused on the application of understanding vortex motion in coherent linear optical beams. So, an introduction to optical vortices is important and will be taken up next.

1.2 Optical Vortices

Inspired by the singularities present in radio pulses returning from land under the Antarctic ice sheet, Nye and Berry examined the structure and properties of dislocations in waves [24, 25]. Originally denoted as "screw dislocations", optical vortices are described by singular points in a macroscopic, coherent optical field with quantized, azimuthal phase wraps. This phase wrap goes as $2\pi\ell$, where ℓ is

an integer (positive or negative) number of azimuthal phase wraps, often called the "topological charge" or just the "charge" of the vortex.

Optical modes containing a single, central vortex are also often referred to as "donut modes" because of their characteristic shape in the beam's intensity [26–29]. When the paraxial equation is solved in cylindrical coordinates, it yields the Laguerre Gaussian (LG) eigenmode (a specific type of such "donut modes"). These modes are mathematically expressed as

$$LG_{\ell,p}(r,\phi,z) = \sqrt{\frac{2p!}{\pi(p+|\ell|)!}}\frac{w_0}{w(z)}\left(\frac{r\sqrt{2}}{w(z)}\right)^{|\ell|} e^{-\frac{r^2}{w^2(z)}} L_p^{|\ell|}\left(\frac{2r^2}{w^2(z)}\right) \times e^{i\ell\phi} e^{i(|\ell|+2p+1)Arctan(z/z_R)} e^{-ik\frac{zr^2}{2(z^2+z_r^2)}}. \quad (1.2.1)$$

Figure 1.2 shows examples of the amplitude and phase for a few LG vortex modes. For the $\ell = 0$ mode, the beam is a simple Gaussian with a flat phase front (hence the uniform color in the phase plot). For higher order ℓ, the phase now wraps in a helical fashion around the beam which goes as $2\pi\ell$, and there is a singularity at the center that goes as $r^{|\ell|}$ in the amplitude.

Subsequent work connecting these vortices to the orbital angular momentum of light by Allen et al [30] catalyzed an entire field of study, including efforts to understand optical vortex kinematics [23, 31–36], utilize the angular momentum in light-matter interactions [23, 37–43], and make use of the orthogonality between vortex modes of differing topological charge for communications purposes [23, 44–50].

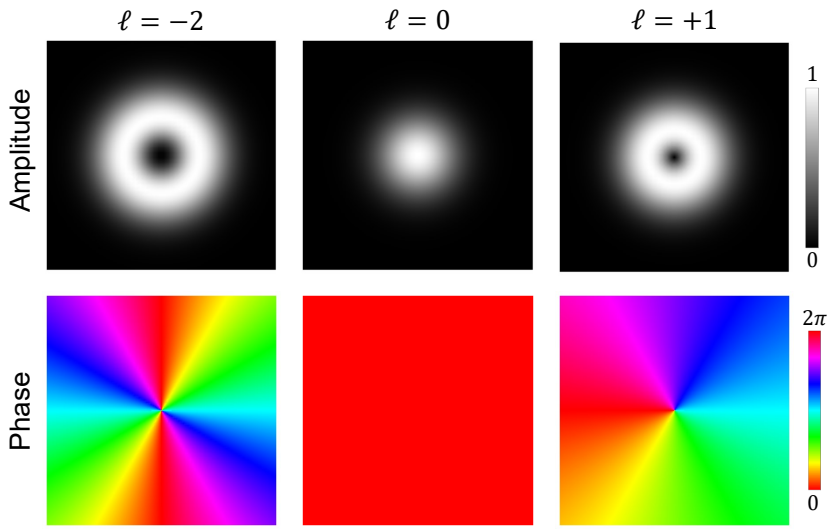

Figure 1.2: Amplitude and phase for LG modes of order $\ell = -2$, $p = 0$ (left), $\ell = 0$, $p = 0$ (middle), and $\ell = +1$, $p = 0$ (right).

Common Generation and Measurement Techniques

There are many ways to generate optical vortices [51–54]. One common and simple way to produce an optical vortex is by using what is called a spiral phase plate [55, 56]. This is a piece of glass etched at a variable azimuthal thickness such that the glass creates a spiral shape with a singularity in the center. Since we know from basic optics principles that light slows down when it enters a medium with a higher index of refraction [57], it is easy to see how this etched piece of glass creates a helical phase: light passing through a thin part of the plate is slowed down for less time than the light passing through a thicker part. Because of the geometry of the etching, the beam acquires the helical phase delay, characteristic of vortex beams.

While simple in concept, there are downsides to using spiral phase plates. Because it is made of glass, the phase delay around the beam will only be appropriate

for the wavelength of light that it is designed for. Additionally, it is typical to want to generate optical vortices of various different charges, and to generate a given charge, a unique spiral phase plate is required. This makes generating more than one type of field containing vortices a cumbersome activity.

Many have created optical vortices using spatial light modulators (SLM) [58–64]. An SLM usually consists of a liquid crystal display (LCD) panel that modulates either the phase or amplitude of an incident field on a pixel-by-pixel basis [65], and they are useful because fields generated can be quickly changed by simply changing what is projected on the LCD panel without moving the optic. SLMs can be used to directly stamp a desired phase onto an incident beam; alternatively, a diffractive hologram can be programmed onto an SLM to control both amplitude and phase. A diffractive hologram is commonly referred to as a forked grating [66], which is created by superposing a planewave with a spiral phase (with topological charge that can be varied). A Gaussian laser beam incident on a forked grating produces a transmitted vortex beam in the first diffracted order with a vortex charge that matches the charge of the grating [23, 67–70].

The LG modes of Equation 1.2.1 make up a set of eigenmodes of free space, and the orthogonality between the modes makes them an interesting candidate for communications purposes. Additionally, there are no theoretical restrictions on the degree of topological charge, and essentially, the modes make up an infinite basis set that can be used to transmit data if one could directly read out the modal content from a beam. Because of such applications to communications, there is a large body of work on measuring the different topological charge states of vortex beams that can be created by forked gratings and spatial light modulators. Since the vortex is intrinsically in the phase winding of a laser beam, the phase must be measured.

Because of this, a common way to measure the charge of a vortex is to interfere the vortex beam with reference beam. For reference beams that are of a planewave nature (like a normal Gaussian laser beam), a fork in the interference pattern can identify a vortex, because the number of prongs determine the charge [71,72]; when the reference is a vortex beam of opposite helicity to the measured beam, one can simply count the number of azimuthal fringes present [73–75]. Counting fringes at the focus of a cylindrical lens can also reveal the topological charge of a given beam [76], and the charge has similarly been measured by transforming a vortex beam using annular gratings [77].

Others have used modal decomposition techniques which take a transverse field measurement and breaks it down into its modal content, therefore measuring the topological charge and radial mode content of a given beam [78–85]. Recent efforts have shown that the detection of the topological charge of a vortex beam can be measured through photocurrents [86,87], bringing the field one step closer to on-chip detection methods of varied topological charges. Most of this work is focused in the realm of single vortices of various, higher order charges or modal superpositions that can be used for communications. But, there is also a separate focus on vortex fields that contain anywhere from a few to hundreds of optical vortices.

Optical vortices can be generated from a set of as little as three random plane waves [88, 89]. Increasing the number of random plane waves creates fields that contain high densities of optical vortices, usually referred to as optical speckle [90], shown in the top row of Figure 1.3. Scattering light from a diffusor or a piece of scotch tape [91] results in a random set of plane waves, and therefore can be used to generate optical speckle. Speckle has been generated by sending light through a screen with multiple apertures at different transverse locations [92] and spatial light

modulators have also been used to generate optical speckle by creating a randomized a vortex lattice that is propagated through a lens [93]. These optical speckle patterns evolve with beam propagation, in complex tangled patterns reminiscent of vortex motion in other quantum fluids. A recent study numerically simulated and experimentally measured the complex vortex dynamics in laser speckle, shown in Figure 1.3. The results of this study particularly motivated the work of this dissertation, with the aim to understand the physical mechanisms behind these complex dynamics.

Whether there are hundreds of vortices or only a few, it is often the case that the vortices present in a beam will move in the transverse plane as the beam propagates. This has been investigated using modal decompositions of vortex fields, Fourier analysis and scalar diffraction theories [31–33, 35, 36, 95] which can be used to analytically or numerically propagate fields. Once the field as a function of propagation are determined, it is possible to identify the vortex locations at various propagation distances [24]. Tracking the evolution of the vortices with propagation allows for in a measurement of the vortex dynamics that occur in the transverse plane. Quantifying these trajectories provides some insight as to how modifying the initial condition can alter a vortex trajectory [96, 97].

While tracking vortices with propagation is useful for quantifying the trajectories and can illuminate how certain changes impact the dynamics, it does not provide a physical understanding for why the vortices move the way they do within the beam. The following section will discuss a perspective of beam propagation that analogizes optical systems to other two-dimensional fluids. Later, this will help us to build a hydrodynamic interpretation of vortex motion in light.

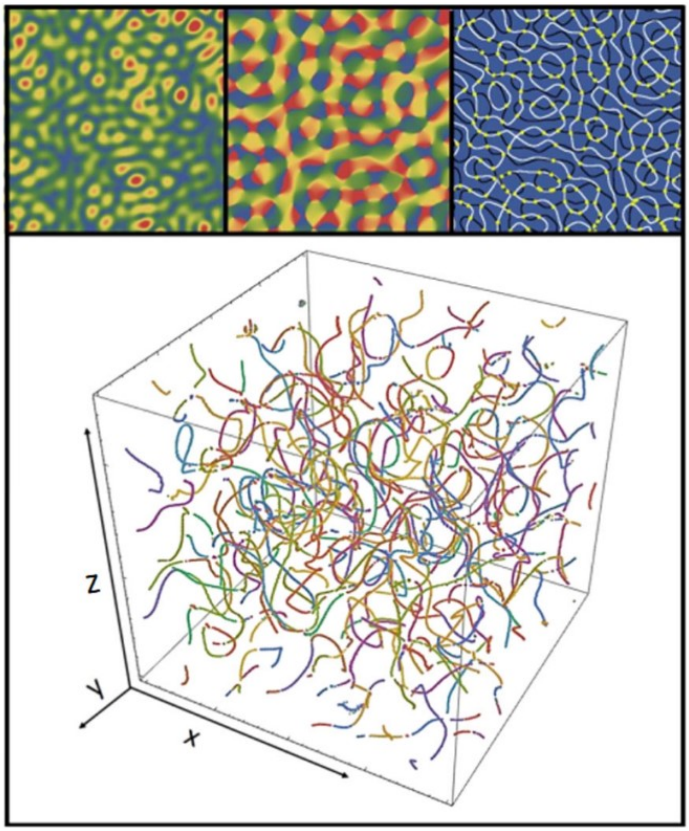

Figure 1.3: The transverse amplitude (top left) and phase (top middle) of a typical random wave. The top right panel shows the zeros of the real (white) and imaginary (black) parts of the wave represented in the top two panels, the intersections of which occur at phase singularities, which are marked in yellow. These singularities can be tracked over the propagation of the wave, the paths of which are shown in the bottom panel. That cell is oriented such that the z axis is vertical. Each vortex line is marked in a different color highlighting a complicated, tangle-like structure. The form of tangled vortex lines shown here appears qualitatively identical to similar plots of vortex lines in condensed matter systems [94]. From Alperin, 2019. [95] © American Physical Society

1.3 Light as a Fluid: Optical Vortex Dynamics

The goal of the work in this thesis is to build a hydrodynamic understanding of vortex motion in optical beams. In essence, there should be a way to use the background phase and amplitude gradients along with the properties of the vortex

itself to predict its motion if optical vortices can be described hydrodynamically. Before we delve into the details, it is important to establish the setting for this problem. The optical system will be treated from the perspective of a "2+1D" system, such that the z-axis no longer represents a spatial coordinate, but instead plays the role of time.

A "2+1D" Fluid Perspective for Optical Vortices

We consider the optical beam as a "2+1D" system: the paraxial propagation axis replaces time via $z = ct$, where c is the speed of light. The laser beam is then a two dimensional, coherent fluid described by a macroscopic wavefunction wherein the dynamics happen in the transverse plane. A schematic of this is shown in Figure 1.4.

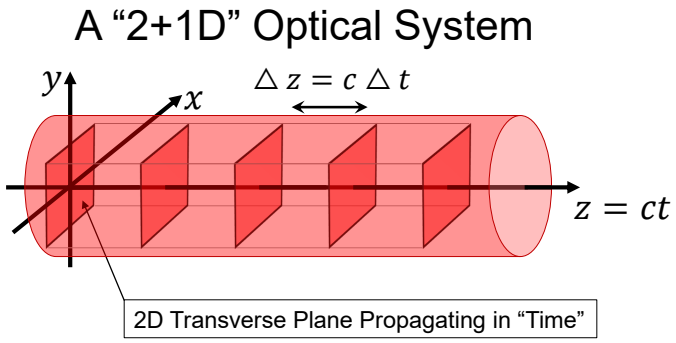

Figure 1.4: Optical beams in the view of a "2+1D" system where the z-axis plays the role of time.

When considering the z-axis as an analogue to the time axis, we can quickly see how our optical system closely resembles that of other two-dimensional fluids by comparing the governing equations for optical systems to that of BECs at low temperatures, for example. For such BECs, the wavefunction evolution is governed

by the Gross-Pitaevskii Equation: [98, 99]

$$i\hbar\partial_t\psi + \frac{\hbar^2}{2m}\nabla_\perp^2\psi - V_{ext} - g|\psi|^2 = 0 \tag{1.3.1}$$

where ψ is the two-dimensional, macroscopic wavefunction of the condensate, V_{ext} describes an external potential, and g describes the strength of the atomic interactions in the system[1]. In the case of no nonlinear interactions and no external potential, the Gross-Pitaevskii Equation reduces down to

$$i\hbar\partial_t\psi + \frac{\hbar^2}{2m}\nabla_\perp^2\psi = 0. \tag{1.3.2}$$

Optical systems on the other hand are governed by the paraxial equation which in the case of no nonlinearity is written as

$$2ik\partial_z\psi + \nabla_\perp^2\psi = 0 \tag{1.3.3}$$

where ψ is the transverse wavefunction and $k = 2\pi/\lambda$ is the usual wavevector. Immediately, it is easy to see the similarities between the two equations. One can loosely transform the linear, Gross-Pitaevskii Equation into the paraxial equation by recalling that $p = mv = \hbar k$ and by replacing ∂_t with ∂_z using the analogy.

Quickly emphasizing these parallels aids in understanding the treatment of light as a two-dimensional fluid and the potential application of results from other fluids to light, but we are far from the first to build such connections between a hydrodynamic interpretation of optics and other quantum fluids [100–110]. More rigorously, a Madelung transformation [111] of the paraxial equation re-casts the

[1]This Gross-Pitaevskii Equation is a form of the Nonlinear Schrödinger Equation for a nondissipative, zero temperature BEC [98]

the bulk dynamics as an Euler equation, allowing for light to be interpreted as an inviscid, compressible, two-dimensional fluid [100, 108]. In fact, light's compressible fluid nature has been directly called out because of the fact that the NLSE for optics can be rewritten in terms of a continuity equation and the Bernoulli Equations [104]. Proukakis provides an overview of the body of work regarding the similarities of BECs in analogy to optical systems [106]. While the similarities between the Schrödinger and paraxial equations are striking and inspiring, it is not exact. Two immediate reasons are that (i) ψ for optical modes are composed of classical electromagnetic fields (that are not quantum wavefunctions) whereas ψ for BECs describes the condensate wavefunction [106] and (ii) position is not the same as time. For these reasons, the connection is referred to as a "formal analogy."

It is important to note that the analogy between the Gross-Pitaevskii Equation and optical systems is valid for both linear and nonlinear optical systems. In fact, the full form of the nonlinear Schrödinger Equation describes the propagation of light in nonlinear optical systems [100, 106]. For example, waveguides with a varied transverse refractive index are analogous to the external potential term in the Gross-Pitaevskii Equation [106]. Perhaps some of the reason the incomplete hydrodynamic picture for the linear optical case has not yet been addressed is because a large shift in focus happened: nonlinear systems in which the light-matter interaction can dominate the fluids interpretation restores GPE physics and superfluid dynamics. This has prompted a diverse body of work dedicated to "Quantum Fluids of Light" which include, for example, light passing through bulk nonlinear crystals to induce photon-photon interactions or to create polaritons, and other systems where light is trapped into cavities and interacts strongly [110, 112–115].

1.3.1 Prior Work: Vortex Dynamics in Linear Optical Systems

Optical vortex dynamics for vortex pairs in a linear system was analytically and numerically treated by Indebetouw in 1993 [32] and shortly thereafter by Rozas et al in 1997 [31]. Rozas and Swartzlander's pioneering exploration of vortex dynamics in a propagating laser beam yielded a hydrodynamic a velocity expression that depends on the background field's amplitude and phase gradients that can be used to predict vortex motion in some cases [31, 100, 116]. They found that a single, linear core vortex displaced in a Gaussian beam moves in the *xy*-plane depending on the background field. However, they also found that the vortex motion was unchanged if another same-charge vortex is added to the system. Their conclusion was that linear core vortices exhibit no effective interactions, since the motion of one vortex is not dependent upon the presence of another. They also concluded that only small, point-like vortices can exhibit "fluid-like" motion in linear light [31, 100].[2]

The search for vortex interaction in optical systems continued and in 2004, Roux discussed vortex interactions amongst pairs of opposite topological charge that morph into non-circular vortices as they move within a propagating beam [117]. Using a modal analysis, he derived an expression for a beam at $z = 0$ in terms of parameters that describe the morphology of each vortex and found a coupling term to describe the strength of the interaction [117]. These oppositely charged vortex pairs have been analytically and numerically shown to annihilate, depending on the initial beam parameters [32, 35, 118]. Based on the implications of the work done by Rozas et al, Chen and Roux later applied a global background phase to a beam

[2] "Fluid-like" in this context is related to a specific subset of fluids where only phase gradients are present and the density is uniform.

containing an oppositely charged vortex pair to change the rate of annihilation of a vortex pair [96], relying on numerical techniques to confirm their predictions.

This collection of work specifically dedicated to vortex motion in linear light mostly relies on analytical or numerical methods, and aside from Rozas, we have not seen the linear dynamics addressed from a hydrodynamic perspective. As we will see in Chapter 2, though, the hydrodynamic models previously derived are only applicable to circular vortices, and they do not work for the simple case of an oppositely charged vortex pair in a linear beam propagation. Indeed, the annihilation between opposite charge vortex pairs seen in linear systems has been attributed to beam diffraction (rather than being consistent with hydrodynamics) [119].

1.4 Dissertation Outline

This dissertation is broken up into three parts. In the first part, I will began with a brief history of vortices and an introduction to optical vortices, providing some context for the topics discussed in this work. This is followed up by Chapter 2, which is written to highlight the issues with applying previous models for predicting vortex motion and the thought process behind our hypotheses for why the models are insufficient. The development of a novel theory for predicting vortex motion in laser beams from a hydrodynamic perspective based on the background field gradients and vortex ellipticity is then discussed in detail in Chapter 3. These theoretical developments are the work of Prof. Mark T. Lusk from the Colorado School of Mines, in collaboration with Prof. Mark E. Siemens, fellow Ph.D student Andrew A. Voitiv, and myself.

The formalism of Chapter 3 is then tested experimentally. Part II consists of the motivation for and use of computer generated holograms, including key issues that

can arise in hologram generation which are spelled out in Chapter 4, followed by a new colinear phase-shifting digital holography approach to measure laser beam amplitude and phase using composite holograms in Chapter 5. A detailed account of the full experimental apparatus developed for measuring vortex dynamics written in Chapter 6 concludes Part II. The final part of this work details the experimental results. Chapter 7 discusses results for linear core vortex dynamics. Numerical and experimental results for vortex annihilation events for vortices initially with a hyperbolic tangent structured vortex core of varying size are the topic of Chapter 8. The dissertation is concluded with a final discussion of the work and future directions this research could head in.

The experimental work in this dissertation was completed by myself, under the supervision of Prof. Mark Siemens. The exceptions are: the single vortex velocity measurements were a collaborative effort between Andrew A. Voitiv and myself with final reported measurements taken by Andrew A. Voitiv, under the supervision of Prof. Mark E. Siemens, contributions from Samuel N. Alperin, Andrew A. Voitiv, William G. Holtzmann, Prof. Juliet T. Gopinath and Mark E. Siemens in the manuscript and data that was used as the basis of chapter 5, and chapter 9 is based on collaborative discussions between myself, Andrew A. Voitiv, Prof. Mark T. Lusk and Prof. Mark E. Siemens.

Chapter 2

The Hydrodynamic Model for 2D Fluids is Incomplete

A portion of this work was published in Physical Review A: Volume 104, Issue No. 3, under the title ***Hydrodynamics of noncircular vortices in beams of light and other two-dimensional fluids***. [120]

The motion of a circular vortex in a two-dimensional fluid is determined by both the background amplitude gradients and background phase gradients at the location of the vortex [98, 100, 101, 121]. Because of this, it is important for characterizing the motion of a given vortex that exists within a system containing multiple vortices to not only consider the phase structure of the other vortices, but also the size and shape of the amplitude in their cores. In this chapter, we will very briefly review the expectations for vortex motion in the case of both incompressible and compressible two-dimensional fluids. These expectations can then be compared to the actual trajectories measured for vortex pairs in a Gaussian beam using the propagation of modes. We will then consider the applicability of a previously derived velocity equation used in other two-dimensional fluids to a set of oppositely charged optical vortices [98]. In doing so, we will see that a previously derived result used to predict vortex dynamics for other two-dimensional, compressible fluids holds for

optical vortices at the beam waist, but fails beyond $z = 0$.[1] This will provide insight and motivation for the theoretical developments of Chapter 3.

In an effort to be very clear for the remainder of this dissertation, unless mentioned otherwise when I refer to hydrodynamics I am using the term generally- i.e. not specifically implying incompressible fluid dynamics. Sometimes in the literature on optical vortices, violation of incompressible hydrodynamics is taken to be a violation of a hydrodynamic interpretation altogether. But, this is not surprising, since a full understanding of vortex hydrodynamics was not presented until the work in this dissertation. For the sake of clarity and being very explicit, my use of the word will encompass both incompressible and compressible fluid dynamics, and will expand to include vortex ellipticity (also referred to as vortex tilt) in Chapter 3.

2.1 Vortex Dynamics in Incompressible vs. Compressible Fluids

Because of the prevalence of vortices in many different types of systems, considerable work has been done to understand the physics of vortex interaction [122, 123]. We can now consider the conceptual differences for various fluids that govern how a given vortex will move depending on the background amplitude and phase gradients present within the fluid.

In a purely incompressible fluid there are no density gradients (except for very steep ones with a characteristic "healing length" typically less than a nanometer), so the density is constant throughout the entire fluid. This means that vortices existing within the fluid can have a long ranged phase structure, but are are near delta functions in their density with no meaningful overlap with other vortices when the

[1] We will see later that the reason for this discrepancy is that vortices at $z = 0$ are circular, making the previous fluid models applicable at the initial condition. However, beyond $z = 0$ the vortices are no longer circular, and the models no longer are accurate.

separation is larger than the healing length. Milne-Thomson showed that in an incompressible fluid, vortex motion follows the phase gradient (fluid velocity) of the underlying fluid at the location of the vortex. The fluid velocity is determined by other vortices and their location in the system [122]. This phase gradient leads to the familiar setting in which vortex pairs of the same rotation circle around each other and those of opposite rotation will propel each other forward [122, 123]. This forward motion in the case of an opposite charge vortex pair is the reason that bubble or smoke rings are propelled forward: these rings are a vortex taurus, where a cross sectional slice of such a ring yields a pair of vortices with opposite circulation [123].[2]

For a compressible fluid, there are usually significant density gradients in the fluid. Recent work has shown that hydrodynamic models derived from the Gross-Pitaevskii equation can be extended to include density inhomogeneity, in which case density gradients also contribute to the vortex velocity [98]. Vortices in this compressible setting have cores that are no longer reminiscent of the delta function-like cores in an incompressible fluid, but are characterized by linear amplitude core. This means that for a given vortex within the fluid, its motion is not simply dictated by the phase gradients present from other vortices, but may also respond according to the total density gradient of their amplitude cores at the location of the vortex.

The contributions to vortex motion for both the incompressible and compressible fluid cases are compared visually in Figure 2.1. For a static fluid with no vortices initially, a vortex placed within the fluid would not move since both the amplitude and phase gradients are zero, shown in the top row of the figure. In the

[2]Dianna Cowern, also known as "Physics Girl" on YouTube, has a very accessible and wonderful video in relation to this type of vortex motion in a pool of water [124].

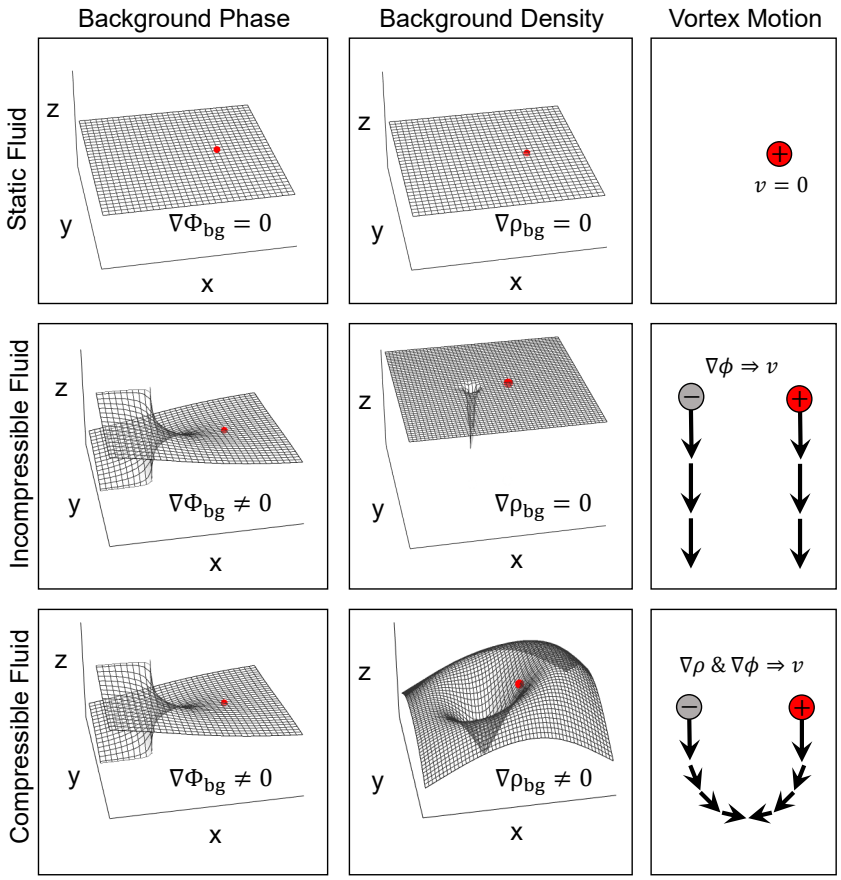

Figure 2.1: Background phase and fluid density are shown for static, incompressible and compressible fluids. The resulting velocity of the vortex on the right (marked in red) is shown for each case as described in the text.

second row, an example for a two vortex system in an incompressible fluid is shown. The phase gradient is that of a circular, negatively charged vortex on the left and the vortex of interest is a positive vortex (marked in red) on the right. The phase gradient of the left vortex is the only contributor to the right vortex's velocity, since the density core is a near delta function. The result of this calculation (and the same calculation accounting for the effect of the right vortex on the left) is that both vortices move downward for the specified geometry. If the charges were reversed, both

vortices would instead move upward. For the last row in the figure, a compressible two vortex system is shown, where neither gradient is zero since the density core of the left vortex has meaningful overlap with the right vortex.

Looking at the propagation dynamics of vortices in a laser beam can reveal whether or not we anticipate the motion of optical vortices to follow incompressible or compressible fluid dynamics. A review of vortex pair dynamics from the propagation of modal superpositions is discussed next, followed by the initial attempt at describing the motion hydrodynamically in terms of the background field.

2.2 Review of Vortex Pair Motion in a Gaussian Beam

It is known that when placing a note card into a laser beam at a fixed propagation distance z, the field distribution in the transverse plane will not evolve as long as the field generated at $z = 0$ remains the same. The motion of optical vortices that we consider is due to the beam evolution as the propagation distance increases. Here, the z coordinate acts as the analogy to time in a two-dimensional fluid, resulting in a "2+1D" optical fluid system as discussed in Section 1.3.

To quantify vortex motion in such a system, we can consider propagating the modal content of a given field and then use the real and imaginary zeros to locate the vortices throughout the trajectory [90]. This has been a successful and straightforward way to quantify vortex dynamics and will be used here to review the anticipated dynamics for vortex pairs in a Gaussian beam, since previous work has already quantified this for pairs of the same charge [31, 32] and opposite charge [32]. Although some have considered the impact of introducing asymmetries into the beam [96, 97], we strictly adhere to symmetric host beams for this discussion.

To create a field of two like charge vortices displaced symmetrically along the x-axis, one needs to simply colinearly superpose an $LG_{\ell=+2,p=0}$ mode with a Gaussian. The addition of the Gaussian to the LG mode splits the single vortex with charge $\ell = +2$ into two separate vortices of unit charge, with the relative power of the modes determining the vortex separation [125–127]. We will say that each vortex is initially displaced by x_0 symmetrically from $x = 0$. This field is given by

$$\psi_{\text{same}}(x,y,z) = 2d^2 LG_{0,0}e^{i\pi} + \sqrt{2}LG_{2,0} \tag{2.2.1}$$

where $d = x_0/w_0$ and w_0 is the beam waist. The trajectory found from propagating a beam of this modal content is consistent with previous observations, where the vortices move in straight line trajectories perpendicular to their radial displacement in the beam [31, 32], shown in Figure 2.2. This straight line, constant velocity occurs regardless of the initial separation, and the observed vortex speed increases with different initial conditions for which the separation is increased.

This motion is in contrast to the expected circular motion of a like charge vortex pair for an incompressible fluid [123]. In general, a vortex located in the center of

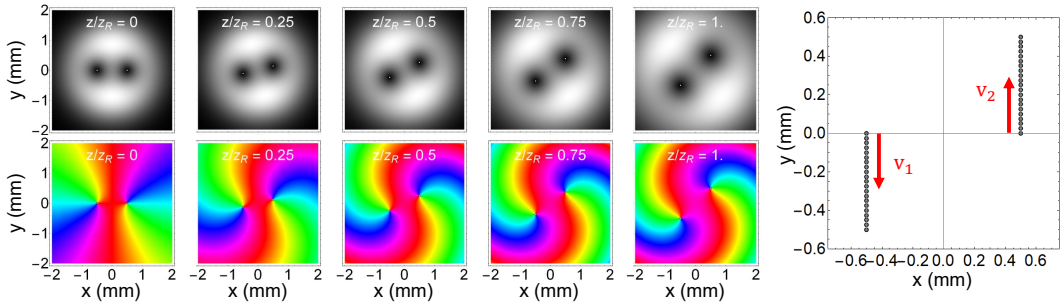

Figure 2.2: Amplitude and phase slices for the propagation of a same charge vortex pair with $w_0 = 1$ mm, $x_0 = 0.5$ mm, and $\lambda = 633$ nm up to a Rayleigh length, along with the tracked vortex trajectories.

an $LG_{\ell,p}$ mode has an amplitude core that is proportional to $(r)^{|\ell|}$ according to the functional form of the *LG* mode in Equation 1.2.1. If an *LG* mode of higher order charge is split into a set of several vortices by superposing it with a Gaussian beam, each vortex is then of charge $|\ell| = 1$, and the vortices then have linear (r^1) amplitude core structures. Consequently, these optical vortices are quite different from vortices with delta function-like cores, and the difference in vortex core shape does impact the motion in the system. Rozas et al. examined this case numerically, and derived the velocities for this same charge vortex pair using his expression based on the background amplitude and phase in the beam at the location of the vortices [31], acknowledging that optical vortex dynamics must account for such compressiblity in the system.

It is possible to prepare an optical system in which the vortices are delta function-like at the beam waist. Rozas et al. showed that for such small core vortices, the vortices follow an incompressible fluid-like motion for small propagation distances. This holds only for small z due to beam diffraction, which will yield a core that increases in size with propagation [31]. These expanding cores approach the linear cores predicted above and likewise the fluid motion approaches the compressible case with propagation.

For an oppositely charged vortex pair with linear vortex cores, like that of Indebetouw's work [32], the field can be written as a sum of LG modes such that

$$\psi_{\text{opp}}(x,y,z) = (1-2d^2)LG_{0,0} + \sqrt{2}dLG_{1,0} - \sqrt{2}dLG_{-1,0} - LG_{0,1} \qquad (2.2.2)$$

where $d = x_0/w_0$ describes the vortex separation relative to the size of the beam waist. Details for obtaining this via a modal decomposition can be found in Ap-

pendix A.1. The vortex dynamics can be wildly different in this case depending on the ratio of x_0/w_0. Vortex annihilation is seen for pairs where $x_0 < w_0/2$ [32, 33], and the annihilation rate increases as x_0/w_0 gets smaller. In contrast, when $x_0 > w_0/2$ the vortices travel farther apart with propagation and do not annihilate each other [32]. In fact, the trajectory can vary from traveling in the $-\hat{y}$ direction to having motion in the $+\hat{y}$ direction, depending on the initial vortex separation as shown in Figure 2.3.

This behavior is dramatically different than the incompressible fluid expectation, where the vortices are expected to only ever move in straight lines. It is also very different from the same charge vortex case, indicating that the velocity in a given system is also dependent on not only on the signs of the charges present, but their *relative* signs. Additionally, while the algebraic expression has been found to

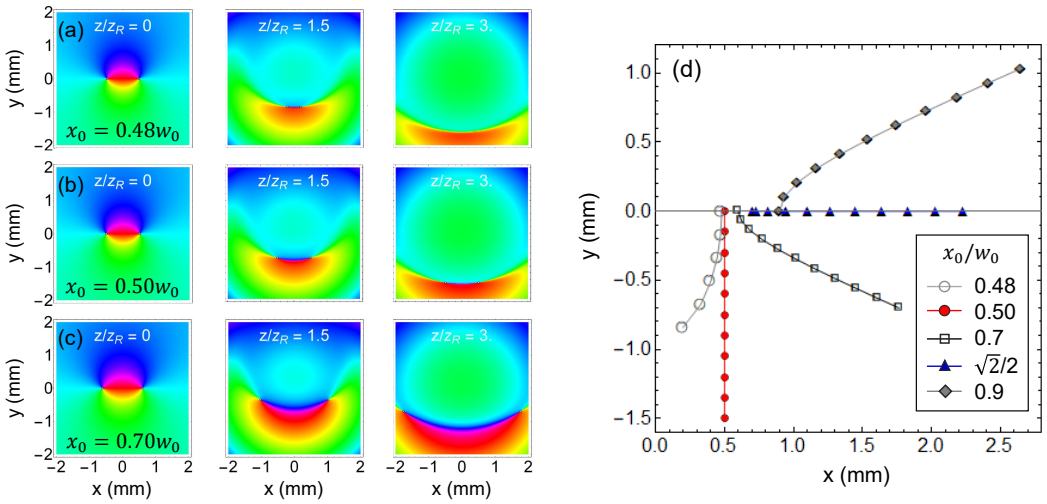

Figure 2.3: (a-c) A set of phase snapshots calculated from propagation of Equation 2.2.2 with $w_0 = 1$ mm and $\lambda = 633$ nm over a distance of three times the Rayleigh length for an oppositely charged pair. (d) tracked vortex trajectories for various initial conditions labeled in the inset of the plot. A variety of velocities and trajectories are possible depending on the initial condition for the vortex separation.

accurately describe the motion for each of these trajectories based on the initial vortex separation, we are still left wondering why exactly these dramatic differences occur.

Our hypothesis at this stage is that a hydrodynamic model that describes optical vortex motion including both the incompressible and compressible fluids contributions may allow us to differentiate these cases. Rozas applied this sort of test to a same charge vortex pair [31] (but, these results were not very exciting since the vortices move independently of each other within a beam), and a reasonable next step can be taken to see if this sort of model can also work for the opposite charge vortex pair.

Vortex Motion in a Fluid

In Section 1.3, we discussed the parallels between the governing equations for BECs and paraxial optics. It is interesting to consider extending the comparison beyond the governing equation and applying it to optical vortex motion as well. With this in mind, we consider an initial system consisting of a Gaussian laser beam with N linear core vortices placed at specified locations. The wavefunction for such a field can be written as

$$\psi(\mathrm{r},\phi) = \mathrm{e}^{-\mathrm{r}^2/\mathrm{w}_0^2} \prod_{\mathrm{j}=1}^{\mathrm{N}} \left(\mathrm{r_j} \ell_\mathrm{j} \mathrm{e}^{\mathrm{i}\phi_\mathrm{j}} \right), \tag{2.2.3}$$

where w_0 is the Gaussian beam waist, $r_j = \sqrt{(x-x_j)^2+(y-y_j)^2}$ and is non-dimensionalized by $\sqrt{2}w_0$, l_j describes the quantized phase wrap, referred to as the topological charge, and $\phi_j = \arctan\left(\frac{y-y_j}{x-x_j}\right)$ for the j^{th} vortex. We will refer to this class of vortices as linear core vortices because of the linear amplitude structure

of each vortex.[3] To characterize the motion of a specific vortex in an N vortex system, we follow Rozas et al. and separate the contributions of that vortex from the rest, and consider all other contributions as comprising the background field for that vortex [31]. For example, we are interested in looking at the motion of the $j = 1$ vortex; the field in Equation 2.2.3 can be rewritten into the form

$$\psi(r,\phi) = r_1 e^{i\ell_1\phi_1}\tilde{\rho}e^{i\tilde{\phi}} \tag{2.2.4}$$

where $r_1 = \sqrt{(x-x_1)^2+(y-y_1)^2}$, $|\ell_1| = 1$ for a unit topological charge, and $\tilde{\rho}$ and $\tilde{\phi}$ are denoted as the background amplitude and phase, respectively. The multiplicative nature of Equation 2.2.3 allows for this simple separation.

This type of vortex wavefunction is not exclusive to linear optics and is also used in the case of the BEC mentioned earlier [98]. In particular, Groszek's work described the motion of linear core vortices in a two dimensional BEC by applying the unitary evolution operator to propagate a wavefunction such as that of Equation 2.2.4 and substituting the result into the Gross-Pitaevskii equation (Equation 1.3.1). Doing so yielded an expression from which the vortex position as a function of time was analytically derived, and therefore the vortex velocity could be extracted [98]. The result was

$$\vec{\mathrm{v}}_{\mathrm{vortex}} = \frac{\hbar}{\mathrm{m}}\left(\nabla\tilde{\phi} - \hat{\kappa}\times\nabla\ln\tilde{\rho}\right), \tag{2.2.5}$$

where $\tilde{\phi}$ and $\tilde{\rho}$ are the background phase and density of the fluid and $\hat{\kappa}$ is the circulation of the vortex whose velocity is being determined. This expression has a familiar, intuitive interpretation based on the discussions of Section 2.1: the back-

[3] Such linear core vortices are also referred to in the literature as large core, conventional or even as point vortices [32, 98, 100]. In Chapter 8, we will use "point vortex" to specifically mean a vortex with a sharp, or delta function amplitude core.

ground amplitude and phase gradients at the location of a particular vortex drive the vortex motion.

With the goal of interpreting the motion of optical vortices from this same perspective, the result can be then be loosely transformed using parameters relevant to optics, just as was done for the Gross Pitaevskii Equation above. Recasting Eq. 2.2.5 in analogy to this result using wavenumber, $k = \frac{2\pi}{\lambda}$, where λ is the wavelength of the laser, and momentum, $p = mc = \hbar k$, we find that the velocity of optical vortices can then be written in terms of optical parameters as

$$\vec{v}_{\text{vortex}} = \frac{\partial \vec{r}}{\partial z} = \frac{\lambda}{2\pi}\left(\nabla_{\perp}\tilde{\phi} - \hat{\kappa} \times \nabla_{\perp} \ln\tilde{\rho}\right) \tag{2.2.6}$$

where $\tilde{\phi}$ remains the background phase of the beam, $\tilde{\rho}$ is now the background amplitude of the beam, and $\hat{\kappa}$ is now the topological charge of the vortex whose motion is being described. If $\ell = +1$, then $\hat{\kappa} = +\hat{z}$, and similarly for $\ell = -1$, $\hat{\kappa} = -\hat{z}$. The subscript has been placed on $\nabla_{\perp}$ to specify that the derivatives are strictly in the transverse plane of the beam, and perpendicular to the propagation direction. Similar expressions for vortex velocity based on background field gradients in optical systems have been obtained previously [100, 101].

The velocity relationship of Equation 2.2.6 can now be applied to optical vortex dynamics for different vortex configurations to test its validity and applicability to our optical systems of interest. In the next two sections, we will see that this model is acceptable at the initial condition where vortices are circular, but once the beam begins to propagate and the vortices become elliptical, the model is no longer accurate.

2.3 Initial Velocity for Optical Vortex Pairs

Calculating the anticipated velocity at the initial condition is a first step toward this goal. We start by using Equation 2.2.3 with $N = 2$ vortices, with the left vortex denoted as vortex 1 and right vortex as vortex 2, and solve for the velocity of vortex 2, $\vec{v}_2$. This initial field amplitude is shown in Figure 2.4 (a) for reference throughout the section. For now, the topological charge of each vortex will not be specified, giving the general form for a two vortex field at $z = 0$ as

$$\psi_0(r,\phi) = r_1 e^{i\ell_1\phi_1} r_2 e^{i\ell_2\phi_2} e^{-r^2/w_0^2} \tag{2.3.1}$$

where vortex 1 is located at $\vec{r}_1 = -x_0\hat{x}$, and vortex 2 is located at $\vec{r}_2 = +x_0\hat{x}$. Although this type of analysis should hold for asymmetric vortex arrangements, only this symmetric case is considered. With this initial wavefunction, the general velocity at $z = 0$ can be found from Eq. 2.2.6 for vortex 2. We write the total field as the product of the right vortex component and the background field such that

$$\begin{aligned} \psi_0(r,\phi) &= r_2 e^{i\ell_2\phi_2}\psi_{bg} \\ \psi_{bg}(r,\phi) &= r_1 e^{i\ell_1\phi_1} e^{-r^2/w_0^2}. \end{aligned} \tag{2.3.2}$$

This background field can be further split into its background amplitude and phase components such that

$$\begin{aligned} \Phi_{bg} &= \ell_1\phi_1 \\ \rho_{bg} &= r_1 e^{-r^2/w_0^2}, \end{aligned} \tag{2.3.3}$$

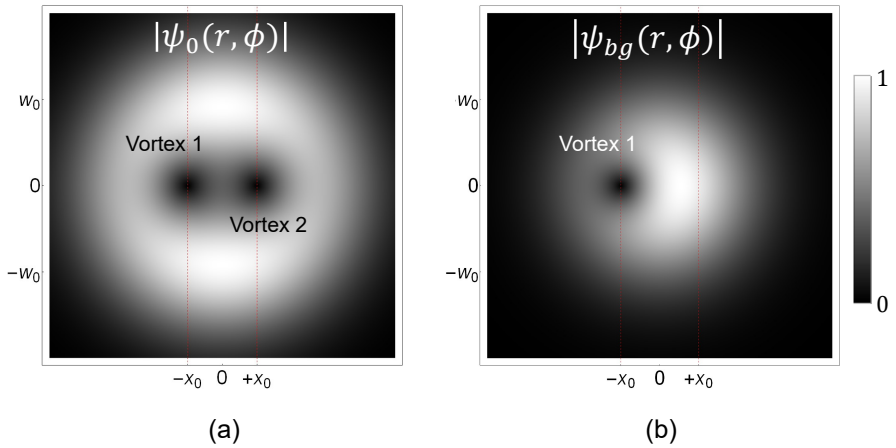

Figure 2.4: (a) Field amplitude is plotted for a two vortex system with vortices located at $(\pm x_0, 0)$. (b) The background field amplitude of vortex 2 consists of the background Gaussian containing only vortex 1 at $x = -x_0$.

where the background field amplitude is shown in Figure 2.4 (b). From this, the background field gradients used in the velocity expression, $\nabla_\perp \Phi_{bg}$ and $\nabla_\perp \ln \rho_{bg}$, can be calculated in Cartesian coordinates as

$$\begin{aligned}
\nabla_\perp \Phi_{bg}|_{\{x_0,0\}} &= \ell_1 \nabla_\perp \tan^{-1}\left(\frac{y}{x+x0}\right)|_{\{x_0,0\}} \\
&= \ell_1 \left(\frac{-y}{(x+x_0)^2+y^2}\hat{x} + \frac{x+x_0}{(x+x_0)^2+y^2}\hat{y}\right)|_{\{x_0,0\}} \\
&= \frac{\ell_1}{2x_0}\hat{y} \qquad (2.3.4)
\end{aligned}$$

and

$$\begin{aligned}\nabla_\perp \ln \rho_{bg}|_{\{x_0,0\}} &= \nabla_\perp \ln\left(r_1 e^{-r^2/w_0^2}\right)|_{\{x_0,0\}} \\ &= \left(\nabla_\perp \ln\left(\sqrt{(x+x_0)^2+y^2}\right) - \nabla_\perp\left(\frac{x^2+y^2}{w_0^2}\right)\right)|_{\{x_0,0\}} \\ &= \left(\frac{x+x_0}{(x+x_0)^2+y^2}\hat{x} + \frac{y}{(x+x_0)^2+y^2}\hat{y} - \frac{2x\hat{x}+2y\hat{y}}{w_0^2}\right)|_{\{x_0,0\}} \\ &= \left(\frac{1}{2x_0} - \frac{2x_0}{w_0^2}\right)\hat{x}. \end{aligned} \tag{2.3.5}$$

Substituting the results of Equation 2.3.4 and Equation 2.3.5 into Equation 2.2.6 results in a final velocity expression for determining the initial vortex motion:

$$\vec{v}_2 = \frac{\lambda}{2\pi}\left(\frac{\ell_1}{2x_0}\hat{y} - \frac{\ell_2}{2x_0}\hat{y} + \frac{2\ell_2 x_0}{w_0^2}\hat{y}\right) \tag{2.3.6}$$

where the second term has been transformed to the $\hat{y}$ direction via the cross-product with the vortex orientation.

Now, we distinguish between the two specific cases of Section 2.2: a pair of like-charge vortices, where $\ell_1 = \ell_2 = +1$, also found in [31], and a pair of unlike-charge vortices, where $\ell_1 = -1$ and $\ell_2 = +1$. Doing so reveals an immediate reasoning behind the difference in each vortex pair's initial dynamics. The results are summarized in Figure 2.5.

A Same Charge Vortex Pair ($\ell_1 = \ell_2 = +1$)

In the like charge pair, the initial velocity predicted for the vortex at $+x_0$ from Eq. 2.3.6 is given by

$$\vec{v}_{2,like} = \frac{\lambda x_0}{\pi w_0^2}\hat{y}, \tag{2.3.7}$$

since the first two terms of Equation 2.3.6 (which come from the phase and amplitude gradients of vortex 1) will cancel out as shown in the top row of Figure 2.5. This expression is equal in magnitude to the velocity for the single, off-center vortex case obtained by Rozas, who observed a vortex speed of x_0/z_R, for Rayleigh range $z_R = \pi w_0^2/\lambda$ in numerical simulations [31]. This result is also is consistent with the initial direction and magnitude of the vortex within the analytically propagated $LG_{\ell=+2,p=0} + LG_{\ell=0,p=0}$ beam of Section 2.2.

If the mode is propagated from the initial condition, the vortices continue with the same velocity described in Equation 2.3.7. This result is consistent with previous observations made by Rozas et al.: vortices of the same sign move in straight line trajectories with propagation [31]. This seems largely responsible for the ac-

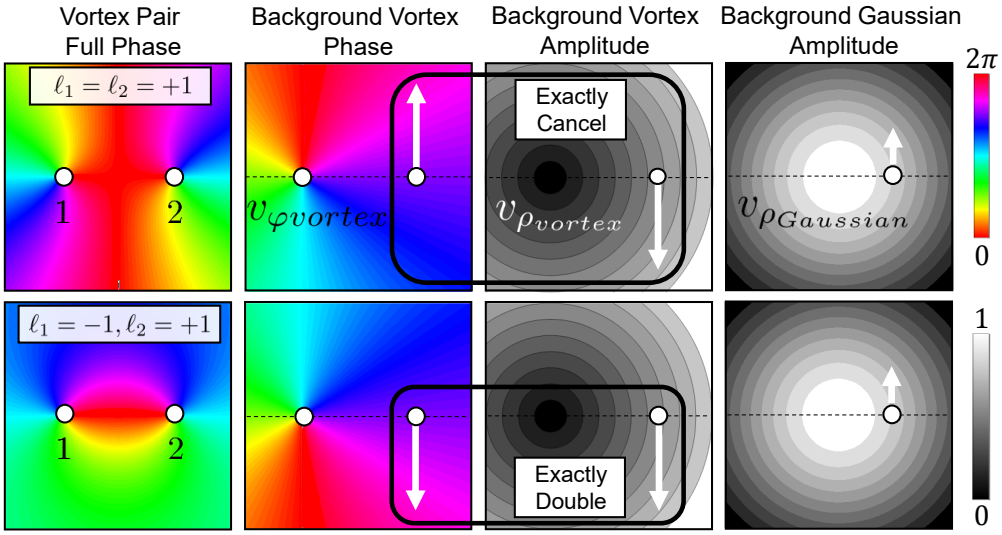

Figure 2.5: For a same-charge vortex pair (top row) and opposite-charge pair (bottom row), the background field components for vortex 2 are shown. Columns two and three show velocity contributions from background phase and amplitude of vortex 1. The last column shows the background Gaussian amplitude contribution to velocity. [Reprinted] from [120].

cepted conclusions that linear core vortices in linear light do not exhibit any effective interaction or fluid-like motion.[4] If the number of vortices in this case is increased, this result still holds which is consistent with Indebetouw's predictions of rigid body motion for lattices of the same charge [32]. It is important to note, though, that the lack of effective interactions between same charged vortices arises strictly from the exact cancellation between the phase and amplitude gradient terms for like-charge vortices. This means that like-charged vortices in a Gaussian beam can still potentially be described hydrodynamically; it just is less straightforward due to the cancellation of terms and relies on both the compressible and incompressible fluid contributions.

An Opposite Charge Pair

As discussed in Section 2.2, vortex pairs of opposite charge can exhibit wildly different dynamics based on the initial separation of the vortices with respect to the host beam size. A brief look at the initial dynamics according to Equation 2.2.6 and the background field gradients can provide some insight as to why this is the case from a hydrodynamic perspective.

We choose to again analyze the dynamics for vortex 2 of Figure 2.4, but set its charge to $\ell_2 = +1$ and vortex 1 to have charge $\ell_1 = -1$. The calculated initial velocity using Equation 2.3.6 for this pair is

$$\vec{v}_{2,opp} = \frac{\lambda}{\pi}\left(\frac{x_0}{w_0^2} - \frac{1}{2x_0}\right)\hat{y}. \tag{2.3.8}$$

[4] Fluid-like in this context meaning exhibiting behaviors as expected in an incompressible fluid.

This vortex velocity for the case of an infinite waist beam is equal to exactly twice that of the velocity, $v = \kappa/(4x_0)$, predicted by Milne-Thompson for incompressible, inviscid fluids [122]. For this opposite charge case at $z = 0$, there are equal contributions to the vortex motion from phase and amplitude gradients, shown in the bottom row of Figure 2.5, and the factor of two predicted by Equation 2.2.6 for an infinite beam comes directly from the amplitude gradient of the other vortex. Interestingly, in a finite beam when the vortex separation is exactly half that of the waist ($x_0 = 0.5w_0$), the non-dimensional magnitude of the velocity calculated from Equation 2.3.6 yields $\vec{v}_{2,opp} = \frac{1}{4x_0}$, equal to the prediction made by Milne-Thompson. When the modal superposition of Equation 2.2.2 is propagated with this ratio, the vortex dynamics actually mimic that of an incompressible fluid, with the vortices moving along straight, parallel lines at constant velocity.

It can be conceptually understood why these differences occur from the very beginning by looking at the initial condition background field for each of the cases. A summary of the background fields for a fixed vortex separation in a beam of various sizes are plotted in Fig. 2.6. At $z = 0$, the phase gradient contribution at the right vortex is in the same $-\hat{y}$ direction, shown in Figure 2.6 (a), regardless of the initial separation distance of the vortices (although the strength is determined only by the separation as is evident in Equation 2.3.4). Both the direction and strength of the velocity contribution from only the amplitude gradients vary depending on the relative beam size and separation, as shown in (b-d) of the figure. For the case where the beam is large compared to the separation, as in (b), vortex annihilation is possible because the field contributions from the left vortex significantly overwhelm the contributions from the host Gaussian field. As the beam reaches the second region where $x_0/w_0 = 0.5$, a critical point is found where the vortices do not separate with

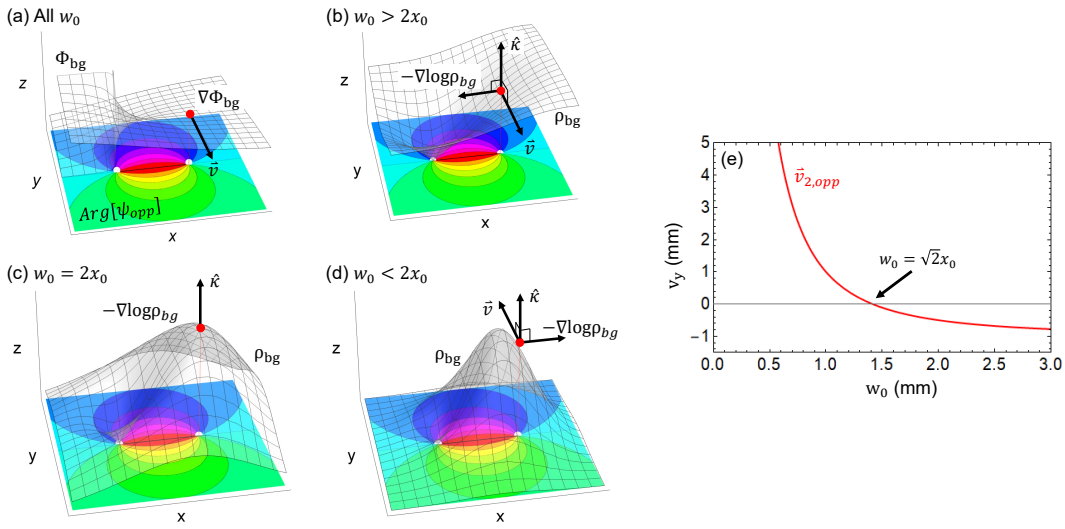

Figure 2.6: Mesh plots show either (a) the phase or (b-d) amplitude of the background of vortex one above a contour plot of the phase of the total field as the beam diameter w_0 is increased with a fixed vortex separation x_0. The fixed location of vortex 2 is marked with a red point, and vectors show the resulting velocity contribution of only the background field gradient in the given plot. (a) The phase contributes a velocity in the $-\hat{y}$ direction, irrespective of the beam size, with magnitude determined by the separation. (b-d) The background amplitude, $\tilde{\rho}$, from the beam and $\ell_1 = -1$ vortex located at $r_1 = -x_0$ shows a difference in the anticipated velocity as x_0/w_0 changes. (e) A plot of the total y velocity based on the sum of the phase and amplitude gradient terms (Equation 2.3.8) as a function of beam size for a fixed vortex separation of $x_0 = 1$ mm aids in visualizing the anticipated velocity based on the field gradients; this can be used to understand the different trajectories of Figure 2.3.

propagation, but remain the same distance apart. In this case, shown in (c) of the figure, it is clear that the sum of the field gradients are perfectly balanced such that the background amplitude gradients at the location of the vortex are equal to zero, allowing this to happen. Here, it is as if only the phase gradients from each vortex are present, giving the illusion of an incompressible fluid from the perspective of the vortex.

For beams with a waist that is small compared to the separation, seen in (d) of the figure, the initial dynamics are dominated by the Gaussian beam gradients and as the beam diverges, the vortices move apart from each other with propagation. Lastly, in (e) of the figure, we can see that by plotting Equation 2.3.8 as a function of beam size with a fixed vortex separation of $x_0 = 1$ mm, $w_0 = \sqrt{2}x_0$ is the critical point that differentiates between whether the right vortex will have an initially positive or negative $\hat{y}$ velocity, aiding in further understanding of the distinct trajectories in Figure 2.3.

In looking at these initial conditions, we are able to say that the initial velocities using Equation 2.2.6 match the initial velocities anticipated from propagating modes, and this hydrodynamic perspective provides physical insight as to why the vortex trajectories of Figure 2.3 have such a large variance. Next, it is worth considering the validity of applying Equation 2.2.6 to the entire trajectory, and we will compliment the similar analysis previously done for the same charge case [31] by considering the opposite charge case where vortex annihilation occurs.

2.4 Beyond the Initial Condition: Compressibility Alone is Not Enough

The mathematical expressions derived by others for vortex velocity in both the incompressible [122] and compressible [98] cases are summarized in Table 2.1. As a reminder, if the vortex velocity is governed purely by the background phase

Fluid Model	Velocity Equation
Incompressible	$\vec{v} = \nabla\varphi_{bg}$
Compressible	$\vec{v} = \nabla\varphi_{bg} - \hat{\kappa} \times \nabla \ln \rho_{bg}$

Table 2.1: Non-dimensional models used to calculate velocities for Fig. 2.7 [98, 122].

gradients, the vortices are expected to propel each other forward along straight lines. On the other hand, in the compressible fluid case vortex motion is determined by not only the phase gradients, but also the background amplitude gradients present. For these incompressible and compressible cases, the background field is found by taking the expression for the paraxial field and dividing out a circular vortex. A similar velocity equation to that of the compressible case in Table 2.1 was derived by Rozas et al. and successfully applied to a same charge optical vortex pair [31, 100], but the opposite charge vortex pair has not yet been compared to this type of model.

The result of applying each of these hydrodynamic theories for the oppositely charged vortex pair of Table 2.1 is shown in Figure 2.7. The total vortex trajectory predicted from Section 2.2 is shown by the blue curve, where the left vortex is negatively charged and the right vortex is positively charged. Insets in the figure

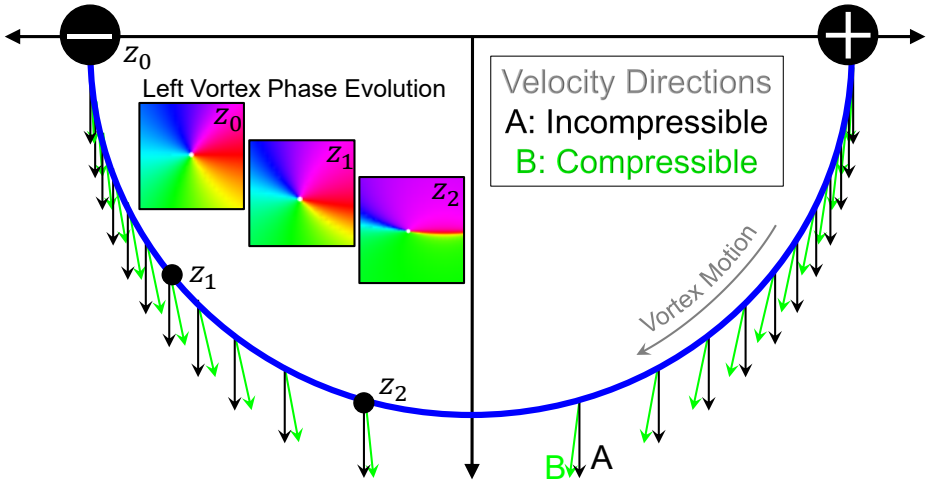

Figure 2.7: The half-circle vortex trajectory found for the oppositely charged pair is shown in blue. The incompressible fluid velocity prediction is shown by the black arrows and the compressible fluid model velocity prediction is shown in green. Each model is as described in Table 2.1.

show plots of the phase of the total field for the left vortex at three locations as the vortex approaches the annihilation event at $x = 0$. At each propagation step, the background fields are calculated by dividing out the circular vortex at the current vortex location from the total field. The velocity vectors, then, can be determined from this background field according to the velocity equations of Table 2.1 and each are plotted for comparison with each other and the actual trajectory. The black vectors (incompressible case) always are perfectly aligned toward the $-\hat{y}$ direction, as anticipated due to the fact the phase gradient of each vortex will move the other vortex downward. The green vectors (compressible case) show a deviation from this, with an evolving component in the $\hat{x}$ direction such that each vortex has a component toward $x = 0$.

For an accurate trajectory, the velocity vectors would be perfectly tangent to the plotted trajectory. Therefore, the incompressible fluid case is clearly insufficient, lacking the necessary velocity evolution in the x-direction to result in a collision. Equation 2.2.6 is much closer to describing the vortex trajectories, but the velocity vectors still are not tangent to the trajectory. In fact, while the prediction seems to work fairly well near the beginning of the trajectory, the discrepancy become larger as the vortices get closer to the annihilation point.

Clearly, more work is needed to understand the vortex motion past the initial condition, and Equation 2.2.6 is insufficient for describing the dynamics. Importantly, though, one key observation can be made from the plot insets of Figure 2.7. The velocity prediction of Equation 2.2.6 is not far from the actual trajectory near $z = 0$. At and close to $z = 0$ (z_0 in the figure), the vortices are circular or near circular. As the field evolves, the shape of the vortices evolves to become more and more elliptical as the annihilation event is approached (z_1 and z_2 in the figure), which was

also pointed out in [117]. It seems that for vortices of a near circular nature, the velocity predictions of prior work show at least reasonable predictions, which makes sense given that the derivation was for motion of circular vortices [98].

Because the previously derived hydrodynamic models are for systems where the vortices are circular, the models are sufficient to describe cases such as the same charge optical vortex pair scenario, where one vortex is not influenced by the other. But, when the shape of the vortex itself becomes distorted as the trajectories evolve, we can no longer rely on these previous models. We shall see a new theory developed in the next chapter that accounts for evolving vortex ellipticity in the hydrodynamic model. The theories will verify that the reason for the discrepancy between previous hydrodynamic models and the predicted trajectory is because of the evolution of vortex ellipticity that takes place during propagation.

Chapter 3

Vortex Tilt: A 3D Interpretation of a Non-canonical Vortex and a New Velocity Equation

A portion of this work was published in Physical Review A: Volume 104, Issue No. 3, under the title ***Hydrodynamics of noncircular vortices in beams of light and other two-dimensional fluids***. [120]

Many have found mathematical expressions for vortex position by propagating modes and using real and imaginary zeros to find the vortex locations. Even the vortex positions in the case of the oppositely charged vortex pair of the previous chapter have already been quantified [32]. Yet, we saw in Chapter 2 that prior methods for calculating vortex velocity based on the background amplitude and phase gradients [98, 121] break down for this simple case.

In this chapter, we will first explore our hypothesis that vortex ellipticity is the culprit for the breakdown. This discussion will be followed by the introduction of a novel formalism developed by Professor Mark T. Lusk, in collaboration with our DU team, for describing elliptical vortices as virtual, three-dimensional objects that are tilted away from the axis of propagation. In this formalism, the projection into the transverse plane is where their elliptical shape will originate. We will then see how this *tilted* vortex perspective allows for a complete description of such elliptical vortices and, more importantly, how it will allow for an accurate hydrodynamic

interpretation of vortex motion within optical systems. Next, the derivation of the final expression for vortex velocity that depends not only on the background field gradients, but also the tilt of the vortex is laid out. The chapter will conclude with predictions for both a single tilted vortex and oppositely charged vortex pair, along with comparisons to the anticipated trajectories found based on mode propagation and vortex tracking methods.

3.1 Canonical vs. Non-canonical Vortices

For a canonical vortex, the phase contours are equally spaced as you travel azimuthally around the vortex. Additionally, the amplitude profile of a canonical vortex will be perfectly azimuthally symmetric (circular). On the other hand, a vortex that is non-canonical has phase contours that are elliptical and the amplitude center is elliptical, rather than circular.[1] Examples of the phase and amplitude for canonical and non-canonical vortices are shown in Figure 3.1.

When looking at the evolution of an opposite charge canonical vortex pair in a Gaussian beam, it is evident even with very small propagation distances that the shape of each vortex changes dramatically. In particular, looking at a distance halfway to the annihilation point for a given set of initial parameters, we can see that the amplitude structure of the vortices has been dramatically changed, stretching out and gaining an intense elliptical shape. This can also be seen in the phase, although the shape is most obvious when looking at the amplitude. Figure 3.2 shows the initial field amplitude and phase, along with the propagated amplitude and phase for comparison.

[1] It is common for elliptical vortices to also be referred to as 'noncanonical' vortices [35,117,128–130] in the literature. I will use 'elliptical' and 'noncanonical' interchangeably, under the assumption that they have the same meaning. I will also use 'circular' and 'canonical' interchangeably.

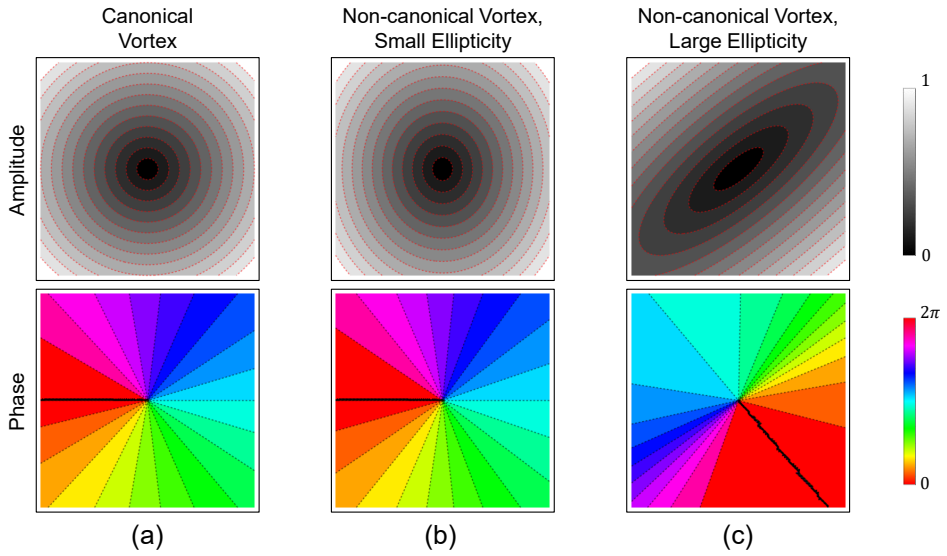

Figure 3.1: *Canonical vs. Non-canonical Vortex.* (a) A canonical vortex has circular amplitude contours and equally distributed azimuthal phase contours. A non-canonical vortex is elliptically shaped in the amplitude, and the phase contours are also elliptical (no longer azimuthally symmetric). A vortex with (b) a small degree of ellipticity vs. (c) a high degree of ellipticity are shown.

When looking only at the phase, it may be tempting to say that the ellipticity in the two vortex case could simply be a visual artifact of the fact that two vortices are present. After all, we did place two canonical vortices into a beam, and without any propagation of that field the phase result is two vortices that each, at a quick glance of the phase, seem to have some ellipticity present. However, it can be seen in the amplitude that each vortex is a perfect circle to begin with, and that the circular nature disappears shortly after the propagation begins. If for no other reason, this change in amplitude structure was enough for us to question the ellipticity of each vortex with propagation.

To fully understand if ellipticity is the reason behind the discrepancy between the hydrodynamic model and the anticipated trajectories from analytical mode propagation, there must be a way to quantify and measure such a parameter. Therefore,

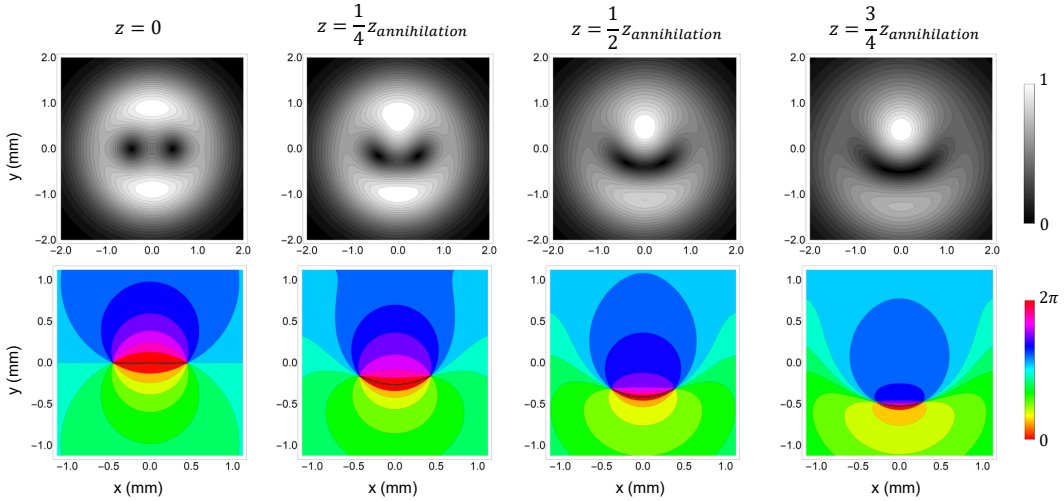

Figure 3.2: *Evolution of Ellipticity in a Two Vortex Field.* Analytically calculated amplitude (top row) and phase (bottom row) snapshots of a vortex pair with $w_0 = 1$ mm, $x_0 = 0.45 w_0$, $\lambda_0 = 633$ nm are shown using the modal decomposition of Section 2.2. As the beam propagates, the vortices very quickly begin to elongate. The circular shape morphs into an elliptical vortex that can most easily be seen in the deformed amplitude contours.

the logical step is to find a way to measure the ellipticity of any given vortex, despite the presence of other vortices or other field contributions that can be present. That task is taken up over the next several sections, and begins with viewing our two-dimensional elliptical vortices from a new virtual three-dimensional perspective.

3.2 A Virtual, 3D Perspective for Elliptical Vortices

A different way to envision elliptical vortices is to imagine that each vortex is a three-dimensional (3D), virtual, circular object in our field that is simply projected into the two-dimensional (2D) transverse plane. This construct is what we will refer to for the remainder of this dissertation as a virtual, *tilted* vortex. These virtual vortices can be oriented in any direction of 3D space, and we will see that any

elliptical vortex that exists purely in the transverse plane can be described in terms of two tilt angles of the virtual counterpart which determine the degree of ellipticity and orientation of the vortex in the 2D plane. The first is the azimuthal angle, ξ, which determines the rotation of the vortex away from the original x-axis, while the second angle, θ, determines the degree of rotation away from the z-axis. It is important to recognize that the vortex is not actually a three-dimensional object, since the propagating light is a "2+1D" system and the vortices exist only in a given xy-plane. However, this mathematical and conceptual representation of the vortex is extremely useful, both for quantifying vortex motion and for providing conceptual insight as to why the vortices move the way that they do within the optical fluid system, which will be discussed toward the end of this chapter. Toward this end, we turn to defining the tilt angles and therefore the orientation of our virtual 3D vortex.[2]

3.2.1 3D Rotation Matrix and Projections into the xy-plane

To describe the orientation of a generic vector in three-dimensional space, it is possible to simply rotate a vector using an Euler Matrix. The form of the matrix for a rotation around the z axis followed by a rotation matrix around the new x-axis is

[2]For the sake of simplicity in the writing, with the emphasis that the vortex is purely two-dimensional, I may at times refer to just "vortex tilt" rather than "virtual vortex tilt", under the assumption that it relates to the virtual counterpart. I will also use "vortex tilt" and "vortex ellipticity" interchangeably.

given by [131]

$$\mathbf{R}_{3\mathrm{D}} = \begin{bmatrix} \mathrm{Cos}\xi & -\mathrm{Sin}\xi\mathrm{Cos}\theta & \mathrm{Sin}\xi\mathrm{Sin}\theta \\ \mathrm{Sin}\xi & \mathrm{Cos}\xi\mathrm{Cos}\theta & -\mathrm{Cos}\xi\mathrm{Sin}\theta \\ 0 & \mathrm{Sin}\theta & \mathrm{Cos}\theta \end{bmatrix}. \tag{3.2.1}$$

The result of operating this rotation matrix onto a circular vortex that lives in the xy-plane is shown by the green disk in Fig. 3.3. To find the expressions for the coordinates in the tilted frame in terms of the original coordinates, one can simply take the product of $\mathbf{R}_{3D}.\{x,y,z\}$ which yields

$$\begin{aligned} \mathrm{x}' &= \mathrm{xCos}\xi - \mathrm{ySin}\xi\mathrm{Cos}\theta + \mathrm{zSin}\xi\mathrm{Sin}\theta \\ \mathrm{y}' &= \mathrm{xSin}\xi - \mathrm{yCos}\xi\mathrm{Cos}\theta - \mathrm{zCos}\xi\mathrm{Sin}\theta \\ \mathrm{z}' &= \mathrm{ySin}\theta + \mathrm{zCos}\theta \end{aligned} \tag{3.2.2}$$

where the primed coordinates are that of the rotated system.

We had previously mentioned that the actual vortex that we measure is the projection of such a tilted vortex into the 2D plane. So, we now want to use the expressions from Equation 3.2.2 to find the projection into the 2D transverse plane.

Projection into the xy-plane along the z'-axis

For the tilted vortex, we can consider the 2D projection into the xy-plane along the rotated coordinate frame, z'. To find this, we first want to know the values for x' and y' that yield $z' = 0$. To find this, we first evaluate the last expression of Equation

3.2.2 at $z' = 0$ to find the original coordinate z as a function of x and y:

$$\begin{aligned} \mathrm{z}' = 0 &= \mathrm{y}\mathrm{Sin}\xi + \mathrm{z}\mathrm{Cos}\theta \\ \mathrm{z} &= -\mathrm{y}\mathrm{Tan}\theta. \end{aligned} \tag{3.2.3}$$

Substitution of this (Equation 3.2.3) back into the expressions for x' and y' of Equation 3.2.2 results in

$$\begin{aligned} \mathrm{x}'(\mathrm{z}' = 0) &= \mathrm{x}\mathrm{Cos}\xi - \mathrm{y}\mathrm{Sin}\xi\mathrm{Cos}\theta - \mathrm{y}\mathrm{Tan}\theta\mathrm{Sin}\xi\mathrm{Sin}\theta \\ \mathrm{y}'(\mathrm{z}' = 0) &= \mathrm{x}\mathrm{Sin}\xi - \mathrm{y}\mathrm{Cos}\xi\mathrm{Cos}\theta + \mathrm{y}\mathrm{Tan}\theta\mathrm{Cos}\xi\mathrm{Sin}\theta. \end{aligned} \tag{3.2.4}$$

Using polar coordinates where $x = \cos\phi$ and $y = \sin\phi$, we can plot Equation 3.2.4 and compare it to the virtual 3D tilted vortex. The result, shown in Figure 3.3 is an elongated ellipse in the xy-plane, with a major axis that increases in size as the vortex tilt is increased to $\theta = \pi/2$ and then decreases as the vortex is tilted from $\theta = \pi/2$ to $\theta = \pi$.

We choose to define tilted vortices in relation to this z' axis so that the larger the tilt angle, the more "stretched out" the vortex becomes. Optical vortices exist in many different forms, but a fundamental eigenmode of free space is the Hermite-Gaussian mode [132, 133] in which the analogous vortex tilt would be perfectly perpendicular to the propagation direction. Designing the tilt such that a vortex with a perpendicular orientation results in an infinitely long line discontinuity is good fit for consistency with this interpretation of the Hermite-Gaussian mode.

With this framework, we can begin to see how we can use a three-dimensional, canonical vortex to describe what an elliptical vortex in the transverse plane looks

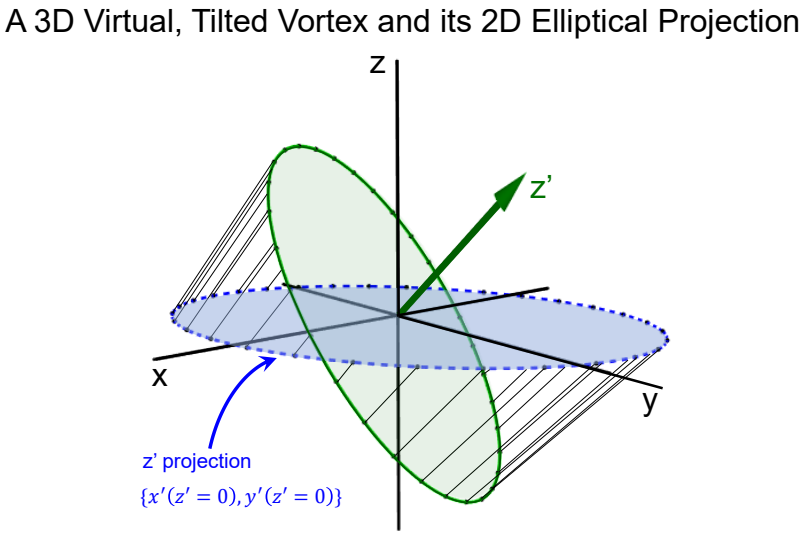

Figure 3.3: The two-dimensional z' projection of a virtual, tilted vortex is shown. As the vortex tilt increases, the projection elongates in the 2D plane and the 2D vortex ellipticity is increased.

like. We must then find a way to quantify the ellipticity and relate it to the orientation of the 3D vortex.

3.3 Polar Decomposition and the Deformation Matrix

We now have the ability to visualize what the vortex would look like as a 3D virtual object that is projected into the *xy*-plane, but we still need a way to mathematically describe and measure these vortices from the actual transverse field that we would acquire in a laboratory. The method that has allowed us to do so is to look at the *xy*-plane projections from the perspective of a deformed circular disk that has been stretched along one axis and then rotated. The natural way to do this mathematically is to use a polar decomposition.

The Polar Decomposition Theorem takes an object deformed by a deformation matrix, **F**, in a 2D plane and transforms it into two individual parts that describe

that deformation as a stretch (or compression), **U**, of an object followed by a rigid rotation, **R**, of that stretched (compressed) object [134, 135]. The deformation can also be broken into a rigid rotation, **R**, first and then followed by a symmetric deformation, **V**. In either case, it is possible to write **F** such that

$$\mathbf{F} = \mathbf{RU} = \mathbf{VR}. \tag{3.3.1}$$

As a quick example of the process, consider Figure 3.4. One way to describe the object in (a) is to begin with a square that first is stretched and then rotated, as seen in the subsequent panels of the figure [134]. Just as this shape can be described by these two successive operations, shown in (b) and (c) of the figure, the same can be done for elliptical optical vortices. For this purpose, it is easiest to visualize what the process looks like with a stretch followed by a rotation, where $\mathbf{F} = \mathbf{RU}$.[3]

[3]For the initial framework we will work with this form of the definition: $\mathbf{F} = \mathbf{RU}$. The alternate definition, $\mathbf{F} = \mathbf{VR}$, will be kept in our back pocket for later use.

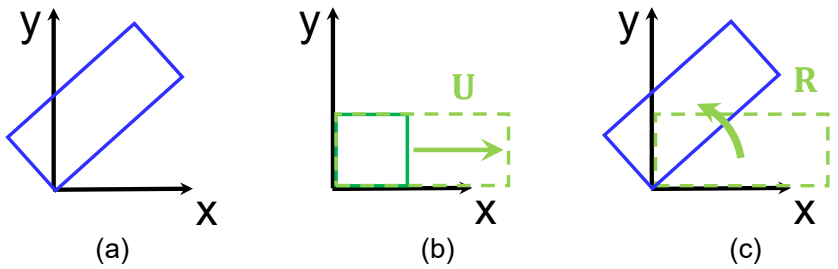

Figure 3.4: *Example of Polar Decomposition.* A deformed object in the *xy*-plane, shown in (a), can be described by $\mathbf{F} = \mathbf{RU}$. An object such as the solid square can be transformed into the rectangle found in (a) by first the uni-axial stretch, (b), followed by the rigid rotation (c).

3.3.1 A Tilted Vortex Deformation Matrix, $\mathbf{F}_{\mathrm{v}}$

For the remainder of this chapter, we will adopt the subscript, v, for the matrices that specifically pertain to a vortex (in particular, a vortex with a linear core amplitude profile).

Scaling Matrix $\mathbf{U}_{\mathrm{v}}$

The typical form of the scaling matrix is

$$\mathbf{U}_{\mathrm{v}} = \begin{bmatrix} 1 & 0 \\ 0 & \mathrm{k} \end{bmatrix} \tag{3.3.2}$$

where k describes the scaling of the object, in this case along the y axis. This is most easily visualized by operating on a vector $\mathbf{r}$ such that

$$\mathbf{U}_{\mathrm{v}}.\mathbf{r} = \begin{bmatrix} 1 & 0 \\ 0 & \mathrm{k} \end{bmatrix} \begin{bmatrix} \mathrm{x} \\ \mathrm{y} \end{bmatrix} = x + ky. \tag{3.3.3}$$

Written in this way, it is easy to see how this matrix creates a uni-axial scaling. The scaling factor, k, can then be any factor that stretches or compresses the object along the y-direction.

As mentioned in Section 3.2.1, for the work in this thesis, we want a k such that the object will be stretched rather than compressed. One way to do this is to choose $k = \sec\theta$, where θ describes the degree of tilt away from the propagation axis. $\mathbf{U}_{\mathrm{v}}$

is therefore given by

$$\mathbf{U}_{\text{v}} = \begin{bmatrix} 1 & 0 \\ 0 & \text{Sec}\theta \end{bmatrix}. \tag{3.3.4}$$

If we remind ourselves of the functional form of $\sec\theta$, shown in Figure 3.5, we can see why this is a logical choice for our vortices.

First, let's remind ourselves that $0 < \theta < \pi$, where at $\theta = 0$ the vortex in the transverse plane is circular with a topological charge of $+1$, and that at $\theta = \pi$ the vortex is again circular with topological charge of -1. As θ increases from zero, the uni-axial scaling will also be increasing until it reaches an asymptote at

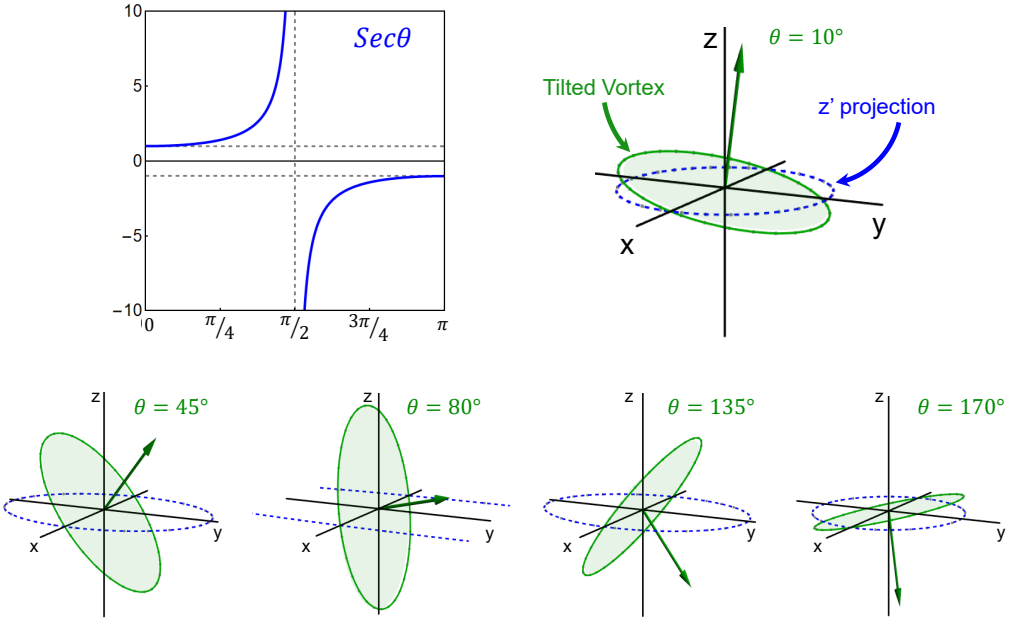

Figure 3.5: The functional form of secant is the best choice for the uni-axial scaling of tilted vortices. At $\theta = 0°$, the vortex is purely circular in the xy-plane, and $\sec\theta = 1$. Similarly, at $\theta = 180°$ where the topological charge is negative, $\sec\theta = -1$. At the critical point where $\theta = 90°$, the vortex is perpendicular to the propagation axis, and the projection becomes undefined.

$\theta = \pi/2$. Just below $\theta = \pi/2$, the vortex will be severely stretched out, and exactly at $\theta = \pi/2$ the vortex is infinitely stretched (technically undefined), and oriented completely perpendicular to the propagation direction. As the vortex continues to rotate above $\theta = \pi/2$, the topological charge switches sign, and the vortex is a negative, very elongated vortex. As it approaches $\theta = \pi$, the scaling decreases with increasing θ as would be expected based on Figure 3.5.

Now that the scaling is set, the next operation is a simple, rigid rotation of our stretched out vortex projection.

2D Rotation Matrix, $\mathbf{R}_{v,2D}$

The second piece that we need to describe the elliptical vortex is to define the amount it has rotated from its original orientation in the *xy*-plane. We use a two dimensional Euler Matrix that performs a counterclockwise rotation by angle ξ:

$$\mathbf{R}_{\mathrm{v,2D}} = \begin{bmatrix} \mathrm{Cos}\xi & -\mathrm{Sin}\xi \\ \mathrm{Sin}\xi & \mathrm{Cos}\xi \end{bmatrix}. \tag{3.3.5}$$

A brief derivation of this matrix can be found in Appendix A.2. With both the scaling and rotation matrices defined, we can then determine the full form of the deformation matrix in terms of our tilt angles θ and ξ.

Deformation Matrix, $\mathbf{F}_{\text{v}}$

The final form of the Deformation Matrix then is given by the substitution of Equation 3.3.4 and Equation 3.3.5 into Equation 3.3.1. The result is

$$\mathbf{F}_{\text{v}} = \mathbf{R}_{\text{v,2D}}\mathbf{U}_{\text{v}} = \begin{bmatrix} \cos\xi & -\sin\xi\sec\theta \\ \sin\xi & \cos\xi\sec\theta \end{bmatrix}. \tag{3.3.6}$$

Note that the top left submatrix of Equation 3.2.1, which is just the xy-projection of $\mathbf{R}_{3D}$, is equivalent to the inverse transpose of $\mathbf{F}_{\text{v}}$, i.e. $\mathbf{F}_{\text{v}}^{-T}$.

With this description laid out, we can fully realize what these tilted vortices look like, both visually and mathematically. The final result, as shown in Figure 3.6, is a view of the circular vortex that has been rotated by angle ξ from the original x-

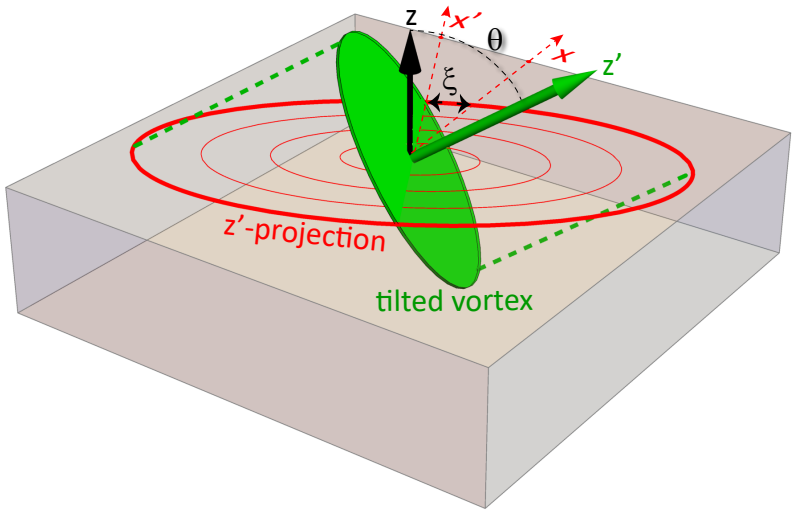

Figure 3.6: *Tilted Vortex Diagram.* A 2D elliptical vortex in the transverse plane can be viewed as the projection, along the tilt axis, of a 3D vortex. The ellipticity can then be described by an azimuthal orientation angle, ξ, and a polar lean, θ. ***Figure credit: Professor Mark T. Lusk. From Andersen, 2021. [120] © American Physical Society

axis, and then rotated by angle θ around this new x-axis, and for which the xy-plane projection can be fully described by deformation matrix, $\mathbf{F}_{\mathrm{v}}$.

Now that we can describe any tilted vortex in terms of our deformation matrix, we want to use this formalism to go the other direction: find the tilt angles of any given vortex in an arbitrary paraxial field. The next section addresses how to do so.

3.4 Finding Vortex Tilt from a 2D Paraxial Field

In the previous section we developed the formalism for describing an elliptical vortex in the transverse plane as a projection of a 3D circular vortex that is tilted by angles θ and ξ. However, we have yet to account for the fact that optical vortices do not exist on their own; they exist within a beam or some other field that may contain other vortices or field contributions. As mentioned in both Chapter 2 and Figure 3.2 of this chapter, in cases such as the oppositely charged vortex pair, the tilt of each vortex seems to evolve as the beam propagates. In order for our tilted vortex description to be truly useful, we must find a way to measure the tilt of any given vortex within any arbitrary field, at any given propagation distance.

Let's first define a few parameters that will be used throughout the remaining derivations. A general complex, paraxial field

$$\psi = \psi_{Real} + i\psi_{imaginary} \tag{3.4.1}$$

can be treated as a two-dimensional vector, $\vec{u}(\vec{r},z)$ mapped into the transverse plane where $\vec{r} = \{x,y\}$. Doing this will simplify the later analysis. The matrix form of

$\vec{u}(\vec{r},z)$ is therefore given by

$$\vec{u}(\vec{r},z) = \begin{bmatrix} \psi_{real} \\ \psi_{imaginary} \end{bmatrix} \tag{3.4.2}$$

As an example, consider the paraxial field for a circular, linear core vortex, $\psi_v = x + iy$. This can now alternatively be written in matrix representation:

$$\vec{u}_v^{circ}(\vec{r},z) = \begin{bmatrix} x \\ y \end{bmatrix} = \vec{r}. \tag{3.4.3}$$

To instead describe an elliptical vortex, we can apply our deformation from the previous section to this circular vortex which is written as

$$\begin{aligned} \vec{u}_v(\vec{r},z) &:= \vec{u}_v^{circ}(\mathbf{F}_{\mathrm{v}}^{-1}\vec{r}) \\ &\equiv \mathbf{F}_{\mathrm{v}}^{-1}\vec{u}_v^{circ}(\vec{r}) \\ &\equiv \mathbf{F}_{\mathrm{v}}^{-1}\vec{r} \end{aligned} \tag{3.4.4}$$

From this perspective, elliptical vortices are obtained through a homogeneous deformation by $\mathbf{F}_{\mathrm{v}}^{-1}$. The vector field, $\vec{u}_v(\vec{r},z)$, can therefore be more compactly visualized as a deformed continuum instead of assigning a distinct vector to each position.

3.4.1 The V^2 Matrix: Eigenvalues and Eigenvectors that Yield Vortex Tilt

With these definitions, we can now approach the problem of determining the tilt for a vortex in an arbitrary paraxial field. We will see near the end of this section

that $\mathbf{V}^2$, the square of the symmetric deformation matrix of Equation 3.3.1, will give us the ability to find the vortex tilt angles. We start by assuming that the tilted vortex component, ψ_v, can be separated from all other contributions of the field. The other contributions to the field comprise the total background field, ψ_{bg}, at the location of the vortex that we are interested in measuring. In this way, we can write any arbitrary paraxial field with a vortex of interest as

$$\psi_{tot} = \psi_{bg}\psi_v. \tag{3.4.5}$$

The 2D derivative of this can be taken, and the product rule dictates that

$$\begin{aligned}\nabla_\perp \psi_{tot} &= \psi_v \nabla_\perp \psi_{bg} + \psi_{bg}\nabla_\perp \psi_v \\ &= \psi_{bg}\nabla_\perp \psi_v \\ &= \rho_{bg} e^{i\varphi_{bg}} \nabla_\perp \psi_v \end{aligned} \tag{3.4.6}$$

where the first term on the first line goes to zero since we will evaluate this derivative at the location of the vortex where $\psi_v = 0$ and the background field has been broken down into its amplitude and phase components. Written in the matrix form, the expression is

$$\nabla_\perp \vec{u}_{tot} = \rho_{bg}\Phi_{\text{bg}}^T \nabla_\perp \vec{u}_v \tag{3.4.7}$$

where Φ_{bg} is a unitary operator that generates vector rotations by φ_{bg}:

$$[\Phi_{\text{bg}}] = \begin{bmatrix} \cos\varphi_{bg} & \sin\varphi_{bg} \\ -\sin\varphi_{bg} & \cos\varphi_{bg} \end{bmatrix} \tag{3.4.8}$$

In looking at Equation 3.4.7, we notice that the gradient field of a general $\vec{u}$ is

$$\nabla_{\perp}\vec{u}_{tot} = \nabla_{\perp}\left(\mathbf{F}^{-1}\mathbf{r}\right) = \mathbf{F}^{-1}, \tag{3.4.9}$$

since $\vec{u} = \mathbf{F}^{-1}\vec{r}$ from Equation 3.4.3. Upon substiting this into Equation 3.4.7, $\nabla_{\perp}\vec{u}_{tot}$ becomes

$$\mathbf{F}_{\text{tot}}^{-1} = \rho_{\text{bg}}\Phi_{\text{bg}}^{\text{T}}\mathbf{F}_{\text{v}}^{-1}. \tag{3.4.10}$$

Let's take a moment and remind ourselves that our goal is to solve for the tilt angles of a specific vortex within the arbitrary field. The left side in Equation 3.4.10 is a matrix that contains the tilt angles of the vortex in the arbitrary field that we are measuring, θ and ϕ. However, to find $\mathbf{F}_{tot}^{-1}$, we must know both the background field amplitude and phase at the location of the vortex. The issue here is that without knowing the exact tilt of the vortex, we cannot successfully separate the vortex from the other background field components.

Earlier we mentioned that by finding $\mathbf{V}^2$, we would be able to find the tilt angles. With this in mind, we recall from the Polar Decomposition Theorem that $\mathbf{V}^2 = \mathbf{F}\mathbf{F}^T$ in general since

$$\begin{aligned}
\mathbf{F} &= \mathbf{V}\mathbf{R} \\
\mathbf{F}\mathbf{F}^T &= \mathbf{V}\mathbf{R}(\mathbf{V}\mathbf{R})^T \\
\mathbf{F}\mathbf{F}^T &= \mathbf{V}\mathbf{R}\mathbf{R}^T\mathbf{V}^T \\
\mathbf{F}\mathbf{F}^T &= \mathbf{V}\mathbf{V}^T = \mathbf{V}^2
\end{aligned} \tag{3.4.11}$$

where we have made use of the fact that $\mathbf{R}\mathbf{R}^T$ is the identity matrix since $\mathbf{R}$ is a unitary rotation matrix [135]. Knowing that $\mathbf{F}_{total} = \rho_{bg}^{-1}\,\mathbf{F}_v\,[\Phi^T_{\text{background}}]^{-1}$ from Eq. 3.4.10, it immediately follows that

$$\begin{aligned}
\mathbf{V}^2_{\text{tot}} &= \rho_{\text{bg}}^{-1}\,\mathbf{F}_{\text{v}}\,[\Phi^{\text{T}}_{\text{bg}}]^{-1}\left[\rho_{\text{bg}}^{-1}\,\mathbf{F}_{\text{v}}\,[\Phi^{\text{T}}_{\text{bg}}]^{-1}\right]^{\text{T}} \\
&= \rho_{\text{bg}}^{-2}\,\mathbf{F}_{\text{v}}\,[\Phi^{\text{T}}_{\text{bg}}]^{-1}\left[[\Phi^{\text{T}}_{\text{bg}}]^{-1}\right]^{\text{T}}\,\mathbf{F}^{\text{T}}_{\text{v}} \\
&= \rho_{\text{bg}}^{-2}\,\mathbf{F}_{\text{v}}\,\mathbf{F}^{\text{T}}_{\text{v}} \\
&= \rho_{\text{bg}}^{-2}\,\mathbf{V}^2_{\text{v}}
\end{aligned} \tag{3.4.12}$$

At this point, we notice that by finding $\mathbf{V}^2$ we have eliminated the need to know φ_{bg} since $[\Phi^T_{\text{bg}}]^{-1}\left[[\Phi^T_{\text{bg}}]^{-1}\right]^T = \mathbf{1}$. The only thing left is to eliminate the need for ρ_{bg}.

One way to do this is to use the eigenvalues and eigenvectors of $\mathbf{V}^2_{tot}$. We solve the typical eigenvalue problem then by taking

$$Det\left[\mathbf{V}^2_{tot} - \mathbf{I}\lambda\right] = 0 \tag{3.4.13}$$

which, as detailed in Appendix A.3, results in

$$(\lambda - \rho_{bg}^{-2})(\lambda - \rho_{bg}^{-2}\sec^2\theta) = 0. \tag{3.4.14}$$

The eigenvalues then are $\lambda = \rho_{bg}^{-2}$ and $\lambda = \rho_{bg}^{-2}\sec^2\theta$. Here, we let the eigenvectors of $\mathbf{V}^2_{tot}$ be denoted by v_j with eigenvalues λ_j, $j = 1,2$. Upon taking the ratio of the eigenvalues, the background amplitude is also eliminated from the expressions such that

$$\frac{\lambda_1}{\lambda_2} = \cos^2\theta, \tag{3.4.15}$$

and the ratio of the corresponding eigenvector components is

$$\frac{v_{1x}}{v_{1y}} = \cot\xi. \tag{3.4.16}$$

Solving each of these equations results in the azimuthal rotation ξ and polar dip θ:

$$\theta = \cos^{-1}\left(\pm\sqrt{\frac{\lambda_1}{\lambda_2}}\right), \quad \xi = \cot^{-1}\left(\frac{v_{1x}}{v_{1y}}\right) + n\pi, \tag{3.4.17}$$

where $\lambda_1 < \lambda_2$ and $n \in \mathbb{Z}$, and the signs can be determined from the sign of the components of $\mathbf{F}_{tot} = \rho_{bg}^{-1}\,\mathbf{F}_v\,\Phi_{\text{bg}}^T$. This result leaves us at a point where we can quantify the tilt angles if we just had the form of the $\mathbf{V}_{tot}^2$ matrix for our paraxial field.

3.4.2 Relationship between $\mathbf{V}_{tot}^2$ and $\vec{u}_{tot}$

Conveniently, we are actually well equipped to find $\mathbf{V}_{tot}^2$ because of the relationships between $\mathbf{V}_{tot}^2$, $\mathbf{F}_{tot}^{-1}$, and $\nabla_\perp \vec{u}_{tot}$. Knowing that $\nabla_\perp \vec{u}_{tot} = \mathbf{F}_{tot}^{-1}$ from Equation 3.4.9, and that $\mathbf{V}_{tot}^2 = \mathbf{F}_{tot}\mathbf{F}_{tot}^T$ from Equation 3.4.11, we can write $\mathbf{V}_{tot}^2$ in terms of the total field gradients only. The result is

$$\begin{aligned}\mathbf{V}_{tot}^2 &= \mathbf{F}_{tot}\mathbf{F}_{tot}^T = [\nabla_\perp \vec{u}_{tot}]^{-1}[\nabla_\perp \vec{u}_{tot}]^{-T} \\ &= \begin{bmatrix} \partial_x \psi_{\text{Re}} & \partial_y \psi_{\text{Re}} \\ \partial_x \psi_{\text{Im}} & \partial_y \psi_{\text{Im}} \end{bmatrix}^{-1} \begin{bmatrix} \partial_x \psi_{\text{Re}} & \partial_y \psi_{\text{Re}} \\ \partial_x \psi_{\text{Im}} & \partial_y \psi_{\text{Im}} \end{bmatrix}^{-T}.\end{aligned} \tag{3.4.18}$$

This means that we are able to directly measure the components of $\mathbf{V}_{tot}^2$ from any 2D data set as long at the full complex field is known. From there, we simply must find

the eigenvalues and eigenvectors, and therefore the vortex tilt angles. The benefit of this formalism is that the tilt angles can be quickly extracted from just the field gradients at the location of the vortex. An example of applying this to a paraxial field with a tilted vortex using Mathematica is laid out in Appendix A.4.

Now that we have the ability to quantify the tilt of any given vortex, we next explore finding the vortex velocity since we should be able to separate the vortex, including its tilt, from the background field.

3.5 A Vortex Velocity Expression that Includes Vortex Tilt

We now consider a general paraxial vector field, $\vec{u}(x,y,z)$, that contains a single moving vortex (of unit charge) with position described by $\vec{r}_v(z)$. The vortex velocity will be denoted by $\vec{v} = \partial_z \vec{r}_v$, since the vortex will be moving within the xy-plane as the beam propagates. At the vortex center, $\vec{u} = \vec{0}$. Because the value of the paraxial field at the vortex location is always equal to zero, and therefore a constant, it is guaranteed that $d_z \vec{u} = 0$ for all z. The total derivative of $\vec{u}$ with respect to z can also be expressed as $d_z \vec{u} = \partial_x \vec{u}\, \partial_z x + \partial_y \vec{u}\, \partial_z y + \partial_z \vec{u} = \nabla_\perp \vec{u}\, \partial_z \vec{r}_v + \partial_z \vec{u}$. Using the relationships just mentioned, the total derivative is

$$d_z \vec{u} = \mathbf{F}_{tot}^{-1} \vec{v} + \partial_z \vec{u} = \vec{0}, \tag{3.5.1}$$

with the transverse position evaluated at $\vec{r}_v(z)$ for all fields. A quick rearrangement of this result yields the vortex velocity as

$$\vec{v} = -\mathbf{F}_{tot} \partial_z \vec{u}. \tag{3.5.2}$$

Here, we remind ourselves of the form of the paraxial equation,

$$\sigma_0 \partial_z \vec{u} = -\frac{1}{2}\nabla_\perp^2 \vec{u} + \mathscr{V}\vec{u}, \tag{3.5.3}$$

where

$$\sigma_0 = \begin{bmatrix} 0 & -1 \\ 1 & 0 \end{bmatrix}. \tag{3.5.4}$$

Equation 3.5.2 can then be rewritten using the paraxial equation such that

$$\vec{v} = -\mathbf{F}_{tot}\partial_z \vec{u} = -\mathbf{F}_{tot}\sigma_0^{-1}(-\frac{1}{2}\nabla_\perp^2 \vec{u} + \mathscr{V}\vec{u}). \tag{3.5.5}$$

Then, we can rewrite F in terms of the background field instead, using $\mathbf{F}_{tot}$ and $\mathbf{F}_{\text{v}}$, $\mathbf{F}_{tot} = \frac{1}{\rho_{bg}}\mathbf{F}_{\text{v}}\Phi_{\text{bg}}$ to obtain

$$\vec{v} = \frac{1}{2\rho_{bg}}\mathbf{F}_{\text{v}}\Phi_{\text{bg}}\sigma_0^{-1}\nabla_\perp^2 \vec{u}. \tag{3.5.6}$$

where $\mathscr{V}\vec{u} = 0$ since this is evaluated at the vortex center where $\vec{u} = 0$.

This expression for vortex velocity can be simplified by noting that a vortex located at $\vec{r}_v$ is described by $\vec{u}_v = \mathbf{F}_{\text{v}}^{-1}(\vec{r} - \vec{r}_v)$ so $\vec{u} = \rho_{bg}\Phi_{\text{bg}}^T\mathbf{F}_{\text{v}}^{-1}(\vec{r} - \vec{r}_v)$. The Laplacian term of Eq. (3.5.6) evaluated at the vortex center, can therefore be written as

$$\nabla_\perp^2 \vec{u} = 2\nabla_\perp \cdot (\nabla_\perp \vec{u}) = 2\nabla_\perp \cdot (\rho_{bg}\Phi_{\text{bg}}^{-1}\mathbf{F}_{\text{v}}^{-1}). \tag{3.5.7}$$

Substitution of this result into Eq. (3.5.6) gives

$$\vec{v} = \frac{1}{2\rho_{bg}}\mathbf{F}_{\text{v}}\Phi_{\text{bg}}\sigma_0^{-1}\nabla_\perp^2 2\nabla_\perp \cdot (\rho_{bg}\Phi_{\text{bg}}^{-1}\mathbf{F}_{\text{v}}^{-1}). \tag{3.5.8}$$

To simplify this, we define $\mathbf{A} \equiv \mathbf{F}_{\mathrm{v}}\Phi_{\mathrm{bg}}$ so that $\vec{v}$ is then

$$\vec{v} = \frac{1}{\rho_{bg}}\mathbf{A}\sigma_0\nabla_\perp \cdot (\rho_{bg}\mathbf{A}^{-1}) = \frac{1}{\rho_{bg}}\mathbf{A}\sigma_0\left(\rho_{bg}\nabla_\perp \cdot \mathbf{A}^{-1} + \mathbf{A}^{-1}\nabla_\perp\rho_{bg}\right). \tag{3.5.9}$$

Since $\mathbf{F}_{\mathrm{v}}$ is not a function of position in the *x*-*y* plane, the first term can be reevaluated in terms of the gradient of the background phase only:

$$\vec{v} = \frac{1}{\rho_{bg}}\mathbf{A}\sigma_0\left(\rho_{bg}(\nabla_\perp\Phi_{\mathrm{bg}}^{-1})\mathbf{F}_{\mathrm{v}}^{-1} + \mathbf{A}^{-1}\nabla_\perp\rho_{bg}\right). \tag{3.5.10}$$

Now, we can expand to two terms and simplify using $\left(\nabla_\perp\rho_{bg}\right)/\rho_{bg} = \nabla_\perp \ln\left(\rho_{bg}\right)$ and the velocity becomes

$$\vec{v} = \mathbf{A}\sigma_0(\nabla_\perp\Phi_{\mathrm{bg}}^{-1})\mathbf{F}_{\mathrm{v}}^{-1} + \mathbf{A}\sigma_0\mathbf{A}^{-1}\nabla_\perp \ln\rho_{bg}. \tag{3.5.11}$$

For clarity, we will rewrite this expression as

$$\vec{v} = \vec{v}_\varphi + \vec{v}_{\xi,\theta,\rho} \tag{3.5.12}$$

Next, we simplify the phase contribution, $\vec{v}_\varphi = \mathbf{A}\sigma_0(\nabla_\perp\Phi_{\mathrm{bg}}^{-1})\mathbf{F}_{\mathrm{v}}^{-1}$, to the vortex velocity. The three tensor,

$$\nabla_\perp\Phi_{\mathrm{bg}}^{-1} = \begin{bmatrix} \begin{pmatrix} -\sin\varphi_{bg}\partial_x\varphi_{bg} \\ -\sin\varphi_{bg}\partial_y\varphi_{bg} \end{pmatrix} & \begin{pmatrix} -\cos\varphi_{bg}\partial_x\varphi_{bg} \\ -\cos\varphi_{bg}\partial_y\varphi_{bg} \end{pmatrix} \\ \begin{pmatrix} \cos\varphi_{bg}\partial_x\varphi_{bg} \\ \cos\varphi_{bg}\partial_y\varphi_{bg} \end{pmatrix} & \begin{pmatrix} -\sin\varphi_{bg}\partial_x\varphi_{bg} \\ -\sin\varphi_{bg}\partial_y\varphi_{bg} \end{pmatrix} \end{bmatrix} \tag{3.5.13}$$

acts on $\mathbf{F}_{\text{v}}$ to produce a vector

$$\left(\nabla_{\perp}\Phi_{\text{bg}}^{-1}\right)\mathbf{F}_{\text{v}}^{-1} =$$
$$\begin{bmatrix} -\left(\cos\theta\cos\xi\cos\varphi_{bg}+\sin\xi\sin\varphi_{bg}\right)\partial_y\varphi_{bg}+\left(\cos\theta\cos\varphi_{bg}\sin\xi-\cos\xi\sin\varphi_{bg}\right)\partial_x\varphi_{bg} \\ \left(\cos\varphi_{bg}\sin\xi-\cos\theta\cos\xi\sin\varphi_{bg}\right)\partial_y\varphi_{bg}+\left(\cos\xi\cos\varphi_{bg}+\cos\theta\sin\xi\sin\varphi_{bg}\right)\partial_x\varphi_{bg} \end{bmatrix}.$$

This vector can now be used in simplifying the entire first term:

$$\vec{v}_{\varphi} = -\mathbf{A}\sigma_0\left(\nabla_{\perp}\Phi_{\text{bg}}^{-1}\right)\mathbf{F}_{\text{v}}^{-1} = \begin{bmatrix}\partial_x\varphi_{bg}\\ \partial_y\varphi_{bg}\end{bmatrix} = \nabla_{\perp}\varphi_{bg} \tag{3.5.14}$$

as expected.

Next, the second term, $\vec{v}_{\xi,\theta,\rho} = \mathbf{A}\sigma_0\mathbf{A}^{-1}\nabla_{\perp}\ln\rho_{bg}$, is directly compared to the result from Equation 3.5.17, $\vec{v}_{\xi,\theta,\rho} = -\frac{\mathbf{V}_{\text{v}}^2}{J_{\text{v}}}\sigma_0\nabla_{\perp}\ln\rho_{bg}$ to verify their equivalence. The derived expression of 3.5.14 evaluates to

$$\begin{aligned} v_{\xi,\theta,\rho} &= \mathbf{A}\sigma_0\mathbf{A}^{-1}\nabla_{\perp}\ln\rho_{bg} \\ &= \begin{bmatrix} -\cos\xi\sin\theta\sin\xi\tan\theta & -\sec\theta\left(\cos^2\theta\cos^2\xi+\sin^2\xi\right) \\ \cos^2\xi\sec\theta+\cos\theta\sin^2\xi & \cos\xi\sin\theta\sin\xi\tan\theta \end{bmatrix}\nabla_{\perp}\ln\rho_{bg}. \end{aligned} \tag{3.5.15}$$

Similarly, the second term of Equation 3.5.17 evaluates to

$$
\begin{aligned}
v_{\xi,\theta,\rho} &= -\frac{\mathbf{V}_{\mathrm{v}}^2}{J_{\mathrm{v}}}\sigma_0\nabla_\perp \ln\rho_{bg} \\
&= \begin{bmatrix} -\cos\xi\,\sin\theta\,\sin\xi\,\tan\theta & -\cos\theta\left(\cos^2\xi+\sec^2\theta\,\sin^2\xi\right) \\ \cos^2\xi\,\sec\theta+\cos\theta\,\sin^2\xi & \cos\xi\,\sin\theta\,\sin\xi\,\tan\theta \end{bmatrix} \nabla_\perp \ln\rho_{bg}
\end{aligned}
\tag{3.5.16}
$$

when plugging in the full forms of $\mathbf{V}_{\mathrm{v}}^2$, J_{v} and σ_0. Subtracting Equation 3.5.16 from Equation 3.5.15 returns a zero matrix, from which we can conclude that the two are equivalent. Therefore, the final velocity expression for a tilted vortex in any arbitrary linear optical field can be written as

$$
\vec{v} = \nabla_\perp \varphi_{bg} - \frac{\mathbf{V}_{\mathrm{v}}^2}{J_{\mathrm{v}}}\sigma_0\nabla_\perp \ln\rho_{bg}. \tag{3.5.17}
$$

where $J_{\mathrm{v}} = \mathrm{Det}(\mathbf{F}_{\mathrm{v}})$.

For incompressible materials, where $\nabla\rho_{bg} = 0$, this equation is consistent with a hydrodynamic interpretation of the paraxial equation [111]—i.e. it is just the phase gradient. However, as we discussed in Chapter 2, light exhibits compressibility, so vortex motion is also influenced by local gradients in fluid density. In the absence of tilt, where $\mathbf{V}_{\mathrm{v}}^2/J_{\mathrm{v}} = 1$, Equation 3.5.17 reduces to a form previously obtained in the context of the Gross-Pitaevskii equation for quantum fluids [98, 121] in which such density gradients are accounted for. Additionally, work done in an optical system by Rozas et. al resulted in a similar expression for the velocity, including both the phase and amplitude gradient contributions [100].

Equation (3.5.17) goes a step further though, revealing a new coupling between vortex tilt and local gradients in the hydrodynamic density. Because of this coupling, vortex speed can be altered by simply changing the degree of vortex ellipticity. As tilt approaches $\theta = 90^\circ$, the vortex speed in the direction of tilt will approach infinity while that in an orthogonal direction approaches zero, which can be seen the two test cases of the next section.

The combination of Eq. (3.4.17) and Eq. (3.5.17) comprise a coupled system that can be solved to predict the evolution of vortex position and tilt, for either linear or non-linear optical media. If axial location, z, is replaced by time, t, the system can be applied directly to predict the dynamics of vortices in quantum fluids within the Gross-Pitaevskii ansatz [17].

3.6 Tilted Vortex Velocity Predictions: Two Cases

Now that the expectation for the vortex velocity based on the field gradients and vortex tilt has been derived, we apply it to two specific examples. The first is a single vortex embedded in a Gaussian beam. The second is the familiar, oppositely charged vortex pair in a Gaussian. In each case, we compare the anticipated vortex velocity to the trajectory found by equating real and imaginary zeros. In both cases, we will find an excellent match with experiments (discussed later in Chapter 7).

3.6.1 A Single, Tilted Vortex in a Gaussian Beam

Consider the initial state of a paraxial field constructed as the product of a vortex, placed on the x-axis at x_0 with initial tilt $\{\xi_i, \theta_i\}$, and a Gaussian beam of waist w_0 and wavenumber k. Position is nondimensionalized with $w_0/\sqrt{2}$ (in-plane) and Rayleigh length (propagation axis). Remembering that a tilted vortex can be de-

scribed by Equation 3.4.4, the paraxial field *at the beam waist* is described by the deformation of the circular vortex such that

$$\begin{aligned}\vec{u}_v(x,y,0) = \mathbf{F}^{-1}\begin{bmatrix} x-x_0 \\ y \end{bmatrix} &= \begin{bmatrix} \cos\xi_i & \sin\xi_i \\ -\cos\theta_i\sin\xi_i & \cos\theta_i\cos\xi_i \end{bmatrix}\begin{bmatrix} x-x_0 \\ y \end{bmatrix} \\ &= \begin{bmatrix} (x-x_0)\cos\xi_i + y\sin\xi_i \\ (x-x_0)(-\cos\theta_i\sin\xi_i) + y\cos\theta_i\sin\xi_i \end{bmatrix} \end{aligned} \tag{3.6.1}$$

in the matrix representation. The full complex field can then be written in the form

$$\psi_v(x,y,0) = (x-x_0)\cos\xi_i + y\sin\xi_i - i(x-x_0)\cos\theta_i\sin\xi_i + iy\cos\theta_i\sin\xi_i. \tag{3.6.2}$$

This field gives our initial condition to propagate, from which we can watch the beam evolution in z ("time") and quantify vortex motion. A convolution of this initial field with the paraxial Green's function [136], which can be found in Appendix A.5, is used to derive the field as a function position along the z-axis such that

$$\begin{aligned}\psi_v(x,y,z) = \frac{1}{(-i+z)^2}\sqrt{\frac{2}{\pi}}(&\cos\xi_i(-x+x_0+ix_0z-iy\cos\theta_i) - y\sin\xi_i... \\ &...+ix\cos\theta_i\sin\xi_i + x_0(-i+z)\cos\theta_i\sin\xi_i)e^{i\frac{x^2+y^2}{2(-i+z)}}\end{aligned} \tag{3.6.3}$$

The coupled Eq. (3.4.17) and (3.5.17) can then be solved to find two key results. The first is that vortex tilt does not evolve from its initial value. Second, the vortex position is given by

$$\begin{aligned} x_v &= x_0 - x_0 z\cos\xi_i\sin\theta_i\sin\xi_i\tan\theta_i \\ y_v &= x_0 z\cos\theta_i\left(\cos^2\xi_i\sec^2\theta_i + \sin^2\xi_i\right). \end{aligned} \tag{3.6.4}$$

Here Eq. (3.5.17) has been integrated to construct this vortex trajectory. Surprisingly, for a vortex with any arbitrary tilt in this scenario, the calculated vortex velocity with propagation is a constant.

The background field can be determined by using the vortex position from Equation 3.6.4, with ξ and θ calculated as described by Equation 3.4.17, and dividing out the total elliptical vortex from the paraxial field of Equation 3.6.3. This background field can be used to compute the gradients needed to predict vortex velocity according to Equation 3.5.17. The background field gradients of the field given in Equation 3.6.3 are

$$\begin{aligned}\nabla_\perp \varphi_{bg} &= \frac{x_0 z}{1+z^2}\begin{bmatrix}(1-z\cos\xi\sin\theta\sin\xi\tan\theta)\\ z\cos\theta\left(\cos^2\xi\sec^2\theta+\sin^2\xi\right)\end{bmatrix}\\ \nabla_\perp \ln\rho_{bg} &= \frac{x_0}{1+z^2}\begin{bmatrix}\frac{1}{2}\left(2z+\sin\theta\sin 2\xi\tan\theta\right)\\ -\frac{1}{4}\left((3+\cos 2\theta)\sec\theta+2\cos 2\xi\sin\theta\tan\theta\right)\end{bmatrix}.\end{aligned} \tag{3.6.5}$$

Figure 3.7 shows a visual depiction of the evolving optical mode and vortex trajectory for a vortex with beam parameters $\lambda = 633$ nm, $w_0 = 1$ mm, $x_0 = 0.75 w_0$, $\xi_i = 80^\circ$ and $\theta_i = 60^\circ$. The velocity is clearly seen to be driven by the phase and tilt+amplitude gradient terms in Equation (3.6.5). The evolution of the background field changes the relative strength of the background phase and tilt+amplitude gradients such that the x and y components perfectly balance throughout the entire beam propagation, resulting in a constant total velocity. We find that this surprising constant velocity results from the equally-surprising vortex decomposition of the propagating field: the background field is a simple diverging Gaussian, and changes in the amplitude and phase gradients exactly cancel.

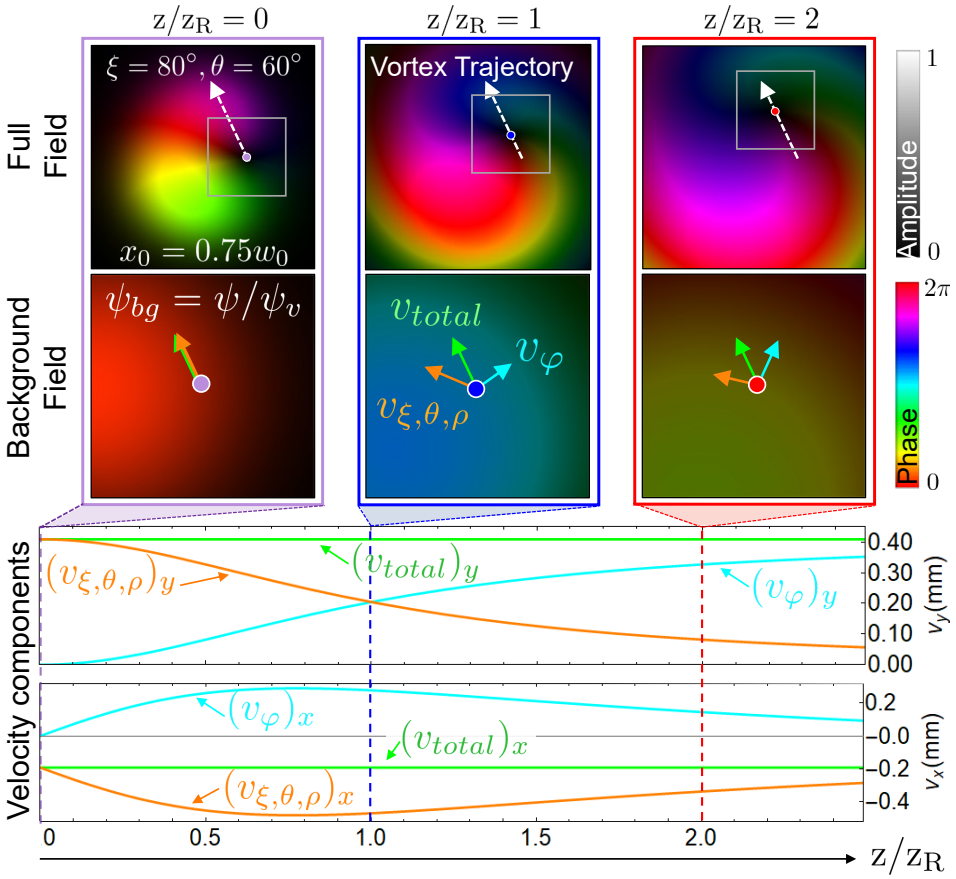

Figure 3.7: The trajectory of a single tilted vortex along with background field gradient velocity contributions are shown. Top: Mode snapshots of an off-center, tilted vortex calculated from Equation (3.6.3) with its location (dots) and predicted trajectory (white arrow) for beam parameters $\lambda = 633$ nm, $w_0 = 1$ mm, $x_0 = 0.75w_0$, $\xi_i = 80°$ and $\theta_i = 60°$. Brightness is amplitude and color shading represents phase. Middle: A cropped window of the background field evolution, along with background gradient vectors to visualize each contribution: cyan (farthest right) arrows show velocity from the first term of Eq. (3.5.17), v_φ, while orange (farthest left) arrows shows the second term, $v_{\xi,\theta,\rho}$; green (middle) arrows are the sum of these terms (v_{total}). Bottom: Evolution of individual components and resulting total velocity for both x and y directions, labeled by the corresponding component, calculated from Equation 3.6.5. From Andersen, 2021. [120] © American Physical Society

To understand how the tilt of a given vortex affects its motion in this scenario, the predicted dynamics for vortices with different tilt angles is summarized in Fig. 3.8. Velocities are measured in terms of the number of millimeters the vortex has moved in the transverse plane per meter of propagation distance. Contour lines are

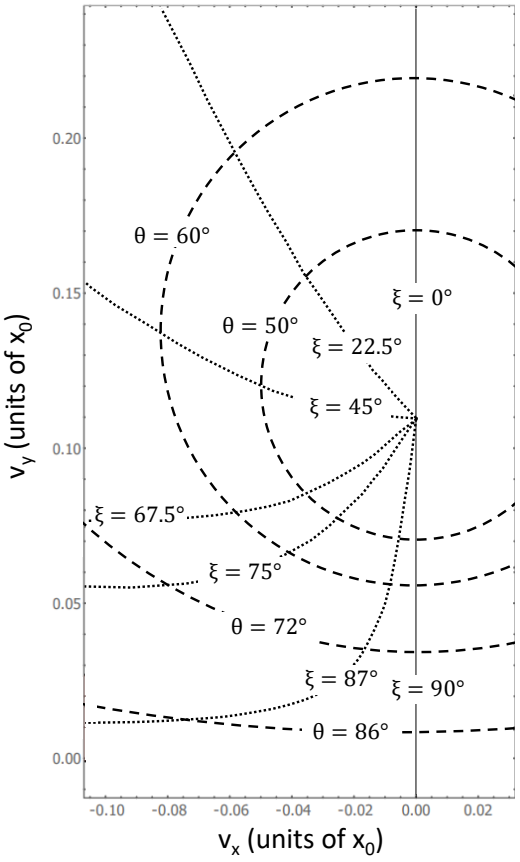

Figure 3.8: *Velocity Predictions for a Vortex on Shoulder of Gaussian Beam.* Velocity predictions in mm/m for both x and y directions are shown for a single vortex with various tilts. Dashed semi-circles show the predicted velocities for a specified polar angle, θ_i, as the azimuthal orientation, ξ_i, is varied. Dotted lines are predictions for a fixed ξ_i and varying θ_i. In the absence of tilt, the vortex moves vertically, but one should note that specific combinations of tilt can also lead to a purely upward velocity. For severe tilt (θ_i near 90°), the vortex can be made to move essentially orthogonal to its untilted trajectory.
Adapted from Andersen, 2021. [120] © American Physical Society

shown in the figure for various tilt angles, with dotted lines showing predictions for a fixed *xi* angle and dashed lines showing results for a fixed θ. In the absence of any tilt($\xi = 0^\circ$ and $\theta = 0^\circ$), a vortex placed on the side of a Gaussian beam will initially move perpendicular to its displacement from the beam center which is consistent with results for the same scenario found within the literature [31]. While the untilted vortex moves vertically when displaced in the positive x direction, one should note that there are other specific combinations of tilt that can also lead to a purely upward velocity (although the magnitude of the velocity will change for a given tilt). For severe tilt (θ_i near 90°), the vortex can be made to move nearly orthogonal to its untilted trajectory. This dependence of the velocity on the degree of ellipticity is also consistent with prior observations [128].

In the figure, polar angles are limited to $\theta_i \in [0, 90]^\circ$ because greater values would correspond to a vortex of opposite charge. Negatively charged vortices move in the direction opposite to their positive counterparts. Interestingly, the vortex velocity is an even function of azimuth angle, ξ_i, despite the initial vortex position being offset from the beam center. Also note that the vortex velocity can never be brought to zero via tilt. This figure will become useful for the experiments discussed in later chapters where the intersection points of the contours are used to test the theory.

3.6.2 An Oppositely Charged Vortex Pair in a Gaussian Beam

Again motivated by the results presented by Indebetouw [32], we are interested in considering two oppositely charged, untilted vortices placed symmetrically in a Gaussian beam. The evolving paraxial field can be obtained via convolution of the

initial field,

$$\psi_{pair,0}(x,y,0) = ((x+x_0)-iy)((x-x_0)+iy)e^{-(x^2+y^2)/w_0^2}, \tag{3.6.6}$$

with the paraxial Green's function, as was done for the single vortex case in Appendix A.5. The solution is particularly simple when considered in the limit of an arbitrarily large beam waist. This leaves only two characteristic lengths: the separation between the vortices, $2x_0$, and the wavelength of the light. Position can then be nondimensionalized using $2x_0$ (in-plane) and $2kx_0^2$ (propagation axis). The resulting paraxial field, in the limit of a large beam waist, is given by

$$\psi_{pair}(x,y,z) = -\frac{1}{4} + x^2 + y^2 + i(y+2z) \tag{3.6.7}$$

The coupled Eqs. 3.4.17 and 3.5.17 can then be solved to find, for instance, that for $z \geq 0$ the evolving vortex tilt as a function of propagation for the right vortex is given by

$$\begin{aligned} \xi(z) &= \tan^{-1}\frac{-1-4z}{\sqrt{1-16z^2}} \\ \theta(z) &= \cos^{-1}\sqrt{-1+\frac{2}{1+4z}}. \end{aligned} \tag{3.6.8}$$

The evolution of the tilt for both the right and left vortices are shown in Figure 3.9.

The trajectory for the vortices in this case is given by

$$x_v = \frac{1}{2}\sqrt{1-16z^2}, \quad y_v = -2z. \tag{3.6.9}$$

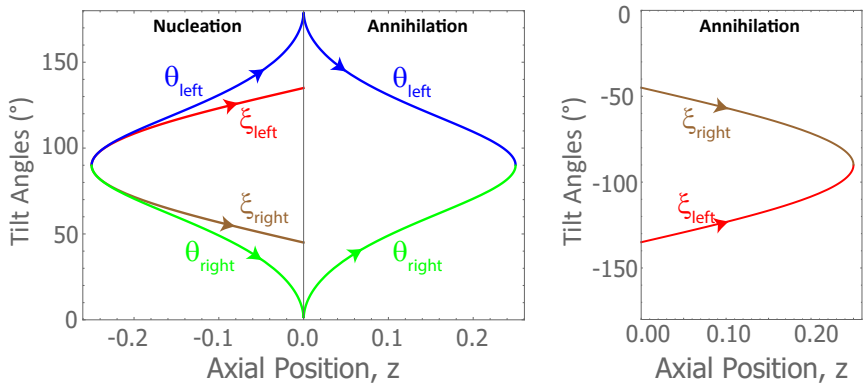

Figure 3.9: The evolution of tilt angles for the oppositely charged vortex pair as described by Equation (3.6.8) is shown.
***Figure credit: Professor Mark T. Lusk. From Andersen, 2021. [120] © American Physical Society

This solution for the field can be propagated both in the positive and negative z direction (essentially looking at the propagation both after and before the beam waist, respectively), which reveals a full vortex loop with a nucleation event occurring at $z = -1/4$ and an annihilation event at $z = +1/4$. The projection of the trajectory into the xy-plane traces out a circle. These dynamics are consistent with the result for $z > 0$ previously obtained using Hankel transforms [32], and also with the result from our propagation of the modes from Section 2.2.

With the tilt quantified at all points within the trajectory, we can then find the background field at any z by unwrapping the tilted vortex of interest: $\psi_{bg} = \psi_{pair}/\psi_{v,tilted}$. From this background field, we are then able to calculate the vortex trajectory using Equation (3.5.17). The result is the same as the the axial derivative of Equation (3.6.9). The full trajectory is shown in three dimensions, including position and tilt in Figure 3.10. When phase gradients within a field get sufficiently steep, a vortex pair can nucleate. In particular, when the phase gradient reaches the

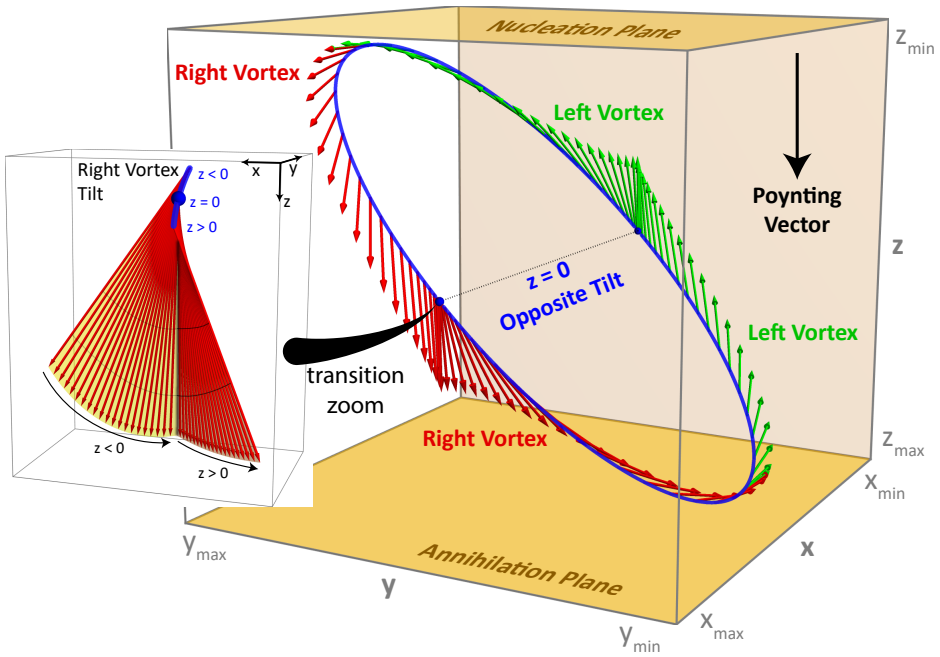

Figure 3.10: *Tilt perspective on nucleation and annihilation.* A pair of identical vortices nucleates at top-left, but subsequently evolve so that they are of opposite charge at the mid-point before becoming once again parallel as they annihilate at lower-right. The envelope of orientations is a mobius strip. The results shown were obtained by combining Eq. (3.6.9) and Eq. (3.6.8).
***Figure credit: Professor Mark T. Lusk. From Andersen, 2021. [120] © American Physical Society

π threshold, two vortices that happen to have the same tilt nucleate [137], as can be seen in the top left of Figure 3.10. The tilts then evolve in opposite directions such that the vortices are of opposite tilt at the midpoint in their life cycle. They subsequently become realigned so that they are once again parallel when annihilation occurs. At both nucleation and annihilation, the polar tilt is 90°, and the eigenvalue analysis implies that the axial speed must be zero while the lateral speed is infinite. This is consistent with the trajectories plotted. We notice that there are corners in the tilt near $z = 0$, which can also be seen by the discontinuities in the derivative for

Figure 3.9. One could imagine finding a field with a smoothly varying tilt throughout the entire trajectory, but that was not done here, as our goal is to understand the dynamics of the same, $z = 0$ field found in [32].

The results of Equations (3.6.7–3.6.8) are the limiting case of an infinite beam waist, but the characteristics of the two vortex tilt evolution discussed above are also relevant to experiments with finite beams if the initial vortex separation is small compared to the beam waist. A finite beam contributes amplitude and phase gradients that affect the vortex motion, just as in the single-vortex case. Therefore, in our quantitative comparison with experiments below, we include the beam in the Fresnel integration solution of paraxial propagation. The solution is consistent with past work [32].

3.7 Summary and Confirming Tilt-Affected Vortex Hydrodynamics for the Two-Vortex Case

At the end of Chapter 2, we left off with the problem that prior hydrodynamic models could not accurately predict vortex motion in the two vortex case. In this chapter, we have presented a new formalism to quantify the tilt angles for a virtual, three-dimensional vortex that results in elliptical vortices within the *xy*-plane. We have seen how in using this formalism, it is possible to derive a tilt-affected vortex velocity expression (Equation 3.5.17) in terms of the background fluid gradients. This model provides a hydrodynamic perspective to vortex motion that works generally, even when vortex ellipticity is present and evolving. To reconnect with the previous chapter, we turn to confirming that that our new model can accurately predict the motion in the two vortex case.

With both position and tilt evolution of the oppositely charged vortex pair established, we can directly compare the known trajectory to the results of the vortex kinematics determined by Equation (3.5.17). For each approach, we calculate the velocity from the background fields at various z steps according to Table 3.1, which is an adapted version of Table 2.1, to include the new vortex velocity expression that we derived in Section 3.5. In the final compressible+tilt case, not only do background phase and amplitude gradients contribute to vortex motion, but the orientation of the vortex contributes to its motion, as it is a feature of the vortex itself. In order to find the background field for this case, the *tilted* vortex, described by Eqs. (3.6.8) and (3.6.9), is divided out from the expression for the paraxial field.

We compare each of these models to the known trajectory of one of the vortices in an opposite-charge pair, which follows a quarter-circle arc to recombination in the limit of an infinite beam waist (blue curve in Fig. 3.11). The incompressible fluid prediction, (black arrows in Fig. 3.11), is clearly inadequate because it lacks any x-component of the velocity. Accounting for compressibility by including the background amplitude gradient, but not tilt (green arrows in Figure 3.11), is a significant correction near $z = 0$ where the vortices are mostly untilted, but it clearly breaks down near recombination where vortices are most tilted. Only if both the phase and amplitude gradients are included *in addition to the evolving tilt of the*

Fluid Model	Velocity Equation
Incompressible	$\vec{v} = \nabla\varphi_{bg}$
Compressible	$\vec{v} = \nabla\varphi_{bg} - \hat{\kappa}\times\nabla\ln\rho_{bg}$
Compressible + Tilt	$\vec{v} = \nabla_{\perp}\varphi_{bg} - \left(\mathbf{V}_{\mathrm{v}}^2/J_{\mathrm{v}}\right)\sigma_0\nabla_{\perp}\ln\rho_{bg}$

Table 3.1: Models used to calculate non-dimensional transverse vortex velocities for Fig. 3.11 [98, 122].

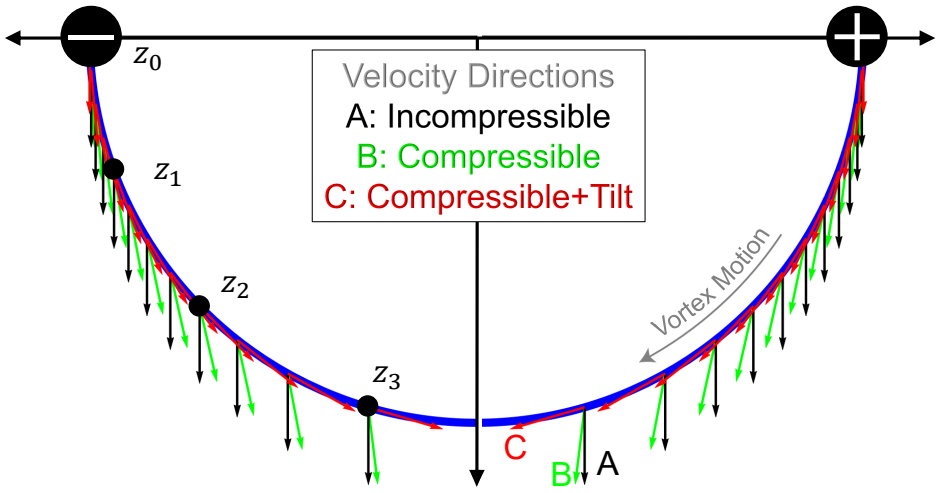

Figure 3.11: *Comparison of Fluid Models for Predicting Vortex Pair Motion*. The quarter-circle trajectory of a vortex in an opposite-pair annihilation event (blue) with arrows show the predicted velocities calculated from three different background fields, as described in the text and in Table 3.1. The incompressible fluid prediction (black), addition of fluid compressibility (green), and inclusion of vortex tilt (red) for the full kinetic theory of Eq. (21). Only the red arrows accurately describe the vortex motion.
***Figure credit: Professor Mark T. Lusk. Adapted from Andersen, 2021. [120]

vortex (red arrows in Figure 3.11, from Equation (3.5.17)) do the velocity vectors fall tangent to the established trajectory.

Clearly, vortex tilt plays an essential role in vortex motion in compressible hydrodynamics. In particular, it is the relationship between the tilt and amplitude gradients in the background fluid that was found to be essential in predicting vortex motion. This is not relevant for incompressible fluids that form the basis for much of our intuition, and it is not observed in compressible fluids for the many scenarios in which vortices are mostly circular in shape (i.e. minimal tilt). However, tilt must be taken into account whenever vortex ellipticity is present or evolves, as we have seen in the two oppositely charged vortex pair setting.

Additionally, we can conceptualize tilt as having an impact on vortex trajectories much in the way that a surfer has on their own motion while riding a wave. A surfer is capable of steering themselves across the water by simply adjusting their body's orientation with respect to the underlying fluid. The analogy can be applied to our vortices, as their orientation plays a role in how they move within the background fluid.

3.8 Part I Summary

In Part I, we established the reasoning behind treating light as a "2+1D" fluid and used an optical medium as a study ground to understand hydrodynamic vortex motion. We also discussed the context for our hypothesis of vortex ellipticity as the culprit behind the failure of previous models for predicting vortex dynamics. This was done by looking carefully at the simple case of propagating a Gaussian laser beam containing an oppositely charged vortex pair. Finally, the newly developed theory for describing vortex motion confirmed that by including the evolution of vortex ellipticity in the velocity expression, vortex motion can be accurately described from a compressible hydrodynamic perspective.

A logical partner to this theoretical framework is to run experiments and test the theoretical predictions. In the following chapters that make up Part II, we will discuss methods for generating and measuring optical fields containing vortices and an experimental apparatus designed specifically for testing the propagation of optical vortices.

II

A Novel Measurement Technique and an Experimental Apparatus

Chapter 4

Using Holograms to Generate Optical Fields in the Lab

Now that a theory has been developed for vortex motion within two-dimensional fluids, the next important step is to validate that theory by comparing it to observations from experiments. To do so, we must first choose a medium in which to test. For the work done in this dissertation, we choose an optical medium. Not only is this consistent with the chosen applications of the theory in the previous chapter, but performing an optical experiment is ideal because it can be done with low power, free space laser propagation, and the experiments are all performed at room temperature, in contrast to other two-dimensional fluids such as BECs that require low temperatures [98].

We must also consider what techniques are available for generating the type of initial condition fields we are interested in testing. There are many ways to generate optical vortices including spiral phase plates [138, 139], digital micromirror displays [140], SLMs [59–63] or even diffusers such as scotch tape [95]. Importantly, not only does convenience matter, but the level of control over and the quality of the experimentally generated optical field becomes important since poor beam quality can impact vortex trajectories within a beam. Some of the methods mentioned can be cumbersome; when using etched pieces of glass, a unique piece of glass is

needed for each field that needs to be generated. In the case of diffusors, they don't offer a lot of control over the generated field.

Using a spatial light modulator, which consists of an array of pixels, referred to as the SLM (or LCD) panel, is of particular interest since it can modulate an incident light field on a pixel-by-pixel basis. Benefits of using such a device include a significant degree of flexibility in the fields that can be generated, the ability to switch from one field to another quickly, and fine control for pixel arrays with high enough resolution. In theory, any pattern can be projected onto the SLM panel. Each of these benefits are appealing for an experiment with more than one initial condition field to generate. One downside is that although commercial-grade SLMs are available, they usually cost on the order of tens of thousands of dollars. The benefits of using such devices can include generating optical fields at high power thresholds, precision phase control, and high power conversion efficiency. A way around the issue of cost, though, is to use a rewired classroom projector LCD panel [141] that costs on the order of tens or hundreds of dollars instead.

For the work done in this thesis, we choose to generate optical vortices by shining laser light onto the low-cost classroom projector SLM that specifically displays a diffractive hologram that has the desired field encoded within it. This is a very common vortex generation technique used within the optics community [23,67–70]. Although this is the case, small imperfections from pixelation or diffraction in the beam can result in a change of the background field gradients that drive the vortex motion. For this reason, the ability to generate high quality holograms becomes a necessity for experimental success.

In this chapter, I will first review the principles of holography that inspire the use of computer generated holograms projected onto an SLM for the experiments. I will

discuss how to make such holograms and a few key elements that are important for creating holograms that generate high-quality vortex beams from such a low-cost SLM.

4.1 Holography Concepts and Overview

To motivate our use of computer generated holograms for experiments used to measure optical vortex dynamics, we will briefly review the basic concepts of holography [65, 142–145].[1] To understand the power of holography, we can first remind ourselves of the limitations of traditional photography. The image of an object can be captured and stored onto a piece of photosensitive material. When a person looks at such a photograph the photograph always maintains the same perspective of the object no matter their viewpoint. This is the reason that a photograph of a person looking directly at the camera seems always to be looking at the observer, even if the photograph is viewed from different perspectives [142]. Additionally, photosensitive material can only record the intensity of the light, so only amplitude information of the wavefront is recorded in a photograph. The loss of phase information is the reason for this loss of perspective information.

In contrast, holography is a method for reconstructing the total wavefront that travels away from an object to an observer. When a hologram is used, unlike in a photograph, the observer is always viewing the actual wavefront, so their view of a reconstructed hologram changes with their viewpoint. To accomplish a full reconstruction of a wave, both amplitude and phase information are needed, so, one may think to draw upon the concepts of coherent interferometry. When two

[1] For a more complete discussion of holography principles, I direct the reader to the fourth edition of "Practical Holography" written by Graham Saxby [142].

waves of coherent light interfere, such as a reference wave and an object wave, the intensity pattern becomes dependent on both the amplitude of the waves and their phase. This can be seen by looking at the time averaged intensity of the field at the location of the recording medium [65, 146]. First, the amplitude is given by the superposition of the fields such that

$$E_{total} = E_{obj} + E_{ref}. \tag{4.1.1}$$

The intensity then can be found by taking the square of the amplitude which results in

$$\begin{aligned} I_h &= |E_{total}|^2 = E^*_{total} E_{total} \\ &= \left|E_{obj}\right|^2 + \left|E_{ref}\right|^2 + E^*_{obj} E_{ref} + E^*_{ref} E_{obj} \end{aligned} \tag{4.1.2}$$

This form of the intensity will become useful for understanding the wavefront reconstruction process later, but it is not readily obvious here that the result depends on both the amplitude and the phase of the fields.

An alternate form of the field can be found, though, if one assumes the generic form of the object and reference fields as

$$\begin{aligned} E_{obj} &= a_o e^{i\phi_o} \\ E_{ref} &= a_r e^{i\phi_r} \end{aligned} \tag{4.1.3}$$

where a_o (a_r) is the amplitude of the object (reference) field and similarly, ϕ_o (ϕ_r) is the phase of the object (reference) field.[2] These expressions can then be substituted into Equation 4.1.2 which yields

$$\begin{aligned} I_h &= a_o^2 + a_r^2 + (a_o e^{-i\phi_o} a_r e^{-i\phi_r} + a_r e^{-i\phi_r} a_o e^{i\phi_o}) \\ &= a_o^2 + a_r^2 + a_r a_o \left(e^{-i(\phi_r - \phi_o)} + e^{i(\phi_r - \phi_o)} \right) \\ &= a_o^2 + a_r^2 + 2a_r a_o \cos(\phi_r - \phi_o). \end{aligned} \tag{4.1.4}$$

From this form of the equation (Equation 4.1.4), we can see that a hologram, unlike a photograph, contains both amplitude *and* phase information. It is important to note that although each phase appears in the equation, it is on only as the difference between the reference and object phase. This is not a problem, though, if the reference wave has a known (and usually constant) phase; if this is the case, then one can obtain the object phase.

To experimentally construct a hologram, a coherent reference wave consisting of monochromatic laser light is generated. The ideal reference wave is a perfect planewave, but an expanded Gaussian beam is often used to approximate such a planewave. This light can then be separated, typically by a beam splitter, into two separate beam paths. One path contains the unaltered reference wave, while in the second path an object is illuminated by the light, and the scattered light creates what is called the object wave. Each of the waves are then sent to interfere at a location where a photosensitive medium, such as photographic film, records the interference

[2]The fields given in Equation 4.1.3 can both be functions the transverse coordinates, since they can describe fields that have a spatially-varying amplitude and phase. For simplicity, we will assume this, but do not write the dependence directly into the equations.

pattern which will become the hologram.[3] An example setup is shown in Figure 4.1 (a). Once the film is exposed, it can be developed, set and used as a hologram.

To reconstruct the original object wavefront, a reference wave is sent onto the set hologram with both the same form and angle of incidence as the original reference wave [65, 142–144]. Light transmitted through the hologram is determined by the

[3]The difference between the path lengths of each arm of the interferometer must be less than the coherence length, and near zero for optimal interference. For a HeNe laser, the coherence length is on the order of 20 cm, and the solid state laser used in the single vortex experiments has a coherence length greater than 50 m. Broadband sunlight on the other hand has a coherence length on the order of μm [147].

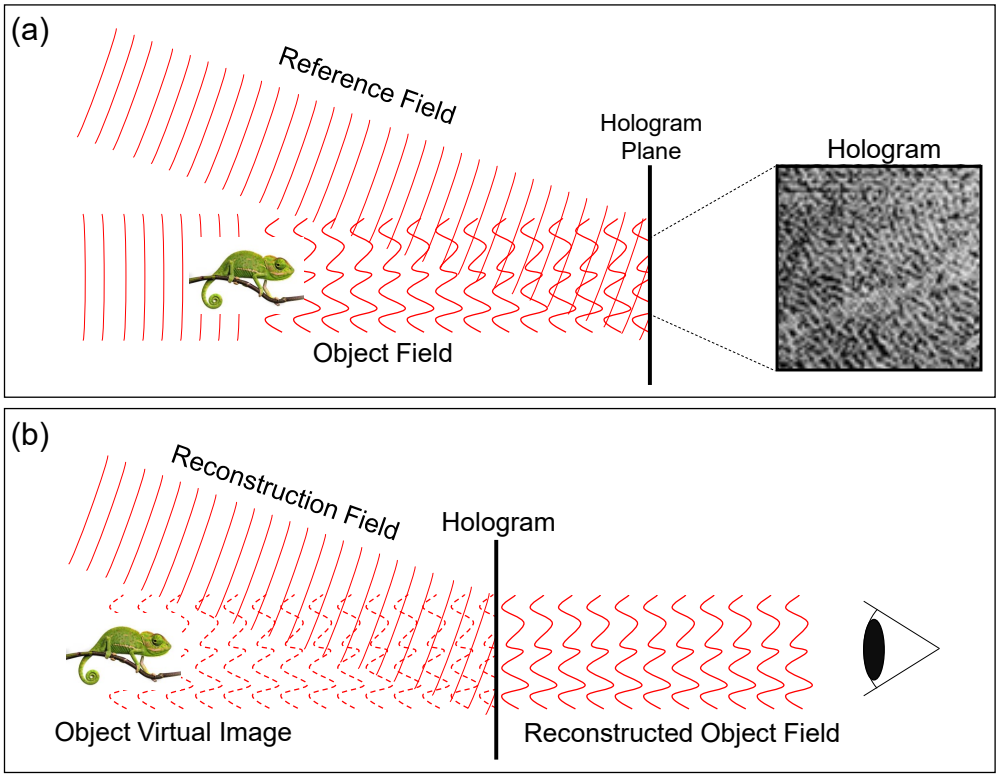

Figure 4.1: (a) A typical geometry for creating an interference pattern that is recorded as a hologram is shown. (b) By illuminating the hologram with a field in the same geometry as the initial recording, an observer sees a reconstructed object field, which yields a virtual image of the object.

transmittance [146], which is simply

$$t = \eta I_h \tag{4.1.5}$$

where η is a constant of proportionality that is determined by physical factors when the hologram was generated, such as the exposure time and the recording medium properties. By substituting in the earlier result for I_h from Equation 4.1.2, the transmitted light is

$$\begin{aligned} E_{trans} &= E_{ref} \times t \\ &= \eta E_{ref} \left(\left|E_{obj}\right|^2 + \left|E_{ref}\right|^2 + E_{obj}^* E_{ref} + E_{ref}^* E_{obj} \right). \end{aligned} \tag{4.1.6}$$

There are four terms of this equation, each of which represents a unique field that is generated by the hologram [146].[4] The first term, which can be written as $E_1 \propto E_{ref}$ is just an attenuated version of the original reference beam, and the second term, $E_2 \propto E_{ref}|E_{obj}|^2$, is an additional modulated wave. The third term, $E_3 \propto E_{ref}E_{obj}^* E_{ref}$ is what is referred to as the conjugate wave that generates a real image of the object [65, 142, 146]. The last term is $E_4 \propto E_{ref}E_{ref}^* E_{obj}$. For the chosen plane wave reference beam, $E_{ref}E_{ref}^* = 1$, so the last term yields $E_4 \propto E_{obj}$, which is the term we've been waiting for that recreates the object field. An observer of the hologram will see this field as a virtual image, as shown in Figure 4.1 (b).

When Gabor presented the first demonstration of the ideas behind holography in 1948, his geometry was such that the reference and object field were collinear [145].

[4]For a more detailed discussion and specific examples of the interpretation of these terms, I direct the reader to Section 9.4 of "An Introduction to Fourier Optics" by John Goodman, or the article "Phase Conjugation and Image Correction" by E. N. Leith. The reader may additionally find their diagrams useful for visualizing each field.

Subsequently, each of the waves described above overlapped, resulting in a distorted version of the object field [145]. While his work was not immediately recognized by others, he was eventually awarded the Nobel Prize in 1971 for his holography work [142]. Importantly, the collinear geometry that Gabor used was not a necessity. In fact, ensuring that the reference field and object field are differentiated by their angle of incidence onto the hologram results in a unique direction for the reconstructed object field [65, 142, 144, 148]. This means that it can be separated from the other fields generated by the hologram and spatially filtered. This so called "off-axis" geometry is commonly used to avoid such distortions of the recreated object field [65, 142, 144, 148].

4.2 Computer Generated Digital Holograms

With modern technology, the need to develop a film is no longer necessary. The process of Figure 4.1 (a) can be done with a computer, and the digital hologram can be displayed onto a spatial light modulator. Benefits of using a computer generated hologram include not only the time saved by skipping the first portion of the experiment entirely, but it also mitigates issues related to choosing the appropriate photosensitive material for the experiment and exposure times or photo-bleaching of the hologram. For the work done in this dissertation, we rely entirely upon computer generated digital holograms.[5]

[5]For all experiments in this thesis, the holograms are designed to match the parameters of an Epson 83H projector used as an SLM; the panel resolution is 1024×768 and the measured pixel pitch is 12.4 μm. Example code used for generating holograms is also laid out in Appendix C.2.

4.2.1 Phase Modulating Holograms

Following the same holography principles as laid out in the previous section, the computer generated hologram can be created by using interferometry. An experimentally generated hologram is created by superposing a reference field (ideally a plane wave) with the object field. With a goal of generating optical vortices, the object field is simply the optical field that contains the vortices in the desired configuration, denoted as $\psi_{field}(x,y)$. The hologram to create the desired phase for an optical field can then be constructed via the superposition of a planewave with the field, written as

$$\mathrm{H}_{\mathrm{phase}}(x,y) = \left| e^{i\,\pi(\cos\alpha\, x + \sin\alpha\, y)/L} + e^{iArg[\psi_{field}(x,y)]} \right|, \tag{4.2.1}$$

where L sets the grating spacing and α determines the angular orientation of the grating. In each hologram, $L = N * d$ where N is the number of pixels and d is the pixel pitch (12.4 μm). As an example, a typical forked grating hologram can be created with a vortex located at (x_0, y_0) by using

$$\psi_{field}(x,y) = e^{i\ell\Phi}, \tag{4.2.2}$$

where ℓ specifies the charge of the vortex and $\Phi = \arctan((y-y0)/(x-x0)))$.[6] A few examples of such forked grating holograms are shown in Figure 4.2. We found that using holograms with grating lines at an angle to the pixel rows and columns of the SLM, such as in rows 2 and 3 of the figure, resulted in cleaner

[6] It should be noted that extra care must be taken with the syntax used for the arctangent function. For example, in Mathematica, the syntax reads as "ArcTan[x,y]", requiring that the denominator be written first.

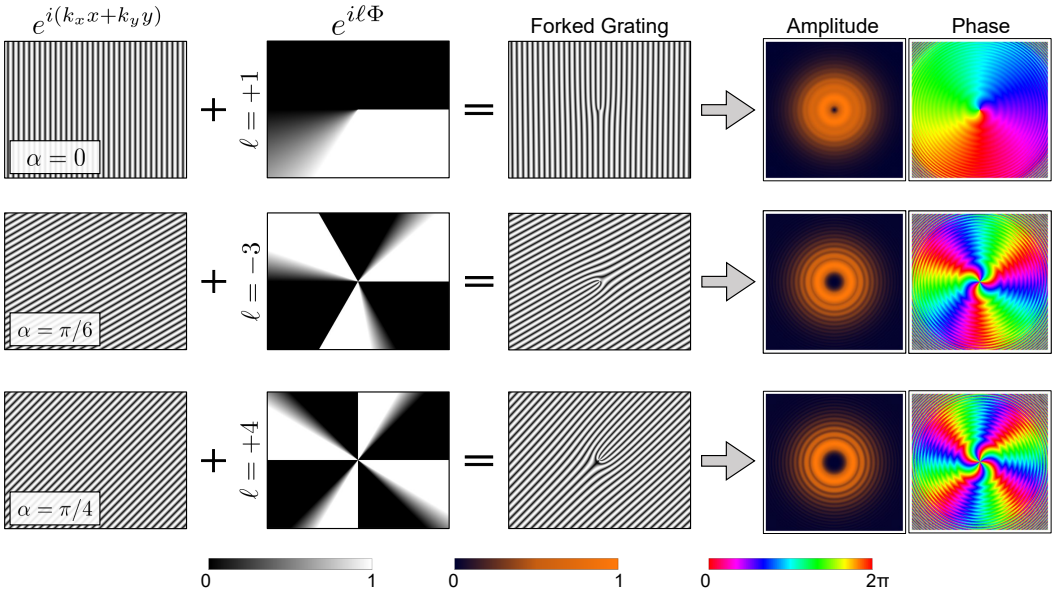

Figure 4.2: Each row shows the constituent parts for building a forked grating hologram and the resulting *HyGG* field at $z/z_R = 0.05$. Each set of gratings displayed has $N = 30$ pixels for clarity.

modes for the single vortex trajectory measurements of Chapter 7, because it is easy to block light diffracting off the pixels. When light is incident on this type of hologram, a Hypergeometric Gaussian (*HyGG*) mode is generated in the first diffracted order [76, 149, 150].

4.2.2 Additional Amplitude Mask

Many have created various holograms or methods for controlling the amplitude of the beam generated from a SLM, each with various degrees of success [45, 60, 61, 67]. Here, I will share the process I used throughout my time at DU, which is most similar to methods found in [61, 151, 152]. It involves just one additional step after creating the forked gratings of the previous section. We have found that the simplest and most effective way to create a beam with both accurate phase and

amplitude is to apply an amplitude mask to the grating. The modified hologram equation for a given vortex field then is

$$\mathrm{H}_{\text{phase\&amplitude}}(x,y) = \mathrm{H}_{\text{phase}}(x,y) * \left|\psi_{field}(x,y)\right|. \tag{4.2.3}$$

For example, say that instead of producing the $HyGG_{\ell=+4}$ mode in Figure 4.2, we want to generate an $LG_{\ell=+4,p=0}$ mode. The hologram can be constructed by simply taking the original $\ell = +4$ forked grating hologram as in Figure 4.2, and multiply it by $\left|LG_{\ell=+4,p=0}\right|$. Examples are shown in Figure 4.3. This same concept can be applied to beams where $\psi_{field}(x,y)$ is the field of a pair of vortices, each with a specified core amplitude, embedded into a host Gaussian beam, and this example is shown in the last row of the figure.

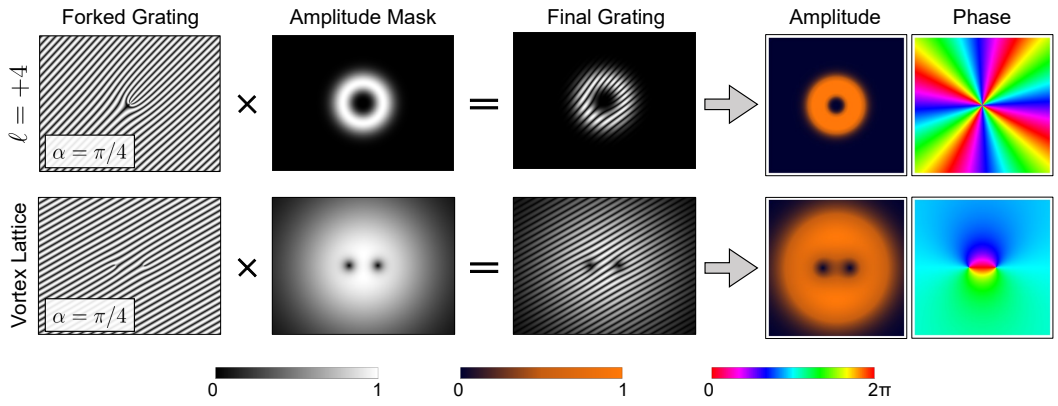

Figure 4.3: Holograms for an $LG_{\ell=+4,p=0}$ (top row) and a vortex lattice (bottom row) are shown. Each row shows the constituent parts for building holograms to modulate both amplitude and phase of the incident field. The resulting fields at $z/z_R = 0.001$ from each hologram are plotted in the last column. The set of gratings displayed has $N = 30$ pixels.

This is the basic set up for making holograms. However, due to the fact that we are using a finite sized pixel grid to generate a field that has azimuthal symmetry, the holograms must be generated with extra care.

4.2.3 A Balancing Act: Large Angle Diffraction and Pixelation

In each of the experiments performed in this work, it is advantageous to use as small of a grating constant as possible in order to increase the diffraction angle of the light from the grating. Larger separation allows for clean observation of the first diffracted order without interference from any other diffracted orders which can cause fringing within the measured field. However, we must take into account the finite size of the pixels and the effect that may have on the hologram quality.

Say for example, you want to create a hologram that has a vortex charge of $\ell = +2$ with a small spacing such that the orders are quickly separated from each other. There is an exact lower limit to the grating spacing period: a grating with one pixel "on", one pixel "off". But, it turns out that superimposing an additional field to a grating of this kind can have a dramatic effect on the generated field. This is because the hologram itself can become distorted from pixelation, as shown in Figure 4.4 (a). It can be seen in the figure that for $N = 2$ pixels, there are regions of constructive and destructive interference as you travel azimuthally around the center. This results in bright and dark azimuthal fringes in the generated optical field, a clear difference from the anticipated $HyGG_{\ell=+2}$ mode that would be anticipated. As ℓ is increased in this type of grating, we observe an increase in the fringes that goes as $2 * \ell$ (ten bright fringes for an $\ell = 5$ mode, for example). The presence such fringes is clearly undesirable and should be minimized or eliminated, if possible.

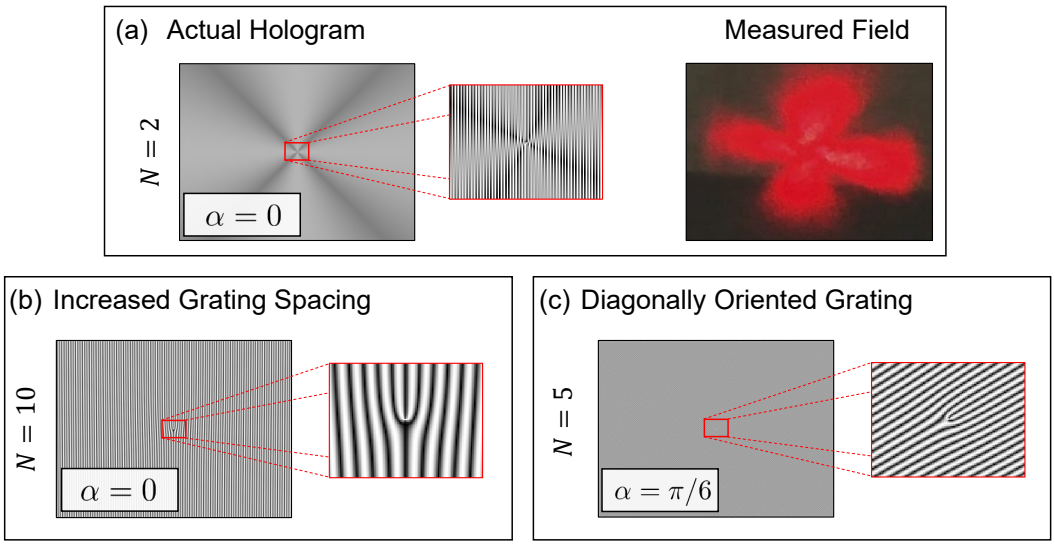

Figure 4.4: (a) An $\ell = +2$ hologram with the smallest possible grating constant is shown (left). A zoomed in version shows the pixelation and distortion present within the hologram. The resulting field (right) is very poor quality, with azimuthal fringes present in the beam and seemingly no vortex at the center. (b) An $\ell = +2$ hologram improved by increasing the grating spacing. (c) An $\ell = +2$ hologram improved by using a diagonally oriented grating.

There are two methods to reduce these distortions that we have used. The first is to simply increase the grating spacing, as in Figure 4.4 (b). The large scale image of the grating no longer carries the same interference present in the finer grating, and the zoomed in image is also much cleaner and lacks the distortions seen in (a). The second method that bypasses this issue is to use a grating that is misaligned to the pixels, as shown in (c) of the figure. These diagonally oriented gratings produce clean data, and have the extra advantage of generating light that is also misaligned to the pixel diffraction. Although we did not use diagonal gratings for all of the experimental work presented in later chapters, we recommend using them for these reasons mentioned here.

One final note on the holograms is that for optimal field generation, the values of the grating should be rescaled such that the grating contrast is maximized. Using the full bit depth of the SLM means that the most light possible is transmitted and the resulting beam seems to have a higher signal to noise ratio.[7] With these details of making holograms established, it is now time to move on to a discussion of methods for measuring the fields generated by the holograms.

[7]This is true for any single hologram used for generating an arbitrary optical field. In the next chapter, this normalization must be done more carefully when implementing the colinear phase-shifting digital holography by using composite holograms.

Chapter 5

Measuring Optical Fields and Collinear Phase-shifting Digital Holography

This work was published in Applied Optics: Volume 58, issue No. 2, under the title ***Characterizing vortex beams from a spatial light modulator with colinear Phase-shifting holography*** [151].

When I first came to DU, the group had not yet learned how to measure the phase of a vortex beam. We were relying on intensity profiles, even when looking at generating pure *LG* modes, and searching for a way to measure the phase. Through this chapter, I will discuss the methods of phase-shifting digital holography and our novel colinear implementation of the process by using composite holograms. The process allows for measurement of the full complex field, without which we cannot track vortices as accurately and precisely. As we will see later in the two vortex annihilation experiment of Ch. 7 and Ch. 8, tracking the vortices accurately is not possible by simply looking at the intensity profiles of the beam and this may be a contributing reason for why such dynamics have not been previously measured in detail by other groups.

5.1 Phase-shifting Digital Holography

When light is generated by a hologram, the full field is generated, but when measuring that field, the same issues arise when taking a photograph: only intensity can be recorded. However, in 1997, Yamaguchi et al. wrote a paper that discussed a clever method called phase-shifting digital holography [153]. This method allows for not only the amplitude information to be measured, but the phase information can also be reconstructed when using the technique. This was an opportunity for us, since we could implement their methods for our purposes: to measure the phase of our vortex beams. Here, we will quickly review the original phase-shifting digital holography work done and follow that with our implementation for vortex beams.

5.1.1 Method Review and Sign Correction

The concept of the phase-shifting holography is fairly simple. An interferometer is used such that there is a signal and reference beam that produces an interferogram which is incident onto a CCD. The field of the interferogram is given by [153]

$$\begin{aligned} U_{\text{interferogram}}(x,y) &= U_{\text{signal}}(x,y,\phi_S) + U_{\text{reference}}(x,y,\phi_R) \\ &= A_S e^{i\phi_S} + A_R e^{i\phi_R}. \end{aligned} \tag{5.1.1}$$

This interferogram's intensity is then written as [153]

$$\begin{aligned} I(x,y,\phi_R) &= \left|U_{signal}(x,y,\phi_S) + U_{reference}(x,y,\phi_R)\right|^2 \\ &= \left(A_S e^{i\phi_S} + A_R e^{i\phi_R}\right)\left(A_S e^{-i\phi_S} + A_R e^{-i\phi_R}\right) \\ &= A_R^2 + A_S^2 + A_R A_S\left(e^{i(\phi_R-\phi_S)} + e^{-i(\phi_R-\phi_S)}\right) \\ &= A_R^2 + A_S^2 + 2A_R A_S \cos\left(\phi_R - \phi_S\right) \end{aligned} \tag{5.1.2}$$

where we have made use of the identity $\cos\theta = \left(e^{i\theta} + e^{-i\theta}\right)/2$.

The goal is to find the phase of the beam, but this expression on its own contains both amplitude and phase information. However, by algebraic convenience, an expression can be constructed such that the amplitude of both the signal beam and reference beam can be eliminated, leaving just the phase of the reference and the relative phase of the signal beam. One way to do this is the four phase step method used in the mentioned paper [153] and in our work. The first thing to notice is that the difference between two of the interferograms of Equation 5.1.2 with different reference phases will eliminate the first two terms in the expression ($A_R^2 + A_x^2$). Second, because only the third term of Equation 5.1.2 remains, by taking a ratio of one set of differences over another the prefactor of $2A_R A_S$ can also be eliminated. Doing this and choosing equal phase steps results in a convenient simplification:

$$\frac{I(x,y,3\pi/2) - I(x,y,\pi/2)}{I(x,y,0) - I(x,y,\pi)} = \frac{\left(\cos\left(3\pi/2 - \phi_S\right)\right) - \left(\cos\left(\pi/2 - \phi_S\right)\right)}{\left(\cos\left(0 - \phi_S\right)\right) - \left(\cos\left(0 - \phi_S\right)\right)} \tag{5.1.3}$$

Using the sum and difference identities, this expression simplifies as follows:

$$\frac{I(x,y,3\pi/2)-I(x,y,\pi/2)}{I(x,y,0)-I(x,y,\pi)} = \frac{\cos\frac{3\pi}{2}\cos\phi_S+\sin\frac{3\pi}{2}\sin\phi_S-\left(\cos\frac{\pi}{2}\cos\phi_S+\sin\frac{\pi}{2}\sin\phi_S\right)}{\cos(-\phi_S)-(\cos\pi cos\phi_S+\sin\pi\sin\phi_S)}$$
$$= -\tan\phi_S. \tag{5.1.4}$$

We can now solve this for the the phase of the signal beam which yields

$$\phi_S(x,y) = -ArcTan\left(\frac{I\left(\phi_R=\frac{3\pi}{2}\right)-I\left(\phi_R=\pi\right)}{I\left(\phi_R=0\right)-I\left(\phi_R=\frac{\pi}{2}\right)}\right) \tag{5.1.5}$$

I want to take a moment to acknowledge Leah Huzak for very carefully working through the algebra and identifying a sign error in Eq. 3 of the original manuscript [153]. While the phase structure will be correct without the negative sign in Equation 5.1.5, the reconstructed phase will be of opposite topological charge to the actual signal (encoded) beam. This certainly matters for our applications and interpretation of the relationships between vortex motion and charge.

5.1.2 Application to Vortex Beams

In the Yamaguchi paper, a two-arm interferometer was used (shown in Figure 5.1 (a)): a reference arm is paired with a phase shifter and a signal arm is sent onto a die which scatters the laser light and generates the object field. The simple modification to apply this to vortex beams is to replace the object with the SLM, as shown in Figure 5.1 (b).[1] In theory, with the flexibility of the SLM, one should be able to generate any desired field, within the experimental constraints of the chosen SLM, and measure the amplitude and phase of the emitted field, using this

[1] In both Figure 5.1 (a) and (b), it can be important to ensure equal path lengths for each arm of the interferometer to optimize the interference.

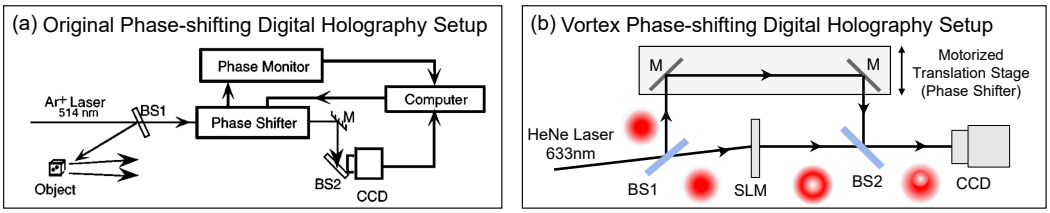

Figure 5.1: *Experimental Setup Comparison.* (a) This is the experimental setup used in the original phase-shifting digital holography paper. [Reprinted] with permission from [153] ©The Optical Society. (b) A similar setup can be used for vortex beams, where the reference arm can be phase stepped using a motorized translation stage. In this case, the object is instead a transmissive SLM that generates a vortex beam.

technique. A shutter may be used in the reference arm to block the reference field when measuring the amplitude of only the signal arm.

Figure 5.2 shows an example of this process and schematic interferograms for an *LG* vortex beam with unit topological charge. In the top row, the intensities for the signal $LG_{\ell=1,p=0}$ mode and a Gaussian reference are plotted followed by superpositions at the four specified phase steps used in the reconstruction. The result is an interferogram with a vortex shifted to the side of the Gaussian, where the direction of the shift is determined by the phase difference between the two modes.

To recover the entire field of the signal beam at a particular propagation distance in an experiment, then, we simply need to take five total images: one image of the signal only intensity (from which we can obtain the field amplitude by taking the square root), and images of the four phase stepped interferograms that are used to calculate the phase. The translation stage that shifts the reference beam, as in Figure 5.1 (b), must be calibrated to accurately shift the phase between the two beams. The CCD can also be moved along the z direction to scan along the beam propagation direction, taking the needed five images at each z-step to build up the vortex

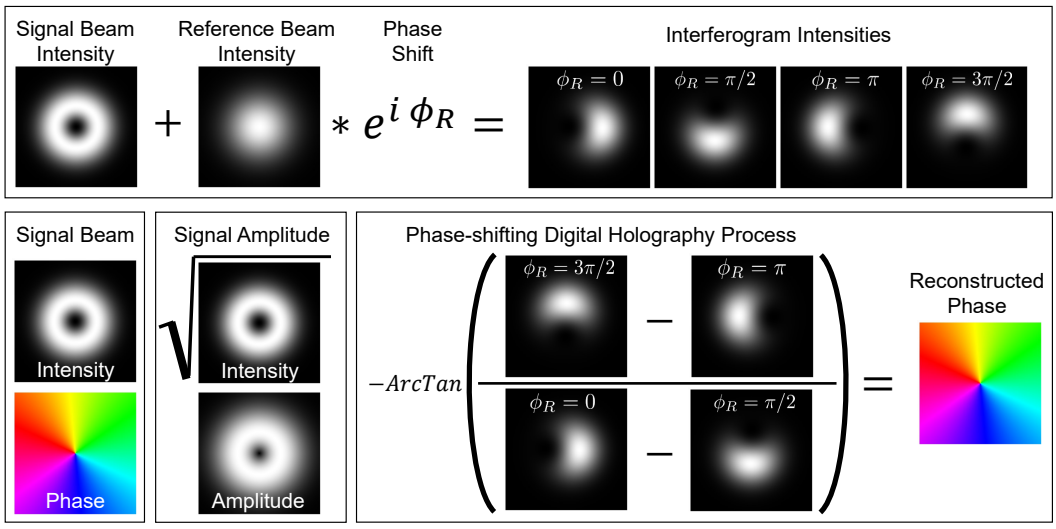

Figure 5.2: The process of measuring amplitude and phase via phase shifting holography is shown. Top: Superposition of a signal beam with a phase shifted Gaussian beam results in varying intensity patterns that depend on the phase shift. Bottom Left: The full complex field of a *LG* beam is shown. Bottom Middle: amplitude of the signal beam can be found by taking the square root of the intensity. Bottom Right: The phase can be reconstructed from the interferograms of the top panel via Equation 5.1.5.

dynamics data. This was successfully implemented for measuring the dynamics of vortices in speckle generated from a piece of scotch tape [91].

While this implementation has been demonstrated, the signal and reference beams travel along different paths, which means they are subject to the difference in vibrations amongst the optics used to direct each beam. This can result in extra phase jitter between the two arms, and less clean measurements. In the next section, we see that a new method can be implemented to eliminate the reference arm, which not only makes the measurement more stable, but it also simplifies the experimental setup.

5.2 Novel Colinear Geometry Phase Shifting Holography by Using Composite Holograms

Using an SLM to generate optical fields has already proven to be a smart choice because of its versatility and ease of changing holograms to create new optical fields in a quick time frame. But, even further, the SLM has become the optimal tool for performing these experiments because of our ability to implement phase-shifting digital holography by using composite holograms. Not only can we generate the desired signal field from a hologram, but we can also simultaneously generate the needed reference beam for reconstructing the phase and let these two fields propagate together.

There are many benefits of this implementation. First, there is no need for a separate arm to recombine the reference beam with the signal beam. This not only eliminates the need for beam splitters in the set up which can cause distortions and vortex shifts in the signal beam [154], but also inherently guarantees that the reference beam will travel in the same direction as the signal beam, removing any fringing or other distortions caused by misalignments between the two. Second, the signal beam and reference beam will also travel along the same path through the experiment. The signal beam and reference beam will therefore pick up the same vibrations through the experiment, whereas an external reference arm can fluctuate with respect to the signal, introducing potential extra noise in the measurement.

5.2.1 Holograms

To generate both the reference and signal beam, we simply add the reference beam to the hologram at the specified phase shift and follow the same methods

from Chapter 4 for producing optimal hologram quality. The expression used for the hologram is then given by

$$\mathrm{H_{PSDH}}(x,y) = \left| e^{i\pi(\cos\alpha\, x + \sin\alpha\, y)/L} + A\psi_{field}(x,y) + B\psi_{ref}(x,y,\phi_R) \right|, \qquad (5.2.1)$$

where $L = N * d$ sets the grating spacing and α determines the angular orientation of the grating, as in Equation 4.2.1. Here, $\psi_{field}(x,y)$ is the field that is intended to be measured and $\psi_{ref}(x,y,\phi_R)$ is the additional reference beam, only used when measuring the phase. A and B are relative weights of the generated field and reference beams.

An example of a set of the five holograms needed to measure the full field is shown in Fig. 5.3. It is easy to see that the resulting holograms match the intensity profiles shown in Fig. 5.2, but with an additional angled planewave that creates the diffraction grating. These superimposed modes each evolve together as the beam propagates, allowing for both amplitude and phase as a function of propagation to be measured. From the amplitude and phase, the vortex location(s) can be identified through tracking real and imaginary zeros, allowing for the measurement of vortex dynamics.

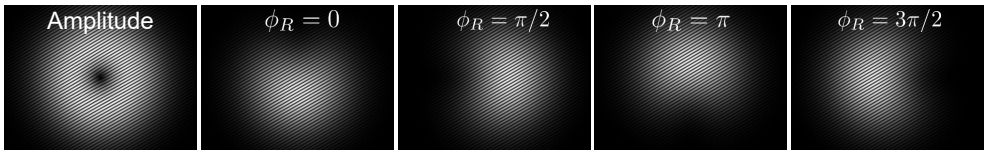

Figure 5.3: Set of composite (reference+signal) holograms used for field measurement of an $LG_{\ell=1,p=0}$ beam with $A = 0.5$, $B = 0.5$, $\alpha = \pi/6$ and $N = 10$ pixels.

Ratio of Signal to Reference Power

The ratio of signal power to reference power used in the experiments of later chapters within this dissertation depend on the specific application. For beams with a single, centered vortex, a 50:50 ratio often resulted in clean phase measurements. However, when there are two vortices close together, having the highest contrast in the grating near the vortex centers tended to yield clearer phase measurements with less noise at the locations of the vortices. It is important to note, though, that going too low, such as 99:01, seemed to optimize the interference for low power noise that may be in the field. In most experiments, the right balance between measuring a clean vortex and minimizing the noise was found by iterating through different power ratios and choosing the holograms that yielded the cleanest phase near the vortex center.

Proper Normalization Methods for Phase Holograms

It was mentioned at the end of Section 4.2.3 that the field generated from the holograms is cleanest when the contrast within the holograms themselves is maximized. While this is generally true, it is important to be careful when generating the holograms needed for reconstructing the phase of the field. This is because to get the proper phase, it is not just the amplitude that is needed, but specifically the *relative amplitude* between each interferogram. If each hologram is rescaled, then the phase calculated is actually incorrect. To avoid this issue, and still maintain the highest contrast possible, the set of four phase holograms are normalized instead to the maximum value within *all four holograms* rather than individually.

5.2.2 Experimental Fields Measured by Colinear Phase-shifting Digital Holography

With each of the holograms made, the experimentally generated fields can be measured and used to reconstruct the full complex field. To test our ability to measure high quality vortex modes, we generated a set of *HyGG* modes and a set of *LG* Modes. The results for modes with topological charge of $\ell = -1$ and $\ell = +4$ are shown in Figure 5.4 along with an $LG_{\ell=0,p=0\&1}$ mode.

The measured amplitude and phase match well with our expectations. In the amplitude measurements, we see smaller vortex cores for smaller ℓ values, and we observe many radial modes in the *HyGG* beams, in contrast to the single, lowest-order mode in the *LG* beams with $p = 0$. The phase information also shows a significantly higher amount of curvature in the *HyGG* modes as compared to the *LG* modes, as expected after some propagation due to the additional radial modes

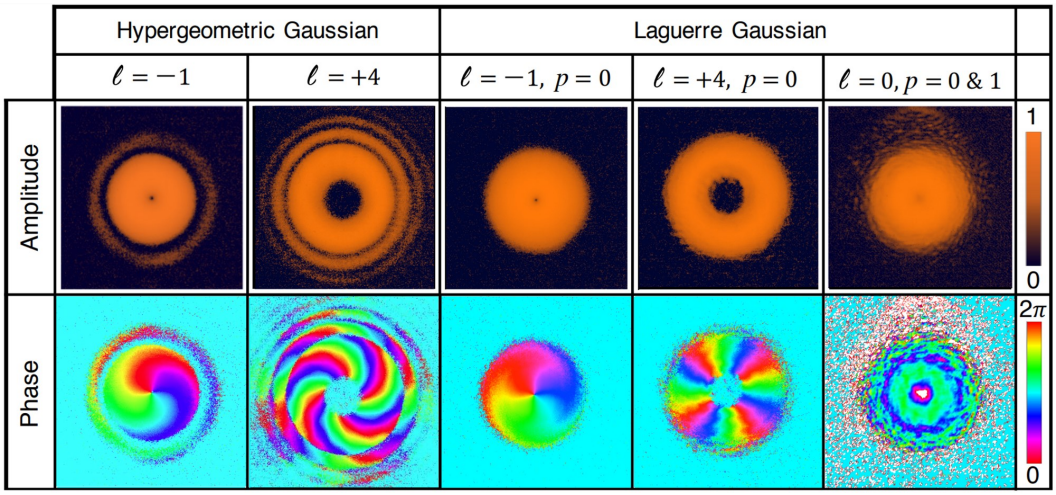

Figure 5.4: Experimental measurements of several complex laser modes measured by colinear phase-shifting digital holography including a "flat donut" mode on the far right. [Reprinted] with permission from [151] ©The Optical Society.

present in *HyGG* beams [155]. The expected topological charge is clearly and directly seen in both the *HyGG* and *LG* beams.

5.3 Modal Decomposition

Since we have both amplitude and phase information from the colinear phase-shifting digital holography process, we can evaluate the quality of the fields generated. One way to quantify this is to perform a modal decomposition of the measured field and compare it to the designed modal content. Any field can be computationally decomposed into any basis [78–85], but if the *LG* basis is used, both ℓ and p power spectra can be determined. This method has many advantages including minimally required data acquisition (one complex beam profile is all that is needed to perform a computational modal decomposition), the ability to check other modal bases without acquiring more data, and minimal alignment error. Here we review the theory for modal decomposition in an *LG* basis and then apply the *LG* modal decomposition to the experimentally measured modes shown in the previous section.

5.3.1 Modal Decomposition Theory

To start, consider the arbitrary optical field, ψ_{field}, such as the fields measured through the techniques of the previous section. This field can be expanded into the sum of *LG* components, so that

$$\psi_{field} = \sum_{l=-\infty}^{\infty} \sum_{p=0}^{\infty} C_p^{\ell} LG_p^{\ell}. \tag{5.3.1}$$

Orthogonality of *LG* modes allow for full characterization of the modal composition of ψ_{field} by way of

$$C_p^\ell = \int_{All} \psi_{field} * \left(LG_p^\ell\right)^* dA, \tag{5.3.2}$$

where $\left(LG_p^\ell\right)^*$ is the complex conjugate of LG_p^ℓ.

Given experimental measurements of the complex image of ψ_{field}, we can measure C_p^ℓ by multiplying that image by a calculated image of $LG_p^{\ell *}$ and then by summing over all pixels. This means that after we have a complex image of a field, our method becomes a matter of iterating through digital transmission filters ($LG_p^{\ell *}$ for all relevant values of ℓ,p) and summing over all pixels, which allows us to measure C_p^ℓ over a very large portion of the $\{\ell, p\}$ parameter space very quickly, without having to take additional physical measurements for each ℓ. Example code used to perform such decompositions can be found in Appendix C.4

5.3.2 Example of Modal Decomposition with Experimental Data

As described in the previous section, the modal decomposition onto an *LG* basis gives the full ℓ-p spectrum measurement, and a projection onto the the ℓ axis yields the ℓ power spectrum. The measurements done for this work used pure *LG* modes as the digital filters. Figure 5.5 shows the results of this decomposition for three experimentally-generated and measured modes: an *HyGG* with topological charge $\ell = -1$, a *LG* mode with $\ell = -1$ and $p = 0$, and the composite "flat donut" that is a sum of *LG* $p = 0$ and $p = 1$ with $\ell = 0$. Calculations of the power spectra confirm high quality mode generation with extremely high ℓ purity for each of the

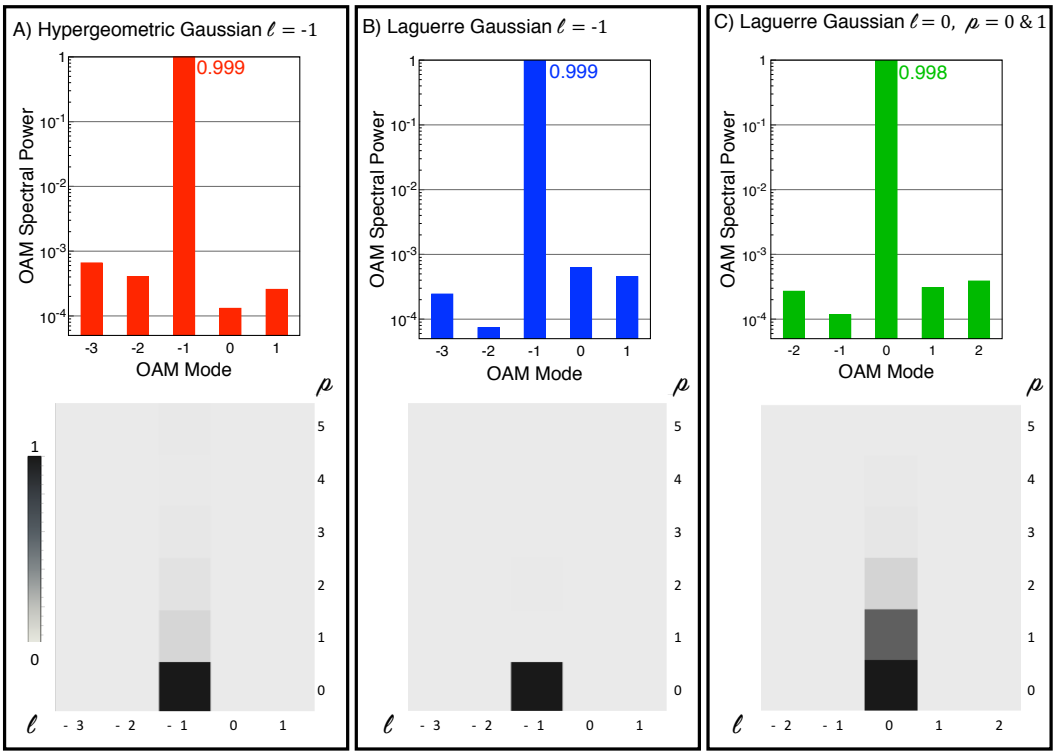

Figure 5.5: Results of modal decomposition on three experimentally measured laser modes: A) a *HyGG* beam with $\ell = -1$, B) an *LG* beam with $\ell = -1, p = 0$, and C) a composite "flat donut" mode composed of $LG_{\ell=0}^{p=0} - LG_{\ell=0}^{p=1}$. The top graphs shows the power spectrum on a logarithmic scale, and the bottom shows the amplitude spectrum in LG_{ℓ}^{p} space. [Reprinted] with permission from [151] ©The Optical Society.

measurements, on the order of 99.9 %. Previous authors were able to attain a modal purity of up to 99.3% [26] and 99.67% [156].

These results show immense promise for our ability to generate optical fields of high purity. However, it is important to consider potential errors in the methods. Successfully quantifying the errors can afford us a high confidence in our ability to accurately measure these modes and confirm that these results are in fact reliable.

5.3.3 Finite Window and Pixelation Error Analysis

As described in Section 3.1, the modal decomposition of a discretized complex field requires the generation of a set of basis fields whose centers must match that of the field of study. The alignment of the pixel edges of the generated basis fields with respect to those of the measured image is extremely important for accurately measuring the modal content. While the pixel edges are generally fixed for a physical measurement, determined by the location of the beam on the CCD and how the image is cropped, the alignment of pixel edges can conveniently take any position during computational analysis. In Figure 5.6 we can see errors from pixelation can be minimized, even for low resolution images.

The errors stemming from pixelation are shown to be less of a function of resolution, and more of a function of pixel-edge alignment, which is surprising. This result can be exploited to achieve high spectral resolution from low resolution data that is easy to measure and compute. Although even inexpensive consumer camera CCDs can be used to record complex images with resolutions on the order of thousands of pixels squared, we analyzed modeled images with only 100 pixels squared to demonstrate that excellent results can be achieved with low resolution, rapidly computable data. The mode spectrum of pure, *LG* modes on a discrete grid (as would be measured by a CCD in an experiment) is calculated using different relative displacements between the modeled image and the calculated transformation filter. Differences in the spectrum for different relative waist sizes of the mode with respect to the size of the image window are also calculated. The error in such a measurement is dependent on the beam size as compared to the window as well: too small and the pixel effects are less forgiving, but too large and the beam is clipped

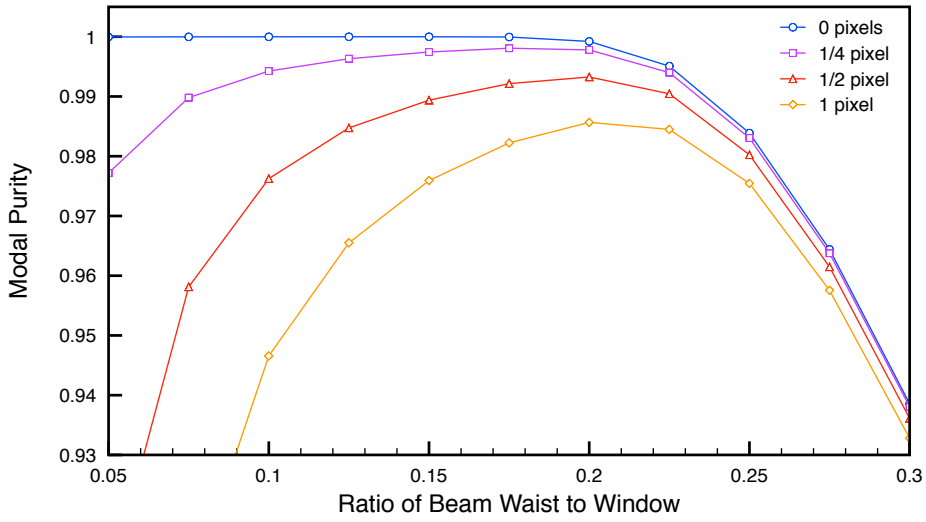

Figure 5.6: Modeled modal purity of a pure LG_0^4 mode as a function of beam waist to the total image window. Each curve shows the misalignment error resulting from the measured mode and calculated mode having: no relative displacement (blue), a quarter pixel displacement (purple), a half pixel displacement (red), one pixel displacement(orange). We conclude there is an optimal ratio for which the error is mostly negligible, and at which very small (sub-pixel) misalignment is at its most forgiving. This relative size is approximately $\frac{2}{5}$ of the window, for all values of ℓ. We find slight variations in these errors for different ℓ values, but the error-minimizing value of the beam to window ratio remains the same. [Reprinted] with permission from [151] ©The Optical Society.

by the window. This trend is shown for LG_0^4 in Figure 5.6, where each line represents the measured modal purity of as a function of beam size in a fixed window, for different pixel-edge displacements.

One important note on this error measurement is that it is not possible to measure a modal content that is of higher purity than the actual mode itself. In other words, it is not possible to adjust the window size around the beam or the center of the calculated *LG* filter to achieve a higher purity measurement; it is only possible to reduce these errors introduced by the modal decomposition process.

5.3.4 Detector Tilt Error Measurements

Further measures could be taken into account such as correcting for any potential misalignments in the detector that is measuring the ℓ content of a given field [157]. However, in Figure 5.7, we show that when measuring the topological charge of a beam our technique is highly insensitive to the tilt of the detector. We see only a small deviation in the ℓ power spectrum as we increase the tilt of the camera to 10 degrees. When increased to 20 degrees, we see slightly more power in the surrounding modes, but continue to measure a purity greater than 99.9% in the ℓ spectrum for this case. The radial mode spectrum proves to follow the same pattern, but we do observe a measurable decrease in the purity of the p=0 mode. That we observe high ℓ purity in the measured mode even in the case of dramatic detector misalignment is indicative of the strength of this technique.

This result makes sense: while a tilted mode may look oblong in the intensity measured on a camera, the reference and signal beam are co-propagating, and therefore maintain the same phase difference and azimuthal phase wrap at the expense

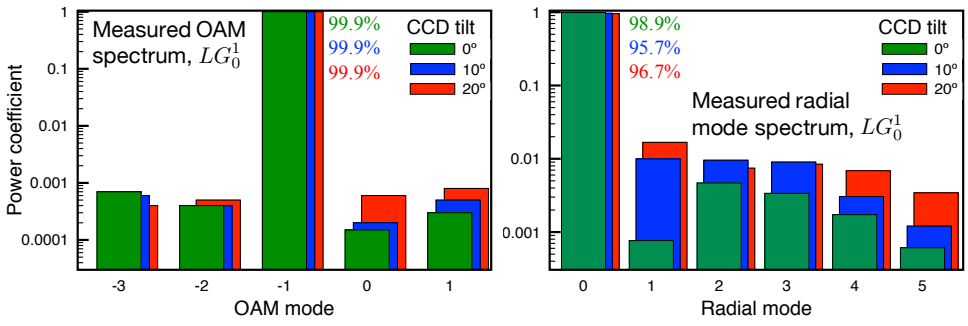

Figure 5.7: Measured modal power spectra of a LG_0^1 beam from CCD images taken at 0, 10 and 20 degrees of misalignment from the axis of propagation. Left and right parts show the same data represented in the ℓ (left) and radial (right) bases. Data is for integer ℓ and radial modes; results for different CCD tilts are slightly offset for clarity. [Reprinted] with permission from [151] ©The Optical Society.

of radial mode purity. These error analyses of decomposition results applied to actual measurements demonstrate the robustness of our colinear phase-shifting digital holography and the digital modal decomposition. In minimizing errors stemming from center mismatches between the experimental field and the digital basis filters, beam to window size, and detector tilt, we can reliably confirm our measured modal purity from Section 5.3.2 of up to 99.9% for the intended topological charge.

In this chapter, we have discussed and implemented a novel colinear geometry of phase-shifting digital holography by using composite holograms. This robust measurement technique allows for quick measurement of both amplitude and phase of any arbitrary field that can be encoded into a hologram in addition to fast computational determination of the *LG* modal spectrum. The modal decomposition results give us confidence that our experimental methods do in fact yield high quality optical fields suitable for testing vortex dynamics for fields as described in Chapter 3. But, we have only discussed how to create holograms for both generating and measuring optical fields. We have yet to discuss the actual apparatus used to do so. This is the topic of the following chapter.

Chapter 6

Experimental Apparatus, Alignment Methods and Other Details

With the theoretical framework laid out, we can consider what the design should be for carrying out experiments used to test the models. The main concept behind the setup is fairly simple: we need an input laser beam to pass through a device that can generate the field we want, and then we need to measure the light that propagates on the other side. My main goal as the experimentalist is to have a set up that can successfully generate and measure the dynamics of optical vortices within beams that is also as simple to work with as possible. Depending on the type of vortex experiment you want to carry out, the vortex generation could be done by anything from a spiral phase plate to a diffuser, as discussed in Ch. 1. I want to take a brief moment here to emphasize that the apparatus designed for the work in this thesis can be used for a wide variety of experiments. However, because I exclusively used holograms displayed on an SLM for the experiments presented here, an external reference path was not needed (that could be necessary for experiments that use another type of vortex generation, such as work done on laser speckle generated from a piece of scotch tape [95], for example).

In this chapter, we will discuss in detail certain aspects of the experimental apparatus and infrastructure that I built, including improvements made to the setup and methods I created through my time here at the University of Denver. While the

number of components in the apparatus is small and the setup is simple in concept, the difficulty of the experiments lies in the need for very high purity modes. Because the vortex trajectories are very susceptible to the quality of the mode produced and propagated through the experiment, any success in the measurements is due to a very high level of precision and care in the experimental setup and alignment. Alignment procedures are discussed in detail in an effort to ease reproducibility of the experiments, and to allow for consistency with future experiments of the same sort that others might perform.

As an aside, I assume any graduate student has something tedious that they must do to maintain an experiment. For me, while getting the alignment as close to perfect as possible is a time consuming endeavor in and of itself, I happened to also spend a surprising amount of time tracking down the most minor specks of dust or scratches on mirrors and lenses that can so easily distort the measurements at the low light vortex centers. Such is the life of many optics experimentalists though, I imagine.

6.1 Experimental Apparatus

6.1.1 Overview of the Optical Set Up

A schematic of the full experimental apparatus is shown in Figure 6.1. A laser, either a 526.5 nm diode laser or a 633 nm HeNe depending on the experiment, is first directed along a line of holes and sent through a telescope with lenses L_1 and L_2 of focal lengths $f_1 < f_2$, which expands the beam. All lenses used in the set up are AR Coated (350 nm-700 nm antireflection) Thorlabs N-BK7 Plano-Convex lenses. An aperture is also placed at the focal plane between the lenses to spatially

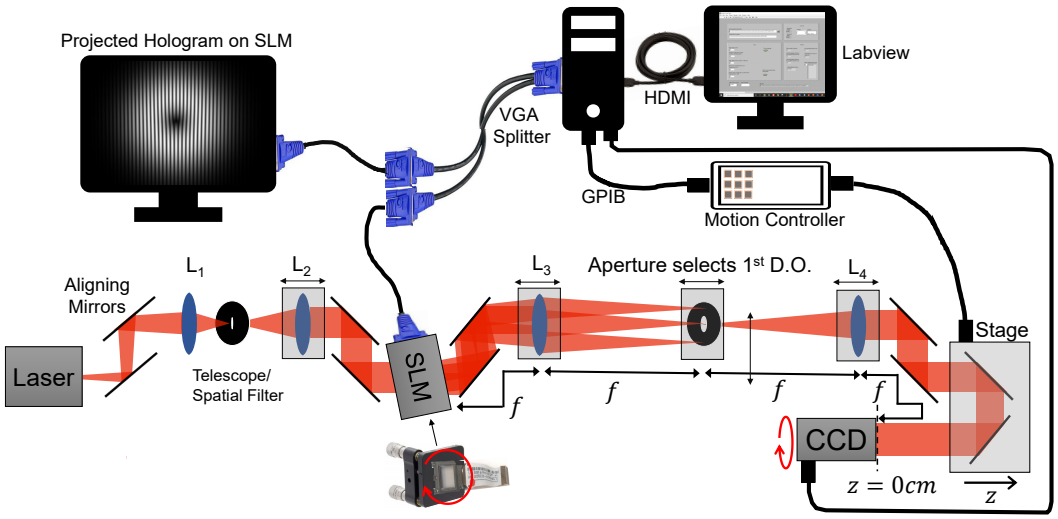

Figure 6.1: A schematic of the complete experimental apparatus is shown. Light incident onto a diffractive hologram projected onto the SLM generates optical vortices in the first diffracted order. This light is then imaged onto a CCD and translation stage is used for changing the path length of the beam to the CCD. Both amplitude and phase are measured by using phase-shifting digital holography.

filter the beam. L_2 is placed on a translation stage that moves along the direction of propagation so that the beam can be collimated very precisely.

The specific values of f_1 and f_2 are chosen depending on the experimental needs and based on the fact that the divergence of the beam coming out of the laser depends on which laser is being used. In general, I found that having a beam size after L_2 that is just small enough to be contained within the smaller edges of SLM panel works best.[1] While it is tempting to use a very large beam to get the incoming field to be as flat as possible across the SLM (and most planewave-like), I do not recommend using beams larger than the SLM panel. These large beams diffract off of the inner SLM panel edges, causing unwanted interference in the

[1]The work in this thesis used an Epson 83H classroom projector LCD panel with resolution of 1024x768 pixels and pixel pitch of 12.4 μm. The panel has a width of 13.97 mm, and an incident beam that has a waist of $w_0 = 2$ mm or less worked well for this SLM.

propagating mode that can distort the mode and subsequently the vortex location in the measurements. Smaller beams can be used when needed, but too small of a beam is also subject to pixelation effects. No matter the size of the incident beam, the incoming Gaussian field and the Gaussian component of the programmed field will be multiplicative, resulting in the same field with a smaller beam waist ($e^{r^2/w_1^2} * e^{r^2/w_2^2} = e^{r^2/(w_1^2 w_2^2/(w_1^2 - w_2^2))}$). Depending on the experimental constraints, it can also be important not to make the encoded field so small that the mode is subject to pixelation effects.

After the telescope, the beam is then aligned along another line of holes on the optical table and a shear interferometer (Thorlabs SI254) is placed at the anticipated SLM location. L_2 is fine tuned such that the beam waist occurs at the surface of the SLM. Having the beam waist at the location of the SLM provides a flat incident phase and alleviates the need to correct for a radius of curvature of the incident beam in the holograms. For the SLM we use a transmissive, red LCD panel of a rewired Epson 83H classroom projector [141], which is mounted onto a 3-axis translation stage in addition to tip and tilt mounts with rotation abilities for precise alignment, described in more detail later in Section 6.2.1. If the incoming beam needs to be realigned, after the SLM is mounted, a check with the shear interferometer a couple of centimeters before seems to be sufficient for beams that have a large Rayleigh length (large, slowly diverging beams). For small beams that have a larger divergence, the SLM may need to be removed and then replaced to ensure accurate collimation at the SLM.

Holograms as described in Section 5.2 are displayed on the SLM and the beam diffracts off of the hologram, generating the programmed field from the hologram in the first diffracted order. Two mirrors immediately follow the SLM to align

this diffracted order along a line of holes. Lenses L_3 and L_4 with $f_3 = f_4 = 50cm$ are then placed on translation stages along this line of holes to spatially filter and image the beam. The stages are in place to fine tune the distance between the lenses in the imaging system. The beam is then finally aligned with a set of mirrors onto a translation stage with a retroreflector that redirects the beam to a CCD for measurements. The CCD used is a 12-bit, $1''$ CMOS Wimcam LCM with resolution of 2048×2048 pixels and pixel pitch of $5.5\mu m$

6.1.2 Computer and Software

To control the experiment, the SLM, translation stage and camera are all connected to the same Windows 10 PC. The main monitor is connected via HDMI whereas the SLM is connected via VGA to prevent communication issues in terms of display resolution on the SLM. It is critical for proper field generation that the resolution of the computer display output match that of the SLM, which in the case of an Epson 83-H projector as used in the experiments is 1024×768. Only one monitor is really necessary, but a VGA splitter was used so that the display on the SLM can be easily viewed for troubleshooting, in addition to having the main computer display. To avoid further communication issues, it can be important to connect the SLM prior to the second monitor. The translation stage is connected to the computer via a motion controller and GPIB or USB connections.

DataRay Software and Labview Automation

Each piece of equipment is controlled simultaneously with an automated Labview program that I wrote. The master program interfaces the available labview programming to run both the stage and the CCD, in addition to programs to control

the SLM. The block diagram and further specifics from the program can be found in Appendix C.1. In each set of data taken, the computer displays the first grating in the set on the SLM and the image on the camera is taken. This cycle repeats for every hologram in the set of data to be taken. After each grating image has been taken, the stage automatically moves back by a step size specified by the user, and the next set of images are taken at the new z location. For ease in data processing later, each recorded image is named with the z location in centimeters followed by the image number in the set. From there, the data is processed via Mathematica files that can be found in Appendix C.3.

6.2 Alignment

Because small misalignments can potentially result in significant changes in the vortex trajectories, throughout my work, I have implemented some best practices that have helped improve the repeatability and quality of the setup. These alignment details address this work's most significant experimental challenges, so they merit a thorough discussion. In addition to the topics discussed within this section, general alignment procedure details that may be beneficial for those who intend to use the same setup are in Appendix B.2.

6.2.1 SLM Alignment when Using a Diffractive Hologram

In general, it is advantageous to put the SLM onto translation stages for fine tuning of its location relative to the incoming beam. The SLM is mounted onto a three-axis translation stage, in addition to a tip and tilt mount. The three axis stage is used for centering the hologram with the center of the beam and to fine tune the

location along the propagation direction in relation to the first imaging lens, L_3. The tip and tilt mount is to ensure that the SLM is oriented as follows.

Angle of Incidence for the SLM with a Diffractive Hologram

When I came to DU, the group had been aligning the SLM such that it was perpendicular to the incoming beam [76]. This seemed reasonable, since generally optics are aligned perpendicular to the propagation axis, and in the case of directly imprinting the phase onto a beam without using a diffractive hologram, the proper alignment is normal incidence [60]. However, we will see in this section that aligning the SLM in this way leads to *LG* modes where the vortex drifts as the beam propagates when it is not supposed to.

Additionally, there seems to be a lack of consistency in the literature regarding the alignment of the SLM when using diffractive holograms. In many cases, including well-known papers, orientation of the SLM is not explicitly mentioned. One might then turn to looking at the schematic of the experimental setup. However, the experimental diagrams are either clearly showing an incident beam that is perpendicular to the hologram [25, 53, 59, 76, 80, 158–161], or it is unclear [59, 81], or neither the incident nor the generated mode are perpendicular to the SLM [162–168]. One study showed it is possible to generate high quality optical vortices using an SLM with a phase-only computer generated hologram [60]. However, this work used a transmission SLM with a hologram that was not diffractive. Another group generated high quality modes at normal incidence, but this was achieved by using a second corrective hologram [169]. In some papers, the orientation of the SLM is shown with a beam coming into the SLM at an angle, with the vortex beam axis perpendicular to the SLM surface [67, 170–172] and the case of high-angle diffrac-

tion has also been studied [173]. The inconsistency throughout the literature shows the need for reasoning behind a given choice, and what orientation produces correct realization of the hologram.

The importance of being explicit about the relative alignment of the SLM and the incident beam became evident in one of my first projects, in which I attempted to generate a variety of high quality *LG* modes using the SLM. *LG* modes are well understood and if we could generate quality modes across a range of topological charges, we'd have confidence in our ability to generate other optical fields. For this side project, there was no imaging system following the SLM, and we simply allowed the beam to propagate far enough such that the diffracted orders were no longer overlapped to take measurements. This is important for the results of the next paragraph, since we did not want to introduce any potential distortions from lenses [97, 174, 175] and wanted to look at the pure mode after only the SLM.

While working through this project, I found that I could generate an $l = 1$, $p = 0$ mode that looked much like what we expected: a round beam with a centered vortex that could be created and viewed on a camera. However, if the SLM was aligned such that the vortex was centered in the beam for a hologram with an $l = +1$ mode, as soon as the hologram was switched to, say, an $\ell = +10$ mode, the vortex was no longer centered in the beam. Additionally, the $\ell = -1$ mode was no longer centered. Even further, if the camera was placed at a certain location and the $\ell = +1$ mode was centered, at another propagation distance, the vortex also would no longer be centered. This is summarized in Figure 6.2.

An *LG* mode is an eigenmode of the paraxial equation governing optical propagation, so we expect that a vortex in an *LG* beam should remain centered throughout the entire propagation distance. This made the results of Figure 6.2 surprising. Af-

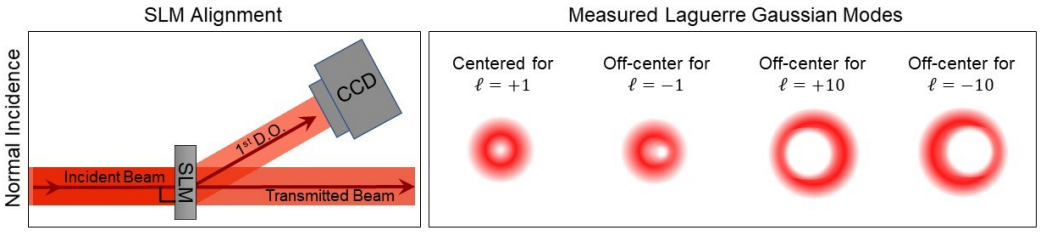

Figure 6.2: For an incident beam that is normal to the SLM, the vortex at the center of *LG* modes in the first diffracted order will drift as the topological charge is varied. The SLM can be moved in the transverse plane such that the vortex is centered in the beam for a single mode at a specific propagation distance, but at all other distances, even that vortex will become off-center.

ter considering many other possibilities, we realized that there must be something wrong with the alignment of the SLM. In particular, because of the mismatch between the $\ell = +1$ and $\ell = -1$ modes, it seemed not to be an issue related to the topological charge or pixelation in the gratings. It is surprising that this issue of SLM alignment has not been identified sooner. We think this is because most work has used unit or unvaried charge beams, for which the problem can be apparently "fixed": it is possible to send in a beam perpendicular to the SLM, place a camera after the SLM at a specific location, and get the vortex centered on the beam by moving the SLM vertically and horizontally. The problem is, the vortex will only be centered at that location, and for those who are relying upon a high quality vortex (or even other more general optical modes), it is imperative to get the SLM alignment right.

In hindsight, it makes sense that the proper alignment for the SLM requires that the first diffracted order carrying the encoded field be perfectly perpendicular to the SLM. The field encoded into the hologram has a mode axis that is perpendicular to the surface of the SLM and the reference beam programmed into the hologram is an angled planewave. So, to imprint the field correctly, the first diffracted order should

be aligned perpendicular to the SLM and the incident beam should be at an angle. This is also consistent with the holography principles discussed in Section 4.1.

The beam incident onto the SLM is therefore aligned along a line of holes and the SLM is placed in the beam path at an angle such that the first diffracted order propagates perpendicular to the SLM, as shown in Figure 6.3. To guarantee that this is the case, the simplest way to align the SLM at the correct angle is to compare the incident beam, first diffracted order and the reflected beam. In the case of a reflective SLM, the first diffracted order is 90° to the SLM when it is exactly in between the incident and reflected beams, such that $\alpha = \beta$ in the figure. For transmissive SLMs, we use the backreflection to align the SLM with the same process. In this case, it is important to use the diffracted order on the side that corresponds to the

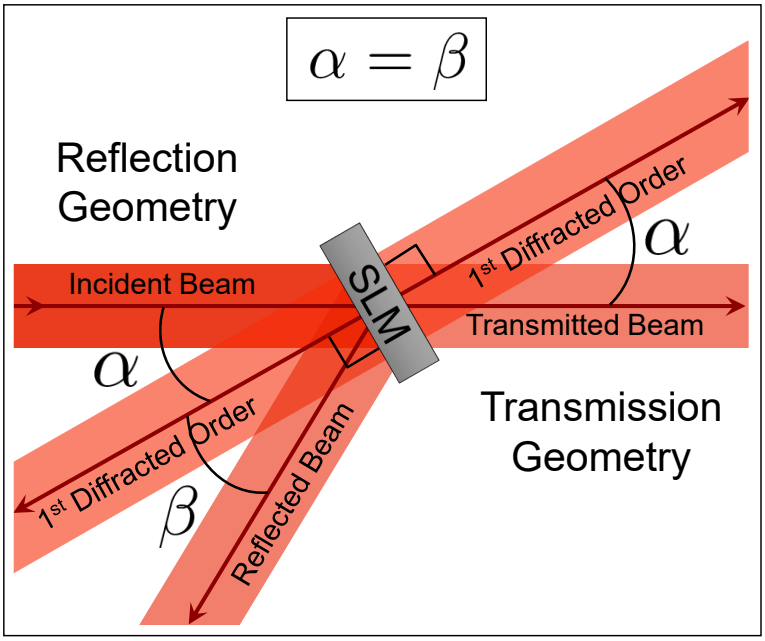

Figure 6.3: *Schematic of the Correct SLM Alignment.* For a reflective SLM, the first diffracted order should be exactly in between the incident and reflected beam, in both the *x* and *y*. Using the same alignment for the backreflection on a transmissive SLM will guarantee proper orientation of the transmitted first diffracted order.

back reflected beam ($m = +1$ is the top diffracted order in the figure for the depicted SLM orientation). The opposite order ($m = -1$ in the figure) is not perpendicular to the SLM and will not authentically reproduce the hologram.

The exact angle of incidence of the beam onto the SLM will depend on the grating constant. Gratings with closer fringes produce higher angles of diffraction, so a grating with a small grating constant will need a larger rotation of the SLM. It is possible to minimize the angle of incidence to the SLM by using a large grating constant (small diffraction angle), reducing the effect of non-optimal alignment, such as coming in at normal incidence. However, cleanly isolating the first diffracted order from the others becomes a challenge, even when spatially filtering the mode with a lens and aperture. In our view, it is more beneficial to illuminate the SLM at the proper angle and use as small a grating constant as possible[2], to get better spatial filtering of the first diffracted order.

Comparing Higher Order Modes at $z = 0$

To check that the SLM is centered and that the angle is also correct, I compare two *LG* modes, each with the same, higher order topological charge, but with opposite sign. I typically compare modes with either $\ell = \pm 10$ or $\ell = \pm 12$. As mentioned earlier, when the SLM is not aligned at the correct angle, the vortex center will drift as you scan through different values of topological charge. When the SLM is oriented correctly, the vortex (propagated some distance, such as a few meters) from the SLM) should be centered for both higher order modes, as can be seen in Figure 6.4. Additionally, the vortex should no longer drift with beam propagation.

[2] As discussed in Chapter 4, the grating constant can only be so small before pixelation in the hologram can distort the generated field.

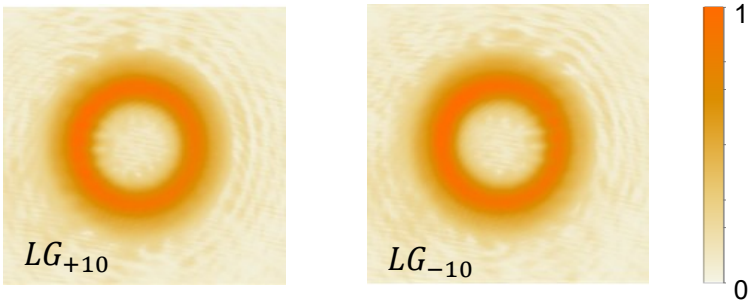

Figure 6.4: *Using Higher Order Modes to Check Alignment.* Toggling between a high order mode with either positive or negative topological charge can indicate if the orientation of the SLM is not quite right. When the SLM is oriented correctly, both modes will be centered, as in these images. When it is not, there will be a shift in the intensity profile and while one mode can be centered, the other will clearly be off-center, as shown in Figure 6.2.

A combination of the SLM orientation of the previous section, and checking the vortex drift across higher order positive and negative charge vortices allowed us to obtain the very high purity modes discussed in Chapter 5, even with a very low cost, used projector LCD panel with pixels that are larger than the typical commercial SLMs designed for use in optical laboratories.

6.2.2 The Imaging System and Minimizing Magnification Errors

Another very important part of the experiment is the imaging system that is placed after the SLM. Depending on the the experiment, the imaging may not always be needed. For example, if one only needed to measure a beam at propagation distances far from the SLM, it is possible to simply wait for the diffracted orders to separate from each other, redirect the first diffracted order onto a CCD, and take the necessary measurements. However, in the case of our vortex dynamics experiments, being able to measure the entire propagation of the field starting at $z = 0$ is beneficial, because only then can we capture the full dynamics. No matter how

small of a diffraction grating that is possible for a given setup, the only way to do this is to use an imaging system. This is comprised of two lenses of equal focal length, for simplicity, placed such that the light emitted from the SLM can be imaged and the first diffracted order can be spatially filtered with an aperture at the focus of the imaging system. The light generated from the SLM will travel through both of the imaging lenses (L_3 and L_4 as shown in Figure 6.1), and their alignment can have a dramatic effect on the outgoing beam.

If the imaging system following the SLM is perfectly set up such that the SLM is located exactly one focal length away from the first lens and the distance between both lenses (L_3 and L_4) is exactly $f_3 + f_4$ apart, then the beam propagating from the SLM will be exactly the same as the beam beginning a distance of f_4 away from L_4. This means that the imaging plane is the new location of the beam waist, as well as the new $z = 0$ point, as shown in Figure 6.5 (a). After the imaging plane, the light propagates just as it would have if the surface of the SLM were located at that imaging plane instead. Another way to think about this is that L_3 and L_4 not only image the light at the surface of the SLM, but also the light propagating beyond the SLM as well. However, this one-to-one propagation is only true for completely perfect alignment, which is not possible in an experimental setting. Although they can be minimized, misalignments will always be present.

One type of misalignment is the transverse alignment of the lens compared to the beam axis. The first diffracted order should be aligned on each lens so that it is incident in the exact middle of the lens. This is to avoid any asymmetric focusing or distortions to the beam that can cause displacements in the vortex locations that can be introduced by the lenses [174, 176] or asymmetries in the host beam that can alter vortex dynamics [97, 177]. A target (such as a Thorlabs SM1 UV/Visible

Alignment Disk, VRC1SM1) is placed on each lens as it is aligned to minimize these types of errors, and the lens is adjusted until the beam is centered on the target (and therefore the lens).

A second type of misalignment in relation to each individual lens is the incoming angle of the beam with respect to the lens. If the beam enters the lens at an angle, the light is no longer focused (or collimated) properly through the lens. These shifts and tilts can cause dramatic changes in the modal content and therefore the beam propagation [175, 176]. The angle of the lens with respect to the beam can

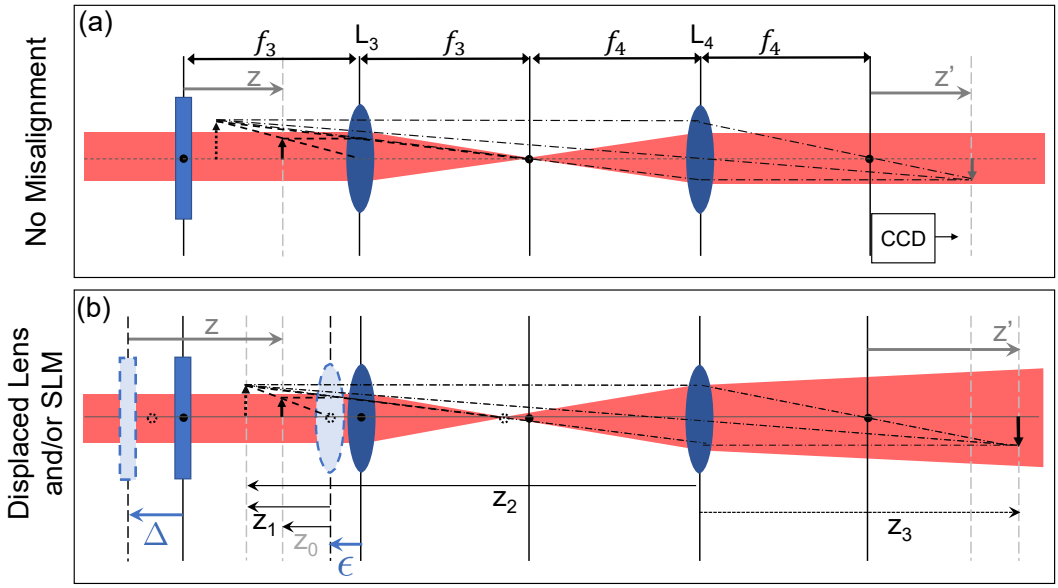

Figure 6.5: Ray diagrams are shown for the case of a perfectly aligned imaging system as shown in (a), or an imaging system with two types of misalignments as described in the text and shown in (b). In both (a) and (b) the object considered for the ray tracing is the field propagated to a certain distance away from the SLM, marked by the black, solid arrow. Application of the thin lens equation to this "object" results in a virtual image created by the first lens, L_3, marked by the dashed black arrow. This virtual image is then used as the object for the second lens, L_4. The location, z', and size of the final image that appears on the right side of L_4 depends on both the error in the placement of the SLM (described by Δ) and the error of the distance between the two lenses (described by ε).

be adjusted using the back-reflection of the beam, as far back down the beam path following the first diffracted order as possible to allow for the smallest misalignment possible. While each of these types of misalignments can be found within the literature, there are other misalignments that are crucial to consider, specifically in the context of accurately measuring vortex dynamics. The remainder of this section is dedicated to understanding these additional sources of misalignment and how to minimize their effects.

The first additional misalignment that we consider is a displacement, Δ, of the SLM from the left focal plane of L_3 as shown in Figure 6.5 (b). A second possible misalignment is of the z distance between the lens pair after the SLM, shown in Figure 6.5 (b). For this, we will consider the first lens, L_3, to be displaced to the left by ε from the correct location. If the distance between the lens pair is not well aligned along z, the result is a magnification of the beam which can not only alter the intended initial condition field at the focal plane of the second lens, but it also scales the meaning of the z propagation after the lenses.

To understand the exact effect on the beam propagation, we can apply a simple ray optics approach to an object located to the left of L_3 and make use of the thin lens equation. We will use the diagram and distances labeled in Figure 6.5 (b) and will solve the problem for the case that includes a displacement from the correct position for both the SLM and L_3.

As a reminder, the thin lens equation is given by

$$\frac{1}{f} = \frac{1}{d_{object}} + \frac{1}{d_{image}} \tag{6.2.1}$$

where f is the focal length of the lens and d is the distance to either the object or the image, indicated here by the subscripts. For a lens pair, we follow the process of applying the first lens to the first object and then the second lens to the image created by the first lens, allowing us to find the relationship between propagation from the SLM and the propagation after the second lens.

For the first lens L_3, consider the field propagated away from the SLM by an amount, z, and located z_0 away from L_3. This is marked as our 'object' by the solid black arrow to the left of L_3 in Figure 6.5 (b). For the sake of this example, let's assume that the focal lengths are not the same for generality, and that $z > \Delta$ such that this object is inside the focal length resulting in a virtual image and thus a negative sign applied to the image distance. The image produced is located at position z_1. The thin lens equation is therefore given by

$$\frac{1}{f_3} = \frac{1}{z_0} + \frac{1}{-z_1} = \frac{1}{f_3 + \Delta - \varepsilon - z} - \frac{1}{z_1} \tag{6.2.2}$$

where we have made use of the fact that in this geometry $z_0 = f_3 + \Delta - \varepsilon - z$. A few algebraic steps gives us the virtual image distance

$$\begin{aligned} z_1 &= \left(\frac{1}{f_3 + \Delta - \varepsilon - z} - \frac{1}{f_3} \right)^{-1} \\ z_1 &= \frac{f_3(f_3 + \Delta - \varepsilon - z)}{z - (\Delta - \varepsilon)}, \end{aligned} \tag{6.2.3}$$

for which the image is represented by the black dashed arrow in the schematic.

This can now be used as the object for the second lens. Since this object is guaranteed to be to the left of the original object because of the specified geometry, we can assume that this new object lies well outside the focal length of the second

lens without concern. Therefore, the next application of the thin lens equation yields

$$\frac{1}{f_4} = \frac{1}{z_2} + \frac{1}{z_3} = \frac{1}{z_1 + f_3 + f_4 + \varepsilon} + \frac{1}{z_3}. \tag{6.2.4}$$

Substituting in Equation 6.2.3 for z_1 and solving for the final image distance, z_3, the resulting expression is

$$\begin{aligned}
\frac{1}{f_4} &= \frac{1}{z_1 + f_3 + f_4 + \varepsilon} + \frac{1}{z_3} \\
\frac{1}{f_4} &= \frac{z - (\Delta - \varepsilon)}{(z - (\Delta - \varepsilon))(f_4 + f_3 + \varepsilon) + f_3(f_3 + \Delta - \varepsilon - z)} + \frac{1}{z_3} \\
\Rightarrow z_3 &= \left(\frac{1}{f_4} - \frac{z - \Delta + \varepsilon}{(f_4 + \varepsilon)(z - \Delta + \varepsilon) + f_3^2} \right)^{-1} \\
z_3 &= \frac{f_4(f_4 + \varepsilon)}{f_3^2}(z - \Delta + \varepsilon) + f_4 \\
\Rightarrow z' &= \frac{f_4(f_4 + \varepsilon)}{f_3^2}(z - \Delta + \varepsilon).
\end{aligned} \tag{6.2.5}$$

In the last step we have made use of the fact that the propagation distance measured by the CCD in the lab begins one focal length away from L_4, since for a perfectly aligned system, that would be the $z = 0$ imaging plane (i.e. $z' = z_3 - f_4$).

With this solution, we can now consider some specific cases. In particular, when $f_3 = f_4$, as is done in our experiments to ensure one-to-one magnification of the field from the SLM, the expression becomes

$$z' = \frac{(f + \varepsilon)}{f}(z - \Delta + \varepsilon), \tag{6.2.6}$$

and for the case where $\Delta = \varepsilon = 0$, the expression simplifies to

$$z' = z. \tag{6.2.7}$$

This simplification verifies that the result of Equation 6.2.6 is consistent with our expectations for no misalignments in the system, as in case (a) of Figure 6.5, where the beam propagates one-to-one from the imaging plane of the second lens.

With this simplification happening as expected, we can now consider other simplifications of the expression that prove to be useful for optimizing the experimental setup. In particular, we will consider the two distinct cases that are most relevant to our experiments: misalignments of only the SLM and misalignments of only the lens pair.

Case 1: $\varepsilon = 0, \Delta \neq 0$

If we assume a positive Δ that moves the SLM to the left, increasing the propagation distance to the first lens by Δ, we recover the result

$$z' = z - \Delta, \tag{6.2.8}$$

where z' is equivalent to z shifted by the same amount (Δ) as the SLM. In hindsight, this makes intuitive sense since a shift in the location of an object on one side of an otherwise perfect imaging system will simply result in the same shift of the image on the other side. The result is plotted with a variety of values for Δ in Figure 6.6 to show the impact. We can quickly note here that the change in position is independent of the focal length of the lenses.

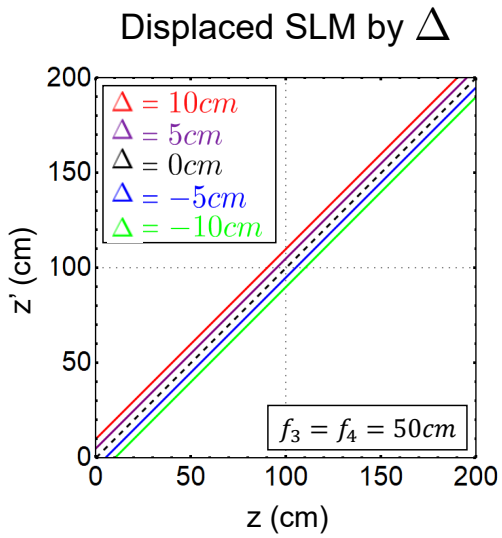

Figure 6.6: A plot of z' as calculated by the thin lens equation as compared to the z location of the camera as measured by a tape measure in the lab is shown for various SLM misalignments assuming perfect alignment between the lenses. If the SLM is moved back by a distance of 10 cm from the left focal plane of L_3, the image of the propagated field will simply move back a distance of 10 cm as well. This means that at the measured $z = 0$ cm in the lab for no misalignment, the actual z of the propagated field will be 10 cm greater.

Case 2: $\Delta = 0$, $\varepsilon \neq 0$

It turns out that misalignment of the lens pair after the SLM is the more important source of error to consider. For $\Delta = 0$, Equation 6.2.6 becomes

$$z' = \frac{f(f+\varepsilon)}{f^2}(z+\varepsilon) \tag{6.2.9}$$

This error is not a systematic shift in the same way as in Case 1. If the lenses are not very close to $f_3 + f_4$ then the propagation measured is not one-to-one with the propagation away from the SLM, as shown in Figure 6.5 (b), and interpreting the vortex dynamics is much more difficult. As anticipated, if the lens pair is perfectly

aligned, $z = 50cm$ away from the SLM corresponds to $z' = 50cm$. However, with a small deviation from this distance between the lenses, there *can* be a significant difference between the propagation distance as measured in the lab, z, compared to the propagation value, z', anticipated based on the misalignment.

Plotting z' as compared to z as measured in the lab, shown in Figure 6.7, reveals a simple strategy to reduce the error introduced by case 2 in particular: increase the focal length of the imaging lenses. This can make some intuitive sense if you consider a very short focal length lens. The depth of focus of a lens with a smaller focal length is much smaller and the divergence is much larger than for a larger focal length lens. If your beam is diverging very quickly, small adjustments to the z location of the second lens can have a greater affect on the collimation.

The expense of using longer focal length lenses, though, is a lower numerical aperture, but this is a small price to pay for minimizing the opportunity for poten-

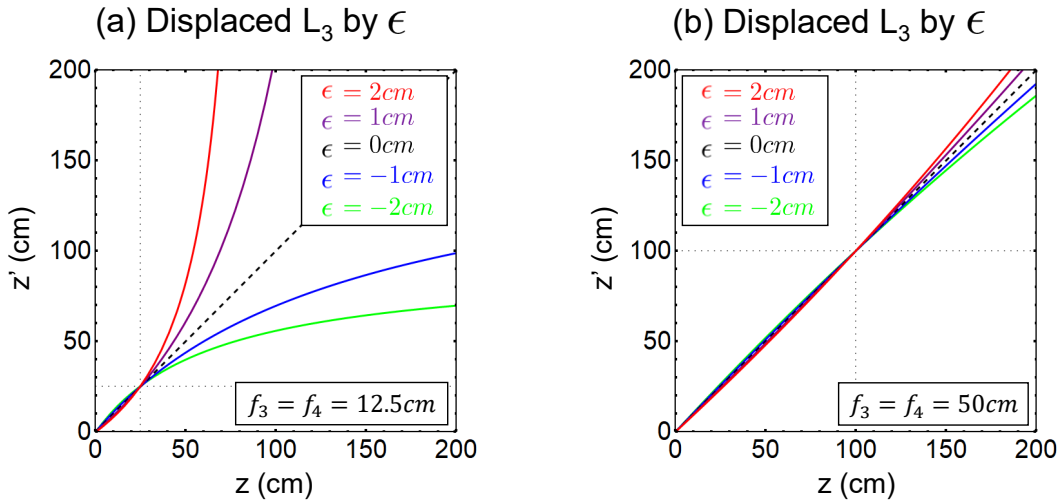

Figure 6.7: (a) shows the discrepancy for lenses with $f = 12.5cm$ and (b) shows the discrepancies for lenses with $f = 50cm$. This shows that such errors can easily be reduced over the scales we propagate our fields, though, by simply increasing the focal length of L_3 and L_4. For this reason, we choose lenses of $f = 50cm$.

tially significant errors from small misalignments that can dramatically affect our observations. For this reason, all experiments performed in this dissertation have imaging lenses L_3 and L_4 of focal lengths $f_3 = f_4 = 50cm$. An additional benefit of using these longer focal length lenses is that accessing the imaging plane is easier, as there is more path length to set up the translation stage before reaching the CCD.

With these results, we can clearly see that the most crucial distance to optimize is the distance separating the two lenses, particularly when the focal length of the lenses is small. A shift of the SLM will manifest itself as a systematic error that is easier to correct. An additional check on the imaging system can be done by placing a resolution standard at the location of the SLM and the CCD at the imaging plane. After the alignment process is complete, a comparison of the actual size of the resolution standard and the size in the image, within the pixel size ($5.5\mu m$), can help verify that the imaging system is one-to-one. Once the distance between the lenses is set, the SLM is translated as close as possible to one focal length from L_3 using a tape measure.

6.2.3 The Aperture, Translation Stage, and Camera

Even if the hologram used were not diffractive, it would be advantageous to spatially filter the light generated by the spatial light modulator, since stray pixel diffraction can potentially interfere with the measurements of the beam. However, particularly because we are using diffractive holograms, it is even more important to spatially filter the light emitted and ensure only the desired first diffracted order passes on to the CCD. As shown in Figure 6.1, the first diffracted order is selected and spatially filtered at the focus of L_3 by an aperture. One must be careful when selecting the size of the aperture to use.

Aperture

A balance between having a small enough aperture to filter out interference from other diffracted orders and a large enough aperture to avoid clipping the beam is needed for accurate and clean data. An adjustable aperture (Thorlabs SM1D12C) was placed at the focal plane on a three-axis translation stage. The aperture was adjusted until the fringing was minimized without causing beam diffraction. An example for a two vortex experiment is shown in Figure 6.8 where the aperture for the specified conditions was set to 4 mm, highlighted by the dashed red box, when taking data. It is also useful to test the centering of the aperture by closing the aperture to the smallest diameter and looking at the distortion of the vortices. If the vortices simply get larger equally in each direction and maintaining an even power distribution (as in the far right of Figure 6.8), the aperture is centered well enough. If the aperture is off-center, one vortex will be distorted more than the other, and the aperture alignment can be fine tuned via the micrometers of the stage it is mounted on. Back-reflection from the aperture can be used to ensure that the

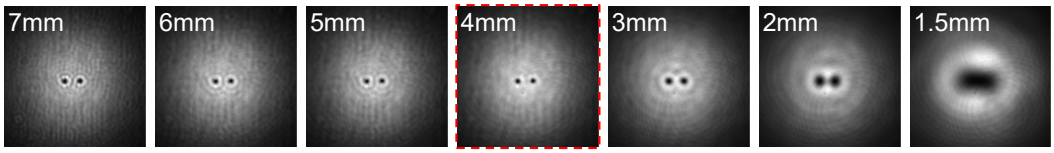

Figure 6.8: For a beam with $w_0 = 1.88$ mm generated from a grating with $L = 10$ pixels, as the aperture at the focal plane of the imaging system is adjusted, the beam quality varies. On the far left, when the aperture is large, fringing from other diffracted orders is prominent. On the far right, the aperture is small and clipping the beam, causing diffraction and preventing higher spatial frequencies from passing through. This distorts the initial field. The optimal aperture size for this beam profile (highlighted by the dashed red box at 4 mm) is large enough to minimize clipping, but small enough to minimize fringing.

aperture is not tilted with respect to the direction of propagation, which can alter the beam propagation as well.

Translation Stage and Retroreflectors

After propagating through the imaging system, the light is directed to a translation stage that is aligned along the propagation direction. Mounted on the translation stage is a retroreflector that redirects the light to a CCD for beam measurement, as shown in Figure 6.1. As the translation stage is moved, the path length of the light to the CCD is increased, so that the light can be measured at various propagation distances. The stage and retroreflector are mounted such that when the stage is set to its closest point, the field measured on the camera is at the imaging plane. This allows for the use of the entire length of the stage, and therefore longest change in propagation distance possible for measuring vortex dynamics.

On the stage, there were different iterations of retroreflectors used at different times. For the linear core, two vortex data, a HeNe laser was used and we used a Thorlabs TIR Retroreflector, B-coated (AR Coating: 650 - 1050 nm). When we switched to using the green diode laser for the single vortex experiment, the retroreflector was no longer close to the wavelength specifications, and we saw extra reflections that interfered with the mode. For this case, I made a retroreflector from two silver mirrors (Thorlabs PF10-03-P01-10) mounted at a 90° angle such that a beam coming in along a line of holes was redirected out along the next line of holes.

Two mirrors placed just after the imaging system, shown in Figure 6.1, are used to align the beam to the stage. For any given experiment, the aim is to obtain the smallest drift introduced by the stage as possible. One could do this with a knife-

edge and power meter. However, the beam wander feature in the DataRay software is what I used to align the stage. The beam wander feature tracks the centroid of the beam, so the camera can be effectively used as an iris. I used the beam's location at the midpoint of the stage and then aligned the first mirror following L_4 when the stage is at the closest point to this location and the second mirror after L_4 when the stage is at the farthest point to the same location. A few iterations of these mirror adjustments results in an aligned stage.

The longer stage used in the original two vortex data was bowed and the smallest drift that could be achieved was on the order of millimeters. In the single vortex case, the Newport stage that was used was much more stable, and the beam could be aligned such that the drift was on the order of tens of microns. In either case, an *LG* beam is used to help account for and mitigate any drifts in the system. No matter the stage used, though, the imaging plane must be determined in order to set the starting point for measurements taken.

Determining the Imaging Plane of the CCD

The CCD is first aligned such that the beam is centered on the sensor and the back reflection of the beam travels exactly along the incoming path. To find the imaging plane of the camera (i.e. the $z = 0$ plane), I used a hologram encoded with the amplitude of a unique image with sharp and distinct features,[3] as in Figure 6.9 (a). The translation stage with the camera mounted on it was moved to a point such that $z < 0$, and the camera was inside the imaging plane, shown in Figure

[3] As a short aside related to scientific outreach amongst young students, I found that using images from popular preteen/teenage shows was a fun and effective way to peak their interest during lab tours. Students, particularly around the middle school age were intrigued that you could imprint fun objects, such as a Mind Flayer [178] or others found in Appendix C.4, onto a laser beam.

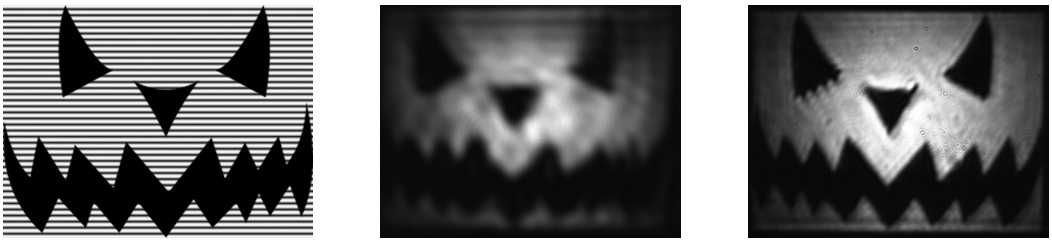

(a) Hologram (b) Out of Focus Image (c) Focused Image

Figure 6.9: (a) A hologram used for determining the $z = 0$ imaging plane is shown. (b) When the camera is placed at $z < 0$, the image is clearly out of focus. (c) When the camera is at the imaging plane, the image stamped onto the hologram is in focus. This point was used to determine the starting point for taking data in each run.

6.9 (b). The stage is then moved until the sharpest image is obtained, such as that of Figure 6.9 (c), and this determines the location of the zero point for a given configuration. Alternatively, the imaging plane can also be found by placing a point vortex hologram onto the SLM and translating the CCD until the core is as small and sharp as possible.

Once the zero point is set, measurements of the beam can be made beginning there and at larger propagation distances as determined for a particular experiment. The location of any vortex in the beam can then be identified at each z location as described in the following section.

6.3 Vortex Tracking Methods

In order to accurately measure the dynamics of vortices within the experiment, despite the steps taken to align the beam to the translation stage, we must carefully account for any beam drift in the system. Only after the drift has been eliminated can we identify and track the vortices. This section details the methods used in each experiment for both accounting for drift and identifying vortex locations once this is done.

Cropping Data to Account for Drift

Even with a careful alignment of the translation stage that controls the propagation distance to the camera, it is very important to account for any inevitable drifting of the beam with propagation. The method we have used in this work is to use a high quality *LG* beam in a given experiment as a "tracer" to track the beam drift, so that it can be eliminated. Using the amplitude and phase measurements of the *LG* mode obtained from the phase-shifting digital holography methods from Section 5.2, and the vortex identification methods discussed in the next subsection, we are able to track the vortex of an $\ell = 1$, $p = 0$ *LG* mode. If the beam drifts, the location of the vortex will move the same amount, which can be used to shift the center-point of the data accordingly.

An example of this is depicted in Figure 6.10. Panels (a-c) are plotted examples of a *LG* mode measured at a fixed camera location while the translation stage is moved back. In this example, there is a large amount of drift present (>1 mm) in the system. The actual amount of drift in the experiments varies depending on the quality of the translation stage that is used, and a large drift is used in the figure for clarity of the concept. The vortex in the *LG* mode is located computationally, and the beam is cropped around this location, creating a window centered around the beam with drift removed, shown in panels (d-f). This centering is then applied to all images taken for a given data set, and the images are then considered to be calibrated with no remaining effects from drift present in the data.

This of course relies on a *LG* mode with a centered vortex that is not drifting with respect to the beam, which can happen if the system is not well aligned. However, our confidence in this method results from our alignment methods discussed

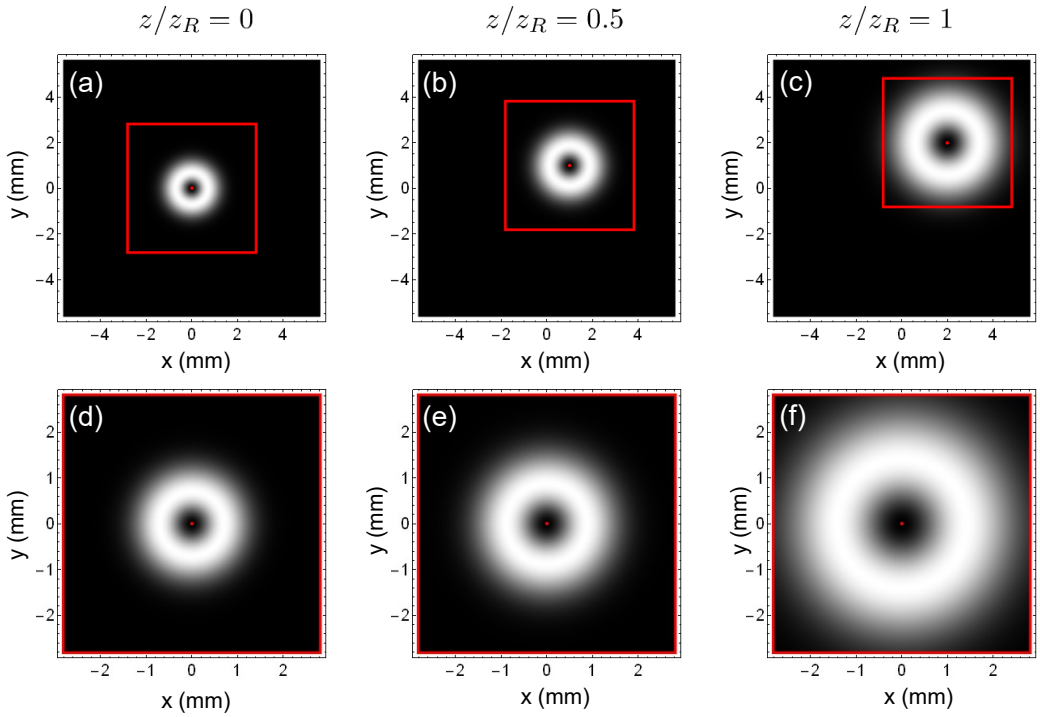

Figure 6.10: A theoretical example of the drift calibration method is shown. (a-c) the beam drifts as it propagates with respect to the camera. (d-f) the calibrated data no longer has this external drift and vortex trajectories can be measured directly from the new window.

in previous sections of this chapter which yielded the high purity modes reported in Chapter 5, particularly for an $\ell = 1$ mode.

Identifying Vortex Locations

Once the drift is accounted for, the vortex locations relative to the corrected beam center can be identified at each z step. From this, we can not only measure quantities such as the x and y positions as a function of propagation, but we can accurately measure the vortex velocities. One might be tempted to locate the vortex using the zeros of the amplitude, but a zero amplitude value cannot guarantee the presence of a vortex on its own [24]. Additionally, locating the true zero point

in potentially noisy experimental data is an extra challenge. The phase at the location of the vortex is undefined, so this may also be less straight forward to use for identifying vortex locations. However, the real and imaginary parts of a vortex field are smoothly varying, shown for an $LG_{\ell=1,p=0}$ mode in Figure 6.11 (a), and the only way the singularity at the center of the vortex can exist is if both real and imaginary parts are simultaneously equal to zero [90].[4] This is why vortices are sometimes referred to as optical nodes [181]. Figure 6.11 compares (a) the real and imaginary representation of a vortex (with zeros marked by the solid red line) to (b) the amplitude and phase representation to illustrate the characteristic shapes near a vortex. As can be seen in the figure, the intersection of the real and imaginary zeros accurately locates the vortex.

The calculation of real and imaginary zero intersections can easily be done computationally on experimental data, but full complex data (i.e. both amplitude and phase, not just an intensity image) are required. We acquire the complex field data

[4]Edge defects can also be detected by the intersections of real and imaginary zeros, but yield continuous zero *lines* (such as the line discontinuities found in Hermite Gaussian Modes) rather than the single point for an optical vortex [24, 179–181]

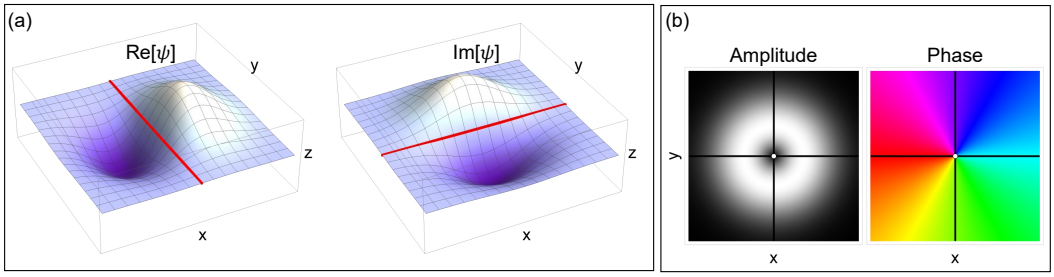

Figure 6.11: (a) Real and imaginary parts of an $LG_{\ell=1,p=0}$ mode are plotted in three dimensions. Both are smoothly varying, and the zeros of each are marked by a solid, red line. (b) When both zero lines are plotted together (black solid lines) in comparison to two dimensional plots of the amplitude and phase, the intersection lines up with the anticipated vortex location (white circle) in the center of the beam.

with the phase-shifting digital holography techniques of Chapter 5. The field measurement and calculation of real and imaginary zero intersections is repeated at each z step and the set of vortex positions is used to measure quantities such as the vortex velocity. An example of a computationally located vortex from experimental data of an $LG_{\ell=1,p=0}$ is shown in Figure 6.12. As seen in the figure, a central vortex is located by the intersection point of the real and imaginary zeros. Many other vortices are also found along the outside edge of the beam, but this is due to low light noise, so they can be disregarded.

This method of vortex tracking also works for fields with more than one vortex, and the number of zero crossings increases with the number of vortices present. For fields with large amounts of noise, and more than one vortex could be in the data where only one should be present; a Gaussian filter can be applied to the data to reduce some of the impacts of experimental noise.

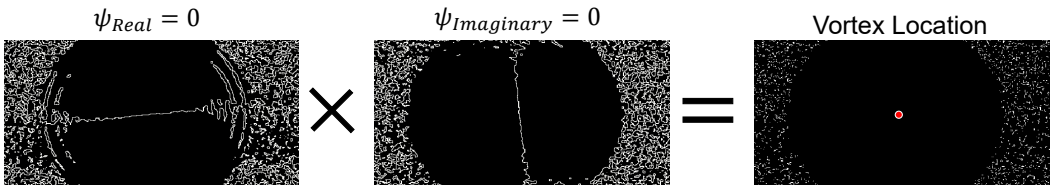

Figure 6.12: An example of the real and imaginary zeros for an experimental field of an $LG_{\ell=1,p=0}$ are shown in the left and middle images, respectively. The vortex location is the intersection, marked by the centered, red point on the right image.

6.4 Part II Summary

In this chapter, and the two preceding it, we have discussed at length the details for building an experiment to measure vortex dynamics. This has included methods for generating holograms, techniques for measuring amplitude and phase of optical fields, details on how to properly align an experimental setup, and reliable

methods for tracking vortex locations with propagation. Each of these topics have contributed to reaching our goal of experimentally testing vortex dynamics for the test cases discussed in Chapter 3. The results of performing these experiments will be discussed next as we move into Part III.

III

Experimental Results and Future Directions

Chapter 7

One and Two-Vortex Experiments for Vortices with a Linear Core

A portion of this work was published in Physical Review A: Volume 104, Issue No. 3, under the title ***Hydrodynamics of noncircular vortices in beams of light and other two-dimensional fluids***. [120]

Now that we have established the experimental needs for measuring vortex dynamics, we are interested in testing the impact of vortex ellipticity on optical vortex trajectories. This chapter discusses the experimental results for linear core vortex motion in Gaussian beams for two test cases. The first case is a single vortex placed on the side of a Gaussian beam with various ellipticities. Recalling the prediction from Chapter 3, as the ellipticity is changed, the velocity of the vortex should also change. The second case is the annihilation of a linear core vortex pair, in which vortex ellipticity evolves with propagation. If both the vortex trajectories and the vortex tilt behave as anticipated in each case, the results will provide compelling evidence that our hydrodynamic model effectively describes these linear optical systems.

As an aside, any specific experimental details that are unique to a given experiment will be discussed followed by the results from the set of experiments performed. Comparisons of the data are made with the predictions from both Section

3.6.1 pertaining to a single, linear core vortex placed within a Gaussian, and Section 3.6.2 for an oppositely charged vortex pair within a Gaussian will be made.

7.1 Single Off-center Vortex within a Gaussian

In the case of a single optical vortex, two unique initial conditions are pertinent: [1] a vortex centered in the beam and [2] a vortex shifted from the center of the beam by some distance, x_0. The background field for each of these is just the underlying Gaussian. For a centered vortex, $\nabla\tilde{\rho} = \nabla\tilde{\phi} = 0$ for the background Gaussian, so Eq. 2.2.6 suggests that the vortex will not move. This is consistent with the propagation of an $\ell = 1$ *LG* mode [30].

7.1.1 Single Vortex Specific Experimental Details

For this experiment, the set up resembles that of Figure 6.1, where a $\lambda = 526.5$ nm diode laser (MSL-III-526.5) was spatially filtered through a single mode fiber and sent through a collimating lens (rather than the first telescope in the figure) before being sent onto the Epson 83H SLM. Imaging lenses of focal length $f_3 = f_4 = 500mm$ were used along with a Newport IMS500 translation stage. Collinear phase-shifting digital holography methods as described in Chapter 5 were used to measure the amplitude and phase of the field at each propagation distance, and a set of thirteen tilt angles for $\psi_{field,i}(x,y)$, shown in Table 7.1, were chosen to sample a variety of locations across the space from Figure 3.8.

The vortex velocity for each pair of angles can be calculated by using the dimensional form of Equation 3.6.4 (i.e. $z \to z/z_R$), and taking the derivative with

respect to z such that

$$v_x = -\frac{\lambda x_0}{\pi w_0^2}(\cos\xi \sin\theta \sin\xi \tan\theta)$$
$$v_y = \frac{\lambda x_0}{\pi w_0^2}\left(\cos\theta(\cos^2\xi \sec^2\theta + \sin^2\xi)\right) \tag{7.1.1}$$

where we have used $z_R = \pi w_0^2/\lambda$. Analytically predicted velocity components for each vortex tilt are shown in Table 7.1 and will be used for comparison with the experimental measurements.

i	ξ (degrees)	θ (degrees)	$v_{x,pred}$ (mm/m)	$v_{y,pred}$ (mm/m)
1	0	0	0	0.11
2	0	50	0	0.17
3	22.5	50	−0.036	0.16
4	45	50	−0.051	0.12
5	67.5	50	−0.036	0.087
6	90	50	0	0.072
7	0	60	0	0.22
8	22.5	60	−0.059	0.20
9	45	60	−0.084	0.14
10	67.5	60	−0.059	0.081
11	90	60	0	0.056
12	75	72	−0.082	0.057
13	87	86	−0.083	0.012

Table 7.1: A set of 13 tilt angles used for comparison with theory of a single, tilted, off-center vortex. The predicted x and y velocities, calculated from Equation 7.1.1, are shown for each field as well.

The holograms used in the setup had input parameters of $\alpha = \pi/6$, $N = 5$ pixels, $A = 0.5$, $B = 0.5$ and $\psi_{field}(x.y)$ is given by Equation 3.6.2 with $x_0 = 0.8$ mm. A subset of the holograms used are shown in Figure 7.1 (a-d). One may notice that it looks like $\alpha = -\pi/3$ in the holograms, but the SLM panel itself needed to be mounted such that it was rotated by 90° in the setup. The holograms are rotated to

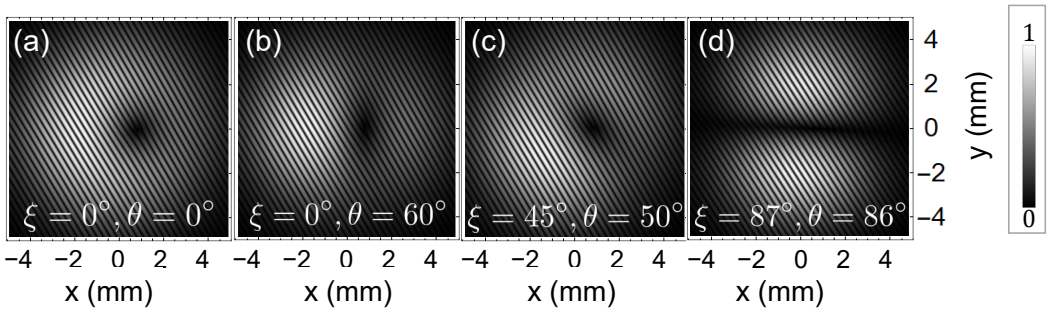

Figure 7.1: (a-d) Four of the projected holograms for vortices with $x_0 = 0.8$ mm and of encoded tilt angles as labeled. Adapted from Andersen, 2021. [120] © American Physical Society

show the correct orientation from the experiment, with the vortex displaced to the right in the beam.

To identify the vortex locations, the intersections of real and imaginary zeros are identified, as described in Section 6.3. For each set of data taken at a particular z distance, the phase was fit to Equation 3.6.2 to extract the experimental vortex tilt. A set of five individual measurements was taken at each z location and averaged. The results are discussed in the following section.

7.1.2 Experimental Results

Figure 7.2 shows experimental measurements of the field amplitude (a-d) and phase(e-f) at the imaging plane. A careful observer will notice that the ratio of the Gaussian mode size to the vortex location is smaller in the measured results than in the holograms. This is because the output beam generated by the hologram is actually the product of the field on the hologram and the incident Gaussian beam. The result is a smaller generated host Gaussian and a larger apparent vortex offset

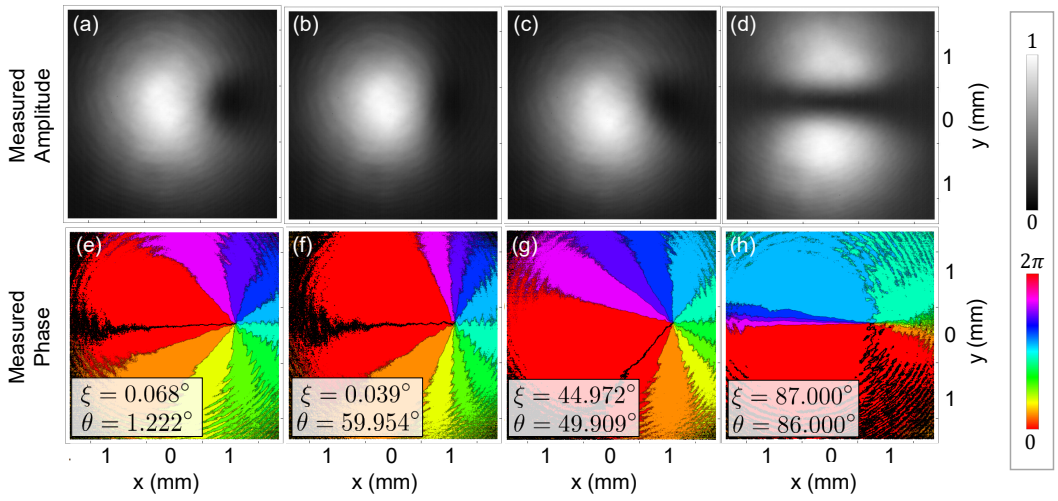

Figure 7.2: Measured amplitudes (a-d), and phases (e-h) that correspond to the holograms displayed in Figure 7.1 are shown. A 2D amplitude fit of (a) at $z = 0$ mm using Equation 3.6.3 at $z = 0$ gives a measurement of $w_0 = 1.1$ mm. (e-h) also show measured tilt angles (insets) at $z = 0$ mm calculated by fitting the phase data to Equation 3.6.2 with fitting parameters x_0, y_0, ξ and θ. Adapted from Andersen, 2021. [120] © American Physical Society
***Experimental data taken by Andrew A. Voitiv.

for the measured mode.[1] However, the vortex tilt and offset from center remain unaffected. The measured tilt angles at the imaging plane show excellent agreement with the programmed tilt angles.

The experimentally measured vortex positions in x (red) and y (blue) as a function of propagation for a subset of the thirteen measurements are shown in Figure 7.3. The error bars in the figure show the standard deviation of five measurements taken at each z position. To be very clear, the dashed lines in Figure 7.3 are not linear fits to the data, but are the analytical prediction from Equation 7.1.1, for which the slopes are displayed in Table 7.1. The predictions are calculated based off of the experimentally measured beam parameters at the imaging plane.

[1]The actual generated beam waist measured at the $z = 0$ plane is used for the vortex velocity calculations of Table 7.1.

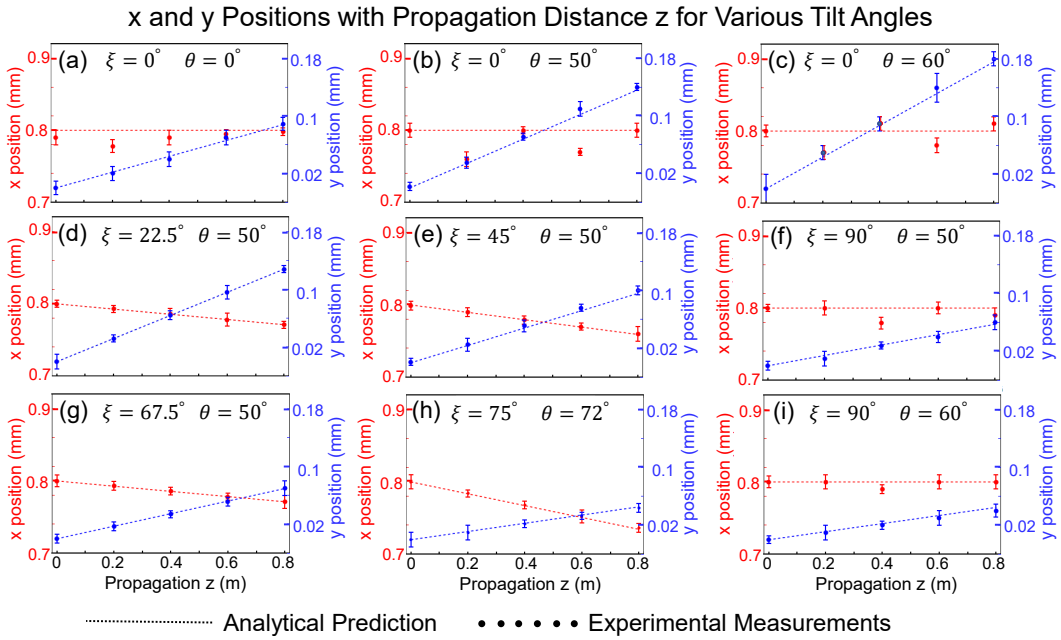

Figure 7.3: Experimentally measured vortex positions as a function of propagation are shown for both x (red) and y (blue) directions. Error bars represent one standard deviation of five independent measurements. The dashed lines are the analytical predictions from Equation 3.6.4.
***Experimental data taken by Andrew A. Voitiv.

The measured data align remarkably well with the analytical prediction in each of the various tilt cases. However, fitted slopes (which are not shown in the figure) for each plot in Figure 7.3 are calculated using the propagated uncertainties for both the x and y motion, described next. These two fitted slopes for each plot are used to create a single uncertainty ellipse in Figure 7.4, which are also well aligned with the analytical prediction.

Error Analysis of Vortex Trajectory Fits for Vortex Velocity Measurements

With the goal of accurately measuring vortex velocity in mind, for each trajectory we want to use the full data, including errors, from Figure 7.3 to do so. Each position, (x_i, y_i), in every trajectory has its own unique uncertainty values,

$(\sigma_{x_i}, \sigma_{y_i})$. We want to determine the velocity by separately fitting the x and y data to $q = A + Bz$, where B is the velocity and q is either the x or y direction. Following the error analysis in "An Introduction to Error Analysis" by John. R. Taylor on pg. 198 [182], we see that the propagating the errors results in a best fit slope B, and uncertainty in slope σ_B, of

$$B = \frac{\sum w \sum wzq - \sum wz \sum wq}{\sum w \sum wz^2 - (\sum wz)^2},$$
$$\sigma_B = \sqrt{\frac{\sum w}{\sum w \sum wz^2 - (\sum wz)^2}}, \tag{7.1.2}$$

where $w_i = 1/\sigma_i^2$. We use these formulas to calculate the slopes and the uncertainty in the slopes. We do not find the intercept as we don't need it to measure the velocity.

As a quick example, in the case of Figure 7.3 (h) the data from that particular measurement in the x direction was:

z (m)	x_i (mm)	σ_i (mm)
0.0	0.80	0.01
0.2	0.784	0.005
0.4	0.768	0.005
0.6	0.752	0.009
0.8	0.736	0.006

The slope and uncertainty are calculated using these values as input to Equation 7.1.2. The result is $v_x = -0.08$ mm/m with $\sigma_x = \pm 0.01$ mm/m.

Single Vortex Velocity Results Summary

These slope fits and uncertainties in the slope fits for a given x and y are used to compare the experimental velocities to the hydrodynamics theory of Figure 3.8 and Table 7.1, as shown in Figure 7.4. The uncertainty in each slope is represented by an ellipse of the appropriate size bounding the cross-hair for that data point.

Overall, the data is an excellent match with the theoretical predictions. The measured velocities for each set of angles indicate not only that vortex ellipticity impacts the vortex trajectory, but that it does so in accordance with the hydrodynamic model derived in Chapter 3 (Equation 3.5.17). There is some small deviation from the predicted values which are likely due to imperfections in the field generated from the SLM. Slight misalignments of the SLM or curvature within the LCD panel itself may affect the generated field and subsequent vortex trajectories. Additionally, pixelation of the forked grating displayed on the SLM can cause distortions in the generated field.

While each of these may only contribute a very small amount to the imperfections in the generated field, the affect is more noticeable when applied to a hologram containing an untilted vortex. The data point with the largest degree of uncertainty in vortex position, as seen in the velocity data of Figure 7.4, is the set with the most extreme tilt of θ nearing 90°. This vortex is approaching the same form as a Hermite Gaussian mode with a line singularity, but no vortex. Due to the highly elongated vortex core, there is less light in the x-direction with which to accurately pin down the vortex position in the x-component with our phase-retrieval measurements.

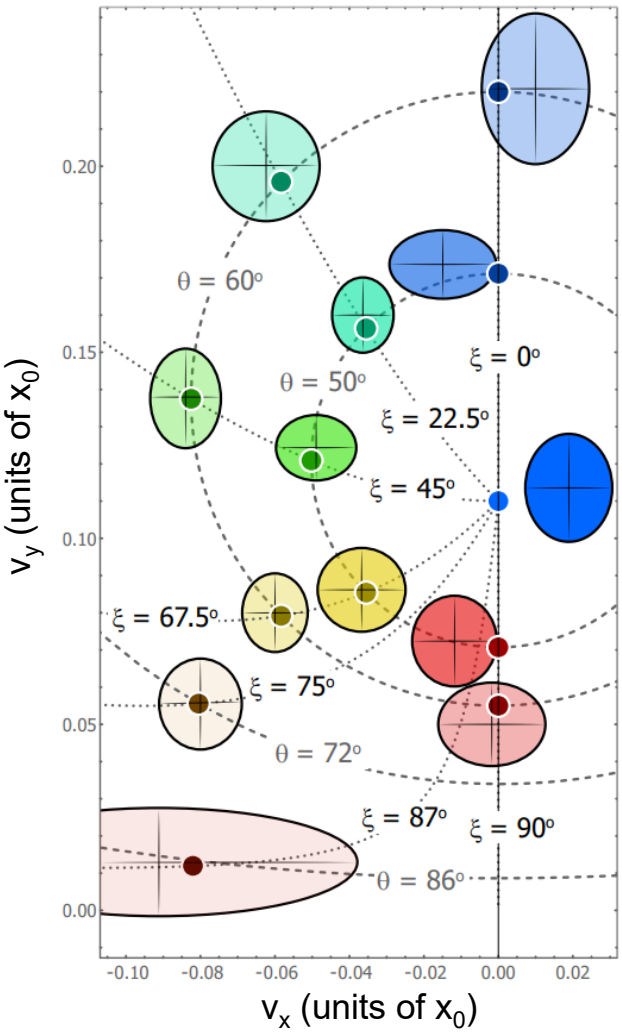

Figure 7.4: Experimentally measured vortex velocities (crosshairs) in mm/m for both x and y directions are shown with comparison to the theoretical predictions (colored dots) from Equation (3.6.4). The elliptical regions show the experimental uncertainty.
***Figure Credit: Mark T. Lusk. From Andersen, 2021. [120] © American Physical Society

Single Vortex Tilt Measurements

In addition to the measurements of vortex location as a function of propagation described in the last section, the vortex tilt with propagation was also measured. A

set of these measurements for various initial vortex tilts are shown in Figure 7.5, where the 2D phase is fit using Equation 3.6.2. The average value along with one standard deviation are shown for each set of measurements, and are in excellent agreement with the expected values. The experimental tilt measurements are in fact constant throughout propagation, and it is clear that the experimental values are very well aligned with the predictions. This non-varying tilt confirms the theoretical prediction of tilt for the single vortex case.

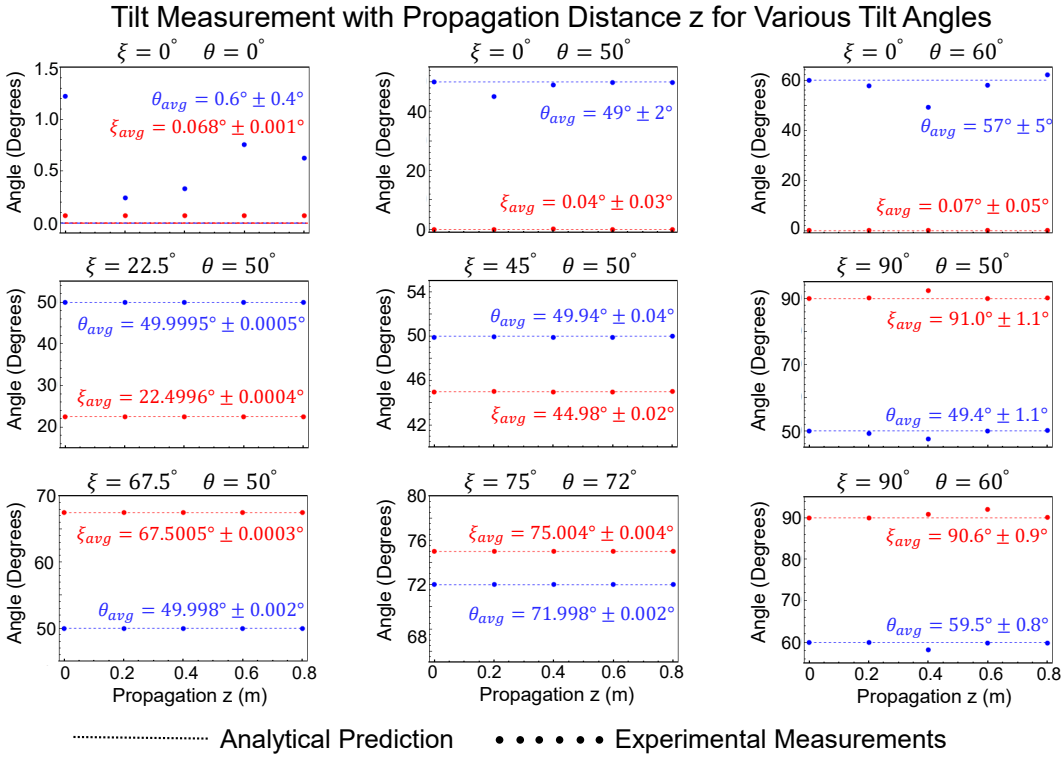

Figure 7.5: A subset of the experimentally measured tilt values at each propagation step are shown for ξ (red) and θ (blue) corresponding to the measurements in Figure 7.3. The labels are the average value and standard deviation of each set of measurements. The dashed lines are the analytically predicted values (labeled at the top of each plot). One should note the scale of the y-axis for each of the figures, as it varies for each plot.
***Experimental data taken by Andrew A. Voitiv.

This experimental agreement with theory for this case is the first step toward confirming the theoretical framework of Chapter 3. We now turn to the case of an oppositely charged (and circular at $z = 0$) vortex pair for a more strenuous test of our hydrodynamic theory in which both the vortex tilt and the velocity are expected evolve with propagation.

7.2 Two Vortex Experiments

The initial condition field discussed in this section is that of a circular, linear core vortex pair, displaced symmetrically across the y-axis such that the vortices are located at $(\pm x_0, 0)$ in a Gaussian beam. The expectations for vortex motion in this case can be found in Section 3.6.2, where the theoretical predictions are discussed. The experimental implementation and results are discussed here.

7.2.1 Two Vortex Specific Experimental Details

For the two vortex experiments, a $\lambda = 633$ nm HeNe laser (Melles Griot) was first spatially filtered using a telescope with an iris at the focal plane, as depicted in Figure 6.1, which then was incident onto the Epson 83H SLM. Imaging lenses of focal length $f_3 = f_4 = 500mm$ were used along with a Ball Screw Linear CNC Slide Stroke 1000mm Long Stage Actuator Stepper Motor translation stage. Getting clean generation and measurement of multiple linear core vortices is particularly challenging because of the significant core overlap and, therefore, very low power regions where the measurement is taken. A way to alleviate extra difficulty in the measurements is to use a larger initial vortex separation, with the trade off of longer annihilation 'times'. This is the reason for the longer translation stage,

despite it having larger deviations across the length of the stage than the stage used in the single vortex case.

Colinear phase-shifting digital holography methods as described in Chapter 5 were used to measure the amplitude and phase of the field at each propagation distance. Holograms used in the setup had input parameters of $\alpha = 0$,[2] $N = 10$ pixels, $A = 0.95$, $B = 0.05$ and $\psi_{field}(x.y)$ is given by Equation 3.6.6. An example hologram with a left vortex with a negative charge and right vortex with a positive charge is shown in Figure 7.6 (a).

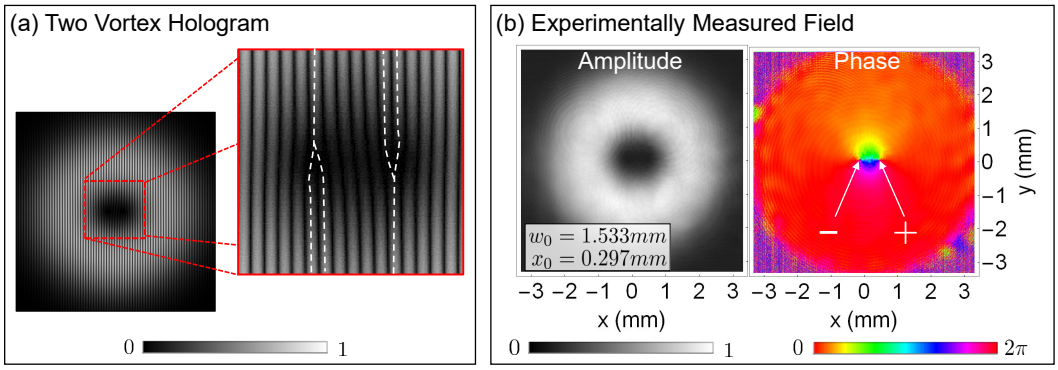

Figure 7.6: A vortex pair hologram on the left in (a) is shown with a zoomed in view of the vortex configuration. White dashed outlines trace over each fork to highlight them. (b) The measured field amplitude and phase are shown with measured beam parameters of $w_0 = 1.553$ mm and $x_0 = 0.297$ mm.
Adapted from Andersen, 2021. [120] © American Physical Society

7.2.2 Experimental Results

First, we measure the beam parameters of the field generated from a chosen hologram at the $z = 0$ imaging plane. Figure 7.6 (b) shows both amplitude and phase measurements obtained when using the hologram in (a). The inset on the amplitude

[2]This experiment was performed before the single vortex experiment, where improvements to holograms by misaligning the grating and pixel axes were made.

plot shows the measured beam waist and vortex displacement from a 2D amplitude fit using Eq. 2.3.1. Measurements of the mode were made with propagation steps of $z = 5$ cm, beginning at $z = 0$ cm up to a final distance of $z = 195$ cm.

Measured Vortex Dynamics

From the amplitude and phase data in Figure 7.7, we qualitatively observe a the near half circle trajectory expected for the two vortex case. The vortices in the figure are marked with white circles in the phase plots, and show a down and inward motion with propagation. This dynamic continues until they annihilate each other and no vortices remain. Measurements made far beyond the annihilation point show a phase front that contains no reappearance of the vortices. While these images are useful for an initial interpretation of the data, it is important to quantitatively track the vortices so that the model can be rigorously checked.

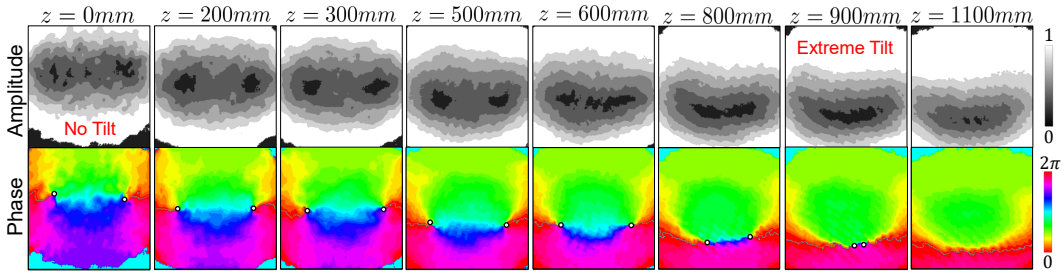

Figure 7.7: Snapshots of amplitude and phase with propagation show the vortex trajectory and annihilation event. Amplitude data has equal resolution to that of the phase measurement, but are plotted with limited contours to highlight tilt evolution in the amplitude structure. Data far beyond the annihilation point confirms that the vortices do not reemerge. Measured beam parameters are the same as in Figure 7.6: $w_0 = 1.553$ mm, $x_0 = 0.297$ mm.
Adapted from Andersen, 2021. [120] © American Physical Society

Although there are two vortices present, real and imaginary zeros can still be used to identify the vortex locations. Using the computationally tracked vortex locations from the amplitude and phase data, quantitative dynamics measurements can be made. In Figure 7.8, we show three separate representations of the data, each with error bars denoting one standard deviation across five measurements. First, the *xy*-plane data is plotted, showing the anticipated nearly half circular *x*-*y* trajectory. The averaged data show reasonable agreement with the analytically predicted trajectory, with each vortex moving in the negative *y* direction and toward $x = 0$ until annihilation. Panel (b) shows the vortex separation along the propagation direction. The measured vortex annihilation event occurs at $z \approx 910$ mm and the data are in

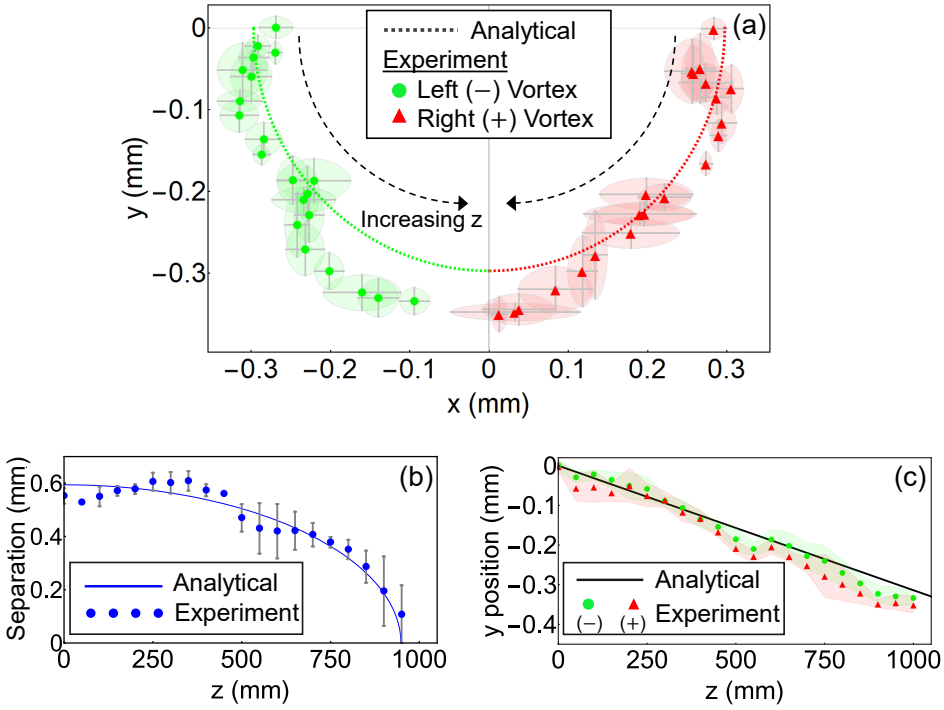

Figure 7.8: Measured (symbols) and analytical (lines) vortex trajectories for (a) the *x*-*y* plane (each green/red symbol pair is a measurement at a specific *z*), and (b) the vortex separation along *z*, and (c) the *y* position as a function of propagation.
From Andersen, 2021. [120] © American Physical Society

excellent agreement with the anticipated annihilation distance prediction [32]. Last, the measurement of the y position as a function of propagation is plotted in (c). Using a weighted linear fit [182] on the combined data for y positions of each vortex, the measured y velocity is $v_{y,meas} = -0.364 \pm 0.009$ mm/m, which compares well to the predicted $v_{y,model} = -0.314$ mm/m from Equation 3.5.17 and calculations from [32].

In the data, x_0 is sufficiently small compared to the beam waist that beam divergence effects are not enough to describe the discrepancy between the data and prediction in (a) and (c). However, the slight disagreement can be attributed to several potential experimental sources of error such as imperfect beam collimation and roundness, and pixelation in the hologram, pixel phase error, and a finite bit depth on the SLM. It should be noted that these types of errors do not impact the measured standard deviation, and could only contribute to a systematic error present in the data. Even with extra care taken, these are all culprits for introducing error, and balancing each of these is very difficult. It may be possible to improve these measurements by implementing the same step taken for the single vortex case, and create holograms that are misaligned with the SLM pixel grid to alleviate any extra stray pixel diffraction that can affect the measurement.

Up until now, each of the measurements taken have been in a host beam with a waist that is large compared to the vortex separation. It is insightful to consider the case where the separation to beam size ratio is much smaller. Because the annihilation is dependent upon both x_0 and w_0, as anticipated from Figure 2.6 the vortices can exhibit very different behavior, since the Gaussian itself contributes to the vortex motion.

We measure vortex separation with propagation for two initial conditions, shown in Figure 7.9 (a-b). The vortex separation data for both of these initial fields are also shown in Figure 7.9 (c). In these measurements, we consider the case of an oppositely charged vortex pair in addition to a same charge pair. However, we only show the amplitude measurements for the oppositely charged pair in (a-b) since the amplitude profile for an opposite and same charge pair is the same at $z = 0$. For beams with a waist that is small compared to the separation ($w_0 < x_0$), we see that the dynamics are dominated by the background Gaussian beam for both the opposite and like charge pairs. For the opposite charge pair, vortices no longer annihilate, but continue to propagate, increasing their separation distance at a rate close to that of the Gaussian beam divergence. For the larger beam relative to the vortex separation ($w)_{>}x_0$), we see steady motion in the same charge vortex case and we see annihilation in the opposite charge pair, both consistent with the predictions for each case [32].

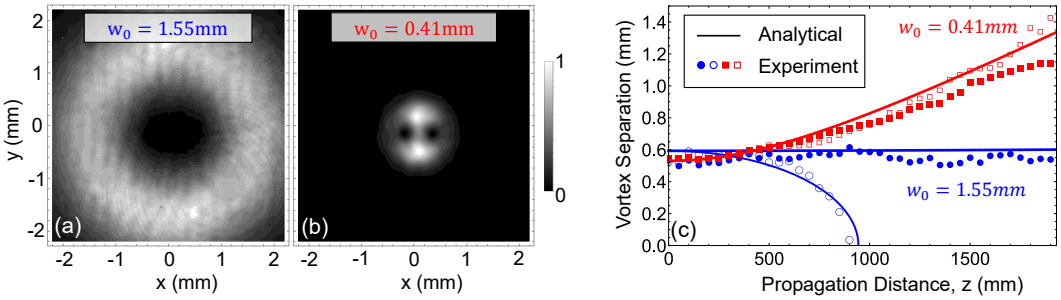

Figure 7.9: We show the experimental intensity for two different beam waists with very similar vortex separation. The measured beam parameters are (a) $w_0 = 1.55$ mm with $2x_0 = 0.59$ mm and (b) $w_0 = 0.41mm$ with $2x_0 = 0.53$ mm. (c) Experimental vortex separation as a function of propagation is shown for a same charge pair (filled points) and for an opposite charge pair (unfilled points). Blue lines are the analytical predictions of the the trajectories for the measurements corresponding to (a) according to [32] and the red line is the divergence of the beam waist corresponding to (b).

So far, the vortex trajectories match well with the predictions, confirming the vortex position results predicted by the hydrodynamic model given in Equation 3.5.17. Next, we evaluate the evolution of the experimental tilt for the case in which the vortices experience an annihilation event.

Measured Vortex Tilt Evolution in the Opposite Charge Pair

In calculating vortex tilt from experimental field measurements, it is important to remember that **F** from Equation 3.4.10 still contains the background field while the eigenvalues and eigenvectors of $\mathbf{V}^2$ from Equation 3.4.12 are independent of both ρ_{bg} and ϕ_{bg}. It is also useful here to remind ourselves that the $\mathbf{V}^2$ matrix can be rewritten in terms of the gradient of an arbitrary field $\vec{u}$, where $\vec{u}$ is the matrix representation of the real and imaginary parts of $\psi_{field}(x,y,z)$ as described in Equation 3.4.2. Using the relationships of the polar decomposition and Equation 3.4.9,

$$\mathbf{V}^2 = \mathbf{F}\mathbf{F}^T = \left[\nabla_\perp \vec{u}^{-1}\right]\left[\nabla_\perp \vec{u}^{-1}\right]^T, \tag{7.2.1}$$

where

$$\nabla_\perp \vec{u}(x,y,z) = \begin{bmatrix} \partial_x Re[\psi(x,y,z)] & \partial_y Re[\psi(x,y,z)] \\ \partial_x Im[\psi(x,y,z)] & \partial_y Im[\psi(x,y,z)] \end{bmatrix}. \tag{7.2.2}$$

This result reminds us that $\mathbf{V}^2$ can be reconstructed in terms of the derivatives of the real and imaginary parts of the complex field at the location of the vortex for a given z position – i.e. the full measured field can be used to calculate the vortex tilt and the background field does not have to be calculated. To determine vortex location and tilt from experimental data, the measured complex field is separated

into its real and imaginary parts with vortex locations in the xy-plane found by the intersection of real and imaginary zeros. The first step is to obtain the slope at each vortex location by cropping a small window around the selected vortex. Then, the real and imaginary parts are separately fit to planes of the form $z = ax + by + c$. These fit parameters, a and b, for both real and imaginary parts are used to find ξ and θ, as shown in Figure 7.10. $\mathbf{V}^2$ can be written in terms of these fit parameters as

$$\mathbf{V}^2 = \frac{1}{(a_{re}b_{im} - a_{im}b_{re})^2} \begin{bmatrix} b_{im}^2 + b_{re}^2 & -(a_{im}b_{im} + a_{re}b_{re}) \\ -(a_{im}b_{im} + a_{re}b_{re}) & a_{im}^2 + a_{re}^2 \end{bmatrix}. \quad (7.2.3)$$

From there, we need only take the eigenvalues and eigenvectors and use Equation 3.4.17 to find both ξ and θ.

In Figure 7.8, there were a set of five measurements taken and averaged to obtain the dynamics results. However, for the tilt measurement, only one data set from

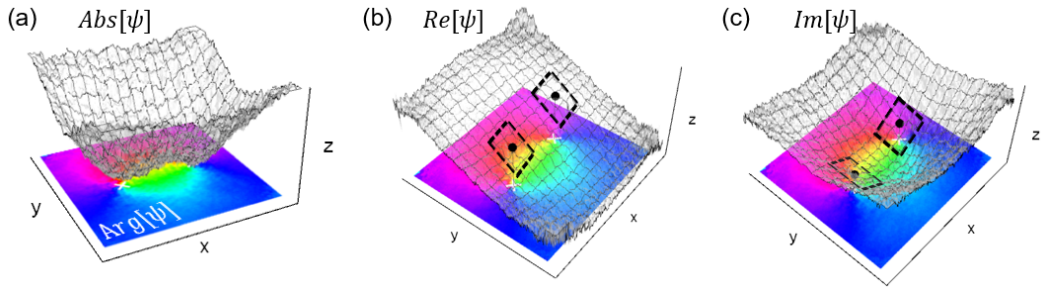

Figure 7.10: *Visualization of Experimental Tilt Measurement for the Two Vortex Case:* (a) The complex field is shown with the absolute value of the field (3D mesh) placed above of the phase (2D color). (b) The real part of the field (3D mesh) is shown, and the vortex locations are marked at the real and imaginary zeros of ψ with black dots. An example of fitted planes for each vortex over a chosen small window in the x-y plane is shown. The fit is given by $z_{re} = a_{re}x + b_{re}y + c_{re}$. (c) the imaginary part of ψ is plotted (3D mesh), with a fit given by $z_{im} = a_{im}x + b_{im}y + c_{im}$.

the five mentioned above was clean enough to extract a reliable tilt measurement. Examples of the real and imaginary parts are plotted in Figure 7.11 for the data set used to measure the tilt along with data that was not suitable for tilt measurements,

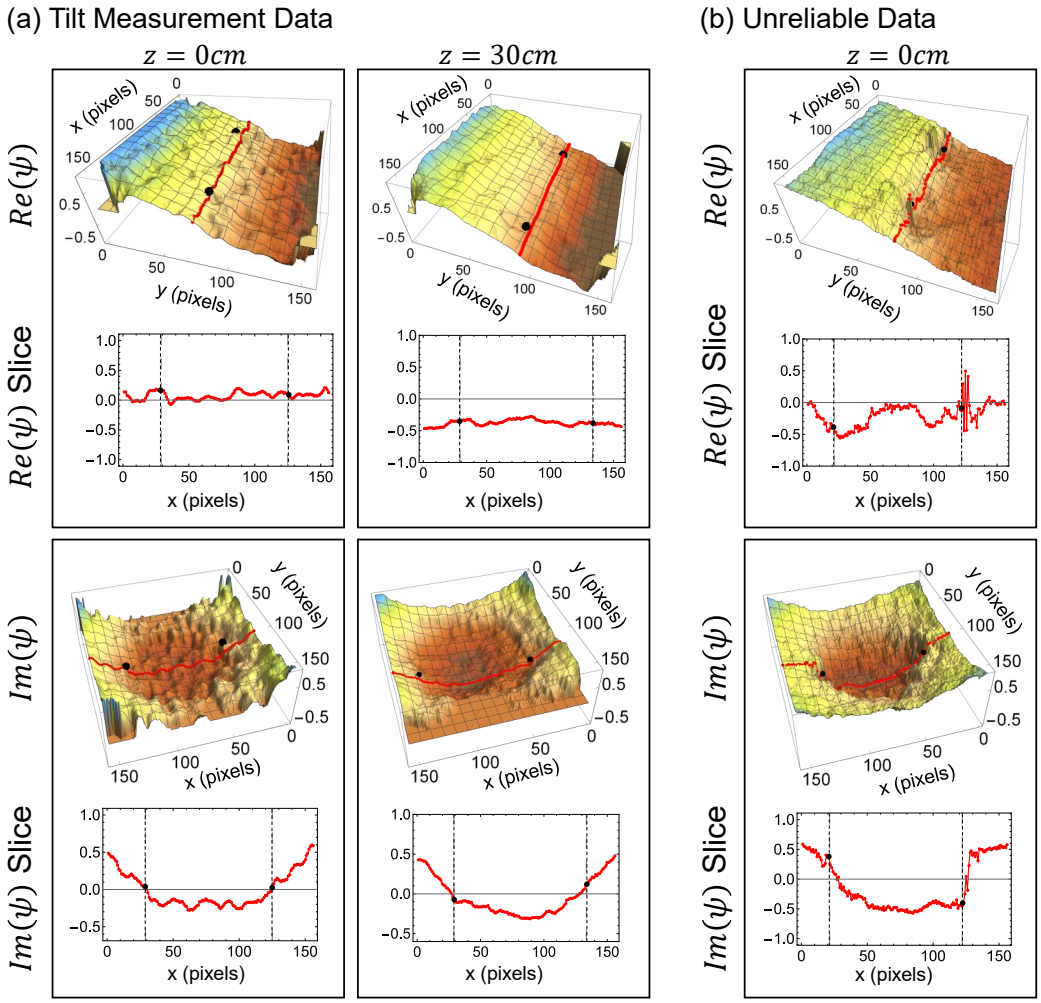

Figure 7.11: (a) Three-dimensional plots of the real and imaginary parts of the two vortex field used to measure tilt along with a slice at the location of one of the vortices are shown. While there is some noise present within the beam, slices show that the field is smoothly varying enough to extract a reliable tilt measurement. (b) shows an example of data with a discontinuity near the vortex location. Slices show that fitting within a small window of the vortex yields extreme values that are not indicative of the actual tilt of the vortex.

to highlight what is meant by "reliable". In cases where there is noise or imperfections in the beam, whether from pixelation in the holograms or stray light that differs from image to image used in the reconstruction of the phase, discontinuities can arise near the vortex center. When there is a sharp discontinuity, as in (b) of the figure, it can be seen that any fit of the data with a small window around the vortex will yield a highly inaccurate gradient measurement. Data that was of high enough quality, such as that seen in Figure 7.11 (a), was used to extract the tilt measurements of Figure 7.12.

The data shown in Figure 7.7 is the same data as in Figure 7.11 (a) and was used for the tilt measurement. A schematic of the tilt vectors for the trajectory is shown in Figure 7.12 (a) for ease in interpreting (b) and (c) of the figure. The

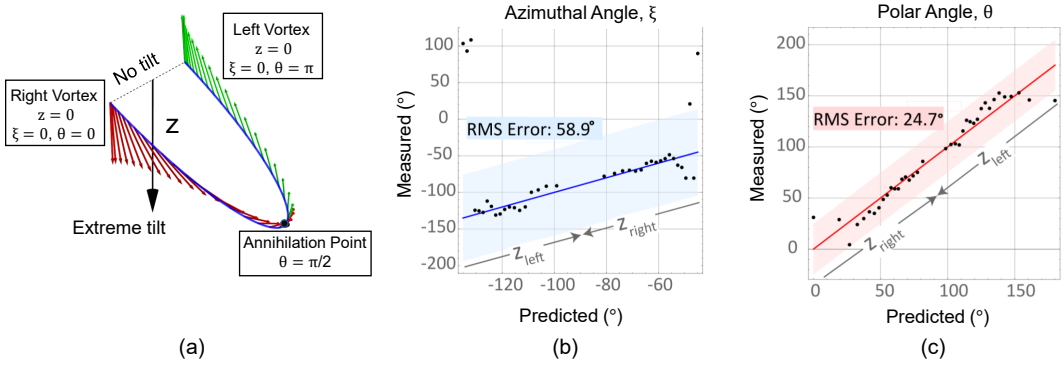

Figure 7.12: (a) Tilt vector evolution of a vortex pair beginning at $z = 0$ up to the annihilation point is shown. The left vortex is negatively charged (anti-aligned with propagation direction, $\theta = \pi$) and the right vortex is positively charged (aligned with propagation direction, $\theta = 0$). This is meant to be a visual aid for interpreting the plots in (b-c). (b) A comparison of the measured (dots) ξ for the left and right vortices with propagation compared to the predicted (solid line) ξ from Eq. 3.6.8 for each vortex is plotted. [Reprinted] from [120] (c) Similarly, a comparison of θ for both experiment and theory is shown. The shaded regions show the RMS error between the data and the predicted values. (b) and (c) From Andersen, 2021. [120] © American Physical Society

experimentally measured tilts are directly compared with the analytical predictions in Figure 7.12. As the vortices evolve with propagation, it is clear that the vortex tilt is not only increasing until annihilation, at which point the orientations become equal, but closely follows the prediction marked by the solid lines in the figure. The experimental measurements of both tilt angles are notably noisier near $z = 0$, which is attributed not to lower-quality acquired data, but to lower sensitivity on both θ and ξ as θ approaches 0 or 180°. For ξ, the orientation of the ellipse axes loses meaning for a circle, and for θ, the change in ellipticity for a small change in θ is greatest near $\theta = 90°$ and approaches zero for θ approaching 0 or 180°. This reduced sensitivity of tilt measurements for near-circular vortices was confirmed with synthetic data. With this in mind, we note that the fit between experiment and theory for tilt angles between $\theta = 90° \pm 60°$ is excellent.

The agreement of the experiment with the theory demonstrates that amplitude and phase gradients alone are not sufficient for describing the vortex motion. Particularly in this two vortex case, the annihilation event (when beams are much larger than the vortex separation, $w_0 >> x_0$) is possible not only because of the compressibility in the system, but specifically because of vortex tilt *and its evolution*. Without both, the dynamics would not be as they are.

7.2.3 Discussion

Collectively in this chapter we have shown experimental results for comparison to the hydrodynamic model from Chapter 3 for two distinct cases: a single vortex placed at the side of a Gaussian beam and an oppositely charged vortex pair placed symmetrically in a Gaussian beam. The excellent match in the single vortex case has shown that it is possible to predict dynamics of a tilted vortex in a

simple setting. The agreement between theory and experiment for the two vortex case provides a very compelling second verification for the compressible fluid + tilt hydrodynamic model, particularly because neither the tilt or vortex location are fixed in the scenario. Each case provides compelling evidence not only for the importance of light's compressibility, but that the ellipticity in the vortex is a key component to understanding vortex dynamics in two-dimensional fluids.

The agreement also gives us reason to believe that the model may generally work for other vortex systems, even if the vortex density is high such as in laser speckle. In addition to the confirmation of the model, the discussions of Chapter 2 and the results of the two vortex case when $w_0 < x_0$ remind us that it is interesting to consider how the compressible nature of the system on its own can alter vortex dynamics. Perhaps it is possible to alter the annihilation dynamics of an oppositely charged pair by simply changing the degree of overlap between the vortex cores at the initial condition. This is the topic of the following chapter.

Chapter 8

How Initial Core Size Affects Vortex Pair Dynamics

After measuring the dynamics of an oppositely charged, linear core vortex pair in a Gaussian beam, an interesting follow up study is to consider and experimentally measure annihilation events between vortices that initially have a smaller core. Since the amplitude gradient helps facilitate the perpendicular motion necessary for recombination in the linear core vortex pair, perhaps it is possible to modify the annihilation dynamics simply by changing the initial overlap of the vortex cores. In free space optics, a linear amplitude core is the default eigenmode-like shape for a *unit* charge vortex (see Equation 1.2.1). A vortex generated with a core shape that is different will quickly evolve with propagation toward a linear core, but the initial shape can introduce transient diffraction waves that alter the background field, affecting the subsquent vortex dynamics.

In this chapter, we investigate the properties of annihilation events for vortex pairs with a hyperbolic tangent shaped amplitude core. By using the hyperbolic tangent function, we can tune the size of the core from a delta function-like core to a linear core, and compare differences in the trajectories. Others have also used hyperbolic tangent cores in their work [104, 116, 183], so it also offers some familiarity amongst the literature. Although we found in Chapter 3 that tilt is also an important piece in predicting dynamics, for simplicity, this chapter is focused

only on the consequences of changing this amplitude structure and the observed dynamic differences. We use numerical simulations to consider different sets of initial conditions and then experimentally verify that core shape has an impact on vortex annihilation dynamics.

8.1 Definitions and Initial Condition Fields

To set up the initial condition, we begin in much the same way as the opposite charge vortex pair of Chapters 2, 3, and 7: two vortices of opposite charge are symmetrically displaced in a Gaussian beam at $(x,y) = (\pm x_0, 0)$. This field is given by the expression

$$\psi(r,\phi,0) = \psi_{vortex_-}\psi_{vortex_+}\psi_{host} = A_- e^{-i\phi_-} A_+ e^{i\phi_+} e^{-r^2/w_0^2} \tag{8.1.1}$$

at $z = 0$ and where the subscripts are related to the $\ell = \pm 1$ vortex charge, $A_\pm$ and $\phi_\pm$ describe the amplitude and phase of the each vortex, and w_0 is the host beam waist. In this two vortex system, the initial separation between the vortices is $v_s = 2x_0$ and the postively charged vortex is on the right, and the negatively charged vortex is on the left. The subsequent phase of each vortex is then given by $\phi_\pm = \arctan(y/(x \mp x_0))$. For the amplitude structure, we use the hyperbolic tangent function such that:

$$A_{tanh}(r,\phi) \quad = \quad \tanh\left(\frac{r-r_0}{c_r}\right), \tag{8.1.2}$$

where $r_0 = \sqrt{(x-x_0)^2 + (y-y_0)^2}$ and c_r determines the effective size of the vortex core (summarized in Figure 8.1). The motivation for choosing the hyperbolic tan-

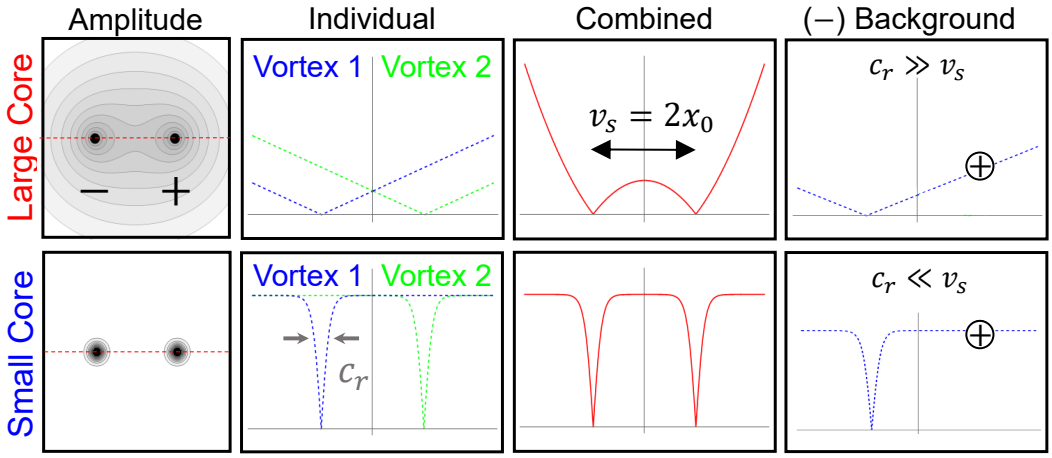

Figure 8.1: A pair of vortices each with a large core (top) or small core (bottom) amplitude are shown. The columns show the combined amplitude contour, the individual vortex slices, the combined slice profile and finally the amplitude gradient of the left vortex at the right vortex. Linear core vortices have immediate overlap, while smaller cores do not have any initial overlap.

gent function is that for very small values of c_r, the core approaches a delta function or point-core amplitude and for large values of c_r, the core approaches the large, linear core limit. This allows us to scale the initial overlap between the amplitudes of each vortex in the initial condition.

With the initial condition set, and the ability to vary the initial overlap of the cores, we can now look at whether or not the vortices annihilate or survive when the beam propagates, as a function of core size.

8.2 Fourier Transform (Far Field) is Not Sufficient for Determining Vortex Pair Annihilation

Our first idea was that we could identify whether or not the vortices would annihilate with propagation by simply looking at the Fourier Transform (far field) of the initial field to see whether or not there were residual vortices. This had been briefly

considered experimentally [158] and analytically at the focus of a high numerical aperture lens [184]. For example, in beams with pairs that quickly annihilate, the expectation is that the far field would not contain any vortices, whereas for vortex pairs that don't annihilate each other the vortices would remain present in the far field. However, upon looking at the two dimensional Fourier Transform of the field for linear core vortex pairs that are expected to annihilate and not [32], it quickly became clear that this would not suffice.

As can be seen in Figure 8.2, the Fourier Transform for linear core pairs below, at, and above the critical $x_0 = 0.5w_0$ annihilation criteria, the Fourier Transform looks remarkably similar. Interestingly, even for the linear core pair, no vortices can be seen in the far field of *any* of the cases.[1] A circular discontinuity sits offset

[1]For vortex pairs with an initial condition that is expected not to annihilate, it is surprising to see that vortices don't exist. However, when back-propagating the far field, we see that the circular discontinuity transforms into a string of many oppositely charged vortices that all eventually recombine except the two vortices present at the initial condition.

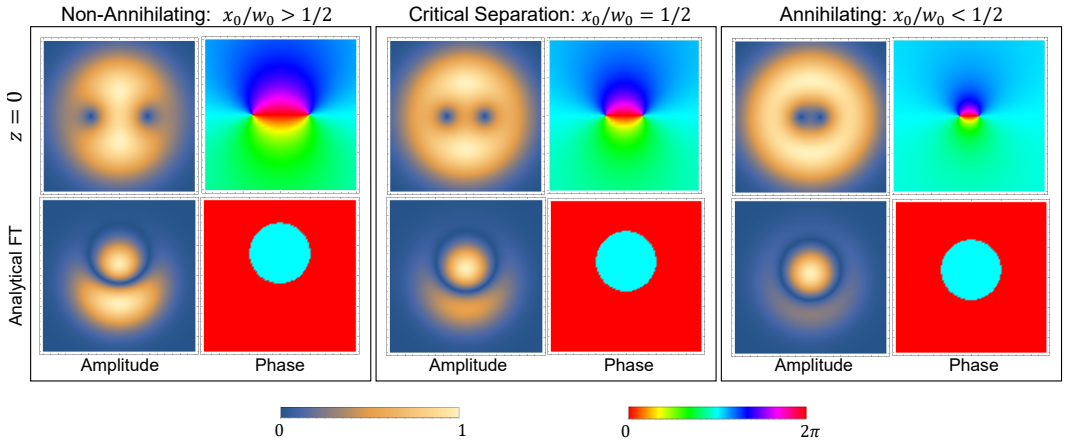

Figure 8.2: The far field (Fourier Transform) of a linear core vortex pair at separations above and below the critical point for annihilation are shown. Here, FT denotes Fourier Transform. The result is a circular phase discontinuity whose position depends on the initial vortex separation. The $z = 0$ field and Fourier Transform are not to scale.

from the center, with its displacement being determined by the initial separation of the vortices. Unfortunately, this result is not particularly useful, since there does not seem to be a meaningful way to use these far field patterns as a diagnostic for vortex annihilation in a reliable way. Even if the position of the circle were used, it would only be relevant to this specific initial condition.

For the case of a hyperbolic tangent core pair, the result is even less friendly than that of the linear core pair. Rather than a circular discontinuity, the result is a forked grating shape, with the width determined by the initial separation. In either case, there is not an intuitive and simple way to consider only the Fourier Transform as a means of determining vortex annihilation. So, we turn to numerical simulations to watch the dynamics unfold with propagation.

8.3 Numerical Simulation Results and Expectations

To look at the difference of vortex pair annihilation dynamics based on the vortex separation and core size, we use numerical simulations to test a variety of initial conditions. The numerical simulations for this chapter rely on the angular spectrum method for propagating light. There are several resources that discuss this method [65, 185] and here, we provide a brief review of the method followed by the results.

8.3.1 Review of the Angular Spectrum Method for Propagating Light

There are many ways to propagate an optical field, including those such as the popular Fresnel integral. However, analytically solving the Fresnel integral can be difficult when using complicated functions, and numerically solving them can be time consuming. Another way is to use the angular spectrum of plane waves

method. A propagated light field can be calculated using a process that breaks the initial field into a spectrum of plane waves with different orientations away from the z axis (hence the name angular spectrum) and then looks at the propagation of that set of fields. To propagate an initial field, $\psi_0(x,y) = \psi(x,y,z=0)$, start by taking the Fourier Transform:

$$\mathscr{F}_\psi(f_x,f_y) = \mathscr{F}\{\psi_0(x,y,z=0)\} \tag{8.3.1}$$

When taking the Fourier Transform of the initial field, it is transformed into a set of plane waves. Intuitively this can make sense when thinking about the conjugate relationship between position and momentum. To find the propagated field, each planewave is then advanced by e^{ikz}, including the phase that is picked up for plane waves travelling at an angle relative to the initial fields z axis. The result is the transfer function, H [65, 185]. For the simulations done here, we use the paraxial limit transfer function [65, 185],

$$H(f_x,f_y,z) = e^{ikz}e^{-i\pi\lambda z(f_x^2+f_y^2)}. \tag{8.3.2}$$

Once the planewaves are advanced by H, the inverse Fourier Transform can be taken to get back to position space and find the propagated field. The propagated field at a given z distance then, is given by

$$\psi(x,y,z) = \mathscr{F}^{-1}\left\{\mathscr{F}\{\psi(x,y,0)\} * H(f_x,f_y,z)\right\}. \tag{8.3.3}$$

A benefit of this method is that the first Fourier Transform only needs to be calculated once for any given initial condition field. Once this Fourier Transform is

taken, we can use it in conjunction with the transfer function to find the field at any given propagation distance.

8.3.2 Numerical Simulations Using the Angular Spectrum Method

We numerically propagate several different initial conditions in which the size of the cores are altered by way of the angular spectrum method. As discussed in Section 6.3 of this dissertation, we use the real and imaginary zero intersections to locate the vortices at each propagation step. For the first comparison, we look at the projection of the trajectories into the transverse plane for a beam with a waist that is large compared to the separation ($w_0 >> x_0$), depicted in Figure 8.3.

The top row shows the phase contours for a linear core vortex pair ($c_r >> x_0$) at increasing propagation distances up until the annihilation point. The results of the numerical simulation show a half circle trajectory in the transverse plane, consistent with the expectations for linear core vortex pairs [32]. With this verification, we then consider vortex pairs with hyperbolic tangent core shapes with decreasing core sizes. The trajectories are tracked up to the annihilation point, which increases as the size of the core decreases. The trajectories for a set of increasingly smaller initial cores are plotted in Figure 8.3 in the bottom panel. The linear core half circle trajectory is plotted as a solid black line for comparison.

As the initial cores decrease in size, two observations can be made: (1) the trajectories increasingly deviate from the linear core half circle in the xy-plane and (2) the beam must propagate a farther distance before the vortices reach the point of annihilation, indicated by the larger number of z-steps. We can interpret these results using what is known about the impact of background phase and amplitude gradients on vortex motion. The phase gradient from the right, positive vortex at

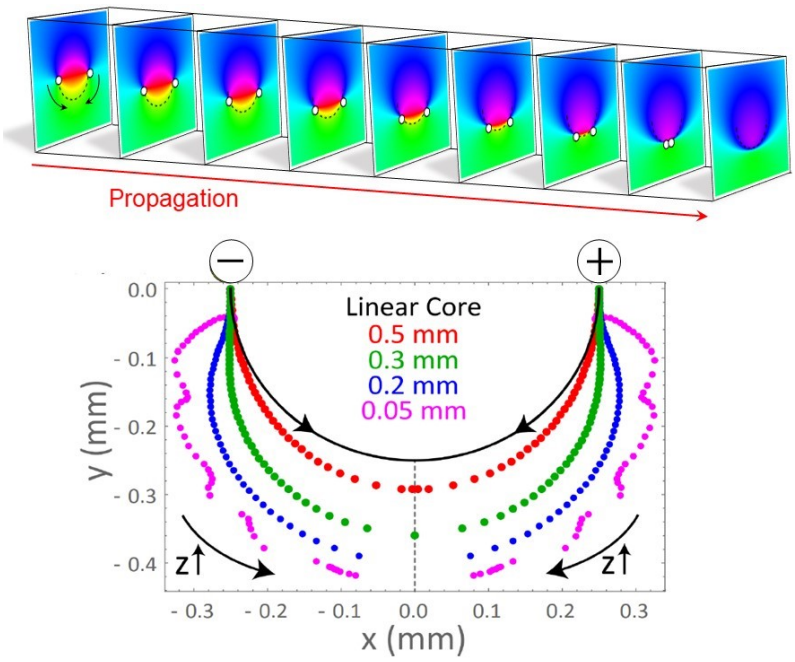

Figure 8.3: Numerical vortex trajectories projected into the *xy*-plane are shown for various core sizes. Top: Slices of the phase for the evolving field of an oppositely charged linear core vortex pair are shown. The vortex locations are marked with white circles and through the propagation the vortices follow a half circle trajectory in the *xy*-plane until the annihilation point. Bottom: A compressed 2D version of the top panel for multiple initial conditions. This plot shows the trajectories for various core sizes ranging from linear to very small cores. Each point is analogous to the white markers in the top panel and represents a successive, equal step in z. As the core size decreases, we see that the trajectories deviate more from the linear core in the *xy*-plane and also take longer in z to annihilate.
***Bottom Figure Credit: Prof. Mark T. Lusk

the location of the left vortex is initially downward via the right hand rule causing the left vortex to move downward. Similarly, the initial phase gradient from the left, negative vortex at the location of the right vortex is also in the downward direction, causing the right vortex to also move downward. This explains the initial vertical $(-\hat{y})$ motion of the vortices.

As a reminder, in the presence of no amplitude gradients, the vortices would simply follow straight line trajectories, as expected for an incompressible fluid sys-

tem [122]. In fact, as the core size decreases, the system approaches an incompressible fluid-like regime for small propagation distances, which was previously discussed for such vortices back in 1997 [116]. But, this only holds for small propagation distances because as the beam propagates, it also diffracts. It can be seen in Figure 8.3, that the downward motion is followed by an outward motion (away from $x = 0$) of each vortex before the recombination event. The hypothesis is that this outward motion is caused by the eventual core overlap that happens due to the diffraction of the beam.

To conceptually understand the impact of amplitude overlap in the vortex motion, we must look at the motion of a vortex in the present background field. For this purpose, we specifically consider the propagation of a single vortex within a Gaussian beam, as shown in Figure 8.4. It is important to note that this will not be the complete background field, since to find the true background field at any given propagation distance one would need to divide out the vortex of interest, including its ellipticity, from the field. Additionally, we know that the evolving orientation of the vortex itself can influence the trajectories, as discussed in Chapter 3. However, we will see that assuming that the background field can be approximated as the single vortex within the Gaussian; measuring at early propagation times where the vortices are expected to be mostly untilted is enough to demonstrate the connection between the outward motion of a given vortex to the arrival of the diffraction wave from the neighboring vortex.

In Figure 8.4, we show the numerically propagated background field, given the assumptions mentioned in the previous paragraph, and calculate the anticipated vortex velocity of the right vortex based on Equation 3.5.17. The same parameters are used for both the background field (only the left vortex in the Gaussian) and the

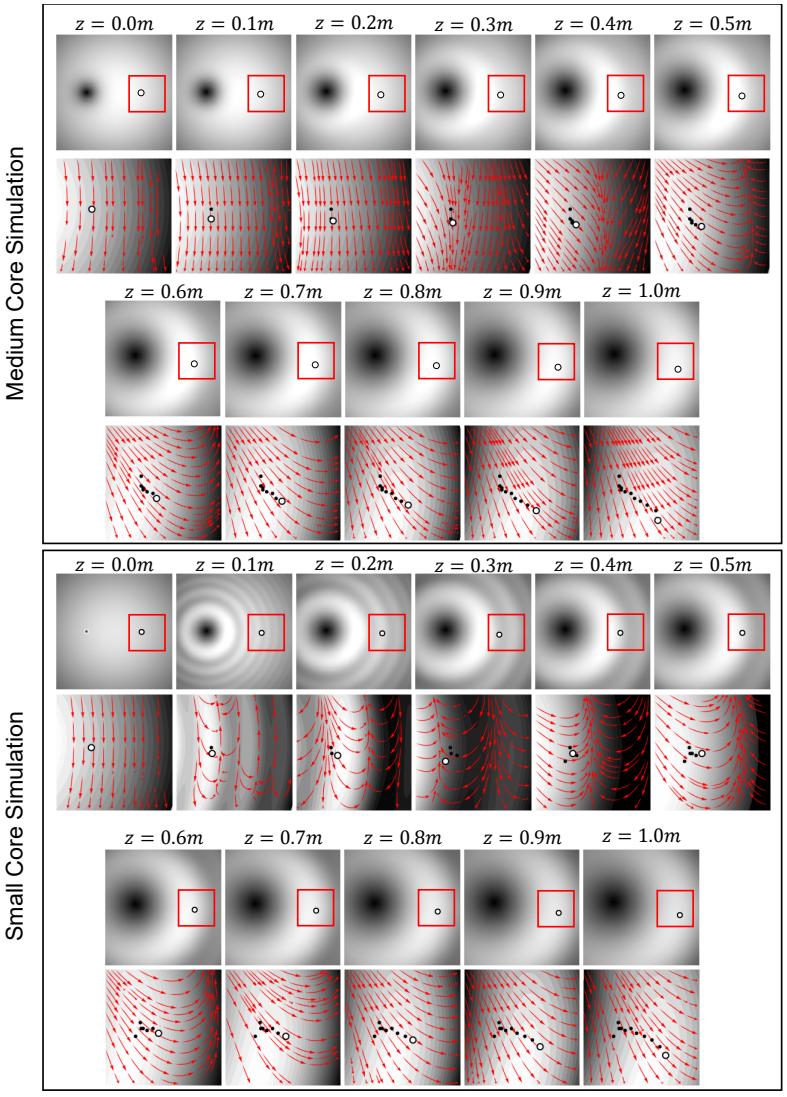

Figure 8.4: Motion of the right vortex compared to the left, diffracting vortex core. Top: Plots of amplitude with propagation of a single vortex in a Gaussian with initial parameters $w_0 = 1$ mm, $x_0 = 0.30w_0$, and $c_r = 0.15w_0$ are shown. Black circles mark the previous right vortex locations and the white circle shows the current vortex location, measured from the two-vortex trajectory. Plots of the highlighted regions from the top row along with red, untilted velocity vectors calculated via $\vec{v}_{vortex} = \nabla\phi_{bg} - \sigma_0\nabla\ln\rho_{bg}$ are shown. Black dots mark the prior vortex locations at each step for comparison of the trajectory with the velocity prediction. Bottom: The same for $w_0 = 1$ mm, $x_0 = 0.30w_0$, and $c_r = 0.005w_0$. *Note that between each z-step, the motion is consistent with the calculated velocity.*

two vortex field, and field gradients are calculated using a two-point finite difference method [186]. In the figure, both a zoomed out region and a close up are shown, with velocity vectors shown by the red arrows in the close up. The vortex locations are also shown, for all previous z-steps (black) and the current step (white). In the medium sized core case, the diffraction of the left vortex mainly comes in one, larger wave that pushes the vortex outward upon its arrival. This can be seen by the initially downward motion of the the right vortex, followed by the motion to the right at $\approx z = 0.3$ m.

In the case of the very small sized core that is reminiscent of a delta function core, ringing in the diffraction field (also seen in [31]) becomes stronger, with several smaller waves followed by a final large diffraction wave. The successive waves create a temporary spiral-like motion of the vortex, with a velocity in the $-\hat{x}$ direction near $z = 0.3$ m, followed by the outward motion from the last diffracting peak just before $z = 0.4$ m. In both cases, despite the approximations mentioned for the comparison, the calculated vortex velocity reliably predicts the vortex motion. It also confirms that the outward motion seen in the vortex trajectories can be attributed to the impact of the diffracting core of the neighboring vortex. In the case of the linear core, the absence of the outward motion can be seen as a result of there being no diffraction wave from the other vortex.

8.4 Experimental Results

With the expectations for the trajectories set, we experimentally measured the trajectories for a few different cases. For the experiment, we use the setup as discussed in Figure 6.1. The same 633 nm HeNe laser and Ball Screw Linear CNC Slide Stroke 1000mm Long Stage Actuator Stepper Motor translation stage used

for the linear core vortex experiments of Section 7.2 are used here. The SLM is still an Epson 83H projector LCD panel, and the imaging lenses have focal length $f_3 = f_4 = 500mm$.

Again, colinear phase-shifting digital holography methods were used to measure the amplitude and phase of the field at each z-step. The holograms are modulated in both the amplitude and the phase to properly create the output beam, and including a Gaussian amplitude in addition to the vortex amplitudes within the grating improved the quality of the data. In other words, ψ_{field} to be used in Equation 4.2.3 for generating the holograms is given in Equation 8.1.1 with $A_{\pm}$ from Equation 8.1.2. The other parameters used in the holograms were: $\alpha = 0$,[2] $N = 10$ pixels, $A = 0.95$, $B = 0.05$. Example holograms for three different core sizes are shown in Figure 8.5.

[2]This experiment was performed before the single vortex experiment, where improvements to holograms by rotating the grating relative to the pixel axes were made.

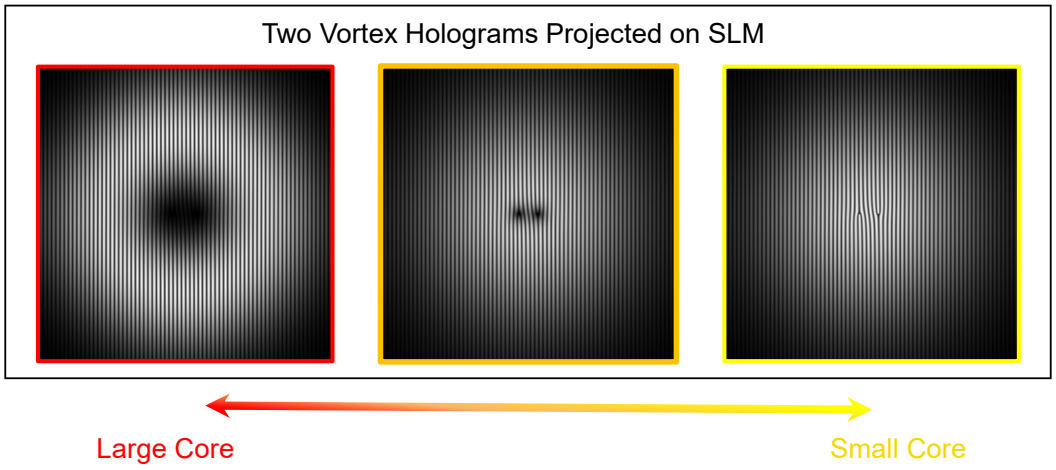

Figure 8.5: Example holograms with varied core sizes are created as described in the text.

Once the experimental field is measured and calibrated (using the drift removal/-calibration methods from Section 6.3), we use the same method of intersecting real and imaginary zeros to locate and track the vortices. With this, we are then ready to analyze the trajectory data. We use a 2D fitting routine, with Equation 8.1.1, on the amplitude of the field at the imaging plane to measure the initial condition parameters including the beam waist, initial vortex separation and core sizes which are then used in the simulation for comparison with the experimental measurement.

Results are shown in Figure 8.6. In the top four rows, we show the simulated amplitude (row 1) and phase (row 2) data followed by the experimentally measured amplitude (row 3) and phase (row 4) data. The qualitative agreement between calculations and experiments is excellent. In the bottom left of Figure 8.6, we show a quantitative comparison of the separation between the vortices. The experimental vortex separation and the numerical simulation also show a very strong agreement between the experiment and simulation, including the fact that the vortices are pushed farther away from each other before moving toward each other and annihilating.

The vortices are not small enough to observe the small oscillations shown in the $c_r = 0.05mm$ case in Figure 8.3 since the measurements are in a finite (smaller) host beam, and the setup is limited by the numerical aperture of the system. It is possible to use lenses of smaller focal lengths, but the trade off of using longer focal length lenses was made to ease in alignment of the imaging system (reducing the likelihood of magnification errors and therefore inaccurate vortex separation measurements with beam propagation as discussed in Section 6.2.2). Additionally, we experimentally measured vortex separation for two additional core sizes. All three vortex separation measurements are shown in the bottom right of Figure 8.6,

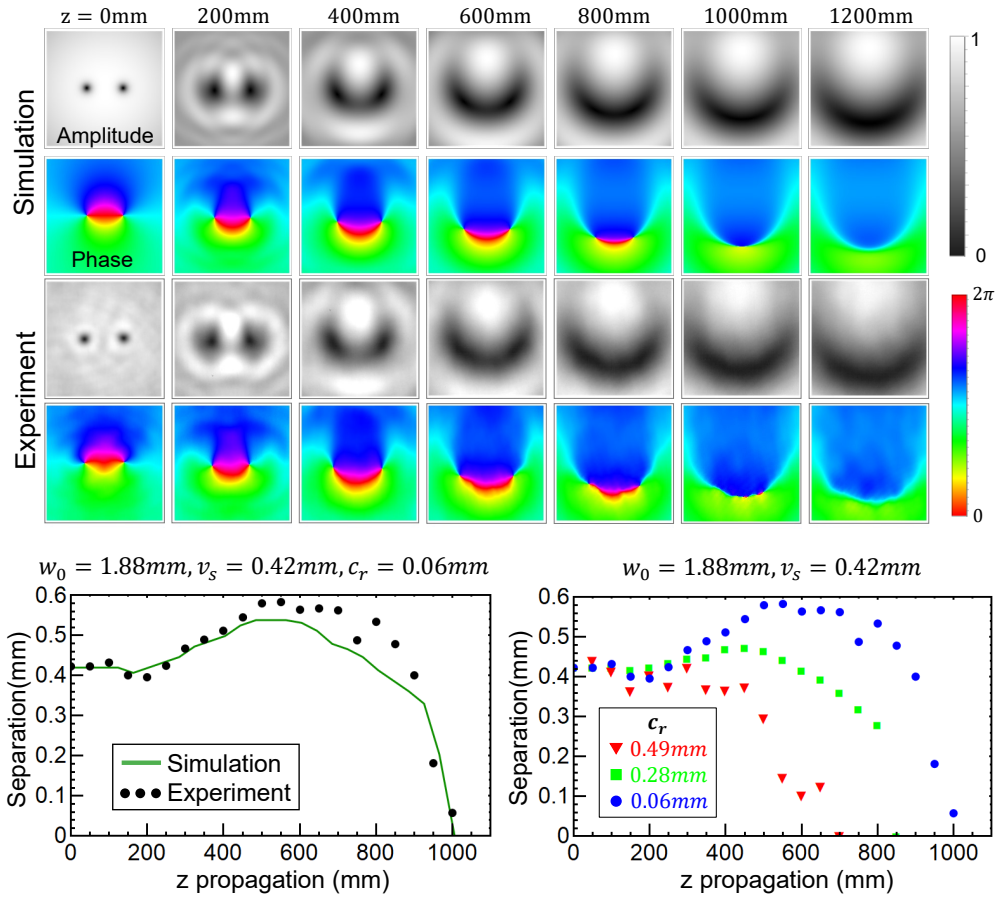

Figure 8.6: Top: Simulated and experimental slices of the field are shown for a set of propagation steps. Bottom Left: Comparison of vortex separation as a function of propagation shows good agreement between simulation and experiment. Bottom Right: A set of measurements for three different sized vortex cores verifies that larger cores annihilate more quickly than small cores.

which confirm smaller annihilation distances for large cores and farther distances for small cores.

8.5 A Vortex Annihilation Phase Diagram

These results prompt some additional questions. If the annihilation distance can be altered based on the initial overlap of the vortices, is there also a way to design

an initial condition such that the annihilation event is prevented from happening altogether? If so, what does that look like? The observation that smaller cores take longer to annihilate prompts the thought that perhaps we can achieve this by simply decreasing the core size as much as possible. To test this, we can again rely on our numerical angular spectrum propagation methods.

We numerically consider a variety of initial conditions to map out regions of annihilation and non-annihilation based on initial beam parameters. The results are summarized in Figure 8.7. As can be seen in the top row of the figure, for initial conditions in which the vortices *do* annihilate, the dynamics resemble those found in Figure 8.3. However, initial conditions can be found such that the trajectories instead move apart from each other. A critical point in between where the vortices seem to be consistently spaced throughout the trajectory can also be found. This critical point is found for a variety of initial conditions, marked by red dots and plotted in Figure 8.7, to show the two unique regions. For vortices with large cores that are spaced close together (moving up and to the left in the figure), annihilation is certain to occur, matching the intuition that highly overlapped cores annihilate more quickly. For vortices that are spaced far enough apart and that have small enough cores (moving down and to the right in the figure), one would expect that the vortices would not have a sufficient overlap before the background Gaussian gradients dominate the vortex motion and keeps them apart for the entirety of the propagation.

One can also imagine a specific separation, for example $x_0/w_0 = 0.48$, in which a linear core pair is expected to annihilate. By simply reducing the size of the core ($c_r/w_0 < 2.7$ for that separation), the annihilation event can be prevented. We also note that there is a maximum initial vortex separation at which even vortices

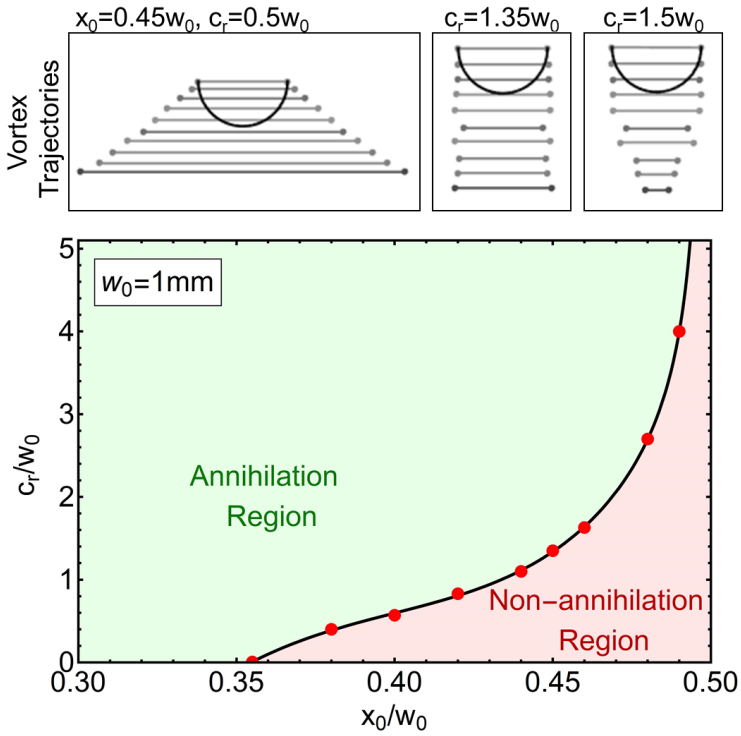

Figure 8.7: Vortex trajectories measured up to $z = 2.8zR$, such as those in the top panel, were used to find critical points between initial conditions that produce annihilating vs. non-annihilating pairs for a variety of initial conditions. The numerically determined data points are fit with a modified polynomial that has a vertical asymptote at $x_0 = 0.5w_0$ to match the diverging linear core pair expectations near $x_0 = 0.5w_0$ [32].

with point cores ($c_r \to 0$) annihilate in the simulations. Though not immediately obvious, it makes intuitive sense that vortex pairs with sufficiently small separation will always annihilate, even with small cores, since the cores will need a much smaller propagation distance before fully overlapping. This maximum initial vortex separation was measured as $x_0 = 0.355w_0$.

8.6 Discussion

In this chapter, we have shown that vortex pair annihilation in linear optical systems can be tuned by simply changing the initial overlap of the vortex core functions. We also showed that the vortex separation in relation to the size of the host Gaussian field can also impact the vortex dynamics. These changes can either facilitate or prevent annihilation events, based on the initial field parameters. These results emphasize the utility in the compressibility of light in vortex dynamics and a way to engineer a desired outcome. Further insights could be gained in more complex, many vortex systems with non-uniform core shapes and sizes using the same principles.

Chapter 9

Conclusions and Future Directions

In this dissertation, I have shared in detail a portion of the work I completed while tackling my PhD. Through my time at DU, I have accomplished much more than I anticipated, including a few publications, and a decent number of conference presentations, including an invitation for a keynote presentation at the DU Research & Scholarship Showcase. I participated in various grant writing opportunities, gave the lab presentation for the W.M. Keck Foundation, and received a few fellowship awards. I also had the opportunity to co-teach the Light-Matter Interactions course here at DU, and found that and interacting with the students to be beyond fulfilling and a wonderful experience. Last, but certainly most influential, I am leaving with a much larger knowledge base in experimental physics than I had when I began. The experimental apparatus that I built can be recreated and used by others both in and out of our group. It should be a useful tool for anyone interested in studying vortex dynamics, and the new theory detailed in this work can be utilized by anyone interested in vortex dynamics within the vast collection of two-dimensional fluids.

9.1 Conclusions

In the context of optical beams, it has long been known that both amplitude and phase gradients contribute to the motion of vortices [100], but a full hydrodynamic model for such systems had not yet been identified because the gradients alone are not sufficient. The inclusion of vortex ellipticity in the kinematics is the missing piece that unlocks a hydrodynamic interpretation of vortex motion in optical laser beams, even for purely linear vortex systems in which the vortex amplitude cores are always overlapping.

In this dissertation, we have presented the novel theory for predicting and understanding the dynamics of vortices in two-dimensional fluids and have applied this theory to a linear optical system. The ellipticity of an optical vortex in any paraxial field can be described using a polar decomposition, and interpreted as the two-dimensional projection of a virtual, circular vortex that lives in a virtual three-dimensional space. This circular vortex is tilted with respect to the propagation direction, resulting in elliptical projections onto the transverse plane. This interpretation of the mathematics gives a more intuitive way of predicting and visualizing the vortex dynamics investigated within the scope of this work, allowing one to think of the vortex like a surfer: to change the direction they travel on a wave, they simply need to reorient themselves (i.e. change their tilt) on the wave they ride. This coupling between vortex ellipticity and the background field gradients was found to be essential in predicting vortex motion with the new kinetic equation given in Equation 3.5.17. Vortex ellipticity, however, is not relevant for incompressible fluids that form the basis for much of our intuition, and it is not observed in compressible fluids for the many scenarios in which vortices are near circular. It

remains evident, though, that vortex ellipticity *must* be taken into account whenever vortex symmetry is lost, as is the case whenever vortices of opposite charge move in optical systems.

We applied this new approach in understanding vortex dynamics experimentally, and tested two specific cases: a single, off-center vortex of various ellipticities, and the annihilation event between two initially circular, oppositely charged vortices. We have designed, constructed and optimized an experimental apparatus for testing vortex dynamics and shared these details in this work. The results from the experiments are a compelling match to the newly developed theory, and give us confidence that accounting for ellipticity in vortex dynamics allows for accurate predictions for vortex dynamics.

We also emphasized the compressible nature of light, and utilized that to modify vortex dynamics in oppositely charged pairs. By simply changing the initial size of the vortices, we have shown that the dynamics can be dramatically altered, including preventing the annihilation of the oppositely charged vortex pair in a Gaussian beam, given the right initial conditions. These results provide insight into the dramatic impact that amplitude gradients of a given fluid can have on vortex dynamics.

Vortex ellipticity (virtual tilt) and its coupling to background amplitude gradients (fluid compressibility) have important implications for understanding and controlling the motion of vortices in other systems. While the hydrodynamic velocity equation has been derived for tilted vortices in the context of propagating paraxial light, the results are equally valid for nonlinear 2D settings as well, including quantum fluids such as superfluid Helium, atomic Bose Einstein condensates, and nonlinear optical media.

As opposed to these other 2D fluids, choosing a linear optical system has been convenient because of the relative simplicity of the experiments. Not only can experiments can be performed at room temperature, but they can be done with relatively inexpensive equipment as well. It is worth noting that we were able to achieve experimental results that closely matched the theoretical expectations with fairly basic holograms, despite using a low cost classroom projector LCD panel not specifically designed for these purposes. The results shared in Chapter 7 could potentially be further improved upon by implementing more elaborate holograms that have been shown to generate very high quality beams [67], or accounting for distortions of the SLM panel itself in the hologram.

Performing this work in an optical context also yields a variety of avenues for future exploration. With the confidence in the apparatus, follow up studies on more complex vortex configurations are possible. A few options are laid out in the next section.

9.2 Future Directions

A natural set of extensions for this work is to consider the wide variety of initial conditions for vortices that are available when using an SLM. It is interesting to consider the application of the theory from Chapter 3 to optical systems with higher order charges, but there still remain many avenues to explore for unit charge vortices. In particular, it could be interesting to explore the effects of small changes to the initial field on the subsequent vortex dynamics in both linear and non-linear systems, and potentially compare them with results seen in other fluid systems [187]. A few interesting options for potential exploration are laid out below.

Asymmetric Core Two Vortex Interactions

In the work discussed throughout this dissertation, we focused on initial condition fields with amplitude cores that were initially circular and of the same size. One might be interested in considering how the dynamics of an opposite pair may change when one core is large while the other is small, as shown in Figure 9.1.

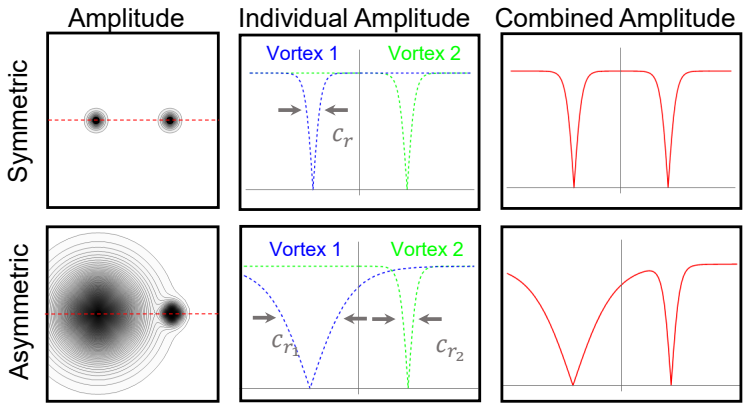

Figure 9.1: Top row: Vortex pairs with equally sized vortex cores. Bottom row: Vortex pairs of unequal size would inevitably exhibit dynamics different than their symmetric counterparts, but the hydrodynamic model would still apply and should explain the subsequent vortex motion.

Lattices of (and Defects Within) Optical Vortices

Another type of initial condition that would be interesting to consider is a vortex lattice of different types. These lattices could be all the same sign, alternating signs, as in Figure 9.2 (a), or randomized lattices. While some work has been done to consider effective ways to generate optical speckle where the result is dependent upon the effective vortex interactions of a lattice sent through the focus of a lens [93], delving into the details of the vortex hydrodynamics both with and without travel-

ing through a lens may lead to better understanding of why the work of that paper is effective.

Many questions can be asked about the stability of optical vortex lattices as well. We know from the 1998 Indebetouw paper that lattices of the same charge are stable upon propagation, since like charge vortices are not influenced by the presence of other vortices in the system. But, further exploration into whether or not this is true for other types of lattice configurations is a question of interest (and has only been explored for lattices of all the same or alternation charges [172,188]), particularly if you wanted to design some initial condition with a specific outcome in the far field.

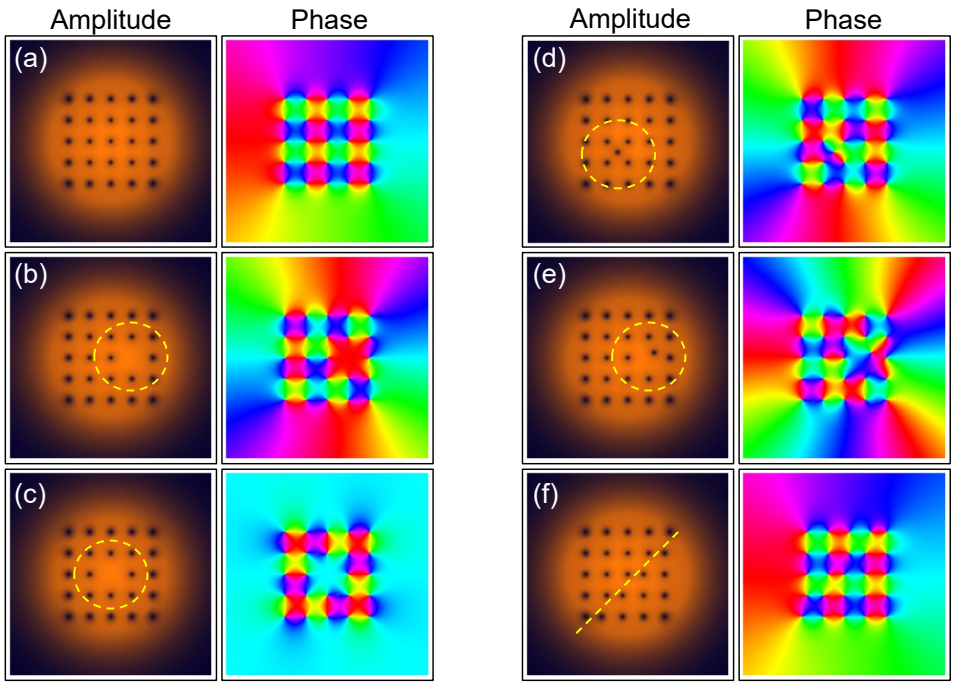

Figure 9.2: (a) Amplitude and phase of an optical lattice with alternating charges is shown. It is possible to consider a range of defects in the optical lattice to test the effect of each type of defect represented in (b-f). Yellow, dashed circles highlight the example defect in each of the amplitudes of (b-f).

From there, one can start considering questions reminiscent of condensed matter physics such as the impact of defects within the lattice on the propagation. A few defects inspired by those found in solid state lattices are shown in Figure 9.2. Consider the optical lattice in (a) of the figure. One possible defect for this lattice is the removal of a vortex at a specific location, such as in Figure 9.2 (b) or (c), and how which vortex is removed may impact the system differently. The effects on the far field patterns for such defects have been previously considered [189], but the changes in their dynamics or stability have not been measured. We can also imagine defects such as those shown in (d-f) of the figure, where interstitial vortices, vortices displaced from their centers or grain boundaries can be introduced into the fields. Each of these cases will have different propagation dynamics and a different far field distribution, but the impact of each type of defect has not been studied.

Optical Vortex Speckle

Finally, we can consider applying the hydrodynamic vortex equation to systems such as optical speckle. In optical speckle, we know that the dynamics are very complex, in part due to the high asymmetry and randomized structure in the system. The hydrodynamic model can be tested by comparison to experimental data of vortex dynamics within this complex system, which would further validate the strength of the model's predictive power and could serve as a means of strengthening the connection between optical fluids and other two-dimensional fluids.

Bibliography

[1] Martin Kemp. Leonardo da vinci's laboratory: studies in flow. *Nature*, 571(7765):322–324, 2019.

[2] Ivan Marusic and Susan Broomhall. Leonardo da vinci and fluid mechanics. *Annual Review of Fluid Mechanics*, 53:1–25, 2021.

[3] Edward Slowik. Descartes' physics. 2005.

[4] I Newton. Principia mathematica, book ii, sec. *VIII (1687)*.

[5] William B. Ashworth. Scientist of the day - rené descartes. https://www.lindahall.org/rene-descartes/, March 2015.

[6] Hermann von Helmholtz. On integrals of the hydrodynamic equations that correspond to vortex motions. *International Journal of Fusion Energy*, 1(3-4):41–68, 1978.

[7] Keith Moffatt. Vortex dynamics: the legacy of helmholtz and kelvin. In *IUTAM symposium on Hamiltonian dynamics, vortex structures, turbulence*, pages 1–10. Springer, 2008.

[8] Lord Kelvin. On vortex atoms. In *Proc. R. Soc. Edin*, volume 6, pages 94–105, 1867.

[9] Ernest Rutherford. The structure of the atom. *Philosophical Magazine*, 27:488–498, 1914.

[10] Sp-168 exploring space with a camera. https://www.kurims.kyoto-u.ac.jp/ kyodo/kokyuroku/contents/pdf/1642-01.pdf, Accessed on 09-19-21.

[11] Richard P Feynman, Robert B Leighton, and Matthew Sands. The feynman lectures on physics; vol. i. *American Journal of Physics*, 33(9):750–752, 1965.

[12] PG Saffman and GR Baker. Vortex interactions. *Annual Review of Fluid Mechanics*, 11(1):95–121, 1979.

[13] Jie-Zhi Wu, Hui-Yang Ma, and M-D Zhou. *Vorticity and vortex dynamics*. Springer Science & Business Media, 2007.

[14] National Oceanic and Atmospheric Administration. What is a gyre? https://oceanservice.noaa.gov/facts/gyre.html. Accessed: 09.07.2021.

[15] Russell J Donnelly. *Quantized vortices in helium II*, volume 2. Cambridge University Press, 1991.

[16] Oliver Gessner and Andrey F Vilesov. Imaging quantum vortices in superfluid helium droplets. *Annual review of physical chemistry*, 70:173–198, 2019.

[17] Christopher J Pethick and Henrik Smith. *Bose–Einstein condensation in dilute gases*. Cambridge university press, 2008.

[18] P Schattschneider and J Verbeeck. Theory of free electron vortices. *Ultramicroscopy*, 111(9-10):1461–1468, 2011.

[19] Gianni Blatter, Mikhail V Feigel'man, Vadim B Geshkenbein, Anatoly I Larkin, and Valerii M Vinokur. Vortices in high-temperature superconductors. *Reviews of modern physics*, 66(4):1125, 1994.

[20] José Benito Llorens, Lior Embon, Alexandre Correa, Jesús David González, Edwin Herrera, Isabel Guillamón, Roberto F Luccas, Jon Azpeitia, Federico J Mompeán, Mar García-Hernández, et al. Observation of a gel of quantum vortices in a superconductor at very low magnetic fields. *Physical Review Research*, 2(1):013329, 2020.

[21] Tzer Han Tan, Jinghui Liu, Pearson W Miller, Melis Tekant, Jörn Dunkel, and Nikta Fakhri. Topological turbulence in the membrane of a living cell. *Nature Physics*, pages 1–6, 2020.

[22] P Coullet, L Gil, and F Rocca. Optical vortices. *Optics Communications*, 73(5):403–408, 1989.

[23] Yijie Shen, Xuejiao Wang, Zhenwei Xie, Changjun Min, Xing Fu, Qiang Liu, Mali Gong, and Xiaocong Yuan. Optical vortices 30 years on: Oam manipulation from topological charge to multiple singularities. *Light: Science & Applications*, 8(1):1–29, 2019.

[24] John Frederick Nye and Michael Victor Berry. Dislocations in wave trains. In *A Half-Century of Physical Asymptotics and Other Diversions: Selected Works by Michael Berry*, pages 6–31. World Scientific, 1974.

[25] Mark R Dennis, Kevin O'Holleran, and Miles J Padgett. Singular optics: optical vortices and polarization singularities. *Progress in optics*, 53:293–363, 2009.

[26] Sharon A Kennedy, Matthew J Szabo, Hilary Teslow, James Z Porterfield, and ERI Abraham. Creation of laguerre-gaussian laser modes using diffractive optics. *Physical Review A*, 66(4):043801, 2002.

[27] Peter Dedecker, Benoît Muls, Johan Hofkens, Jörg Enderlein, and Junichi Hotta. Orientational effects in the excitation and de-excitation of single molecules interacting with donut-mode laser beams. *Optics Express*, 15(6):3372–3383, 2007.

[28] Russell Pollari and Joshua N Milstein. Accounting for polarization in the calibration of a donut beam axial optical tweezers. *PloS one*, 13(2):e0193402, 2018.

[29] Yiping Huang, Fan Shi, Teng Wang, Xiaomin Liu, Xianglong Zeng, Fufei Pang, Tingyun Wang, and Pu Zhou. High-order mode yb-doped fiber lasers based on mode-selective couplers. *Optics Express*, 26(15):19171–19181, 2018.

[30] Les Allen, Marco W Beijersbergen, RJC Spreeuw, and JP Woerdman. Orbital angular momentum of light and the transformation of laguerre-gaussian laser modes. *Physical review A*, 45(11):8185, 1992.

[31] D Rozas, CT Law, and GA Swartzlander. Propagation dynamics of optical vortices. *JOSA B*, 14(11):3054–3065, 1997.

[32] Guy Indebetouw. Optical vortices and their propagation. *Journal of Modern Optics*, 40(1):73–87, 1993.

[33] Filippus Stefanus Roux. Dynamical behavior of optical vortices. *JOSA B*, 12(7):1215–1221, 1995.

[34] Alan E Willner, Hao Huang, Yan Yan, Yongxiong Ren, Nisar Ahmed, Goudong Xie, Changjing Bao, L Li, Y Cao, Z Zhao, et al. Optical com-

munications using orbital angular momentum beams. *Advances in Optics and Photonics*, 7(1):66–106, 2015.

[35] Filippus S Roux. Canonical vortex dipole dynamics. *JOSA B*, 21(3):655–663, 2004.

[36] Sean J Kirkpatrick, Kosar Khaksari, Dennis Thomas, and Donald D Duncan. Optical vortex behavior in dynamic speckle fields. *Journal of Biomedical Optics*, 17(5):050504, 2012.

[37] Lynn Paterson, Michael P MacDonald, Jochen Arlt, W Sibbett, PE Bryant, and K Dholakia. Controlled rotation of optically trapped microscopic particles. *Science*, 292(5518):912–914, 2001.

[38] Christian T Schmiegelow, Jonas Schulz, Henning Kaufmann, Thomas Ruster, Ulrich G Poschinger, and Ferdinand Schmidt-Kaler. Transfer of optical orbital angular momentum to a bound electron. *Nature communications*, 7(1):1–6, 2016.

[39] Kristan Bryan Simbulan, Teng-De Huang, Guan-Hao Peng, Feng Li, Oscar Javier Gomez Sanchez, Jhen-Dong Lin, Chun-I Lu, Chan-Shan Yang, Junjie Qi, Shun-Jen Cheng, et al. Selective photoexcitation of finite-momentum excitons in monolayer mos2 by twisted light. *ACS nano*, 15(2):3481–3489, 2021.

[40] Jan Gieseler, Juan Ruben Gomez-Solano, Alessandro Magazzù, Isaac Pérez Castillo, Laura Pérez García, Marta Gironella-Torrent, Xavier Viader-Godoy, Felix Ritort, Giuseppe Pesce, Alejandro V Arzola, et al. Optical tweezers—from calibration to applications: a tutorial. *Advances in Optics and Photonics*, 13(1):74–241, 2021.

[41] Zhe Shen, Zhiyuan Xiang, Ziyao Wang, Yaochun Shen, and Baifu Zhang. Optical spanner for nanoparticle rotation with focused optical vortex generated through a pancharatnam–berry phase metalens. *Applied Optics*, 60(16):4820–4826, 2021.

[42] Yuanjie Yang, Yuxuan Ren, Mingzhou Chen, Yoshihiko Arita, and Carmelo Rosales-Guzmán. Optical trapping with structured light: a review. *Advanced Photonics*, 3(3):034001, 2021.

[43] PG Kevrekidis, R Carretero-González, G Theocharis, DJ Frantzeskakis, and BA Malomed. Vortices in a bose–einstein condensate confined by an optical lattice. *Journal of Physics B: Atomic, Molecular and Optical Physics*, 36(16):3467, 2003.

[44] Jian Wang, Jeng-Yuan Yang, Irfan M Fazal, Nisar Ahmed, Yan Yan, Hao Huang, Yongxiong Ren, Yang Yue, Samuel Dolinar, Moshe Tur, et al. Terabit free-space data transmission employing orbital angular momentum multiplexing. *Nature photonics*, 6(7):488–496, 2012.

[45] Carmelo Rosales-Guzmán, Nkosiphile Bhebhe, Nyiku Mahonisi, and Andrew Forbes. Multiplexing 200 spatial modes with a single hologram. *Journal of Optics*, 19(11):113501, 2017.

[46] Nenad Bozinovic, Yang Yue, Yongxiong Ren, Moshe Tur, Poul Kristensen, Hao Huang, Alan E Willner, and Siddharth Ramachandran. Terabit-scale orbital angular momentum mode division multiplexing in fibers. *science*, 340(6140):1545–1548, 2013.

[47] Zhenwei Xie, Ting Lei, Fan Li, Haodong Qiu, Zecen Zhang, Hong Wang, Changjun Min, Luping Du, Zhaohui Li, and Xiaocong Yuan. Ultra-broadband on-chip twisted light emitter for optical communications. *Light: Science & Applications*, 7(4):18001–18001, 2018.

[48] Yuanhui Wen, Ioannis Chremmos, Yujie Chen, Guoxuan Zhu, Junwei Zhang, Jiangbo Zhu, Yanfeng Zhang, Jie Liu, and Siyuan Yu. Compact and high-performance vortex mode sorter for multi-dimensional multiplexed fiber communication systems. *Optica*, 7(3):254–262, 2020.

[49] Jianchun Xu, Yaxian Guo, Puyu Yang, Ru Zhang, Xiaojun Zhai, Shanguo Huang, and Ke Bi. Recent progress on rf orbital angular momentum antennas. *Journal of Electromagnetic Waves and Applications*, 34(3):275–300, 2020.

[50] Yuntao Zhu, Heyun Tan, Nan Zhou, Lifeng Chen, Jian Wang, and Xinlun Cai. Compact high-efficiency four-mode vortex beam generator within the telecom c-band. *Optics letters*, 45(7):1607–1610, 2020.

[51] Xuewen Wang, Zhongquan Nie, Yao Liang, Jian Wang, Tao Li, and Baohua Jia. Recent advances on optical vortex generation. *Nanophotonics*, 7(9):1533–1556, 2018.

[52] Andrew Forbes. Structured light from lasers. *Laser & Photonics Reviews*, 13(11):1900140, 2019.

[53] Shaoxiang Li and Zhenwei Wang. Generation of optical vortex based on computer-generated holographic gratings by photolithography. *Applied Physics Letters*, 103(14):141110, 2013.

[54] VV Kotlyar, AA Kovalev, RV Skidanov, SN Khonina, and J Turunen. Generating hypergeometric laser beams with a diffractive optical element. *Applied Optics*, 47(32):6124–6133, 2008.

[55] MW Beijersbergen, RPC Coerwinkel, M Kristensen, and JP Woerdman. Helical-wavefront laser beams produced with a spiral phaseplate. *Optics communications*, 112(5-6):321–327, 1994.

[56] Victor V Kotlyar, Anton A Almazov, Svetlana N Khonina, Victor A Soifer, Henna Elfstrom, and Jari Turunen. Generation of phase singularity through

diffracting a plane or gaussian beam by a spiral phase plate. *JOSA A*, 22(5):849–861, 2005.

[57] Mark Fox. Optical properties of solids, 2002.

[58] Ashok Kumar, Pravin Vaity, J Banerji, and RP Singh. Making an optical vortex and its copies using a single spatial light modulator. *Physics Letters A*, 375(41):3634–3640, 2011.

[59] J Arlt, K Dholakia, L Allen, and MJ Padgett. The production of multiringed laguerre–gaussian modes by computer-generated holograms. *Journal of modern optics*, 45(6):1231–1237, 1998.

[60] Nelson Anaya Carvajal, Cristian H Acevedo, and Yezid Torres Moreno. Generation of perfect optical vortices by using a transmission liquid crystal spatial light modulator. *International Journal of Optics*, 2017, 2017.

[61] Thomas W Clark, Rachel F Offer, Sonja Franke-Arnold, Aidan S Arnold, and Neal Radwell. Comparison of beam generation techniques using a phase only spatial light modulator. *Optics express*, 24(6):6249–6264, 2016.

[62] Ashok Kumar, Pravin Vaity, Jitendra Bhatt, and RP Singh. Stability of higher order optical vortices produced by spatial light modulators. *Journal of Modern Optics*, 60(20):1696–1700, 2013.

[63] Angela Dudley, Darryl Naidoo, and Andrew Forbes. Characterising laser beams with liquid crystal displays. In *Fourth Conference on Sensors, MEMS, and Electro-Optic Systems*, volume 10036, page 100360W. International Society for Optics and Photonics, 2017.

[64] Andrey S Ostrovsky, Carolina Rickenstorff-Parrao, and Víctor Arrizón. Generation of the "perfect" optical vortex using a liquid-crystal spatial light modulator. *Optics letters*, 38(4):534–536, 2013.

[65] Joseph W Goodman. *Introduction to Fourier optics*. Roberts and Company Publishers, 2005.

[66] Suzana Topuzoski and Ljiljana Janicijevic. Fraunhofer diffraction of a laguerre–gaussian laser beam by fork-shaped grating. *Journal of Modern Optics*, 58(2):138–145, 2011.

[67] David Bowman, Tiffany L Harte, Valentin Chardonnet, Caroline De Groot, Samuel J Denny, Guillaume Le Goc, Matthew Anderson, Philip Ireland, Donatella Cassettari, and Graham David Bruce. High-fidelity phase and amplitude control of phase-only computer generated holograms using conjugate gradient minimisation. *Optics express*, 25(10):11692–11700, 2017.

[68] Carmelo Rosales-Guzmán and Andrew Forbes. *How to shape light with spatial light modulators*. SPIE Press, 2017.

[69] Mateusz Szatkowski, Jan Masajada, Ireneusz Augustyniak, and Klaudia Nowacka. Generation of composite vortex beams by independent spatial light modulator pixel addressing. *Optics Communications*, 463:125341, 2020.

[70] Alicia V Carpentier, Humberto Michinel, José R Salgueiro, and David Olivieri. Making optical vortices with computer-generated holograms. *American Journal of Physics*, 76(10):916–921, 2008.

[71] Guy Indebetouw and Siuying Raymond Liu. Defect-mediated spatial complexity and chaos in a phase-conjugate resonator. *Optics communications*, 91(3-4):321–330, 1992.

[72] AG White, CP Smith, NR Heckenberg, H Rubinsztein-Dunlop, R McDuff, CO Weiss, and Chr Tamm. Interferometric measurements of phase singularities in the output of a visible laser. *Journal of Modern Optics*, 38(12):2531–2541, 1991.

[73] M Harris, CA Hill, and JM Vaughan. Optical helices and spiral interference fringes. *Optics communications*, 106(4-6):161–166, 1994.

[74] MS Soskin, VN Gorshkov, MV Vasnetsov, JT Malos, and NR Heckenberg. Topological charge and angular momentum of light beams carrying optical vortices. *Physical Review A*, 56(5):4064, 1997.

[75] Alexander Jesacher, Severin Fürhapter, Stefan Bernet, and Monika Ritsch-Marte. Spiral interferogram analysis. *JOSA A*, 23(6):1400–1409, 2006.

[76] Samuel N Alperin, Robert D Niederriter, Juliet T Gopinath, and Mark E Siemens. Quantitative measurement of the orbital angular momentum of light with a single, stationary lens. *Optics letters*, 41(21):5019–5022, 2016.

[77] Shuang Zheng and Jian Wang. Measuring orbital angular momentum (oam) states of vortex beams with annular gratings. *Scientific reports*, 7(1):1–9, 2017.

[78] Gregorius C G Berkhout, Martin P J Lavery, Johannes Courtial, Marco W. Beijersbergen, and Miles J. Padgett. Efficient sorting of orbital angular momentum states of light. *Physical Review Letters*, 105(15):8–11, 2010.

[79] Gabriel Molina-Terriza, Liis Rebane, Juan P Torres, Lluis Torner, and Silvia Carrasco. Probing canonical geometrical objects by digital spiral imaging. *Journal of the European Optical Society-Rapid Publications*, 2, 2007.

[80] Christian Schulze, Angela Dudley, Daniel Flamm, Michael Duparre, and Andrew Forbes. Measurement of the orbital angular momentum density of light by modal decomposition. *New Journal of Physics*, 15:073025, 2013.

[81] Igor A Litvin, Angela Dudley, Filippus S Roux, and Andrew Forbes. Azimuthal decomposition with digital holograms. *Optics Express*, 20(10):10996–11004, 2012.

[82] Siddharth Ramachandran and Poul Kristensen. Optical vortices in fiber. *Nanophotonics*, 2(5-6):455–474, 2013.

[83] Jonathan Leach, Eric Yao, and Miles J. Padgett. Observation of the vortex structure of a non-integer vortex beam. *New Journal of Physics*, 6:1–8, 2004.

[84] Jonathan Leach, Mark R Dennis, Johannes Courtial, and Miles J Padgett. Vortex knots in light. *New Journal of Physics*, 7(1):55, 2005.

[85] Kevin O'Holleran, Miles J Padgett, and Mark R Dennis. Topology of optical vortex lines formed by the interference of three, four, and five plane waves. *Optics Express*, 14(7):3039–3044, 2006.

[86] Zhurun Ji, Wenjing Liu, Sergiy Krylyuk, Xiaopeng Fan, Zhifeng Zhang, Anlian Pan, Liang Feng, Albert Davydov, and Ritesh Agarwal. Photocurrent detection of the orbital angular momentum of light. *Science*, 368(6492):763–767, 2020.

[87] Li Ge. Twisted light on a chip. *Science*, 368(6492):707–708, 2020.

[88] K. O'Holleran, M. Dennis, and M. Padgett. Illustrations of optical vortices in three dimensions. *Journal of the European Optical Society - Rapid publications*, 1(0), 2006.

[89] Jan Masajada and Bogusława Dubik. Optical vortex generation by three plane wave interference. *Optics Communications*, 198(1-3):21–27, 2001.

[90] Gregory J Gbur. *Singular optics*. CRC press, 2016.

[91] Samuel N Alperin, Robert D Niederriter, Juliet T Gopinath, and Mark E Siemens. Quantitative measurement of the orbital angular momentum of light with a single , stationary lens. *Optics Letters*, 41(21), 2016.

[92] Liu Man, Song Hong-Sheng, Chen Xiao-Yi, Liu Gui-Yuan, Teng Shu-Yun, and Cheng Chuan-Fu. Intensity distribution and phase vortices of speckle fields generated by multi-aperture random scattering screens. *Chinese Physics Letters*, 27(3):034202, 2010.

[93] A Balbuena Ortega, S Bucio-Pacheco, S Lopez-Huidobro, L Perez-Garcia, FJ Poveda-Cuevas, JA Seman, AV Arzola, and K Volke-Sepúlveda. Creation of optical speckle by randomizing a vortex-lattice. *Optics express*, 27(4):4105–4115, 2019.

[94] Andrew W Baggaley, Carlo F Barenghi, Anvar Shukurov, and Yuri A Sergeev. Coherent vortex structures in quantum turbulence. *EPL (Europhysics Letters)*, 98(2):26002, 2012.

[95] Samuel N Alperin, Abigail L Grotelueschen, and Mark E Siemens. Quantum turbulent structure in light. *Physical review letters*, 122(4):044301, 2019.

[96] Mingzhou Chen and Filippus S Roux. Accelerating the annihilation of an optical vortex dipole in a gaussian beam. *JOSA A*, 25(6):1279–1286, 2008.

[97] Wendi Zhao, Wenjing Cheng, and Guo Liang. Spacing dependent interaction of vortex dipole and induced off-axis propagations of optical energy. *Optik*, 202:163729, 2020.

[98] Andrew J Groszek, David M Paganin, Kristian Helmerson, and Tapio P Simula. Motion of vortices in inhomogeneous bose-einstein condensates. *Physical Review A*, 97(2):023617, 2018.

[99] Alan Aversa. The gross-pitaevskii equation: A non-linear schrödinger equation, 2008.

[100] David Rozas. *Generation and propagation of optical vortices*. PhD thesis, Worcester Polytechnic Institute, 1999.

[101] Yuri S Kivshar, Jason Christou, Vladimir Tikhonenko, Barry Luther-Davies, and Len M Pismen. Dynamics of optical vortex solitons. *Optics Communications*, 152(1-3):198–206, 1998.

[102] Mankei Tsang, Demetri Psaltis, Jeffrey H Shapiro, and Seth Lloyd. Optical hydrodynamics. In *Frontiers in Optics*, page FWO3. Optical Society of America, 2008.

[103] A Bekshaev, M Soskin, and M Vasnetsov. Paraxial light beams with angular momentum. *arXiv preprint arXiv:0801.2309*, 2008.

[104] GA Swartzlander Jr and CT Law. Optical vortex solitons observed in kerr nonlinear media. *Physical Review Letters*, 69(17):2503, 1992.

[105] FDM Haldane and Yong-Shi Wu. Quantum dynamics and statistics of vortices in two-dimensional superfluids. *Physical review letters*, 55(26):2887, 1985.

[106] NP Proukakis, NG Parker, DJ Frantzeskakis, and CS Adams. Analogies between dark solitons in atomic bose–einstein condensates and optical systems. *Journal of Optics B: Quantum and Semiclassical Optics*, 6(5):S380, 2004.

[107] Janne Ruostekoski and Zachary Dutton. Engineering vortex rings and systems for controlled studies of vortex interactions in bose-einstein condensates. *Physical Review A*, 72(6):063626, 2005.

[108] M Brambilla, LA Lugiato, V Penna, F Prati, Chr Tamm, and CO Weiss. Transverse laser patterns. ii. variational principle for pattern selection, spatial multistability, and laser hydrodynamics. *Physical Review A*, 43(9):5114, 1991.

[109] Luca Perfetti. Superfluidity of light, March 2016.

[110] Claire Michel, Omar Boughdad, Mathias Albert, Pierre-Élie Larré, and Matthieu Bellec. Superfluid motion and drag-force cancellation in a fluid of light. *Nature communications*, 9(1):1–6, 2018.

[111] E. Madelung. Quantentheorie in hydrodynamischer form. *Zeitschrift für Physik*, 40(3):322–326, Mar 1927.

[112] Iacopo Carusotto and Cristiano Ciuti. Quantum fluids of light. *Reviews of Modern Physics*, 85(1):299, 2013.

[113] Francesco Marino, Calum Maitland, David Vocke, Antonello Ortolan, and Daniele Faccio. Emergent geometries and nonlinear-wave dynamics in photon fluids. *Scientific reports*, 6:23282, 2016.

[114] Jan Klaers, Julian Schmitt, Frank Vewinger, and Martin Weitz. Bose–einstein condensation of photons in an optical microcavity. *Nature*, 468(7323):545–548, 2010.

[115] Inés Urdaneta. Liquid light at room temperature! https://www.resonancescience.org/blog/Liquid-light-at-room-temperature, November 2018.

[116] D Rozas, ZS Sacks, and GA Swartzlander Jr. Experimental observation of fluidlike motion of optical vortices. *Physical review letters*, 79(18):3399, 1997.

[117] Filippus S Roux. Coupling of noncanonical optical vortices. *JOSA B*, 21(3):664–670, 2004.

[118] Isaac Freund. Optical vortex trajectories. *Optics communications*, 181(1-3):19–33, 2000.

[119] AV Mamaev, M Saffman, and AA Zozulya. Vortex evolution and bound pair formation in anisotropic nonlinear optical media. *Physical review letters*, 77(22):4544, 1996.

[120] Jasmine M. Andersen, Andrew A. Voitiv, Mark E. Siemens, and Mark T. Lusk. Hydrodynamics of noncircular vortices in beams of light and other two-dimensional fluids. *Physical Review A*, 104(3):033520, 2021.

[121] Halvor M Nilsen, Gordon Baym, and CJ Pethick. Velocity of vortices in inhomogeneous bose–einstein condensates. *Proceedings of the National Academy of Sciences*, 103(21):7978–7981, 2006.

[122] Louis Melville Milne-Thomson. *Theoretical hydrodynamics*. Courier Corporation, 1996.

[123] Tom E Faber. *Fluid dynamics for physicists*. Cambridge university press, 1995.

[124] Crazy Pool Vortex. https://www.youtube.com/watch?v=pnbJEg9r1o8. 2021-11-22.

[125] Taro Ando, Naoya Matsumoto, Yoshiyuki Ohtake, Yu Takiguchi, and Takashi Inoue. Structure of optical singularities in coaxial superpositions of laguerre–gaussian modes. *JOSA A*, 27(12):2602–2612, 2010.

[126] EJ Galvez, N Smiley, and N Fernandes. Composite optical vortices formed by collinear laguerre-gauss beams. In *Nanomanipulation with Light II*, volume 6131, page 613105. International Society for Optics and Photonics, 2006.

[127] Sujuan Huang, Zhuang Miao, Chao He, Fufei Pang, Yingchun Li, and Tingyun Wang. Composite vortex beams by coaxial superposition of laguerre–gaussian beams. *Optics and Lasers in Engineering*, 78:132–139, 2016.

[128] Gabriel Molina-Terriza, Ewan M Wright, and Lluis Torner. Propagation and control of noncanonical optical vortices. *Optics letters*, 26(3):163–165, 2001.

[129] Satyajit Maji and Maruthi M Brundavanam. Controlled noncanonical vortices from higher-order fractional screw dislocations. *Optics letters*, 42(12):2322–2325, 2017.

[130] RP Singh and SR Chowdhury. Trajectory of an optical vortex: canonical vs. non-canonical. *Optics communications*, 215(4-6):231–237, 2003.

[131] D Rose. Rotations in three-dimensions: Euler angles and rotation matrices, 2015.

[132] S Saghafi and CJR Sheppard. Near field and far field of elegant hermite-gaussian and laguerre-gaussian modes. *Journal of Modern Optics*, 45(10):1999–2009, 1998.

[133] S Saghafi, CJR Sheppard, and JA Piper. Characterising elegant and standard hermite–gaussian beam modes. *Optics communications*, 191(3-6):173–179, 2001.

[134] Jörgen Bergström. 4 - continuum mechanics foundations. In Jörgen Bergström, editor, *Mechanics of Solid Polymers*, pages 131–207. William Andrew Publishing, 2015.

[135] Morton E Gurtin. *An introduction to continuum mechanics*. Academic press, 1982.

[136] Timothy M. Pritchett and A. David Trubatch. A differential formulation of diffraction theory for the undergraduate optics course. *American Journal of Physics*, 72:1026–1034, 2004.

[137] Vyacheslav N Gorshkov, Anna N Kononenko, and Marat S Soskin. Topology of optical vortices spontaneous birth. In *Selected Papers from Fifth International Conference on Correlation Optics*, volume 4607, pages 13–24. International Society for Optics and Photonics, 2002.

[138] M Massari, G Ruffato, M Gintoli, F Ricci, and F Romanato. Fabrication and characterization of high-quality spiral phase plates for optical applications. *Applied Optics*, 54(13):4077–4083, 2015.

[139] G Ruffato, M Massari, and F Romanato. Generation of high-order laguerre–gaussian modes by means of spiral phase plates. *Optics letters*, 39(17):5094–5097, 2014.

[140] Vitaly Lerner, David Shwa, Yehonathan Drori, and Nadav Katz. Shaping laguerre–gaussian laser modes with binary gratings using a digital micromirror device. *Optics letters*, 37(23):4826–4828, 2012.

[141] Derek Huang, Henry Timmers, Adam Roberts, Niranjan Shivaram, and Arvinder S Sandhu. A low-cost spatial light modulator for use in undergraduate and graduate optics labs. *American Journal of Physics*, 80(3):211–215, 2012.

[142] Graham Saxby. *Practical holography*. CRC Press, 2003.

[143] Max Born and Emil Wolf. *Principles of optics: electromagnetic theory of propagation, interference and diffraction of light*. Elsevier, 2013.

[144] Emmett Leith and Juris Upatnieks. Wavefront reconstruction photography. *Physics Today*, 18(8):26, 1965.

[145] Dennis Gabor. A new microscopic principle. *nature*, 161:777–778, 1948.

[146] EN Leith. Phase conjugation and image correction. 2005.

[147] Klaus Jäger, Grit Köppel, Martin Hammerschmidt, Sven Burger, and Christiane Becker. On accurate simulations of thin-film solar cells with a thick glass superstrate. *Optics express*, 26(2):A99–A107, 2018.

[148] Emmett N Leith and Juris Upatnieks. Reconstructed wavefronts and communication theory. *JOSA*, 52(10):1123–1130, 1962.

[149] Ljiljana Janicijevic and Suzana Topuzoski. Fresnel and fraunhofer diffraction of a gaussian laser beam by fork-shaped gratings. *JOSA A*, 25(11):2659–2669, 2008.

[150] A Mawardi, S Hild, A Widera, and D Meschede. Abcd-treatment of a propagating doughnut beam generated by a spiral phase plate. *Optics express*, 19(22):21205–21210, 2011.

[151] Jasmine M Andersen, Samuel N Alperin, Andrew A Voitiv, William G Holtzmann, Juliet T Gopinath, and Mark E Siemens. Characterizing vortex beams from a spatial light modulator with collinear phase-shifting holography. *Applied optics*, 58(2):404–409, 2019.

[152] R Bowman, V D'Ambrosio, E Rubino, O Jedrkiewicz, P Di Trapani, and Miles J Padgett. Optimisation of a low cost slm for diffraction efficiency and ghost order suppression. *The European Physical Journal Special Topics*, 199(1):149–158, 2011.

[153] Ichirou Yamaguchi. Phase-shifting digital holography. *Optics Letters*, 22(16):1268–1270, 1997.

[154] Konstantin Y Bliokh and Andrea Aiello. Goos–hänchen and imbert–fedorov beam shifts: an overview. *Journal of Optics*, 15(1):014001, 2013.

[155] V. V. Kotlyar, R. V. Skidanov, S. N. Khonina, and V. A. Soifer. Hypergeometric modes. *Opt. Lett.*, 32(7):742–744, Apr 2007.

[156] Shu-Chun Chu and Kenju Otsuka. Doughnut-like beam generation of laguerre–gaussian mode with extremely high mode purity. *Optics communications*, 281(6):1647–1653, 2008.

[157] Peng Zhao, Shikang Li, Yu Wang, Xue Feng, Cui Kaiyu, Liu Fang, Wei Zhang, and Yidong Huang. Identifying the tilt angle and correcting the orbital angular momentum spectrum dispersion of misaligned light beam. *Scientific Reports*, 7(7873), Aug 2017.

[158] IV Basistiy, V Yu Bazhenov, MS Soskin, and M Vu Vasnetsov. Optics of light beams with screw dislocations. *Optics communications*, 103(5-6):422–428, 1993.

[159] Johannes Courtial and Kevin O'Holleran. Experiments with twisted light. *The European Physical Journal Special Topics*, 145(1):35–47, 2007.

[160] AT O'neil, I MacVicar, L Allen, and MJ Padgett. Intrinsic and extrinsic nature of the orbital angular momentum of a light beam. *Physical review letters*, 88(5):053601, 2002.

[161] SSR Oemrawsingh, ER Eliel, G Nienhuis, and JP Woerdman. Intrinsic orbital angular momentum of paraxial beams with off-axis imprinted vortices. *JOSA A*, 21(11):2089–2096, 2004.

[162] Shiyao Fu, Tonglu Wang, and Chunqing Gao. Perfect optical vortex array with controllable diffraction order and topological charge. *JOSA A*, 33(9):1836–1842, 2016.

[163] Virendra K Jaiswal, Ravindra P Singh, and R Simon. Producing optical vortices through forked holographic grating: study of polarization. *Journal of Modern Optics*, 57(20):2031–2038, 2010.

[164] Ravindra P Singh and Sanjoy Roychowdhury. Optical vortices produced by forked holographic grating and sign of their topological charge. *Indian Journal of Physics*, 80:491–494, 2006.

[165] Sonja Franke-Arnold, Jonathan Leach, Miles J Padgett, Vassilis E Lembessis, Demos Ellinas, Amanda J Wright, John M Girkin, P Öhberg, and Aidan S Arnold. Optical ferris wheel for ultracold atoms. *Optics Express*, 15(14):8619–8625, 2007.

[166] Miles Padgett and Roberto Di Leonardo. Holographic optical tweezers and their relevance to lab on chip devices. *Lab on a Chip*, 11(7):1196–1205, 2011.

[167] Kun Huang, Hong Liu, Sara Restuccia, Muhammad Q Mehmood, Sheng-Tao Mei, Daniel Giovannini, Aaron Danner, Miles J Padgett, Jing-Hua Teng, and Cheng-Wei Qiu. Spiniform phase-encoded metagratings entangling arbitrary rational-order orbital angular momentum. *Light: Science & Applications*, 7(3):17156–17156, 2018.

[168] TD Huang and TH Lu. Controlling an optical vortex array from a vortex phase plate, mode converter, and spatial light modulator. *Optics letters*, 44(16):3917–3920, 2019.

[169] Mahdi Khodadadi Karahroudi, Bahman Parmoon, Mohammadreza Qasemi, Abolhasan Mobashery, and Hossein Saghafifar. Generation of perfect optical vortices using a bessel–gaussian beam diffracted by curved fork grating. *Applied optics*, 56(21):5817–5823, 2017.

[170] Genevieve Gariepy, Jonathan Leach, Kyung Taec Kim, Thomas J Hammond, Eugene Frumker, Robert W Boyd, and Paul B Corkum. Creating high-harmonic beams with controlled orbital angular momentum. *Physical review letters*, 113(15):153901, 2014.

[171] Naoya Matsumoto, Taro Ando, Takashi Inoue, Yoshiyuki Ohtake, Norihiro Fukuchi, and Tsutomu Hara. Generation of high-quality higher-order laguerre-gaussian beams using liquid-crystal-on-silicon spatial light modulators. *JOSA A*, 25(7):1642–1651, 2008.

[172] Alexander Dreischuh, Sotir Chervenkov, Dragomir Neshev, Gerhard G Paulus, and Herbert Walther. Generation of lattice structures of optical vortices. *JOSA B*, 19(3):550–556, 2002.

[173] A Bekshaev, O Orlinska, and M Vasnetsov. Optical vortex generation with a "fork" hologram under conditions of high-angle diffraction. *Optics communications*, 283(10):2006–2016, 2010.

[174] Aleksandr Ya Bekshaev, MS Soskin, and MV Vasnetsov. Transformation of higher-order optical vortices upon focusing by an astigmatic lens. *Optics Communications*, 241(4-6):237–247, 2004.

[175] Haitao Chen, Zenghui Gao, Huajun Yang, Fanhou Wang, and Xiaoping Huang. Propagation of a pair of vortices through a tilted lens. *Optik*, 124(20):4201–4205, 2013.

[176] Y Cai and Sailing He. Propagation of a laguerre–gaussian beam through a slightly misaligned paraxial optical system. *Applied Physics B*, 84(3):493–500, 2006.

[177] Rakesh Kumar Singh, P Senthilkumaran, and Kehar Singh. The effect of astigmatism on the diffraction of a vortex carrying beam with a gaussian background. *Journal of Optics A: Pure and Applied Optics*, 9(5):543, 2007.

[178] Stranger things, 2016. Premiered on Netflix.

[179] Dmitri V Petrov. Vortex–edge dislocation interaction in a linear medium. *Optics communications*, 188(5-6):307–312, 2001.

[180] IV Basistiy, MS Soskin, and MV Vasnetsov. Optical wavefront dislocations and their properties. *Optics Communications*, 119(5-6):604–612, 1995.

[181] Kevin O'holleran, Mark R Dennis, and Miles J Padgett. Topology of light's darkness. *Physical review letters*, 102(14):143902, 2009.

[182] John R Taylor. Error analysis. *University Science Books, Sausalito, California*, 1997.

[183] Florian Flossmann, Ulrich T Schwarz, and Max Maier. Propagation dynamics of optical vortices in laguerre–gaussian beams. *Optics Communications*, 250(4-6):218–230, 2005.

[184] Xinying Zhao, Xiaoyan Pang, Jingcheng Zhang, and Guobin Wan. Transverse focal shift in vortex beams. *IEEE Photonics Journal*, 10(1):1–17, 2018.

[185] Optics: The Website, Diffraction. https://www.opticsthewebsite.com/Circular. Accessed: 2021-05-02.

[186] Timothy Sauer. Numerical analysis pearson addison wesley, 2006.

[187] J Stockhofe, S Middelkamp, PG Kevrekidis, and P Schmelcher. Impact of anisotropy on vortex clusters and their dynamics. *EPL (Europhysics Letters)*, 93(2):20008, 2011.

[188] L Stoyanov, G Maleshkov, M Zhekova, I Stefanov, DN Neshev, GG Paulus, and A Dreischuh. Far-field pattern formation by manipulating the topological charges of square-shaped optical vortex lattices. *JOSA B*, 35(2):402–409, 2018.

[189] L Stoyanov, G Maleshkov, M Zhekova, I Stefanov, GG Paulus, and A Dreischuh. Far-field beam reshaping by manipulating the topological charges of hexagonal optical vortex lattices. *Journal of Optics*, 20(9):095601, 2018.

[190] Avery Elizabeth Hurt. Cheatgrass thrives on the well-lit urban night scene. https://www.sciencenewsforstudents.org/article/cheatgrass-weed-urban-night-light-streetlights, 2021.

[191] Shannon M Murphy, Dhaval K Vyas, Jennifer L Hoffman, Clara S Jenck, Brooke A Washburn, Kelsie E Hunnicutt, Angie Davidson, Jasmine M Andersen, Rachel K Bennet, Amarin Gifford, et al. Streetlights positively affect the presence of an invasive grass species. *Ecology and evolution*, 11(15):10320–10326, 2021.

Appendix A: Theory Details

A.1 LG Decomposition for Oppositely Charged Vortex Pair***

The modal decomposition for the oppositely charged vortex pair can be performed to find the modal content, and subsequently the beam evolution with propagation. The result was obtained using the $z = 0$ field

$$U(x,y) = \frac{\sqrt{2}}{w_0}\sqrt{(x-x_0)^2+y^2}e^{itan^{-1}(y/(x-x_0))}\sqrt{(x+x_0)^2+y^2}e^{-itan^{-1}(y/(x+x_0))} \times \sqrt{\frac{2}{\pi}}\frac{1}{w_0}e^{-\frac{x^2+y^2}{w_0^2}} \quad \text{(A.1)}$$

from Indebetouw [32]. The coefficients of the modal decomposition are determined via

$$C_{\ell,p} = \int_{-\infty}^{-\infty}\int_{-\infty}^{-\inf} U(x,y) \times LG^*_{\ell,p}(x,y)dxdy \quad \text{(A.2)}$$

where $LG^*_{\ell,p}(x,y)$ is the complex conjugate of $LG_{\ell,p}(x,y)$. For example, one can calculate the coefficient for the $LG_{1,0}(x,y)$ mode via

$$C_{1,0} = \int_{-\infty}^{-\infty}\int_{-\infty}^{-\inf} U(x,y) \times LG^*_{1,0}(x,y)dxdy \quad \text{(A.3)}$$

***The modal decomposition was performed by University of Denver PhD student Patrick Ford.

which yields a value of

$$C_{1,0} = \frac{\sqrt{2}x_0}{w_0} \tag{A.4}$$

The final result for the opposite pair field for all ℓ and p is

$$\psi_{opp}(x,y,z) = (1-2d^2)LG_{0,0} + \sqrt{2}dLG_{1,0} - \sqrt{2}dLG_{-1,0} - LG_{0,1} \tag{A.5}$$

where $d = x_0/w_0$.

A.2 Derivation of the 2D Rotation Matrix

To derive the 2D rotation matrix, we start with a vector, $\vec{v}$, that exists in the xy-plane and is rotated by angle α from the x-axis, as shown in Figure A.1. Vector $\vec{v}$ can be described by its vector components where

$$\vec{v} = \begin{bmatrix} x \\ y \end{bmatrix} = \begin{bmatrix} \cos\alpha \\ \sin\alpha \end{bmatrix}. \tag{A.1}$$

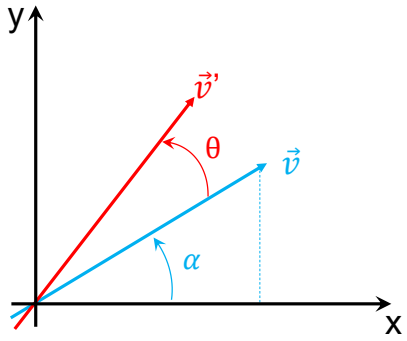

Figure A.1: A vector, $\vec{v}$, is rotated by angle θ to become vector $\vec{v}'$, as described by Equation A.5.

Similarly, $\vec{v}'$ can be expressed in terms of its own vector components such that

$$\vec{v}' = \begin{bmatrix} x' \\ y' \end{bmatrix} = \begin{bmatrix} \cos(\alpha+\theta) \\ \sin(\alpha+\theta) \end{bmatrix}. \tag{A.2}$$

Using the sum and difference formulas from trigonometry, this can be rewritten to

$$\vec{v}' = \begin{bmatrix} \cos\alpha\cos\theta - \sin\alpha\sin\theta \\ \sin\alpha\cos\theta + \cos\alpha\sin\theta \end{bmatrix}. \tag{A.3}$$

Remembering that $\cos\alpha = x$ and $\sin\alpha = y$ from Equation A.1, this can be rewritten into the form

$$\vec{v}' = \begin{bmatrix} \cos\theta & -\sin\theta \\ \sin\theta & \cos\theta \end{bmatrix} \begin{bmatrix} x \\ y \end{bmatrix}, \tag{A.4}$$

where

$$\mathbf{R} = \begin{bmatrix} \cos\theta & -\sin\theta \\ \sin\theta & \cos\theta \end{bmatrix} \tag{A.5}$$

The matrix is defined as the 2D rotation matrix which takes an input vector and rotates it by angle θ.

A.3 Finding the eigenvalues of the $V^2 Matrix$

Recall that the V^2 matrix for the total field is described as $\mathbf{V}^2_{Total} = \mathbf{F}_{total}\mathbf{F}^T_{total}$ which is simplified in Eq. 3.4.12 to

$$\mathbf{V}^2 = \rho_{\text{bg}}^{-2}\,\mathbf{V}^2_{\text{vortex}}. \tag{A.1}$$

This can then be rewritten in terms of $\mathbf{F}_{vortex}$ where $\mathbf{F}_{vortex}$ is given by 3.3.6 such that

$$\mathbf{V}^2 = \rho_{\text{bg}}^{-2}\, \mathbf{F}_{\text{vortex}} \mathbf{F}_{\text{vortex}}^{\text{T}} \tag{A.2}$$

From here, we can simply substitute in the matrix form of $\mathbf{F}_{vortex}$ and carry out the matrix algebra:

$$\mathbf{V}^2 = \rho_{\text{bg}}^{-2} \begin{bmatrix} \text{Cos}\xi & -\text{Sin}\xi\text{Sec}\theta \\ \text{Sin}\xi & \text{Cos}\xi\text{Sec}\theta \end{bmatrix} \begin{bmatrix} \text{Cos}\xi & \text{Sin}\xi \\ -\text{Sin}\xi\text{Sec}\theta & \text{Cos}\xi\text{Sec}\theta \end{bmatrix}. \tag{A.3}$$

$$\mathbf{V}^2 = \rho_{\text{bg}}^{-2} \begin{bmatrix} \text{Cos}^2\xi + \text{Sin}^2\xi\text{Sec}^2\theta & \text{Cos}\xi\text{Sin}\xi - \text{Sin}\xi\text{Cos}\xi\text{Sec}^2\theta \\ \text{Sin}\xi\text{Cos}\xi - \text{Sin}\xi\text{Cos}\xi\text{Sec}^2\theta & \text{Sin}^2\xi + \text{Cos}^2\xi\text{Sec}^2\theta \end{bmatrix} \tag{A.4}$$

Factor:

$$\mathbf{V}^2 = \rho_{\text{bg}}^{-2} \begin{bmatrix} \text{Cos}^2\xi + \text{Sin}^2\xi\text{Sec}^2\theta & \text{Cos}\xi\text{Sin}\xi(1 - \text{Sec}^2\theta) \\ \text{Sin}\xi\text{Cos}\xi(1 - \text{Sec}^2\theta) & \text{Sin}^2\xi + \text{Cos}^2\xi\text{Sec}^2\theta \end{bmatrix} \tag{A.5}$$

Use trig identity to simplify:

$$\mathbf{V}^2 = \rho_{\text{bg}}^{-2} \begin{bmatrix} \text{Cos}^2\xi + \text{Sin}^2\xi\text{Sec}^2\theta & \text{Cos}\xi\text{Sin}\xi\text{Tan}^2\theta \\ \text{Sin}\xi\text{Cos}\xi\text{Tan}^2\theta & \text{Sin}^2\xi + \text{Cos}^2\xi\text{Sec}^2\theta \end{bmatrix} \tag{A.6}$$

Take the determinant:

$$\mathrm{Det}\left[\mathbf{V}_{\mathrm{total}}^2 - \mathbf{I}\lambda\right] = 0 \tag{A.7}$$

$$0 = \left| \begin{bmatrix} \rho_{\mathrm{bg}}^{-2}(\mathrm{Cos}^2\xi + \mathrm{Sin}^2\xi\,\mathrm{Sec}^2\theta) - \lambda & \rho_{\mathrm{bg}}^{-2}\mathrm{Cos}\xi\,\mathrm{Sin}\xi\,\mathrm{Tan}^2\theta \\ \rho_{\mathrm{bg}}^{-2}\mathrm{Sin}\xi\,\mathrm{Cos}\xi\,\mathrm{Tan}^2\theta & \rho_{\mathrm{bg}}^{-2}(\mathrm{Sin}^2\xi + \mathrm{Cos}^2\xi\,\mathrm{Sec}^2\theta) - \lambda \end{bmatrix} \right| \tag{A.8}$$

Carry out the algebra:

$$0 = (\rho_{\mathrm{bg}}^{-2}(\mathrm{Cos}^2\xi + \mathrm{Sin}^2\xi\,\mathrm{Sec}^2\theta) - \lambda)(\rho_{\mathrm{bg}}^{-2}(\mathrm{Cos}^2\xi\,\mathrm{Sec}^2\theta + \mathrm{Sin}^2\xi) - \lambda) - \mathrm{Cos}^2\xi\,\mathrm{Sin}^2\xi\,\mathrm{Tan}^4\theta,$$

$$0 = \rho_{\mathrm{bg}}^{-4}\mathrm{Cos}^4\xi\,\mathrm{Sec}^2\theta + \rho_{\mathrm{bg}}^{-4}\mathrm{Cos}^2\xi\,\mathrm{Sin}^2\xi - \rho_{\mathrm{bg}}^{-2}\lambda\,\mathrm{Cos}^2\xi + \rho_{\mathrm{bg}}^{-4}\mathrm{Sin}^2\xi\,\mathrm{Cos}^2\xi\,\mathrm{Sec}^4\theta +$$
$$\rho_{\mathrm{bg}}^{-4}\mathrm{Sin}^4\xi\,\mathrm{Sec}^2\theta - \rho_{\mathrm{bg}}^{-2}(\lambda\,\mathrm{Sin}^2\xi\,\mathrm{Sec}^2\theta + \lambda\,\mathrm{Cos}^2\xi\,\mathrm{Sec}^2\theta + \lambda\,\mathrm{Sin}^2\xi) + \lambda^2 -$$
$$\rho_{\mathrm{bg}}^{-4}\mathrm{Cos}^2\xi\,\mathrm{Sin}^2\xi\,\mathrm{Tan}^4\theta$$

$$0 = \lambda^2 + \rho_{\mathrm{bg}}^{-4}\mathrm{Cos}^2\xi\,\mathrm{Sin}^2\xi\,(1 + \mathrm{Sec}^4\theta - \mathrm{Tan}^4\theta) + \rho_{\mathrm{bg}}^{-4}\mathrm{Sec}^2\theta(\mathrm{Cos}^4\xi + \mathrm{Sin}^4\xi)\ldots$$
$$\ldots - \lambda\rho_{\mathrm{bg}}^{-2}\left(\mathrm{Cos}^2\xi + \mathrm{Sin}^2\xi + \mathrm{Sin}^2\xi\,\mathrm{Sec}^2\theta + \mathrm{Cos}^2\xi\,\mathrm{Sec}^2\theta\right)$$

Simplify $\left(\mathrm{Cos}^2\xi + \mathrm{Sin}^2\xi + \mathrm{Sin}^2\xi\,\mathrm{Sec}^2\theta + \mathrm{Cos}^2\xi\,\mathrm{Sec}^2\theta\right)$:

$$\left(\mathrm{Cos}^2\xi + \mathrm{Sin}^2\xi + \mathrm{Sin}^2\xi\,\mathrm{Sec}^2\theta + \mathrm{Cos}^2\xi\,\mathrm{Sec}^2\theta\right) = \left(1 + (\mathrm{Sin}^2\xi + \mathrm{Cos}^2\xi)\mathrm{Sec}^2\theta\right),$$
$$= 1 + \mathrm{Sec}^2\theta,$$

Simplify $1+Sec^4\theta-Tan^4\theta$:

$$\begin{aligned}
1+\mathrm{Sec}^4\theta-\mathrm{Tan}^4\theta &= 1+\mathrm{Sec}^4\theta-\mathrm{Sin}^4\theta\mathrm{Sec}^4\theta,\\
&= 1+\mathrm{Sec}^4\theta(1-\mathrm{Sin}^4\theta),\\
&= 1+\mathrm{Sec}^4\theta(1+\mathrm{Sin}^2\theta)(1-\mathrm{Sin}^2\theta),\\
&= 1+\mathrm{Sec}^4\theta(1+\mathrm{Sin}^2\theta)(\mathrm{Cos}^2\theta),\\
&= 1+\mathrm{Sec}^2\theta(1+\mathrm{Sin}^2\theta),\\
&= 1+\mathrm{Sec}^2\theta(1+(1-\mathrm{Cos}^2\theta)),\\
&= 1+\mathrm{Sec}^2\theta(2-\mathrm{Cos}^2\theta),\\
&= 1+2\mathrm{Sec}^2\theta-\mathrm{Sec}^2\theta\mathrm{Cos}^2\theta,\\
&= 2\mathrm{Sec}^2\theta,
\end{aligned}$$

Substitute in:

$$\begin{aligned}
0 &= \lambda^2-\lambda\rho_{\mathrm{bg}}^{-2}(1+\sec^2\theta)+\rho_{\mathrm{bg}}^{-4}\mathrm{Cos}^2\xi\,\mathrm{Sin}^2\xi\,(2\mathrm{Sec}^2\xi)+\rho_{\mathrm{bg}}^{-4}\mathrm{Sec}^2\theta(\mathrm{Cos}^4\xi+\mathrm{Sin}^4\xi)\\
&= \lambda^2-\lambda\rho_{\mathrm{bg}}^{-2}(1+\sec^2\theta)+\rho_{\mathrm{bg}}^{-4}\mathrm{Sec}^2\theta(2\mathrm{Cos}^2\xi\,\mathrm{Sin}^2\xi+\mathrm{Cos}^4\xi+\mathrm{Sin}^4\xi)\\
&= \lambda^2-\lambda\rho_{\mathrm{bg}}^{-2}(1+\sec^2\theta)+\rho_{\mathrm{bg}}^{-4}\mathrm{Sec}^2\theta(\mathrm{Cos}^4\xi+\mathrm{Sin}^2\xi(\mathrm{Sin}^2\xi+2\mathrm{Cos}^2\xi)\\
&= \lambda^2-\lambda\rho_{\mathrm{bg}}^{-2}(1+\sec^2\theta)+\rho_{\mathrm{bg}}^{-4}\mathrm{Sec}^2\theta(\mathrm{Cos}^4\xi+\mathrm{Sin}^2\xi(1+\mathrm{Cos}^2\xi)\\
&= \lambda^2-\lambda\rho_{\mathrm{bg}}^{-2}(1+\sec^2\theta)+\rho_{\mathrm{bg}}^{-4}\mathrm{Sec}^2\theta(\mathrm{Cos}^2\xi(\mathrm{Cos}^2\xi+\sin^2\xi)+\mathrm{Sin}^2\xi)\\
&= \lambda^2-\lambda\rho_{\mathrm{bg}}^{-2}(1+\sec^2\theta)+\rho_{\mathrm{bg}}^{-4}\mathrm{Sec}^2\theta(\mathrm{Cos}^2\xi+\mathrm{Sin}^2\xi)\\
&= \lambda^2-\lambda\rho_{\mathrm{bg}}^{-2}(1+\sec^2\theta)+\rho_{\mathrm{bg}}^{-4}\mathrm{Sec}^2\theta
\end{aligned}$$

The final expression from the eigenvalue problem is

$$(\lambda - \rho_{\text{bg}}^{-2})(\lambda - \rho_{\text{bg}}^{-2}\text{Sec}^2\theta) = 0 \tag{A.9}$$

and the ratio of the eigenvalues, which is independent of ρ_{bg} is given by

$$\frac{\lambda_1}{\lambda_2} = \text{Cos}^2\theta \tag{A.10}$$

allowing a solution for *theta* from the total paraxial field. The eigenvectors are then used to find ξ from the total paraxial field.

A.4 Using Mathematica to Find Vortex Tilt from a Paraxial Field

Below is an example code for measuring the tilt of a single vortex placed within a Gaussian host beam. The process for finding the tilt of a vortex would still be the same for a more complicated input field.

Code Example: Measuring Vortex Tilt.

```
assumptions={Element[x,Reals],Element[y,Reals],Element[z,
    Reals],\[Xi]>0,\[Theta]>0,Element[Sec[\[Theta]],Reals],
    Element[Sec[\[Theta]]^2,Reals]};

x0set=0.5*10^-3; (* input Subscript[x, 0] in meters *)
w0set=1*10^-3;(* input Subscript[w, 0] in meters *)
\[Xi]set=60 Degree; (* input azimuthal angle, \[Xi] *)
\[Theta]set=25 Degree;(* input polar angle, \[Theta] *)
\[Lambda]0set=633*10^-9; (* input laser wavelength *)

(* Expression for a Gaussian containing a tilted vortex *)
\[Psi]field[x_0_,x_,y_,z_,\[Xi]_,\[Theta]_]:=1/(k w0^2+2 I z
    ) k Sqrt[2/\[Pi]] w0^2 E^(-((k (x^2+y^2))/(k w0^2+2 I z))
    ) (Cos[\[Xi]](-x +x0 + I x0 z -I y Cos[\[Theta]]) - y Sin
    [\[Xi]] + I x Cos[\[Theta]] Sin[\[Xi]] + x0(-I +z)Cos[\[
    Theta]]Sin[\[Xi]])/.{w0->w0set,k->(2\[Pi])/\[Lambda]0set
    };

realpart=Simplify[ComplexExpand[Re[\[Psi]field[x0set,x,y,z,
    \[Xi]set,\[Theta]set]]],assumptions];
imaginarypart=Simplify[ComplexExpand[Im[\[Psi]field[x0set,x,
    y,z,\[Xi]set,\[Theta]set]]],assumptions];
```

```
dxreal=FullSimplify[D[realpart,x]]/.{x->x0set,y-> 0,z-> 0}//
    N;
dyreal=FullSimplify[D[realpart,y]]/.{x->x0set,y-> 0,z-> 0}//
    N;

dximag=FullSimplify[D[imaginarypart,x]]/.{x-> x0set,y0,z->
    0}//N;
dyimag=FullSimplify[D[imaginarypart,y]]/.{x-> x0set,y-> 0,z
    -> 0}//N;

grad\[Psi]={{dxreal,dyreal},{dximag,dyimag}};
vsqmatrix=Inverse[grad\[Psi]].Transpose[Inverse[grad\[Psi]
    ]];

evals=Eigenvalues[vsqmatrix];
Print[Style["Calculated \[Theta] from Field Gradients:"]]
ArcCos[Sqrt[evals[[2]]/evals[[1]]]] *180/\[Pi]
evecs=Eigenvectors[vsqmatrix];

Print[Style["Calculated \[Xi] from Field Gradients:"]]
ArcCot[evecs[[2]][[1]]/evecs[[2]][[2]]]*180/\[Pi]
```

A.5 Fourier Transform Method for Analytical Fresnel Integration***

The propagation of optical fields with vortices can be calculated with the Fresnel integral. We analytically implement this calculation with Fourier transforms, following Pritchett and Trubatch [136].

Basic setup for the calculation

We want to solve the following system:

$$\partial_{xx}u + \partial_{yy}u + 2ki\partial_z u = 0, \tag{A.1}$$

which is the paraxial equation for the complex field

$$u(x,y,z=0) = u_{Gauss}(x,y,0)\tilde{u}(x,y), \tag{A.2}$$

***This appendix section was written by University of Denver PhD student Andrew A. Voitiv, originally used as supplemental information for the work in [120].

where $u_{Gauss}(x,y,0)$ represents the complex-valued initial background mode, a Gaussian function for these purposes, which is modulated by the amplitude and phase of one or more vortices described by $\tilde{u}(x,y)$.

The solution to this system is the following Fresnel integral, a convolution of the initial condition with the paraxial Green function:

$$u(x,y,z) = \frac{-ik}{z}\int dx' \int dy' u(x',y',0) e^{\frac{ik}{2z}\left((x-x')^2+(y-y')^2\right)}. \tag{A.3}$$

Non-dimensionalize the paraxial equation using:

$$x \to w_0 x, y \to w_0 y, z \to k w_0^2 z. \tag{A.4}$$

The non-dimensional paraxial equation is then

$$\partial_{xx} u + \partial_{yy} u + 2i\partial_z u = 0 \tag{A.5}$$

and the non-dimensional Fresnel integral is:

$$u(x,y,z) = \frac{-i}{z}\int dx_1 \int dy_1 u(x_1,y_1,0) e^{\frac{i}{2z}\left((x-x_1)^2+(y-y_1)^2\right)}. \tag{A.6}$$

Then the Fresnel integral is

$$u(x,y,z) = \frac{-i}{z}\frac{1}{2\pi}\int dx_1 \int dy_1 \frac{2}{\sqrt{\pi}} e^{-(x_1^2+y_1^2)} \tilde{u}(x_1,y_1) e^{\frac{i}{2z}\left((x-x_1)^2+(y-y_1)^2\right)}. \tag{A.7}$$

We can write this with the x_1 and y_1 terms grouped by integral:

$$u(x,y,z) = \frac{-i}{z}\frac{1}{2\pi}\frac{2}{\sqrt{\pi}}\int dx_1 e^{-x_1^2(1-\frac{i}{2z})}e^{-ix_1\frac{x}{z}}\int dy_1\tilde{u}(x_1,y_1)e^{-y_1^2(1-\frac{i}{2z})}e^{-iy_1\frac{y}{z}}. \tag{A.8}$$

Now define the following:

$$\alpha = 1-\frac{i}{2z}, \beta_x = \frac{-x}{z}, \beta_y = \frac{-y}{z}. \tag{A.9}$$

Then the non-dimensional Fresnel integral is

$$u(x,y,z) = \frac{-i}{\pi^{3/2}}e^{\frac{i}{2z}(x^2+y^2)}\int dx_1 e^{-\alpha x_1^2}e^{i\beta_x x_1}\int dy_1\tilde{u}(x_1,y_1)e^{-\alpha y_1^2}e^{i\beta_y y_1}, \tag{A.10}$$

which is in the form of a two-dimensional Fourier transform. Define the Fourier transform as follows:

$$F_q(\beta_q,q) = \frac{1}{\sqrt{2\pi}}\int dq f_q(q)e^{i\beta_q q}, \tag{A.11}$$

where q represents x or y, and define the following kernel functions:

$$f_x(x_1) = \tilde{u}(x_1,y_1)e^{-\alpha x_1^2} \tag{A.12}$$

$$f_y(y_1) = e^{-\alpha y_1^2}F_x(\beta_x;x_1). \tag{A.13}$$

With this, the Fresnel integral becomes

$$u(x,y,z) = \frac{-i}{z}2\sqrt{\pi}e^{i\frac{x^2+y^2}{2z}}F_y(\beta_x;\beta_y) \tag{A.14}$$

Parameters listed after semicolons serve as reminders of functional dependence.

Implementation for single titled vortex on the shoulder of a Gaussian beam

We take the initial field

$$\tilde{u}(x,y) = ((x-x_0)+i(y-y_0)\cos\theta)\cos\xi + ((y-y_0)-i(x-x_0)\cos\theta)\sin\xi, \tag{A.15}$$

to be a single vortex that may be tilted at any initial angles ξ and θ and which may be shifted along the x- or y-axes by x_0 and y_0, respectively. For this demonstration, we set: $y_0 = 0$.

To reach the desired field, we begin by inserting Equation A.15 into Equation A.12 and then using Equation A.11:

$$F_x(\beta_x) = \frac{1}{\sqrt{2\pi}} \int dx f_x(x_1) e^{i\beta_x x}. \tag{A.16}$$

The result of this Fourier transform is used to construct the next (using Equation A.13):

$$F_y(\beta_y) = \frac{1}{\sqrt{2\pi}} \int dy f_y(y_1) e^{i\beta_y y}. \tag{A.17}$$

The final Fresnel-integrated field is thus evaluated by finding (Equation A.14):

$$u(x,y,z) = \frac{-i}{z} 2\sqrt{\pi} e^{i\frac{x^2+y^2}{2z}} F_y(\beta_y), \tag{A.18}$$

with result:

$$u(x,y,z) = \sqrt{\frac{2}{\pi}} e^{\frac{i\left(x^2+y^2\right)}{2(z-i)}} \times \frac{(\cos\xi(-x+ix_0z+x_0-iy\cos\theta)+\sin\xi(-y+\cos\theta(x_0z+i(x-x_0))))}{(z-i)^2} \tag{A.19}$$

Implementation for a vortex pair on a Gaussian

We take our vortex pair to consist of opposite unit charge vortices with linear amplitude cores, $(x+iy)$ and $(x-iy)$, which are neither initially tilted but are each shifted from the origin by $\pm x_0$:

$$\tilde{u}(x,y) = ((x+x_0)-iy)\times((x-x_0)+iy). \tag{A.20}$$

The order of calculations follows directly the order used in the previous implementation for the single-vortex case, for the new expression of $\tilde{u}(x,y)$. The final Fresnel-integrated result is:

$$u(x,y,z) = \sqrt{\frac{2}{\pi}} e^{\frac{i\left(x^2+y^2\right)}{2(z-i)}} \frac{\left(x^2+x_0^2(z-i)^2-2x_0y(z-i)+y^2-2z(z-i)\right)}{(1+iz)^3} \tag{A.21}$$

Appendix B: Additional Experimental Details

B.1 Epson 83H as a Spatial Light Modulator

The Epson 83H Projector LCD Panel is used as a spatial light modulator. The panel resolution is 1024×768 with a pixel pitch of 12.4 μm. Typically, we used the “red" LCD panel for our experiments.

A Few Tips when Using a Projector

Before rewiring the projector and removing the panel, it is beneficial to navigate through the menus, shown in Figure B.1, and ensure that the the Auto Keystone is set to “Off" and that the Keystone is set to “0". If this is not the case, the SLM will automatically distort the light coming from the panel and all beams will be oblong. If the projector is rewired already, it is still possible to scan through the menus; an imaging system can be used to magnify and image laser light passing through the SLM to navigate through the menus. This may not be the same for a other projectors, but classroom projectors in general have a Keystone feature. I recommend looking at the user manuals for any projector you may use to ensure that this is disabled.

When taking out the lamp, you can use a small flat head screwdriver between the metal brace of the panel and the glass cube. It may come off easily, but be careful because the glass can chip. Best to wear safety glasses to protect your eyes in the

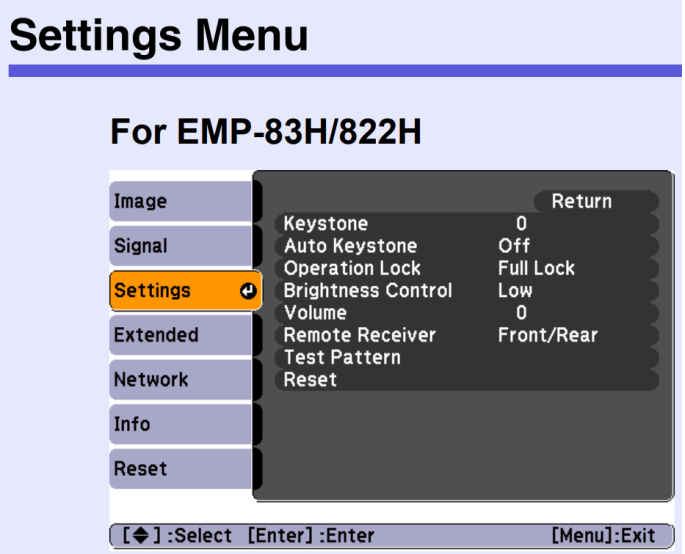

Figure B.1: Menu for navigating to Keystone options: Keystone should be set to “0" and Auto Keystone should be “Off".

process. For some projectors, the panel will not easily come off of the glass cube in which case you may be tempted to use a heat gun to soften the epoxy and more easily take off the panel. However, it is very important to minimize any heating of the cube and panel because excessive heat can damage or warp the panel which can result in poor mode quality or potential lensing effects.

It is easy to use a VGA splitter to set up the second monitor, and be able to see the dislay that is projected onto the SLM. However, because the resolution is so critical, I found it important to plug in the SLM first, and then the second monitor. This way, the computer recognizes the SLM first, rather than the monitor and the display will then match the Epson Projector’s recommended resolution (1024x768) rather than what the recommended resolution is of the monitor, which can vary from monitor to monitor. A simple way to check this is to go into Microsoft’s Settings $\rightarrow$ System $\rightarrow$ Display $\rightarrow$ Advanced Display Settings. Choosing the display that matches the SLM, the display should read, “Epson 83H Projector".

B.2 Experimental Alignment Suggestions

There are a few notable choices made in the experimental setup that help alleviate the need for realignment of the entire experiment each time along the way. First, I used lens mounts that allow the lenses to easily screw in and out. This makes re-aligning along a line of holes (using the same set of irises that are fixed in their position) through an imaging system or telescope much quicker and prevents the need for realignment of the lens mount each time. Second, the lenses in my experiments are always placed such that the planar side of the lens faces the threads of the screw mount. This makes it easy to always orient the lenses in telescopes and imaging systems such that there are the fewest chances for introducing aberrations. Additionally, it is simplest to check the stability of all mounts before using them to ensure they are not easily moved. While the colinear phase-shifting holography is more robust against vibrations, it remains highly beneficial to minimize vibrations and fluctuations in the beam, especially when we look at vortex trajectories.

Because the vortices themselves are very dark, dust and mirror scratches can cause significant distortions in the vortex location. Using the smallest number of optics helps reduce the number of places where dust can collect along the way. Placing the experiment inside of a box and building extra walls along the optical path helps mitigate this and also prevents excess scatter from reaching the camera which can also affect the vortex measurement.

B.1.1 Telescope and Shear Interferometer

Because it is important to not introduce any ellipticity into the beam prior to the SLM, the telescope alignment is very important. First, align beam along a line of

holes with the irises spaced as far apart as possible. Ideally one right after the mirror directing the beam down the table, and the other at the opposite end of the table. Place the first lens in a mount and the second lens on a translation stage with motion along the propagation direction such that they are approximately $f_1 + f_2$ apart from each other when the stage for the second lens is in the middle of its translational motion. Precisely align the first lens such that the back reflection goes directly along the incoming beam and the transmitted beam is centered on the second iris. If the second iris is too far away such that the beam is no longer visible, a third iris can be used at a closer distance for centering the beam.

After that, I take the first lens out for aligning the second lens. Repeat the same process, using back reflection and the second iris, on the second lens. After both lenses are aligned individually, put both lenses in and check that the transmitted beam is very well centered on the second iris and check that the ellipticity of the beam is low using the DataRay software. If either of these are not well aligned, this process must be repeated. An iris or pinhole can be placed at the focal plane and adjusted to spatially filter the beam and improve the mode quality. Once this alignment is completed once, the lenses can be easily unscrewed and the beam aligned along the line of holes as needed since the laser can output can drift over time.

A set of mirrors then redirects the beam along a line of holes where the SLM will be placed. A shear interferometer is placed (temporarily) just before the location of the SLM panel such that it is perpendicular to the laser propagation direction. By checking that fringes are parallel to the marked line on the shear plate, it is easy to see if the beam is collimated or not. If they are not parallel to the marked line as in B.2 (a), move the micrometer on the translation stage of the second lens in

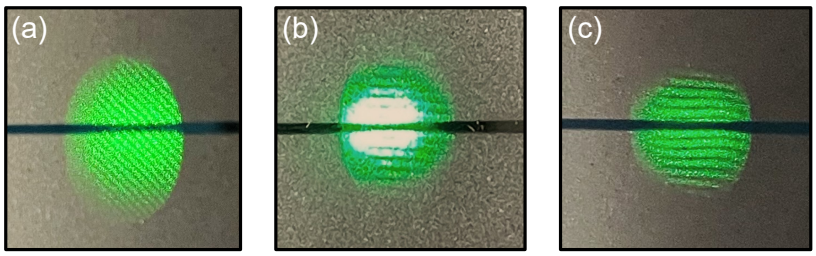

Figure B.2: Shear interferometer when (a) not at the waist, (b) at the waist and (c) close to the waist, but the incident beam is not of the highest quality.

the telescope until they are, as in Fig. B.2 (b). If the interference fringes are not perfectly straight, shown in (c) of the figure, it can be an indicator of higher order mode content within the beam [142] and the need for adjustment of the aperture or lenses.

Once each of these checkpoints are fully satisfied, then the next step is to align the SLM.

B.3 Data Ray Software and Aligning the to the Translation Stage

For taking data, alignment procedures and day to day troubleshooting, the Data Ray software proved to be incredibly useful. The software for the Data Ray cameras can be found online at: https://dataray.com/blogs/software/downloads. In particular, the beam wander feature was used as the iris for aligning the beam to the translation stage. When the translation stage is at its zero value, the beam wander feature collects data regarding the drift of the beam at that location. As the stage is moved, the beam wander feature will track the displacement of the beam from the initial location. When the beam is located at the center for both ends of the translation stage, the beam is aligned to the stage. This also can be used to quantify the maximum drift introduced by the stage. For the case of the Newport stage used in

the single vortex measurements, it was possible to align the beam to the stage such that the largest deviation across the length of the stage was < 30 μm, as shown in Figure B.3.

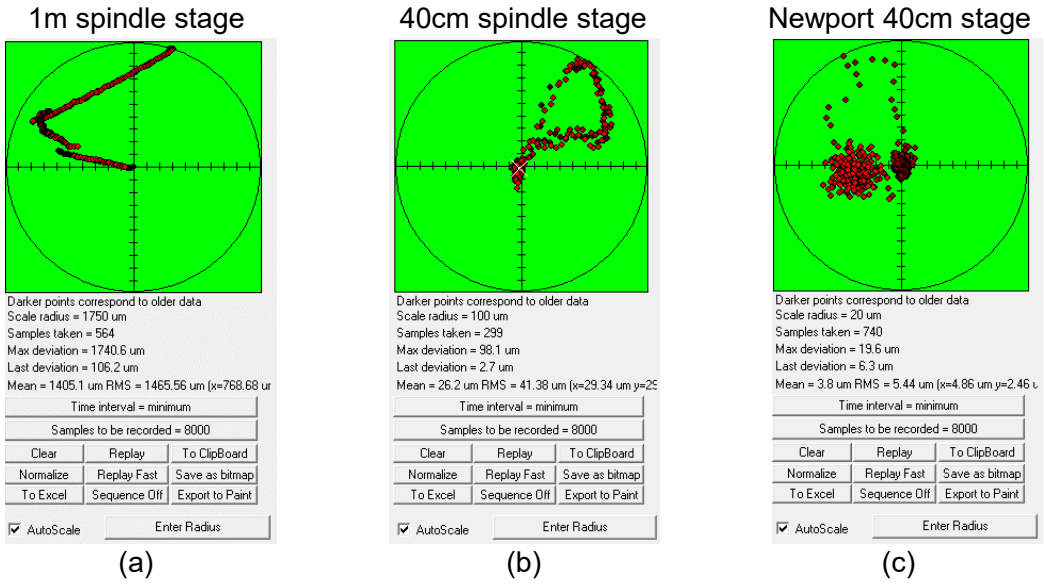

Figure B.3: A comparison of beam wander for three stages is shown. The center point of the beam wander is where the beam is located at both the front and back of the stage, and the motion away from the center is due to beam drift along the stage. The maximum deviations are (a) ≈ 1750 μm for the 1 m Ball Screw Linear CNC Slide Stroke 1000mm Long Stage Actuator Stepper Motor translation stage used in the two vortex experiments, and (b) ≈ 100 μm for another spindle stage not used in the experiments, but shown for comparison with (c), and (c) ≈ 20 μm for the Newport IMS500 translation stage used in the single vortex measurements.

B.4 Checking Camera Orientation

In order to accurately measure vortex dynamics in the *xy*-plane, it is important that the camera be aligned with the *xy*-axis of the SLM. For example, in the single linear core vortex case, we anticpate that a vortex displaced to the right of the beam will have a purely upward (y directional) velocity. If there is a mismatch between

the orientation of the camera and the SLM, the velocity may read the correct magnitude, but the measured components will not be correct. It is much easier to rotate the camera than it is to do a coordinate transformation in data processing, so a vortex lattice is used to check the relative alignment between the camera and SLM. This calibration is done at the imaging plane of the imaging system containing L_3 and L_4 in Figure 6.1.

As shown in Figure B.4, a hologram containing a vortex lattice is projected onto the SLM and measured by the CCD where the crosshairs in the Data Ray program are set to 0°. Using the locations of a vortex row and column, the rotation stage that the camera is mounted on can be adjusted until the xy-planes of both the SLM and CCD are aligned.

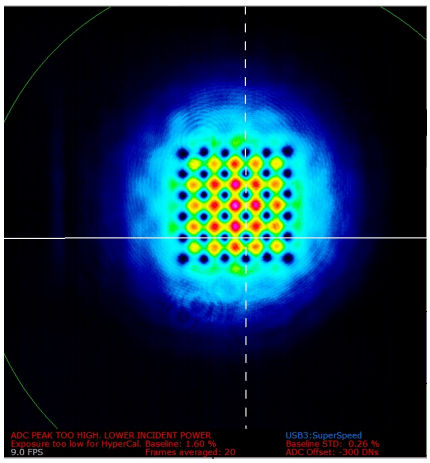

Figure B.4: When the crosshairs perfectly intersect a row and column of vortices in the lattice, the CCD is at the correct rotation with respect to the SLM. The vortex lattice is created using the code from Section C.1.2 with $N_x = 6$ and $N_y = 6$ and $c_r << w_0$. Using the smallest cores possible makes the alignment the most precise.

Appendix C: Experimental Programs

C.1 Experimental LabVIEW Program

A master program was written in LabVIEW to simultaneously control the SLM panel display, camera and translation stage, automating the data taking process. For a given set of data to be taken, the user uploads the desired set of holograms to the program and specifies the desired parameters for the data set. When run, the program cycles through each of the holograms in the set, saving an image on the CCD for each hologram, and then moves the translation stage to the next z location where the same process is then repeated.

The front panel of the program included several input parameters including the folder path containing the gratings that will be used for the specific data set, and the exported file path for the data. Other input parameters include the number of grating sets, propagation step size, total propagation distance, and any additional distances to account for if the camera is not at the imaging plane to begin with. Additionally, the exposure time can be adjusted within the program and the parameters including the size of the aperture at the focal plane are entered. Each of these parameters are recorded in a notes folder located in the same folder that the data are saved to. An image of the front panel is shown in Fig. C.1.

The image files are stored in the folder specified by the user and the designed file format of the images is such that each file is labeled first by the current z location of

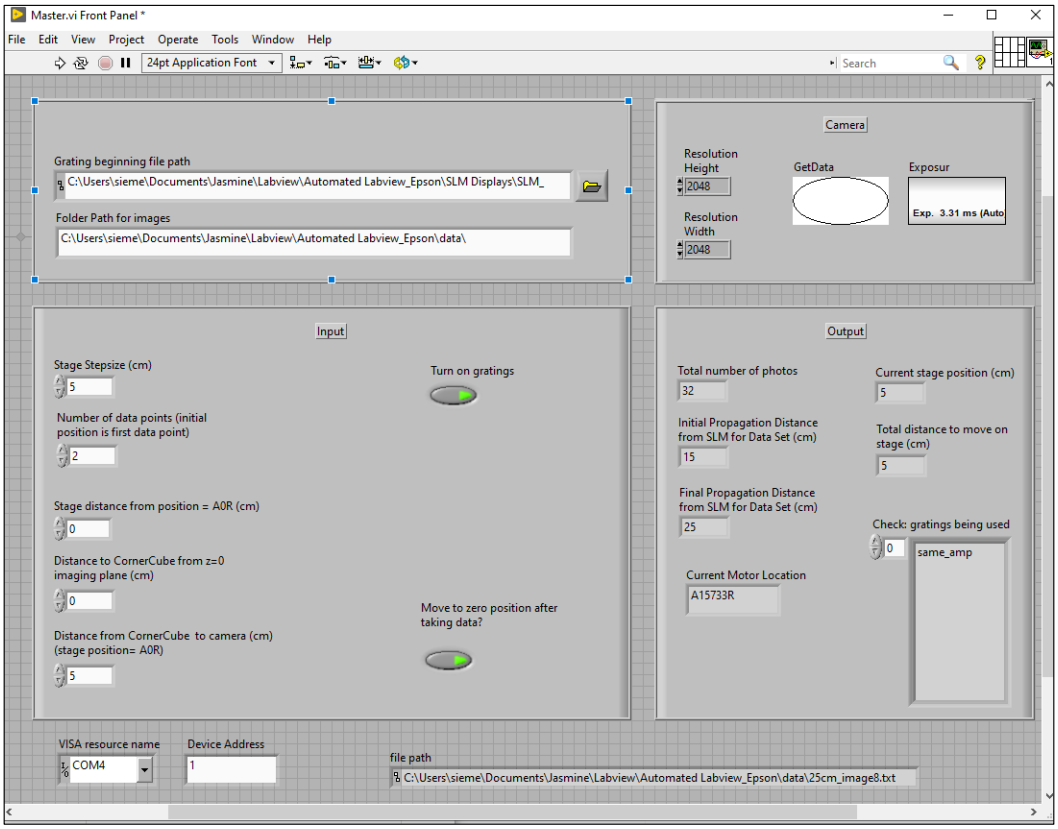

Figure C.1: A user can specify the necessary parameters for taking a data set from the front panel. The top left shows the folders storing the VIs that display the holograms as described later in Figure C.2 and the folder path that will be used to store the data taken. The top right shows the resolution and exposure time of the camera, which can be adjusted. In the bottom left, there are input parameters to determine the z step size, number of data points to take as well as other relevant distances that may need to be taken into account if the physical set up is changed. The bottom right displays updates with the current data set information as data is being taken.

the stage in centimeters, followed by the image number. As an example, for a data set with 3 gratings displayed at each z-step and data taken at $z = 0$ cm, and $z = 10$ cm the set of images would be where the image number corresponds the grating number as they are displayed for data taking. This file format was used for ease in data processing. The benefits of the format are that it is easy to directly read out

D:\\000cm_image01.txt
D:\\000cm_image02.txt
D:\\000cm_image03.txt
D:\\010cm_image01.txt
D:\\010cm_image02.txt
D:\\010cm_image03.txt

the z positions from the file names, and it ensures the order of the files stayed in the order that the data was taken.

To display the holograms, the master program initializes a SubVI, shown in Figure C.2, that displays the hologram on the SLM.[1] A unique SubVI is made for each grating that is to be used, and stored in a folder that is specified by the user in the master program “Grating beginning file path" input. In the figure, an example

[1] Here, I’d like to acknowledge William G. Holtzmann for writing the SubVI and working through the details of getting it to display correctly on the SLM.

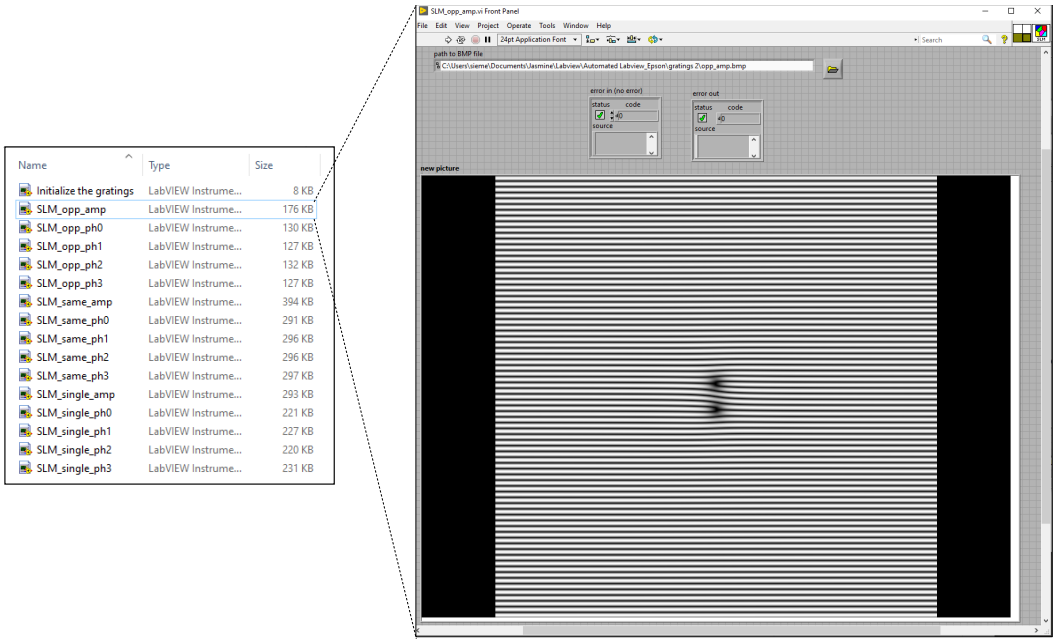

Figure C.2: Left: Example set of SubVIs used to display a set of holograms. Right: SubVI front panel used to display a hologram.

of a set of SubVIs and the front panel of the highlighted SubVI is shown. When the SubVI is initialized, the window containing the grating goes to full screen, and the hologram is correctly displayed on the SLM.

The order of the holograms is determined by the user in the block diagram. Figure C.3 shows the relevant section of the block diagram where a user can specify the file names for the SubVIs. The user should take note of the order so that during data processing, the correct files are used to reconstruct the amplitude and phase of the complex field according to Equation 5.1.5.

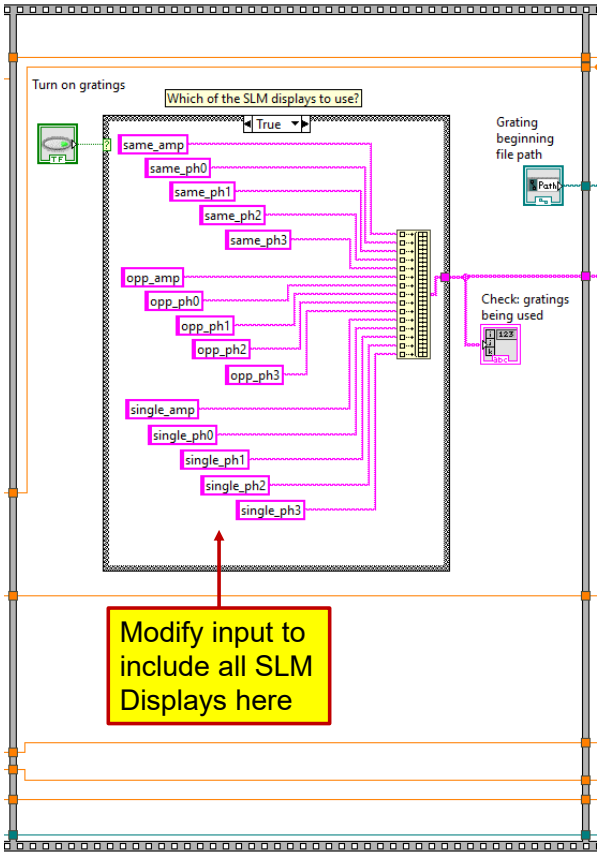

Figure C.3: The file names in Figure C.2 are used to specify which SubVIs will be used for the given data set. These can be modified as needed by the user for a given set of holograms.

Further improvements can be made to increase the efficiency and user friendliness of the code, but the program is fairly straightforward to use and can be adapted to any stage or CCD. The holograms used in the SubVI's are created in Mathematica as described in the next section.

C.2 Hologram Generating Mathematica Code

When using the automated LabVIEW program, applying an additional amplitude mask such that the grating region was a square of dimensions 768×768 and the remaining pixels were black (zero valued) resulted in the cleanest data. Example holograms are shown in Figure C.4, which are each generated as described in Chapters 4 and 5, with code for both a linear core vortex pair and a hyperbolic tangent core shared below.

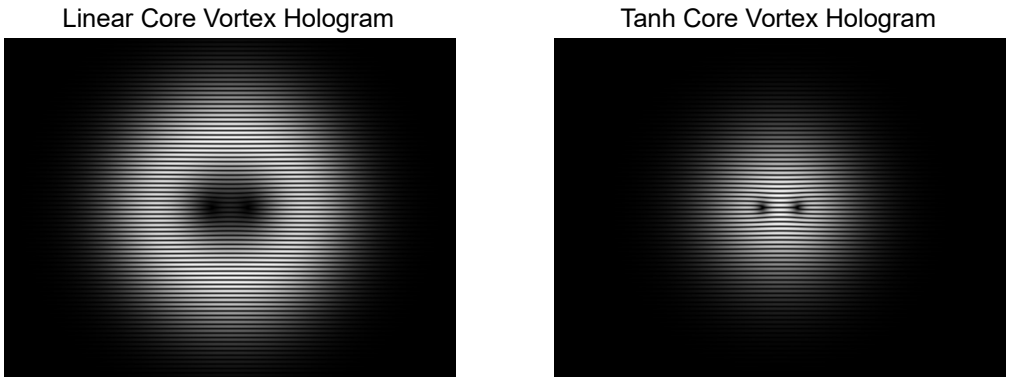

Figure C.4: A linear core vortex pair hologram (left) and a hyperbolic tangent core vortex pair hologram (right) are shown generated from the code in Sections C.1.1 and C.1.2, respectively. The parameters used in generating the holograms are as displayed in the code.

C.1.1 Linear Core Vortex Holograms

For linear core vortex gratings, the field amplitude goes as r. Code to generate an equally spaced vortex lattice is shown below. Input parameters are displayed first, followed by code describing the field amplitude and phase used to generate the hologram. Both the amplitude hologram and all four phase reconstructing holograms are generated from the code.

Code Example: Linear core vortex lattice holograms.

```
num = 10;(* number of pixels per grating period *)
set = 1; (* set number of gratings *)
w0set = 2*10^-3; (* beam waist for mode in hologram *)
Nxset = 2; (* Number of Vortices in the x direction*)
Nyset = 1;(* Number of Vortices in the y direction*)
vsset = 1*10^-3; (* vortex separation in m *)
alpha = 0 Degree; (* angle of grating lines *)

(********* Create File Directory to Export Gratings To
   **********)
which = "opp";
whichfile = "\\opp";
filepath =
  "D:\\Dissertation\\Epson Gratings\\" <> ToString[num] <>
   " pix grating constant\\Linear Core\\" <> ToString[Nxset]
    <> "x" <>
    ToString[Nyset] <> " with input w0 " <> ToString[w0set
   *10^3] <>
   "mm\\set" <> ToString[set] <> "_" <> which <> "_vs " <>
   ToString[vsset*10^3] <> " mm Linear\\";
CreateDirectory[filepath]
filepathinfo = CreateDirectory[filepath <> "\\info"];
filepathdata = CreateDirectory[filepath <> "\\data"];

(******** INPUT Experimental Parameters and Definitions
   *******)
\[Lambda0=532*^-9; (* wavelength *)
w0=w0set; (* waist size of Background Gaussian *)
pixpitch=12.4*10^-6; (* pixel pitch for SLM *)
k=(2\[Pi])/(num*pixpitch); (* Determine grating constant *)
Ny=Nxset; (* Number of Vortices in the x direction*)
Nx=Nyset;(* Number of Vortices in the y direction*)
vs=vsset; (* vortex separation in m *)
ref=0.05; (* reference beam power *)
sig=0.95; (* signal beam power *)
sign=4;
(* Choose,
sign = 1 for all negative charges,
sign = 2 for all positive,
sign = 3 for random charges,
sign = 4 for alternating *)
```

```
(******** Set up Gridspace Parameters for Gratings ********
    *)
xres=768; (* x resolution to match SLM *)
yres=1024; (* y resolution to match SLM *)
xpanelsize=pixpitch*xres;(* use pixel pitch and resolution
    to define panel size *)
ypanelsize=pixpitch*yres;(* use pixel pitch and resolution
    to define panel size *)
xStep = pixpitch;(* set stepsize to match pixel size *)
yStep=pixpitch;(* set stepsize to match pixel size *)

(******** Set up vortex lattice location matrix *********)
xbound=(Nx-1)/2;
ybound=(Ny-1)/2;
x0matrix=Table[x,{x,-xbound*vs,xbound*vs,vs},{y,- ybound*vs,
    ybound*vs,vs}];
y0matrix=Table[y,{x,-xbound*vs,xbound*vs,vs},{y,- ybound*vs,
     ybound*vs,vs}];

(******** Set up vortex lattice charge matrix *********)
If[sign==1,
qmatrix=Table[-1,{x,-xbound*vs,xbound*vs,vs},{y,- ybound*vs,
     ybound*vs,vs}];,];
If[sign==2,
qmatrix=Table[1,{x,-xbound*vs,xbound*vs,vs},{y,-ybound*vs,
    ybound*vs,vs}];,];
If[sign== 3
qmatrix=Table[2 RandomInteger[]-1,{x,-xbound*vs,xbound*vs,vs
    },{y,-ybound*vs, ybound*vs,vs}];,];
If[sign==4 && Nx==Ny,
qmatrix=Table[(-1)^(x/vs) (-1)^(y/vs),{x,-xbound*vs,xbound*
    vs,vs},{y,-ybound*vs, ybound*vs,vs}];,];
If[sign==4 && Nx!= Ny,
qmatrix=Table[Im[(-1)^(x/vs) (-1)^(y/vs)],{x,-xbound*vs,
    xbound*vs,vs},{y,-ybound*vs, ybound*vs,vs}];,];


(********** Create Vortex Field **************)
\[Psi]vortex[x_,y_,x0_,y0_,q_]:=Sqrt[2]/w0 ((x-x0)+q I (y-y0
    ));(* linear core vortex wavefunction *)
\[Psi]vortexlattice=Product[\[Psi]vortex[x,y,x0matrix[[nx,ny
    ]],y0matrix[[nx,ny]],qmatrix[[nx,ny]]],{nx,1,Dimensions[
    x0matrix][[1]]},{ny,1,Dimensions[y0matrix][[2]]}];

(********** Create Gaussian Amplitude **************)
gaussian=Sqrt[2/\[Pi]] E^(-((x^2+y^2)/w0^2));

(********** Create Full Field **************)
\[Psi]field= gaussian*Abs[\[Psi]vortexlattice]*E^(I Arg[\[
    Psi]vortexlattice]);

(********** Create Planewave **************)
planewave=E^(I k(Cos[alpha]x +Sin[alpha]y));

(******** Create Amplitude Mask **********)
\[Psi]abs=Table[Abs[\[Psi]field],{x,-(xpanelsize/2)+xStep/2,
    xpanelsize/2-xStep/2,xStep},{y,-(ypanelsize/2)+yStep/2,
    ypanelsize/2-yStep/2,yStep}];
tab=Table[1,{i,1,1024},{j,1,768}];
```

```
LabVIEWmask=Table[If[y>128 &&y<897,tab[[x,y-128]],0],{x
    ,1,768},{y,1,1024}];

AmplitudeMask=\[Psi]abs/Max[\[Psi]abs](*LabVIEWmask*);

(******* Set up Amplitude Measurement Diffraction grating
    *******)
Ixy=(.5planewave+.5 E^(I Arg[\[Psi]field])); (* Planewave +
    vortex field phase*)
IxyAmp=Abs[Ixy]; (* Need to take Absolute Value*)

DiscreteGratingAmp=AmplitudeMask*Table[IxyAmp,{x,-(
    xpanelsize/2)+xStep/2,xpanelsize/2-xStep/2,xStep},{y,-(
    ypanelsize/2)+yStep/2,ypanelsize/2-yStep/2,yStep}];(*
    Apply Amplitude Mask to grating *)
expamp=Chop[DiscreteGratingAmp,10^-200];
(* Export Amplitude Grating*)
Export[filepath<> whichfile<>"_amp.bmp",Image[expamp]];

(********* Create Amplitude Mask for Gratings for PSDH
    ***********)
interferogramamplitude={};
For[phase=0,phase<= 3, phase+= 1,

(********** Create Gaussian Reference **************)
gaussianREF=gaussian E^(I \[CapitalDelta]\[Phi])/.{\[
    CapitalDelta]\[Phi]->phase*\[Pi]/2};

(********** Superimpose with Vortex Field **************)
interferogram=(sig*\[Psi]field+ref*gaussianREF);
interferogramamp=Table[Abs[interferogram],{x,-(xpanelsize/2)
    +xStep/2,xpanelsize/2-xStep/2,xStep},{y,-(ypanelsize/2)+
    yStep/2,ypanelsize/2-yStep2,yStep}];
AppendTo[interferogramamplitude,interferogramamp];
];
interferogrammasks=interferogramamplitude/Max[
    interferogramamplitude];

(*********** Create Phase Step Gratings for PSDH
    *************)
phasegratings={};
For[phase=0,phase<= 3, phase+= 1,
(* Create Gaussian Reference *)
gaussianREF=gaussian E^(I \[CapitalDelta]\[Phi])/.{\[
    CapitalDelta]\[Phi]->phase*\[Pi]/2};
(* Superimpose Reference Mode with Vortex Field *)
interferogram=(sig*\[Psi]field+ref*gaussianREF);
(* Interferogram Phase + PlaneWave *)
interferogramplusPW=Abs[(0.5planewave+0.5E^(I Arg[
    interferogram] ))];
interferogramgrating=interferogrammasks[[phase+1]]*Table[Abs
    [interferogramplusPW],{x,-(xpanelsize/2)+xStep/2,
    xpanelsize/2-xStep/2,xStep},{y,-(ypanelsize/2)+yStep/2,
    ypanelsize/2-yStep/2,yStep}];
AppendTo[phasegratings,interferogramgrating];
];

For[i=0,i<=3,i+=1,
(* Export Phase Gratings *)
```

```
Export[filepath<>whichfile<>"_ph"<>ToString[i]<>".bmp",Image
    [phasegratings[[i+1]]]];
]
```

C.1.2 Tanh Core Vortex Holograms

The following code shows a subset of the code from the previous section where modifications were made to create a hyperbolic tangent core vortex lattice rather of a linear core vortex lattice. The variables with new definitions as compared to the previous section are highlighted in red.

Code Example: Hyperbolic tangent core vortex lattice holograms .

```
num = 10;
set = 1;
w0set = 2*10^-3;
Nxset = 2; (* Number of Vortices in the x direction*)
Nyset = 1;(* Number of Vortices in the y direction*)
vsset = 1*10^-3; (* vortex separation in m *)
crset = 0.25*10^-3;(* vortex core size in m *)
alpha = 0 Degree;
.
.
.
filepath =
  "D:\\Dissertation\\Epson Gratings\\" <> ToString[num] <>
   " pix grating constant\\Tanh Core\\" <> ToString[Nxset]
   <> "x" <>
   ToString[Nyset] <> " with input w0 " <> ToString[w0set
   *10^3] <>
   "mm\\set" <> ToString[set] <> "_" <> which <> "_vs " <>
   ToString[vsset*10^3] <> " mm_cr " <> ToString[crset*10^3]
    <> "\\";
.
.
.
(********** Create Vortex Field **************)
\[Psi]vortex[x_, y_, x0_, y0_, q_, cr_] := Tanh[Sqrt[(x - x0
    )^2 + (y - y0)^2]/ cr] E^(I q ArcTan[(x - x0), (y - y0)
   ]);
\[Psi]vortexlattice =
  Product[\[Psi]vortex[x, y, x0matrix[[nx, ny]], y0matrix[[
   nx, ny]], qmatrix[[nx, ny]], crset], {nx, 1,
    Dimensions[x0matrix][[1]]}, {ny, 1, Dimensions[y0matrix
   ][[2]]}];
.
.
.
```

C.3 Data Processing Mathematica Code

All of the data processing for the experiments of this dissertation was done with Mathematica. In the next few sections, I will highlight the main processes used for data processing and provide supplemental code. For each of the example codes throughout the section, there were three different fields from three different sets of holograms recorded: (i) a same charge vortex pair, (ii) an oppositely charged vortex pair, and (iii) the single vortex (LG) mode, in that order (as determined by the order of holograms in Figure C.3).

C.1.1 Initial Crop of the Data

The first step of data processing after the images are taken is to do an initial crop around the beam. The full CCD window is not typically needed, and a lot of time can be saved in processing if the fields are cropped. To determine the window of the initial crop, I used MatrixPlot to quickly check that the beam at $z = 0$, the beam at the final z value of the set and the beam halfway in between are all fully in the cropped window. Once this is confirmed, to save both time and storage space on the computer, the cropped data text file overwrites the initial data text file in the same folder. The notebook is saved into the same file folder as the data, and sample code for this is as follows:

Code Example: Initial crop of data.

```
(* Import file names *)
files = FileNames["*.txt", NotebookDirectory[]];

Monitor[For[k = 1, k <= Length[files], k += 1,
   x1 = 300;
   x2 = 1200;
   x3 = 300;
   x4 = 1200;
```

```
    (* the initial crop of the vortex data- exported file
    replaces file in same folder*)
    Filename = files[[k]];
    data = Import[Filename, "CSV"][[x1 ;; x2, x3 ;; x4]];
    Export[files[[k]], data, "CSV"];
    ];
  , k]
```

C.1.2 Phase-shifting Digital Holography Processing

Once the data is cropped, we can use all 5 images from each set of gratings to construct the full complex field from each set according to Equation 5.1.5.

Code Example: Calculating the complex field via phase-shifting digital holography.

```
files = FileNames["*.txt", NotebookDirectory[]];

filepathsint = Table[Table[StringDrop[files[[i]], -4], {i,
   1, Length[files]}][[j]], {j, 1, Length[files], 5}];

filepathsph = Table[Table[StringDrop[files[[i]], -4], {i, 1,
    Length[files]}][[
    j]], {j, 2, Length[files], 5}];

croppeddata = {};
vortexlocations = {};
fields = {};

zvals = ToExpression[Table[Table[StringDrop[StringDrop[files
   [[i]], -14], StringLength[NotebookDirectory[]]], {i, 1,
   Length[files]}][[j]], {j, 1, Length[files], 5}]];

fieldvalue = Flatten[Table[Table[i, {i, 1, 3}], {j, 1,
   Length[zvals]}]];


For[k = 1, k <= Length[files]/5, k += 1,
fieldspath = StringDrop[files[[5*k]], -14] <> "field" <>
   ToString[fieldvalue[[k]]] <> ".mat";

image2data = Import[StringJoin[files[[5*k - 4]]], "CSV"];

phase0data = Import[StringJoin[files[[5*k - 3]]], "CSV"];
phasepi2data = Import[StringJoin[files[[5*k - 2]]], "CSV"];
phasepidata = Import[StringJoin[files[[5*k - 1]]], "CSV"];
phase3pi2data = Import[StringJoin[files[[5*k - 0]]], "CSV"];

intensitydatasin = image2data;
phasedatasin = -ArcTan[(phase0data - phasepidata),(
   phase3pi2data - phasepi2data)];
```

```
beamsin = (Sqrt[Abs[intensitydatasin]]*Exp[I *phasedatasin])
    // N;

Export[fieldspath, beamsin];
]
```

Using the ArcTan Function

It is important to note the syntax of the ArcTan function in Mathematica (and also in any other language as well). In Mathematica, the argument of the ArcTan function takes the denominator first, and the numerator second. If the order is reversed, the sign of the charges will be opposite than expected, and the comparison between theory and experiment for the hydrodynamic models will be inconsistent.

C.1.3 Drift Calibration Code

After the complex field data is saved for each z-step, the next step is to crop the data according to the drift calibration methods of Section 6.3. This ensures accurate trajectory measurements that are not dependent on motion of the entire beam. The Mathematica code to do so is written such that the real and imaginary zeros intersection at the center of the $LG_{\ell=1,p=0}$ mode for each z-step are located and used as the center point of the cropping window. Since it is experimental data, there are often many vortices near and outside the beam edges. In order to locate the correct vortex, the location of the $z = 0$ vortex is approximated by the user in looking at the plotted data and used as the initial guess. The measured vortex nearest the guess (which is the central vortex of the *LG* mode) is stored and used to crop the $z = 0$ data.

A plot of the vortex location in the beam is exported for comparison to ensure the right vortex was selected, as shown in Figure C.5. The data in the figure was

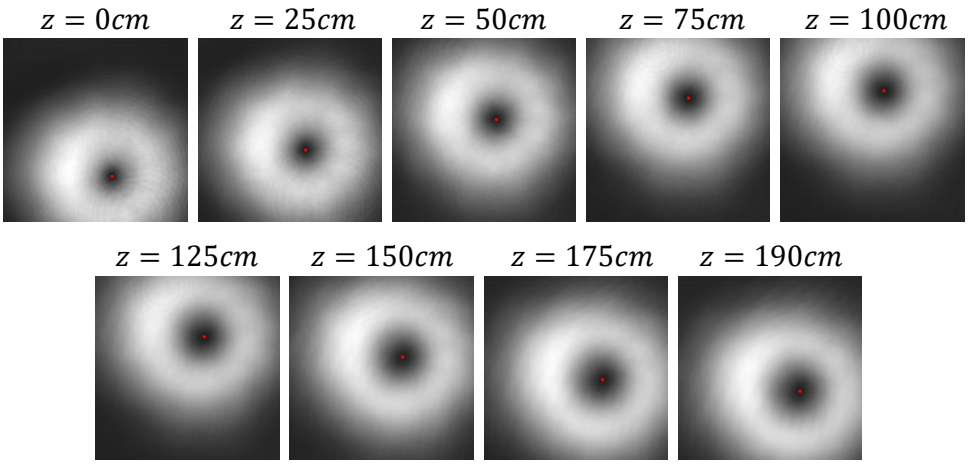

Figure C.5: An example of the center vortex located by real and imaginary zeros for an LG mode used to check the accuracy of the program. The red dots mark the computationally determined vortex location.

taken with the Ball Screw Linear CNC Slide Stroke 1000mm Long Stage Actuator Stepper Motor translation stage used in the two vortex experiments. For this specific set, a small difference in the initial and final positions indicate that the beam is aligned to the same position at the beginning and end of the translation. From the images, we see minimal displacement in the x direction, and large displacement in the y direction, indicating that the stage is bowed. The code used to generate these images and crop the data with a window centered around the located vortex is written out below:

Code Example: Removing beam drift.

```
(* Import 2D .mat data files *)
files=Partition[FileNames["*.mat",NotebookDirectory[]],3];
(* allocate space to store vortex locations *)
priorvortexlocation = Table[0, {i, 1, Length[files]}];
(* read z values from filenames *)
zvals = ToExpression[
   Table[StringDrop[StringDrop[files[[i]], -10],
     StringLength[NotebookDirectory[]]], {i, 1, Length[files
   ]}]];

(* identify first center location based on plot of data at z
   =0 *)
pick=1;
```

```
window=150; (* specify size of cropped window/2 *)

(* import filepaths for data to be used *)
filepaths =
  Table[StringTake[files[[i]],
     3 + StringLength[NotebookDirectory[]]], {i, 1,
     Length[files]}][[;; , 1]];

(* use single vortex data to identify vortex location*)
Filename = files[[pick]][[3]];
fielddata = Import[Filename][[1, ;; , ;;]] /. {Indeterminate
    -> 0};
dim = Dimensions[fielddata];
Clear[vorticesa]
(* identify real and imaginary zeros *)
vorticesa =
  ComponentMeasurements[
    Binarize[
     GaussianFilter[
       ImageMultiply[Image[CrossingDetect[Re[fielddata]]],
        Image[CrossingDetect[Im[fielddata]]]], 1] //
   ImageAdjust],
    "Centroid"][[All, 2]];

(* identify vortex closest to initial guess *)
singindex = Flatten[Round[Nearest[vorticesa, {530, 188}(*
   initial guess for central vortex location*)]]];
priorvortexlocation[[pick]] = singindex;
centimg =
 HighlightImage[
  Image[Abs[fielddata]/Max[Abs[fielddata]],
   ImageSize -> Small], {singindex}]
(* export image to check that the correct vortex was
   identified *)
Export[filepaths[[pick]] <> "highlightimg.png", centimg];


(* use actual vortex location to crop the data for the
   single vortex data and export *)
newfielddata3 =
  fielddata[[(dim[[1]] - singindex[[2]]) -
     window ;; (dim[[1]] - singindex[[2]]) + window,
   singindex[[1]] - window ;; singindex[[1]] + window]];
Export[filepaths[[pick]] <> "croppedfield3.mat",
   newfielddata3];

(* use actual vortex location to crop the data for the same
   charge two vortex data and export *)
Filename = files[[pick]][[1]];
fielddata = Import[Filename][[1, ;; , ;;]] /. {Indeterminate
    -> 0};
dim = Dimensions[fielddata];

newfielddata1 =
  fielddata[[(dim[[1]] - singindex[[2]]) -
     window ;; (dim[[1]] - singindex[[2]]) + window,
   singindex[[1]] - window ;; singindex[[1]] + window]];
Export[filepaths[[pick]] <> "croppedfield1.mat",
   newfielddata1];
```

```
(* use actual vortex location to crop the data for the
   opposite charge two vortex data and export *)
Filename = files[[pick]][[2]];
fielddata = Import[Filename][[1, ;; , ;;]] /. {Indeterminate
    -> 0};
dim = Dimensions[fielddata];

newfielddata2 =
  fielddata[[(dim[[1]] - singindex[[2]]) -
     window ;; (dim[[1]] - singindex[[2]]) + window,
   singindex[[1]] - window ;; singindex[[1]] + window]];
Export[filepaths[[pick]] <> "croppedfield2.mat",
   newfielddata2];
```

C.1.4 Location and Storing the Vortex Locations

As mentioned in Section 6.3, we use real and imaginary zeros to track the field. For the work done in this thesis, the code below was used to locate and store the vortex locations via image processing techniques. A slight Gaussian filter can be applied to reduce the effects of noise in the experimental fields.

Code Example: Locating and storing vortex locations from centered field data.

```
(* import files *)
files = Partition[FileNames["*.mat", NotebookDirectory[]],
   3];
filepathbmp = StringDrop[FileNames["*.bmp",
   NotebookDirectory[]], -4];

(* Allocate space to store vortices for each field*)
vortices1 = {};
vortices2 = {};
vortices3 = {};
(* read z locations from file names *)
zvals = ToExpression[Table[StringDrop[StringDrop[files[[i]],
    -17], StringLength[NotebookDirectory[]]], {i, 1, Length[
   files]}]];

(* identify vortices in each set of images at each z step*)
For[k = 1, k <= Length[files], k += 1,
fielddata = Import[files[[k]][[1]]][[1, ;; , ;;]] /.{
   Indeterminate -> 0};
(* find real and imaginary zeros *)
vorticesa = ComponentMeasurements[Binarize[GaussianFilter[
   ImageMultiply[Image[CrossingDetect[GaussianFilter[Re[
   fielddata], 1]]],Image[CrossingDetect[GaussianFilter[Im[
   fielddata], 1]]]],1] // ImageAdjust], "Centroid"][[All,
   2]];
AppendTo[vortices1, vorticesa];
```

```
fielddata = Import[files[[k]][[2]]][[1, ;; , ;;]] /. {
    Indeterminate -> 0};
vorticesb = ComponentMeasurements[Binarize[GaussianFilter[
    ImageMultiply[Image[CrossingDetect[GaussianFilter[Re[
    fielddata], 1]]],Image[CrossingDetect[GaussianFilter[Im[
    fielddata], 1]]]],1] // ImageAdjust], "Centroid"][[All,
    2]];
AppendTo[vortices2, vorticesb];

fielddata = Import[files[[k]][[3]]][[1, ;; , ;;]] /. {
    Indeterminate -> 0};
vorticesc = ComponentMeasurements[Binarize[GaussianFilter[
    ImageMultiply[Image[CrossingDetect[GaussianFilter[Re[
    fielddata], 1]]],Image[CrossingDetect[GaussianFilter[Im[
    fielddata], 1]]]],1] // ImageAdjust], "Centroid"][[All,
    2]];
AppendTo[vortices3, vorticesc];
]

(*Export vortex data to a new folder*)
Export[StringDrop[files[[1]][[1]], -20]<>"vortices\\
    vortices1.mat", vortices1];
Export[StringDrop[files[[1]][[1]], -20]<>"vortices\\
    vortices2.mat", vortices2];
Export[StringDrop[files[[1]][[1]], -20] <>"vortices\\
    vortices3.mat", vortices3];
```

C.1.5 Measuring and Plotting Vortex Separation

Once the locations are stored, they can be used to calculate relevant quantities such as the vortex separation with propagation. The built in function “Euclidean-Distance" to calculate the separation. An example of the full separation measurement is written here:

Code Example: Measuring vortex separation.

```
(* import vortex location files *)
files = FileNames["*.mat", NotebookDirectory[] <> "vortices
    \\"];

(* convert pixels to physical dimensions using pixel size *)
vortices1 =
  5.5*10^-3*Import[StringDrop[files[[1]], -13] <> "vortices1
    .mat"];
vortices2 =
```

```
  5.5*10^-3*Import[StringDrop[files[[1]], -13] <> "vortices2
    .mat"];
vortices3 =
  5.5*10^-3*Import[StringDrop[files[[1]], -13] <> "vortices3
    .mat"];

(*convert z values to mm *)
zprop = Table[zvals[[i]][[1]], {i, 1, Length[zvals]}]*10;

(*measure vortex separation for the same charge vortex pair
    *)
dist1 = Table[EuclideanDistance[vortices1[[i]][[1]],
    vortices1[[i]][[2]]], {i, 1, Length[vortices1]}] // N;
points1 = Partition[Flatten[Riffle[zprop, dist1]], 2];
p1 = ListPlot[points1, PlotRange -> {{0, 2000}, {0, 1.5}},
    PlotStyle -> Red];

(*measure vortex separation for the opposite charge vortex
    pair *)
dist2 = Table[EuclideanDistance[vortices2[[i]][[1]],
    vortices2[[i]][[2]]], {i,1, Length[vortices2]}] // N;
points2 = Partition[Flatten[Riffle[zprop, dist2]], 2];
p2 = ListPlot[points2, PlotRange -> {{0, 2000}, {0, 1.5}},
    PlotStyle -> Blue];

(* plot separation together with formatting *)
FinalPlot =
 Labeled[Show[p1, p2, ImageSize -> {600, 400}, Frame -> True
    ,
    FrameStyle -> Directive[Black, 16, FontFamily -> "
    Helvetica"],
    PlotLabel -> Style[" w0 = 1.553  vs = 0.594mm  \!\(\*
    SubscriptBox[\(c\ \), \(r\)]\) = Linear ", Black, 16,
    FontFamily -> "Helvetica"]], {Style["Separation (mm)",
    Black, 16, FontFamily -> "Helvetica"], Style["Propagation
     Distance (mm)", Black, 16, FontFamily -> "Helvetica"]},
    {Left, Bottom}, RotateLabel -> True]
```

The output plot from the code is displayed in Figure C.6. The separation between both opposite (blue) and like (red) charge pairs are shown with propagation for fitted beam parameters $w_0 = 1.553$ mm, $v_s = 0.594$ mm, and linear cores. The separation shows an annihilation event between the oppositely charged vortex pair while the same charge vortex pair appears to be at roughly the same separation throughout the propagation for the data set used here.

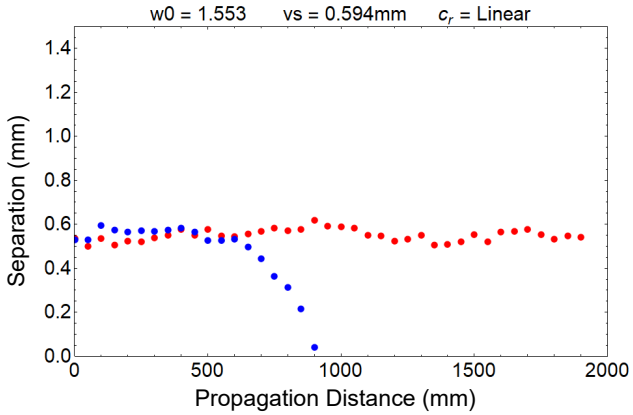

Figure C.6: The resulting vortex separation plot from the Mathematica code of Section C.1.5.

C.4 Modal Decomposition Code

The modal decompositions described in Sections 5.3.1 and 5.3.2 are done digitally using Mathematica. The code first downsamples the experimental data and crops the field around the beam center. A set of digital LG filters are created, and the overlap between the experimental field and each digital filter is calculated to build a full ℓ, p spectrum. The total ℓ mode content is also calculated. The full code is found just below.

Code Example: Modal decomposition on data.

```
(* Import amplitude and phase data *)
am = NotebookDirectory[]<>"LG-1amp.txt";
ph = NotebookDirectory[]<>"LG-1phase.txt";
beam = (Sqrt[Abs[Import[am, "CSV"]]] Exp[I Import[ph, "CSV"
   ]]);

(* downsample data for processing *)
input = Downsample[beam, 10];

(* find beam center using image processing *)
cent2 = ComponentMeasurements[MorphologicalComponents[
   Binarize[Image[Sqrt[Abs[input]]/Max[Sqrt[Abs[input]]]],
   .95]],"Centroid"];

(* crop the data to a 100X100 window around the beam *)
window=49;
```

```
cropinput = input[[Round[cent[[2]]]-window;;Round[cent
    [[2]]]+(window+1)]];
fullcropinput =
  cropinput[[All,Round[cent[[1]]]-(window+1);;Round[cent
    [[1]]]+(window+1)]];

(* Create definitions needed for modal decomposition *)
(* mathematical form of LG mode*)
LGfull[m_, q_]=Sqrt[(2 Factorial[q])/(\[Pi](Factorial[q+Abs[
    m]]) )] 1/wz ((r*Sqrt[2])/wz)^Abs[m]*Exp[-r^2/wz^2]
    LaguerreL[q,Abs[m],2r^2/wz^2]*Exp[I \[Phi] m]*Exp[+I k r
    ^2/(2 Rz)]*Exp[-I (Abs[m]+2 q+1)ArcTan[z/zR]];

wz=w0 Sqrt[1+(z/zR)^2];(* beam waist divergence *)
Rz=z(1+(zR/z)^2); (* radius of curvature *)
zR=\[Pi] w0^2/\[Lambda]0; (* Rayleigh length *)
k=2\[Pi]/\[Lambda]0; (* wavenumber *)
\[Lambda]0=632*^-9; (* laser wavelength*)

pix = 7.7 10^-6; (* size of pixels on camera *)
x0 = 0;(* x shift of digital filter center in fraction of a
    pixel*)
y0 = 0;(* x shift of digital filter center in fraction of a
    pixel*)

(* Center LG based on inputs above*)
LGcentered[m_, q_] =
  LGfull[l, p] /. {w0 -> .0021049, z -> 1*10^-10,
    r -> Sqrt[(x - pix x0)^2 + (y - pix y0)^2], \[Phi]->
    ArcTan[y - pix y0, x - pix x0], l -> m, q -> p};
yRange = 2*5*^-3; xRange = yRange;
Nsteps = 100;
xStep = 2*xRange/Nsteps; yStep = xStep // N;

(* Create digital filters over l-p spectrum *)
tabs = Monitor[Table[img1 = ParallelTable[LGcentered[l,p],{x
    , -xRange - xStep/Nsteps, xRange - xStep, xStep}, {y, -
    yRange - xStep/Nsteps, yRange- yStep, yStep}], {l, -10,
    10}, {p, 0, 10}]
, {l, p}];

(* calculate overlap of data and digital filters *)
cc = Monitor[Table[input2 = tabs[[m, p]] fullcropinput[[1 ;;
    100, 1 ;; 100]]; Total[Total[input2]], {m, 1, 21}, {p,
    1, 11}], {m, p}];

(* Calculate the projection onto l to measure vortex purity
    *)
ll = {};
For[i = 1, i <= 21, i++,
 AppendTo[ll, Total[((Abs[cc]^2)/Max[Abs[cc]^2])[[i]]]]]
purity = ll[[12]]/Total[ll[[1 ;; 21]]];
```

Appendix D: Outreach

While pursuing an intense degree with many pressures, deadlines and never ending to do lists, it can feel impossible to find the time to do outreach. Yet, it is one of the most important aspects of the scientific field. Outreach not only helps foster interest and curiosity amongst younger students who will become the next generation of scientists, but it also increases our own ability to communicate complex material to others in an accessible way. This is an often underdeveloped skill set amongst scientists, and in an age of misinformation and pressing issues relevant not only to scientists, but the general population and their quality of life, it is more important than ever for those doing the work to save a little time for outreach. Outreach can be an ongoing process and doesn't require formal events to do so. Reach out to your friends and family, kids that they might have, and bring outreach as a mindset into your daily life.

Through my time at DU, I was fortunate to participate as a camp counselor for both the "Femme in STEM" summer camp (2017) and the "DU SciTech" summer camp (2017, 2019). The latter was organized and run by Prof. Shannon Murphy, Associate Prof. Robin Tinghitella, and Prof. Jennifer Hoffman. The camp included many fun activities for students to engage in concepts, current research and the scientific process. It also included tours of our (and other graduate students') labs. In my lab tours, I used holograms to generate fun patterns in beams for young

folks that included pop culture references and other topics relevant to their lives. Examples are shown in Figure D.1.

In the most recent SciTech camp before the pandemic hit, the students were able to engage in real research including devising an experiment under the guidance of Prof. Shannon M. Murphy (and the rest of the adults in the camp), going out into the field, and taking real data [190]. This resulted in a publication (with the writing and analysis pushed forward by Prof. Shannon M. Murphy, Teaching Assistant Prof. Dhaval Vyas, and Associate Prof. Robin Tinghitella) of girls in the summer camp and the graduate students who participated [191]. With creativity, guidance, and collaboration, leading scientists can create inclusive environments to engage younger students that also results in tangible and impactful outcomes for both parties involved.

I also hosted a lab tour for high school students, co-presented with fellow students Alisha Humphries and Angie Davidson in a faculty meeting centered around gender discrimination issues, attended Inclusive Excellence workshops run by the Director of Inclusive Teaching, Dr. Valentina Iturbe-LaGrave, and consistently engaged in inclusive practices throughout my PhD. I was lucky to participate as an

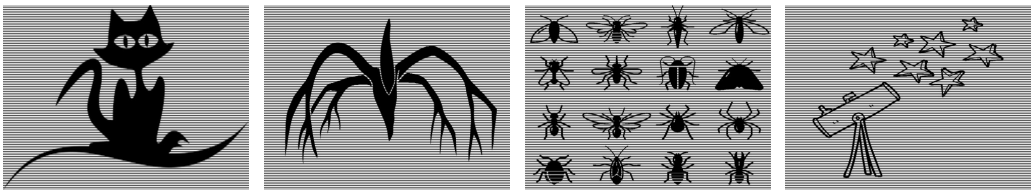

Figure D.1: A set of gratings is shown that were used during lab tours, particularly inspired by the DU SciTech Summer Camp. Included are (a) a cat hologram, (b) a Mind Flayer [178] hologram, (c) a set of insects inspired by the entomology unit of the summer camp, and finally (d) a telescope hologram inspired by the astronomy/optics section of the summer camp.

assistant for one quarter in the Academic Excellence Workshops spearheaded, designed, and implemented by Angie Davidson during her time at DU. These workshops were made to provide extra help specifically to the bottom third of the students in the University physics classes, and the preliminary data showed a positive increase in the grades of students who participated. I am grateful to have had an opportunity to make a difference and work with Angie in this, even for a short time.

I also must mention that I am grateful for the support and community of the American Association of Physics Teachers CO/WY section. I have been a board member since 2017, and that is because of the tremendous amount of support I have received from the organization, starting all the way back in my undergraduate years. I have been able to meet high school teachers, professors from other universities, participate in and see wonderful demonstrations (with many thanks to The Little Shop of Physics at CSU for their incredible outreach efforts) and better enjoy the process of my career development. I strongly encourage anyone in the CO/WY region to participate.